



SAPIENZA
UNIVERSITÀ DI ROMA


Dark sector searches in final states with long-lived or prompt neutral particles with the ATLAS detector and upgrade of the L0 muon trigger for HL-LHC

Scuola di Scienze Matematiche Fisiche e Naturali
Scuola Dottorale Vito Volterra
Dottorato di Ricerca in Fisica (XXXVI cycle)

Elena Pompa Pacchi

ID number 1583418

Advisor

Prof. Stefano Giagu 

Co-Advisor

Dr. Valerio Ippolito 

Director

Federico Ricci Tersenghi

Academic Year 2023-2024



A thesis submitted in partial fulfillment of the requirements for the degree of Doctor
of Philosophy in Physics, May 2024

**Dark sector searches in final states with long-lived or prompt neutral particles
with the ATLAS detector and upgrade of the L0 muon trigger for HL-LHC**
Sapienza University of Rome

© 2024 Elena Pompa Pacchi. All rights reserved

This thesis has been typeset by L^AT_EX and the Sapthesis class.

Author's email: elena.pompapacchi@uniroma1.it

Ad Alessandro

*I was lying on the grass
Thinking about your opinion on my past
You said: "You, you'll never reach the skies
And you'll never see the world with eagle eyes"
Oh no...*

*So I sat and stare at the stars
And I felt like a fever in my arms
And a spell on my mind
My head was aching and my eyes where blind
Oh no... See, I jumped on an air balloon and I flied the skies*

*Took a trip at light speed on the Enterprise
I traveled on my legs for a hundred miles or more
And I danced 'till my feet felt sore
I danced 'till my feet felt sore*

Acknowledgements

I consider myself a lucky person. I have many people to thank for these years and these will be, in full Elena style, very long acknowledgements.

First of all, I would like to thank Stefano Giagu and Valerio Ippolito for their support during these PhD years, for their suggestions and guidance. I am also grateful for the opportunities I have been given thanks to the Rome-1 ATLAS group.

Without Cristiano and Iacopo this thesis work would not exist. I am grateful for all their help, affection and for believing in me. I know they always had my back and I owe them a lot. I had the chance to see in Cristiano how to be an happy researcher, and in Iacopo how to learn and grow together with others.

I want to thank Luis for joining the analysis effort and teaching me so much in such a short time, always with a smile and lots of excitement.

Thank you Tingyu, for sharing these PhD years with me. And thanks to Bernardo, for being a kind and humble master student.

I want to thank all the Rome-1 ATLAS PhD students (past and present) who were friends to me. Their support was important. Specifically, I want to thank Graziella for our Doctoral Student experience. Sharing our struggles (but not your snacks!) made us stronger. I want also to thank Davide, whose positivity has always shedded a light into his surroundings.

I want to thank Luca for being one of my best supporters and for telling me to get out of my own way. However, please reduce the amount of stupid jokes.

I am grateful to Giuliano for listening with interest and respect. And to Francesco, for your suggestions in front of a dahl.

I was lucky enough to be part of different PhD groups that were my compass during hard times. They were examples of how to give to the University community without asking anything back in return. I am grateful to the PhD seminars group and its members through these years for the fights we engaged in (almost all won!) to let the PhD community be more active and lively. I particularly cherish the moments spent with the Gender Balance Working Group, our fruitful discussions and our efforts to make our Physics Department a more welcoming place for everybody.

Among the opportunities I have been given, the ones that really changed my PhD experience were the Physics School I attended. I met many beautiful people from all over the world who had enriched me deeply.

In the first Physics School I attended, in Paestum, I met Diego, with whom I shared a single morning run and then I bailed all the others. Thanks for still being my friend.

In the ISOTDAQ School, I had the luck to become close friend with Leonardo, Luigi and Roy. Thank you guys for being an example of friendship and love despite our differences and for discovering together “Il Professore”.

In my last school, ESHEP in Greena, I met a wonderful group of good friends and good people, with a positive and happy attitude towards life. I want to thank Ana for our instantaneous and genuine connection and Arnau for our beautiful friendship that has grown with time.

I am grateful to Beth, I am so happy we found each other again after Pisa. Thank you for supporting me and understanding me and for having shared so much with me in all these years. It will be strange to “finally” not be in the same University but I know we will always be friends.

To Rodrigo and Lorenzo P., to our dinners, walks, laughs. Thank you for being part of this journey.

I am so lucky to have found Flore and Julie, my flatmates without whom my thesis writing would have been much more painful. Thank you for looking out for me and accepting my messiness in those days, I felt accepted and loved. I want to particularly thank Julie for starting this co-living journey together though the initial conditions were, at the least, sub-optimal.

I also want to thank Almu, you have been an important part of my Geneva year, being a safe harbour to which I could get back. Thank you for introducing me to your friends, and particularly to Diksha, who is always full of energies and inspiring.

I am grateful for the CERN community I was immediately welcomed by, for the climbing, the hiking, the pizzas, the fondues.

I am finally extremely happy of being part of the ATLAS EXOTICS community and in particular of UEH. Seeing the wit of the members, their passion and their positive attitude towards research has always been inspiring.

I want now to thank the many people who supported me throughout all these years, though they had not worked directly with me and even if they were afar.

I want to thank Chiara B., for sharing with me our first steps into the Physics world, for Clebsh-Gordan, for our shared studies but even more so for everything else. Thank you for being a real friend and for showing me how to love each other even when we don't agree. Thank for introducing Marco C. to my life, that, despite his strange love for rocks, I am happy to have met.

I want also to thank Federica, for your friendship and for being my bit of Rome in Geneva. Thank you for Agostino, who, even though he dissimulates, is grateful for me too.

I had beautiful friendships in my high school years too, and I am lucky that most of them are still here after many years. I want to thank Giovanni B. for his

friendship which I never doubted. I am grateful to Giulia T., who has always been a true friend since the beginning. I really thank Paolo, who is one of the smartest and kindest people I have ever met, and with whom I always had a very genuine friendship, with fights, differences, but most of all love. I want to thank Mattia, that has shared this path with me, from high school until the end of the PhD. It will be strange not being in the same institution anymore, after all these years.

I really have to thank the Sant'Agnese Idoli group. As we often say, you are my second family, my safe place where I feel loved. We were filled with joy and shattered by pain, and seeing how we shared both these things with the same commitment, emotion and deepness really tells me how lucky I am to have met all of you. Each and every one of you holds a very special place in my heart.

I am also grateful for the Sant'Agnese educators I shared my path with. You were a big part of my PhD years too and we have always been an amazing team. Thank you to all the Confirmation group, which welcomed me from day one. I want to thank Laureana, for accepting this challenge and for wanting me to be her partner in this. We really understand and cherish each other, despite our differences (and our inability of telling us so).

I am grateful to the Supergang. You were one of the things I missed the most in Geneva and seeing you grow in these years was an honour.

I am really thankful to Adriana, Alice L. and Edoardo P.; thank you for loving me and for seeing in me things that I don't see myself. Being able to accompany you for part of your life has always been a true pleasure.

I want to thank Chiara M., Giulia S. and Elisa. For being always my supporters and real friends. I am thankful to Chiara M., for being my classmate since we were three years old until the end of high school. Growing up together has always been enriching and we challenged and inspired each other to be our better version. I am grateful to Giulia S., for being one of the people that understands me most. Thank you for making me feel as one of your priorities even when I am not able to do the same. I really want to thank Elisa, I know that if I call you you will be there. We shared so much and we have seen really the beautiful and the ugly bits of each other, and we are still here.

I want to thank Riccardo, for growing together between school, beaches, deserts, mountains, and still being friends and support each other.

To Marco, who, like a true brother, struggles to show his affection but never fails me.

I am extremely grateful to all my family. I know how lucky I am and how much this is uncommon, so I really want to thank all of them, and life in general, for handing me this gift.

I want to thank my brother, who always hopes what's best for me and who encourages me to take my life in my own hands. We are different and I don't always accept your suggestions, but I never once doubted they come from a place of love. I am grateful of being your sister and having shared our lives.

I want to thank my parents, who, as all parents, have an extremely difficult job.

I have always felt supported, encouraged and enabled to follow whichever path I had set myself to. Thank you for not pushing me in any direction, besides the one leading me to better myself day by day. You have always been there along the way, walking next to me. Thank you for doing so when I fell down, when I got back up and when I won a race. I never doubted your love.

I want finally to thank Farshid, who has been always by my side in this Physics journey. Thank you for having been a partner of studies, laboratories, exams. Thank you for being now a partner in this researchers' life. Thank you for being a friend and a life partner. Thank you for being there in all the important moments of my life, sad ones and joyous ones. I feel loved and seen like with nobody else. I am truly inspired by your optimism, your hope and your constant effort to shape your present so to get closer to your desired future, and I look forward to sharing it with you.

This thesis is for all of you.

And for me.

Abstract

Dark Matter (DM) is one of the outstanding questions to which the Standard Model (SM) of particle physics still has no answer. There is a large body of evidence which points to the existence of a non-baryonic matter component in the Universe, interacting with ordinary matter only through gravity. Weakly Interactive Massive Particles (WIMPs) have always been an appealing DM candidate, as they naturally account for the amount of DM seen nowadays. For this reason, different experiments have been developed in order to detect these elusive particles, but so far they have all proved to be inconclusive.

In recent years, a new paradigm has started to be investigated, in which a new sector of particles, the so-called Dark Sector (DS), is foreseen. In such a scenario, the DM would be a stable particle among those predicted in the DS. Particles in this new sector are neutral under all SM forces and the connection between the dark and the visible sector is granted through different *portals*, in which SM particles mix with Beyond the Standard Model (BSM) ones.

This work exploits the simplest DS model, foreseeing a dark interaction which is similar to the electromagnetic one, mediated by a so-called Dark Photon (DP). In this case, the connection between the two sectors can be granted via the *vector portal*, where the dark and the visible photons mix kinematically, so that the DP can decay into SM particles. Such models have been investigated thoroughly and no evidence of DPs have been found up to now. The region with a small coupling between the two sectors and large DP masses is accessible only at Higgs factories, such as the Large Hadron Collider (LHC), where an additional connection between the dark and the visible sector can be granted via the *Higgs portal*. Through such portal, the SM Higgs boson can decay into BSM particles, this possibility being viable since Higgs boson decays into invisible particles are still largely unconstrained.

Using the dataset collected during Run-2 by the A Toroidal LHC ApparatuS (ATLAS) experiment at the LHC, this work investigates the scenario where the DPs decay inside the ATLAS innermost detector, yielding collimated jet-like structures. This search aims to extend the sensitivity of the Run-1 search that was targeting the same final state, by improving the reconstruction techniques (both at the online and at the offline level) and by exploiting new background estimation strategies. Preliminary results already show better sensitivities than those obtained in the Run-1 search, probing a larger DP mass range.

This work investigates in addition for the first time the possibility that the coupling between the SM photon and the dark one is so suppressed that DPs decay outside the ATLAS detector. DPs escaping detection would leave missing energy as signature of their passage, which could be sizeable if recoiling against highly energetic jets. Final states with this signature, referred to as *monojet*, are thus here used to probe this scenario. The results of this search are presented in terms of both this DP already introduced and for two additional models foreseeing the production of Long Lived Particles (LLPs) too. Complementary sensitivities with respect to the ones of the different dedicated searches are observed, probing previously uncovered scenarios with detector stable LLPs.

Searches for unconventional final states, like the ones described in this thesis, are mostly limited by the trigger system, which performs an online event selection that often discards non-standard events. Increasing the performance of this system is thus of utmost importance to improve the sensitivity to such BSM scenarios. Such performances will be even more crucial during the High-Luminosity (HL) phase of the LHC, where the trigger system will have to cope with 200 pp collisions occurring every event. Therefore, this thesis will cover as well a study dedicated to the upgrade of the trigger system of the ATLAS experiment, that is necessary for the correct operation under the conditions of the HL-LHC.

Contents

1	The Standard Model of Particle Physics	5
1.1	An introduction	5
1.2	Electro-Weak Spontaneous Symmetry Breaking	6
1.3	Higgs boson properties	10
1.3.1	Higgs production in pp collisions	11
1.3.2	Higgs decay modes	12
2	Dark Matter and Dark Sector	14
2.1	Dark Matter evidence	14
2.1.1	Galactic scale: galaxies rotational curves	15
2.1.2	Cluster of galaxies: Gravitational lensing	16
2.1.3	Cosmological scale	18
2.2	Dark Matter halo	22
2.3	Standard Dark Matter candidates	23
2.3.1	Astrophysical candidates and experimental constraints	23
2.3.2	Particle candidates and experimental constraints	23
2.3.3	Particle candidates and the WIMP miracle	25
2.4	Unconventional Dark Matter candidates: Dark Sector	29
2.4.1	Vector portal and Gauge sector	30
2.4.2	Higgs portal and Higgs sector	33
2.4.3	Dark Sector simplified models	36
3	The ATLAS experiment at the LHC	39
3.1	The CERN facility	39
3.1.1	The CERN accelerator complex	39
3.1.2	The LHC	40
3.1.3	pp collisions, bunch filling scheme, luminosity and Pile-Up	42

<i>CONTENTS</i>	10
3.2 ATLAS detector	46
3.2.1 Coordinate system	48
3.2.2 Magnet system	49
3.2.3 Inner Detector	50
3.2.4 Calorimeter system	52
3.2.5 Muon Spectrometer	54
3.2.6 Trigger system	56
3.2.7 Event simulation	58
4 Physics objects reconstruction in ATLAS	61
4.1 Tracks and vertices	61
4.2 Jets	63
4.2.1 Jets reconstruction	63
4.2.2 Jets calibration	65
4.2.3 Jets identification	66
4.3 Missing Energy Transverse	69
4.4 Electrons and Photons	69
4.4.1 Reconstruction	70
4.4.2 Identification and isolation	72
4.5 Muons	74
4.5.1 Reconstruction	74
4.5.2 Identification and isolation	75
4.6 Overlap Removal	78
5 Prompt Dark Photon signatures at the ATLAS experiment	80
5.1 Data and simulated event samples	80
5.1.1 Full Run-2 dataset	81
5.1.2 MC samples	81
5.2 Signal MC truth-level kinematics	82
5.3 Muons and electron reconstruction	85
5.3.1 Isolation for collimated muons	86
5.3.2 Collimated electrons	90
5.3.3 Overlap removal	91
5.4 Prompt Lepton-Jets reconstruction	92
5.4.1 Muonic Lepton-Jets reconstruction efficiencies	93

5.4.2	Electronic Lepton-Jets reconstruction efficiencies	95
5.4.3	Selection criteria for Lepton-Jets	100
5.4.4	Invariant mass reconstruction	101
5.5	Triggers	102
5.5.1	Muonic channel triggers	103
5.5.2	Electronic channel triggers	108
5.5.3	Mixed channel triggers	111
5.5.4	Benchmark samples trigger efficiency	112
6	ATLAS full Run-2 search for prompt Lepton-Jets	114
6.1	Events selection	114
6.1.1	Muonic channel	115
6.1.2	Electronic channel	116
6.1.3	Mixed channel	121
6.2	Background estimation	123
6.2.1	Bump-hunt for muonic Lepton-Jets	124
6.2.2	ABCD method for the electronic channel	146
6.3	Systematic Uncertainties	153
6.3.1	Experimental systematics	154
6.3.2	Signal model uncertainties	160
6.3.3	Background modelling systematics	162
6.4	Results for the electronic channel	167
6.4.1	Fitting technique	167
6.4.2	Expected sensitivity	168
6.5	Results for the muonic and mixed channel	169
6.5.1	Fitting technique	169
6.5.2	Expected sensitivity for the mixed channel	170
6.5.3	Observed limits for the muonic channel	172
6.6	Comparison with the Run-1 search	176
7	LLPs search using the monojet signature	178
7.1	The life-time frontier	179
7.2	Data and simulated event samples	180
7.2.1	Full Run-2 dataset	180
7.2.2	Monte Carlo simulated samples	180

7.3	Monojet search in a nutshell	181
7.3.1	Analysis regions	182
7.3.2	Fitting technique	184
7.3.3	Systematic uncertainties	185
7.4	MC signal samples reweightings	186
7.4.1	Higgs p_T reweighting	186
7.4.2	Life-time reweighting	187
7.5	Reinterpretation results	190
7.5.1	Constraints for the FRVZ benchmark model	191
7.5.2	Constraints for the $H \rightarrow ss$ benchmark model	194
8	The ATLAS Phase-II upgrade of the L0 barrel muon trigger	196
8.1	Overview of the ATLAS Phase-II upgrade	197
8.1.1	The Inner TracKer	197
8.1.2	The High Granularity Timing Detector	197
8.1.3	The calorimeter system	197
8.1.4	The muon system	198
8.1.5	The TDAQ	198
8.2	The ATLAS L0 muon barrel trigger upgrade	198
8.2.1	Overview of the TDAQ interface	199
8.2.2	SL FPGA-SoC interface	201
8.2.3	MPSoC interface test using the ZCU104 evaluation board . .	205
9	Conclusion	219
	List of Acronyms	222

Introduction

The Standard Model (SM) of particle physics has been tested thoroughly in the past few decades, looking for discrepancies that could explain some of the open issues of the theory, such as the matter-antimatter asymmetry or the existence of Dark Matter (DM). As no evidence of new physics has been found up to now, new and more complex searches have started to take place in High Energy Physics experiments, such as the ATLAS experiment. These searches rely on the assumption that there exists a Dark Sector (DS) made of new particles neutral under all SM forces and governed by new kinds of interactions. So-called portals grant a connection between the DS and SM particles. In such searches, the interest is shifted from the structure of the new hidden interactions towards their mediators.

This work investigates thoroughly the hypothesis that the Dark Sector is governed by an interaction arising from the $U(1)_d$ symmetry group and whose mediator is called Dark Photon (DP) γ_d . Dark Photons could be massless or massive, and they could decay back into SM particles by coupling to SM photons, via the so-called *vector portal*. If this coupling is suppressed, Dark Photons can acquire a sizeable mean proper life time.

Dark Photons have been looked for since their theorisation by many different experiments, assuming that they are produced and that they decay through the vector portal. As no conclusive evidence of DPs has been found up to now in such scenarios, constraints on the free parameters of these models, namely the DP mass and its coupling to the visible sector ε , are found. Extremely light and prompt DPs are already ruled out, while heavier DP hypotheses and smaller couplings to the visible sector are accessible only assuming an additional connection between the dark and the visible sector, through which the DP could be produced.

In collider experiments, such a connection is often assumed to be granted by the so-called *Higgs portal*, where the SM Higgs boson couples with a dark Higgs boson (which provides masses to all DS particles, analogously to the SM Higgs boson) allowing for Beyond the Standard Model (BSM) decays of the SM Higgs boson. This possibility is viable since invisible decays of the Higgs boson are still not ruled out, with an upper limit on $\mathcal{B}(H \rightarrow \text{inv})$ of the order of 10%.

This thesis work assumes the existence of both these portals, so that the SM Higgs boson decays through the Higgs portal into DS particles, and among these DPs are produced. Such DPs decay back into SM particles via the vector portal. Different DP masses and different strengths of the coupling between the dark and

the visible photon produce different signatures in the detectors, leading to different analysis techniques to detect them.

I investigated this DS model exploiting the full Run-2 dataset collected by the ATLAS collaboration.

For the first part of my work, I focused on the possibility that DPs decay promptly inside the ATLAS Inner Detector (ID), producing collimated pairs of soft SM fermions. This is the first search investigating such a scenario using the Run-2 dataset collected by the ATLAS experiment, and it aims at probing a wider parameters space than that probed in the Run-1 search. A wider DP mass range is investigated, from $m_{\gamma_d} \in [0.2, 2]\text{GeV}$ probed during Run-1 to $m_{\gamma_d} \in [0.017, 15]\text{GeV}$ studied here. This mass range is tested assuming $\mathcal{B}(H \rightarrow \text{inv}) < 10\%$.

This search looks for DPs decaying only into light leptons (electrons and muons), since other decays would be indistinguishable from the multi-jet backgrounds. In the investigated mass range, the DP are so boosted and the light leptons are so collimated that they are reconstructed as a single object known as *prompt Lepton-Jet* (*pLJ*). LJs are referred to as *muonic* LJs (μLJs) if only muons are found within their cone and *electronic* LJs ($e\text{LJs}$) if they are built only with electrons. To enhance the sensitivity to these DP models, events in which a pair of pLJs is produced are searched for. Three *search channels* are thus defined as follows: the muonic channel, with two μLJs , the mixed channel, with one μLJ and one $e\text{LJ}$, and the electronic channel, with two $e\text{LJs}$.

I am the main analyser of the muonic channel and I supervised a master student in the study of the mixed channel. I contributed to the development of the common framework for the analysis as well to studies for the electronic channel, specifically regarding the $e\text{LJ}$ reconstruction.

In the muonic channel, in order to cope with the high multiplicity, collimation and softness of the reconstructed muons, I developed an ad-hoc trigger strategy as well as a corrected isolation computation, the latter exploited in the mixed channel as well.

In both the muonic and the mixed channels, a very good resolution of the μLJ invariant mass is observed. Thus, for these channels the so called *bump-hunt* technique is exploited for the background estimation, where the background modelling is tested in a dedicated CR defined per each channel. The signal is also modelled, both in terms its shape and of its normalisation, in order to probe different DP masses than the simulated ones.

Electrons in $e\text{LJs}$ are so collimated that they are often reconstructed as a single electron. The resulting channel signature yields a very large number of background events. For this reason, different selections are applied onto $e\text{LJs}$ to reduce the otherwise overwhelming background.

In addition, $e\text{LJs}$ show a poorer reconstruction in terms of their invariant mass. The background estimation in the electronic channel thus cannot rely on the bump-hunting technique, and instead the so-called *ABCD method* is employed.

I presented the results of my work at the 2022 SIF national congress, where my

talk in the parallel session was awarded as one of the best communications at the conference [1].

I then extended my work towards the possibility that the coupling between the visible sector and the DPs (or a new scalar mediator) is extremely suppressed, so that DPs are so long-lived that, after being produced, they decay outside the ATLAS detector. Such a scenario could be investigated by looking for events with high missing energy, which could be sizeable when recoiling against a highly energetic jet, yielding the so-called *monojet* signature. For this reason, the *monojet* search [2] has been reinterpreted in the context of extremely long lived Dark Photons (or new hidden scalars). I was the main analyser of this work and in this context I investigated the sensitivity of this search to the different LLP models and decay channels and I developed a procedure to extrapolate (and interpolate) the constraints obtained for LLP mean proper life-times that were not simulated.

This search extends the sensitivity of previous dedicated searches to life-time ranges never covered before. Specifically, assuming a $\mathcal{B}(H \rightarrow \text{inv}) = 50\%$, $\varepsilon \leq 3 \cdot 10^{-6}$ is excluded for $m_{\gamma_d} \in [0.2, 0.6] \text{ GeV}$ while $\varepsilon \leq 2 \cdot 10^{-6}$ is excluded for $m_{\gamma_d} > 0.6 \text{ GeV}$.

I presented the results of my work, which were published in Ref. [3], at the LHC Physics (LHCP) conference in 2021 (poster [4] and proceeding [5]), as well as at the 2021 Società Italiana di Fisica (SIF) national congress, where my talk in the parallel session was awarded as one of the best communications at the conference [6].

The main challenges of BSM searches which foresee unconventional signatures, such as the ones described in this thesis, are usually met at the trigger level. As an example, muons arising from DP decays are often so collimated that they fall within the same so-called Region Of Interest (ROI). As the muon trigger can only select one muon candidate per ROI, such an event would be reconstructed as a single muon event, thus losing sensitivity to high multiplicity and collimated final states. In addition, muon triggers constrain muons to come from the reconstructed pp collision vertex, loosing sensitivity to displaced non-pointing scenarios. A finer granularity of the ROIs or the ability to consider multiple candidates within the same ROIs would imply faster trigger algorithms as well as their parallelization. The removal of the constraint on the pp collision vertex would imply instead a Trigger and Data AcQuisition (TDAQ) system able to cope with busier environments with larger event rates. Improving the performances of the trigger system so to include these features would thus greatly benefit searches for unconventional final states.

Trigger performances will be even more crucial during the next ATLAS data taking, where the number of pp collisions per second will increase by a factor of five, with more than 200 pp collisions happening per event. In this phase, referred to as High-Luminosity (HL), an extensive upgrade plan of the Large Hadron Collider (LHC) experiments is foreseen, in order to cope with the extreme conditions that will be reached.

The ATLAS muon trigger system will be upgraded in order to deal with the higher pile-up and provide a more effective event selection. Additional Resistive Plate Chamber (RPC) detectors will be installed and the electronics connecting the

existing ones with the rest of the ATLAS TDAQ system will be upgraded.

The new Barrel Sector Logic (SL) will exploit fast trigger algorithms, implemented in the firmware of a large Field Programmable Gate Array (FPGA), providing muon candidates to the ATLAS central trigger. FPGAs will play a fundamental role in the HL-LHC phase, as they allow programming of highly complex systems by combining a large number of small, simple elements, offering a high flexibility of the board after the hardware is built. In this way, the development of more complex trigger algorithms selecting signatures arising from BSM scenarios will be possible.

The Rome group is responsible for all the RPC-based trigger and for the L0Muon trigger logic in the ATLAS Barrel region. Monitoring and configuring the FPGA that will perform the trigger algorithm is a crucial task performed by a so-called Multi-Processor System on Chip (MPSoC), an on-chip multi-core Central Processing Unit (CPU). I developed a communication protocol between the MPSoC and the FPGA, allowing for the monitoring and initialization procedures.

This manuscript is organised as follows. Chap. 1 gives a very brief outline of the SM, with particular focus upon the Electro-Weak Spontaneous Symmetry Breaking and the Higgs boson production mechanisms and decay modes. In Chap. 2, evidence pointing to the existence of DM is discussed and DM candidates are described along with their experimental constraints, with particular focus on Weakly Interactive Massive Particle (WIMP)s. The DS paradigm is then introduced, with specific focus on the portals assumed in this thesis and the simplified DS models exploited. Chap. 3 covers the ATLAS experiment at the LHC, focusing on the LHC working conditions during Run-2 as well as on the different ATLAS sub-detectors and their performances. In Chap. 4, the procedure of assigning detectors signals to physics object candidates, such as electrons and muons, are described along with their performance. Chap. 5 and Chap. 6 give instead an overview of the search for promptly decaying DPs, focusing respectively onto the online and offline reconstruction of such signature and onto the background suppression and estimation, the systematic uncertainties evaluation and the results of the search. In Chap. 7, instead, the search for detector stable DPs (or hidden scalars) using the *monojet* signature is described, along with its results. Finally, Chap. 8 covers the future upgrades that the ATLAS detector will undergo, with particular focus onto the muon trigger system in the barrel and onto the work I carried out in this context.

Chapter 1

The Standard Model of Particle Physics

The Standard Model (SM) is the model that now best describes the matter constituents and the interactions among them. In this chapter a brief overview of the SM is given in Sec. 1.1, highlighting the Electro-Weak (EW) Spontaneous Symmetry Breaking (SSB) via the Higgs boson in Sec. 1.2. A review of the Higgs boson properties can be found in Sec. 1.3, with a focus on the Higgs boson production and decay modes in pp collision, as they are relevant for this thesis work.

1.1 An introduction

The SM is the cornerstone of modern particle physics, offering a comprehensive framework to understand the properties and interactions of known particles, excluding gravity. It's constructed within the principles of quantum field theory, where particles are depicted as quantum fields governed by the Lagrangian.

Particles exhibit distinct behaviours based on their spin s : fermions, with half-integer spins, adhere to Fermi-Dirac statistics, while bosons, with integer spins, conform to Bose-Einstein statistics. Scalar fields are denoted by particles with $s = 0$ while vector field by $s = 1$ particles. In the SM, particles fall into three principal groups: quarks, elementary fermions making up the hadrons, which are therefore composite particles and are further divided into mesons (bosons) and baryons (fermions); leptons, another class of elementary fermions; vector bosons, responsible for mediating interactions between SM particles. The joint ATLAS and CMS 2012 discovery of a particle whose properties are compatible with the ones of the Higgs boson [7, 8] which is the only scalar particle of the SM, marked the last great success of the SM.

The SM's Lagrangian formulation showcases its invariance under the Poincaré group (the group of Lorentz transformations and translations in Minkowski space) and under $SU(3)_c \otimes SU(2)_W \otimes U(1)_Y$. The strong force, described by the Quan-

tum Chromo Dynamics (QCD) theory, is associated to the $SU(3)_c$ group and is mediated by eight gluons, one per each colour charge, which are massless vector bosons. Particles carrying the so-called *colour charge*, interact primarily through this force. Quarks and gluons making up the hadrons are *coloured*, but, as a consequence of colour confinement, they cannot be observed as asymptotic states and therefore hadrons are *colourless*. The Electro-Weak (EW) interaction, governed by the $SU(2)_W \otimes U(1)_Y$ symmetry group, encompasses the weak force, mediated by the electrically charged and massive W^+ and W^- vector bosons and by the massive electrically neutral Z vector boson, alongside the Electro-Magnetic (EM) force, mediated by the electrically neutral and massless photon γ . Since the photon is massless, the EM interaction has infinite range. The strong interaction, though being mediated by massless vector bosons too, is instead local, as a consequence of the colour confinement.

All particles interact weakly, only electrically charged particles interact electromagnetically and only hadrons interact strongly. However, interaction strengths follow a hierarchy: the strong force dominates, followed by the EM and then the weak one. Therefore charged hadrons primarily interact strongly, then electromagnetically and then weakly. Neutral hadrons interact predominantly via the strong force, then weakly. Charged leptons primarily interact electromagnetically and then weakly, while neutral leptons interact solely weakly. A scheme of the SM particles divided according to the categories they belong to is given in Fig. 1.1.

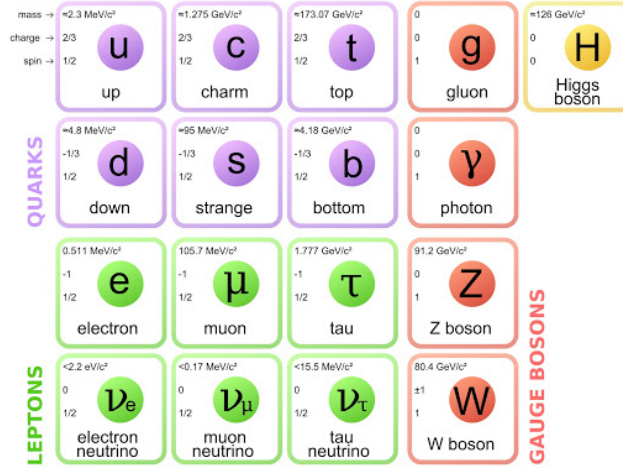


Figure 1.1. Elementary particles with their mass, spin and electric charge: quarks are depicted in lilac, leptons in green, vector bosons (the box of the gluon refers to all the gluons, since they are all massless vectors) in red and the Higgs boson in yellow. Plot from Ref. [9].

1.2 Electro-Weak Spontaneous Symmetry Breaking

The first theory of weak interactions was proposed by Enrico Fermi [10] and was therefore called *Fermi theory*. Its main feature is the presence of contact inter-

actions. Though providing a good estimate of some physical quantities, such as the muon decay time, the predicted cross sections¹ σ of processes such as electron-neutrino (e - ν) scattering diverge at high energy E , so unitarity is violated (in fact $\sigma \propto G_F^2 E^2$, where $G_F \sim 10^{-5} \text{ GeV}^{-1}$ is the Fermi constant).

The Fermi theory is therefore an effective theory which can be used to describe processes with low energy involved. The necessity of a new theory able to describe processes involving higher energies arose. Such a theory required the existence of particles mediating the interactions, in order to overcome the issues rising from the contact interactions foreseen in the Fermi theory.

Furthermore, the most general weak current had to be a combination of vector and axial currents, as theorized by Yang and Lee [11] and as then verified by the Madame Wu experiment [12]. The weak current J^μ can therefore be written as

$$J^\mu = \frac{1}{2} \bar{\psi} \gamma^\mu (g_V + g_A \gamma^5) \phi, \quad (1.1)$$

with $g_V^2 = g_A^2 = 1$, where $\gamma^\mu = (\gamma^0, \gamma^i)$ and

$$\gamma^0 = \begin{pmatrix} 0 & \mathbb{1} \\ \mathbb{1} & 0 \end{pmatrix} \quad \gamma^i = \begin{pmatrix} 0 & \sigma_i \\ -\sigma_i & 0 \end{pmatrix} \quad \gamma^5 = i\gamma_0\gamma_1\gamma_2\gamma_3$$

being the gamma matrices (with $i = 1, 2, 3$) and

$$\sigma_1 = \begin{pmatrix} 1 & 0 \\ 0 & -1 \end{pmatrix} \quad \sigma_2 = \begin{pmatrix} 0 & i \\ -i & 0 \end{pmatrix} \quad \sigma_3 = \begin{pmatrix} 1 & 0 \\ 0 & -1 \end{pmatrix}$$

are the Pauli matrices, ϕ and ψ are Dirac spinor fields, referring to fermions and $\bar{\psi} = \psi^\dagger \gamma_0 = (\psi^*)^T \gamma_0$ is the adjoint spinor.

Through the study of the differential cross section of the muon decay, it was established that the interaction has the V-A form (*Vector - Axial*), hence Eq 1.1 becomes

$$\begin{aligned} J^\mu &= \frac{1}{2} \bar{\psi} \gamma^\mu (1 - \gamma^5) \phi = \bar{\psi} \gamma^\mu \left(\frac{1 - \gamma^5}{2} \right)^2 \phi \\ &= \bar{\psi} \frac{(1 + \gamma^5)}{2} \gamma^\mu \frac{(1 - \gamma^5)}{2} \phi = \bar{\psi}_L \gamma^\mu \phi_L, \end{aligned} \quad (1.2)$$

where the equality $\left(\frac{1 - \gamma^5}{2} \right)^2 = \frac{1 - \gamma^5}{2}$ is used and where $\phi_L = \frac{1 - \gamma^5}{2} \phi$ and $\bar{\psi}_L = \psi^\dagger \frac{1 - \gamma^5}{2} \gamma_0 = \psi^\dagger \gamma_0 \frac{1 + \gamma^5}{2} = \bar{\psi} \frac{1 + \gamma^5}{2}$. Only left-handed particles and right-handed antiparticles are therefore involved in weak interactions².

¹the cross section σ of a process is related to the transition amplitude for that given process to happen, $[\sigma] = \text{cm}^2$ or $[\sigma] = \text{b}$, with $1 \text{ b} = 10^{-24} \text{ cm}^2$

²The Dirac representation is a reducible representation of the Lorentz group and it can be decomposed in the direct sum of two irreducible representation, one left-handed and one right-handed (obtaining the so-called Weyl fermion).

The discovery of weak charged currents implied the existence of 2 charged vector bosons (W^+ e W^-) mediating the interaction, in order for the electric charge to be preserved. It was then straightforward assuming that there existed also a neutral current (soon discovered in the Gargamelle experiment [13]), so a neutral vector boson was needed. Since EM interactions do not violate parity (while instead weak ones do, as already said), the neutral vector boson could not be the well known photon γ ; thus the existence of another neutral particle had to be postulated.

It was easy to assume that the three currents were

$$j_\mu^+ = \frac{g_W}{\sqrt{2}} \bar{\psi}_L \gamma_\mu \sigma_+ \phi_L \quad j_\mu^- = \frac{g_W}{\sqrt{2}} \bar{\psi}_L \gamma_\mu \sigma_- \phi_L \quad j_\mu^3 = \frac{g_W}{\sqrt{2}} \bar{\psi}_L \gamma_\mu \sigma_3 \phi_L \quad ,$$

with $\sigma_\pm = \frac{\sigma_1 \pm i\sigma_2}{2}$ and g_W being the weak coupling constant. However, the results of the Gargamelle experiment indicated that the weak neutral current had a different nature with respect to the charged ones and it was not simply due to the exchange of a neutral W_3^μ boson with the same coupling of the charged currents. In order to account for the different nature of charged and neutral currents, it was thought to unify weak and EM interactions [14], writing a Lagrangian invariant under $SU(2)_W \otimes U(1)_Y$, with Y being the hypercharge and W_i^μ (with $i = 1, 2, 3$) and B^μ being the vector bosons³ associated to the generators respectively of $SU(2)_W$ and $U(1)_Y$. Rotating these fields by the Weinberg angle θ_w

$$\begin{bmatrix} B_\mu \\ W_\mu^3 \end{bmatrix} = \begin{bmatrix} \cos(\theta_w) & -\sin(\theta_w) \\ \sin(\theta_w) & \cos(\theta_w) \end{bmatrix} \begin{bmatrix} A_\mu \\ Z_\mu \end{bmatrix} ,$$

with

$$\cos \theta_w = \frac{g_W}{\sqrt{g_W^2 + g_Y^2}} \quad \sin \theta_w = \frac{g_Y}{\sqrt{g_W^2 + g_Y^2}} ,$$

g_Y being the hypercharge coupling, the currents observed experimentally are recovered, finding the EM current to be associated with the neutral vector boson A^μ and the neutral weak current to be associated with the neutral vector boson Z^μ [15].

The Gauge symmetry forbids however Gauge boson fields to acquire any mass. Nevertheless, W^+ , W^- and Z must be massive, since they are the vector bosons of a short range interaction. A way to provide a mass to these fields without breaking the Gauge symmetry requested is through the EW SSB via the Higgs Boson [16, 17]. Such mechanism is briefly described in the following. Let a complex scalar field ϕ be

$$\phi(x) = \begin{bmatrix} \frac{\pi^1(x) + i\pi^2(x)}{\sqrt{2}} \\ \frac{H(x) + i\pi^0(x)}{\sqrt{2}} \end{bmatrix} ,$$

³Thanks to the result of the Yang-Mills theory, it was known that the number of vector bosons in a theory is equal to the number of generators of the symmetry group under which the Lagrangian is invariant. Thus in total 4 generators are needed, 3 per $SU(2)_W$ and 1 per $U(1)_Y$.

where $\pi^i(x)$ and $H(x)$ are real scalar fields and $\phi(x)$ is a doublet under $SU(2)_W$. The potential $V(\phi)$ associated to the field $\phi(x)$ takes the form

$$V(\phi) = \mu^2 (\phi^\dagger \phi) - \lambda (\phi^\dagger \phi)^2,$$

with $\lambda \geq 0$, so that the potential as well as the Hamiltonian are bounded from below, granting the existence of an equilibrium state. This potential, often referred

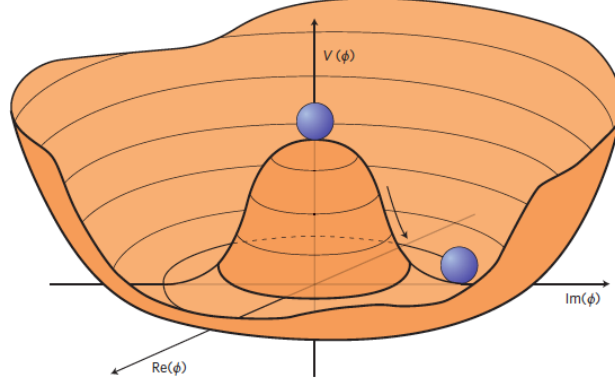


Figure 1.2. Schematic representation of the Higgs boson potential. Plot from Ref. [18].

to as *mexican hat potential* from its shape (as can be seen from Fig. 1.2), has an infinite number of minima, satisfying the condition

$$H^2(x) + |\vec{\pi}(x)|^2 = \frac{\mu^2}{\lambda}.$$

In order to break this degeneracy, an external field hH , with $h > 0$, can be added⁴. One of the viable minima is $\pi^i(x) = 0$ and $H(x) = v$. The potential (and the full Lagrangian) can be expanded around this minimum, so that

$$\pi^i(x) \rightarrow \pi^i(x) \quad H(x) \rightarrow v + H(x). \quad (1.3)$$

The masses of the scalar fields are thus found to be

$$m_H^2 = \frac{h + 2\lambda v^3}{v} \quad m_{\pi^i}^2 = \frac{h}{v}. \quad (1.4)$$

In the limit $h \rightarrow 0$ Eq. 1.4 takes the form

$$m_H^2 = 2\lambda v^2 \quad m_{\pi^i}^2 = 0, \quad (1.5)$$

hence $m_H = \sqrt{2\lambda}v$ and $m_{\pi^i} = 0$, the latter being the result of the Goldstone theorem⁵ [19]. By replacing the standard derivative ∂_μ with the covariant one⁶

⁴and then is eventually h set to 0.

⁵The Goldstone theorem states that if a Lagrangian is invariant under a global continuous symmetry group, the theory will present as many massless fields as the number of generators under which the ground state is not invariant. In this case the three generators which do not leave the vacuum invariant are σ_1, σ_2 and $\mathbb{1} - \sigma_3$ and the three related massless particle are the π^i fields.

⁶by keeping in mind that left-handed and right-handed fields transform differently under $SU(2)_W$, hence their covariant derivatives are different

D_μ , the Lagrangian becomes invariant under $SU(2)_W \otimes U(1)_Y$. The vector bosons $W^\pm = \frac{W^1 \pm W^2}{2}$ and Z acquire their masses via the term $|D_\mu \phi|^2$, with

$$D_\mu = \partial_\mu + ig_W \frac{\sigma_i}{2} W_\mu^i + ig_Y \frac{Y}{2} B_\mu, \quad (1.6)$$

after having expanded the ϕ field as in Eq. 1.3 and after having imposed the unitary Gauge, through which the π^i fields disappear and their degrees of freedom are absorbed by the longitudinal polarization of the vector bosons W^+ , W^- and Z . The photon field remains massless as expected. EW SSB provides mass to all leptonic fields as well through the term

$$Y_{ij}^d \bar{L}^i \phi d_R^j + Y_{ij}^u \bar{L}^i \phi^c d_R^j + h.c.,$$

where $h.c.$ stands for hermitian conjugate, Y_{ij}^d and Y_{ij}^u are 3×3 (since $i, j = 1, 2, 3$, one for each generation of leptons⁷) complex matrices determining the coupling between different leptonic states, $L = (l, \nu_l)$, with $l = e^-, \mu^-, \tau^-$, and $\phi^c = i\sigma_2 \phi^*$.

1.3 Higgs boson properties

The mass of the Higgs boson, as shown in Eq. 1.5, depends on the Higgs quartic coupling λ and on the Vacuum Expectation Value (VEV) v . There is no a priori prediction for the Higgs boson mass, since λ is a free parameter of the SM. The VEV can instead be determined through the measurement of the muon decay time, since $\tau_\mu^{-1} \propto G_F^2 (m_\mu)^5$, where $G_F = \sqrt{2}/2v^2$ and so $v = \left(\sqrt[4]{2}\sqrt{G_F}\right)^{-1} \approx 246 \text{ GeV}$. A particle with a mass of $m_H \approx 125 \text{ GeV}$ whose properties are compatible with the one of the Higgs boson was discovered in 2012 [7, 8].

The Higgs boson couples with Gauge bosons (V) and fermions (f) through couplings depending on their masses, as in

$$g_{Hf\bar{f}} = \frac{2m_f}{v} \quad g_{HVV} = \frac{2m_V^2}{v}.$$

The primary channels for Higgs production and decay thus predominantly entail interactions between the Higgs boson and the W and the Z bosons, along with the third generation of quarks and leptons. Furthermore, direct couplings between the Higgs boson and gluons or photons, which are massless vector bosons, are absent. Such interactions occur instead indirectly through loops involving preferably heavy massive particles.

In the following the Higgs boson production mechanisms in pp colliders as well as its decay modes are presented respectively in Sec. 1.3.1 and in Sec. 1.3.2. The readers is referred to Ref. [20] for more details.

⁷The same can be done with quarks.

1.3.1 Higgs production in pp collisions

Higgs boson production cross sections in pp collisions for an Higgs boson with $m_H = 125$ GeV, taking into account QCD and EW corrections, are shown in Tab. 1.1 for the LHC Run-2 center of mass energy ($\sqrt{s} = 13$ TeV) and the LHC nominal one ($\sqrt{s} = 14$ TeV) (see Sec. 3.1.3). Such production cross sections are depicted in Fig. 1.3 as a function of \sqrt{s} , for $\sqrt{s} \in [6 \text{ TeV}, 15 \text{ TeV}]$. In the analyses described

\sqrt{s} [TeV]	σ_{ggF} [pb]	σ_{VBF} [pb]	σ_{WH} [pb]	σ_{ZH} [pb]	$\sigma_{t\bar{t}H}$ [pb]	total [pb]
13	$48.6^{+4.6\%}_{-6.7\%}$	$3.78^{+2.2\%}_{-2.2\%}$	$1.37^{+2.6\%}_{-2.6\%}$	$0.88^{+4.1\%}_{-3.5\%}$	$0.50^{+6.8\%}_{-9.9\%}$	55.1
14	$54.7^{+4.6\%}_{-6.7\%}$	$4.28^{+2.2\%}_{-2.2\%}$	$1.51^{+1.9\%}_{-2.0\%}$	$0.99^{+4.1\%}_{-3.7\%}$	$0.60^{+6.9\%}_{-9.8\%}$	62.1

Table 1.1. Predicted Higgs boson production cross sections, assuming $m_H = 125$ GeV, in pp collisions at a centre of mass energy of $\sqrt{s} = 13$ TeV and $\sqrt{s} = 14$ TeV. Here ggF stands for gluon-gluon Fusion, VBF for Vector Boson Fusion, VH for Higgs-strahlung of a Vector boson (or associated production with a Gauge Boson), where such vector boson is either the W or the Z), while $t\bar{t}H$ stands for Higgs production with an associated $t\bar{t}$ pair. Table adapted from Ref. [20].

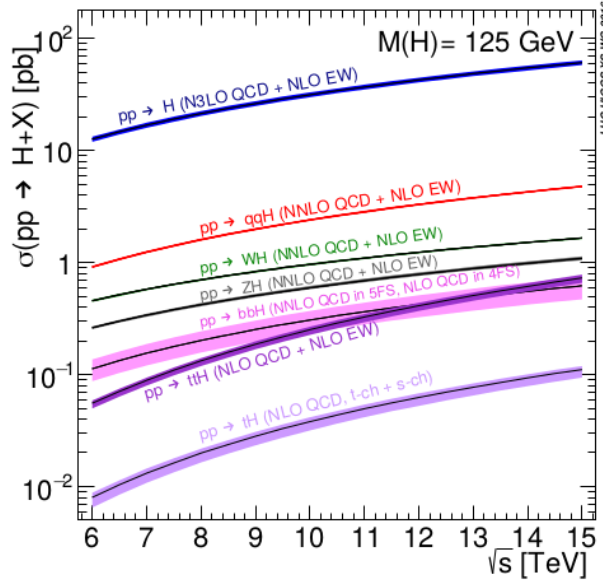


Figure 1.3. Predicted Higgs boson production cross sections, assuming $m_H = 125$ GeV, in pp collisions as a function of the centre of mass energy \sqrt{s} . Here $pp \rightarrow H$ stands for ggF, while $pp \rightarrow qqH$ stands for VBF. Here the Higgs boson production associated with a single t -quark, labelled as $pp \rightarrow tH$ and negligible with respect to the other production mechanism, is included, differently from Tab. 1.1. The production of the Higgs boson in association with a $b\bar{b}$ system, competitive with the $t\bar{t}H$ one at $\sqrt{s} = 13$ TeV, is here reported too. The shown bands are theoretical uncertainties. Plot from Ref. [20].

in Chap. 5, 6, 7, only the gluon-gluon Fusion (ggF) is considered as production

mechanism of the Higgs boson, being the one with largest associated cross section. The Feynman diagram for this production mechanism is shown in Fig. 1.4. Being

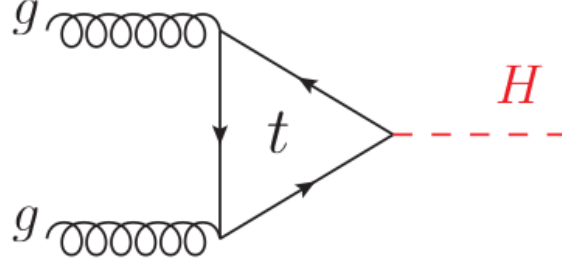


Figure 1.4. Feynman diagram of the ggF Higgs production mechanism. Picture adapted from Ref. [20].

the gluons massless, this production mechanism would not occur at the tree level and instead is possible via a loop of top quarks.

1.3.2 Higgs decay modes

Since the Higgs boson is very short-lived ($\tau_H \sim 10^{-22}$ s), it can be detected only through its decay products. Different decay modes are available, to each of which a so-called Branching Ratio (BR) is associated, defined as

$$BR_i = \frac{\Gamma_i}{\Gamma_H},$$

where Γ_i is the partial decay width associated to the i -th decay process and $\Gamma_H = \sum_i \Gamma_i$ is the total decay width of decaying particle (in this case the Higgs boson). Fig. 1.5 shows the BRs associated to the different Higgs boson decay modes as a function of the Higgs boson mass, for $m_H \in [80, 200]$ GeV (left) and for $m_H \in [120, 130]$ GeV (right). Unlike m_H , which, as already said, is a free parameter of the

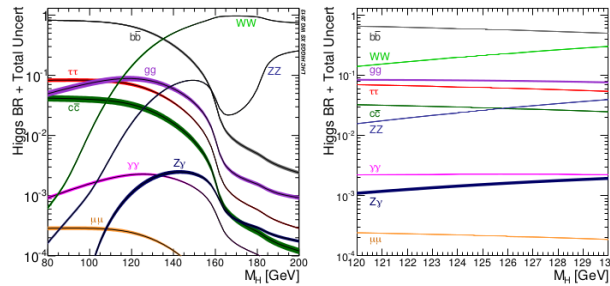


Figure 1.5. Predicted Higgs boson BRs as a function of its mass M_H , for $[80, 200]$ GeV (left) and $M_H \in [120, 130]$ GeV (right). Plots from Ref. [20].

SM, the Higgs boson total decay width Γ_H is known once m_H is determined, as can be seen from Fig. 1.6, where Γ_H is shown as a function of m_H . The expected

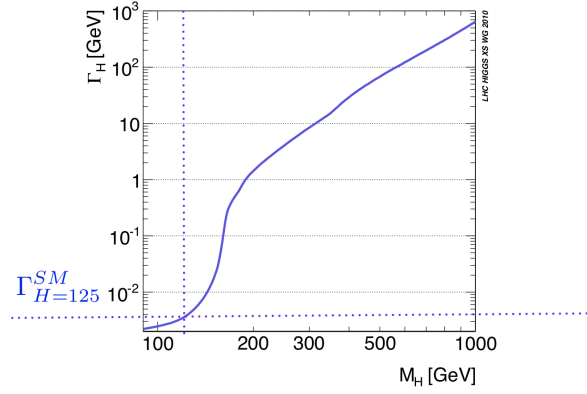


Figure 1.6. Predicted Higgs boson decay width as a function of its mass M_H . The Γ_H for $m_H = 125$ GeV is highlighted. Plot from Ref. [20].

total decay width for a Higgs boson with a mass of 125 GeV is 4.2 MeV. If Γ_H exceeds its expected value, new Beyond the Standard Model (BSM) Higgs boson decay modes would be possible, while any decrease in Γ_H from its expectation could hint to the existence of additional Higgs scalars, so that the couplings to fermions and Gauge boson with the eigenstate of mass $m_H = 125$ GeV are reduced. Measuring Γ_H with a high precision is therefore of utmost importance in order to rule out (or discover!) any possible BSM physics. Since the energy resolution of detectors exploited in facilities where Higgs bosons are produced is well above the value of Γ_H , BSM scenarios cannot be excluded from direct constraints, and indirect constraints on Γ_H have to be found. The ATLAS (CMS) collaboration (see Chap. 3) has set an upper limit on the BR of the Higgs boson decaying into BSM particles of $BR(H \rightarrow inv) \sim 10.7\%$ [21] ($BR(H \rightarrow inv) = 15\%$ [22]). Such loose constraints on $BR(H \rightarrow inv)$ does not rule out the existence of the so-called *Higgs portal* (see Sec. 2.4.2), through which Higgs boson decays into hidden BSM particles could occur. This possibility is investigated in this thesis work, as will be discussed in the searches outlined in Chap. 5,6,7.

Chapter 2

Dark Matter and Dark Sector

The SM has been thoroughly tested since its formulation, with these tests always confirming its validity. However, the SM still does not provide answers to some fundamental questions, such as the nature of Dark Matter (DM). This chapter describes the DM problem in the context of this thesis work. In Sec. 2.1 DM evidence ranging from the galactic to the cosmological scale are discussed. In Sec. 2.2 the expected density and velocity profile of the DM halo are derived. In Sec. 2.3 conventional DM candidates are listed, along with their properties and experimental constraints. Finally, in Sec. 2.4, Dark Sector (DS) models are introduced and the simplified models relevant for this thesis work are described.

2.1 Dark Matter evidence

Since the beginning of time natural philosophers have speculated about the matter content of the Universe and about the fact that it may contain elements that are not perceivable – because they are too far away, too faint, or intrinsically invisible.

After Galileo discovered with his telescope the multitudes of stars making up the Milky Way, it became clear that the Universe could contain matter which cannot be perceived by ordinary means and that our discovery potential is strictly bounded to technology advancements.

The fact that the motion of astrophysical objects could be influenced by other faint/invisible objects was for the first time hinted by Bessel in 1844 [23]. The German astronomer was additionally the first one to suggest that the amount of matter inside a galaxy cannot be determined only via light measurements, leading to the concept of *mass-to-light ratio*. Since then, astronomers looked for probes of what they started to call *dark* objects, ranging from dark stars, dark planets and dark clouds. In 1906 Poincaré coined the term **Dark Matter**, to collectively refer to these dark astrophysical objects [24]. In order to measure effects of this unknown and invisible new matter, it was necessary to find visible objects that could act as indicators of it. These indicators must be collisionless, so that their distribution is only due to gravitational effects, through which one can infer the DM distribution. For these reasons, stars and galaxies, which are essentially collisionless due to their

large reciprocal distances, have always been used to look for DM.

2.1.1 Galactic scale: galaxies rotational curves

In 1931 Hubble and Humason were able to measure through optical telescopes the velocity of galaxies within the COMA cluster using their red-shift¹ [25]. In 1933 the astronomer Zwicky noticed a large velocity dispersion of the measured speeds of those galaxies [26] and compared them with the ones obtained using the virial theorem:

$$\begin{aligned} 2 \langle T \rangle &= - \langle U \rangle \\ \Rightarrow 2 \frac{1}{2} m \langle v \rangle^2 &= \frac{GmM}{R} \\ \Rightarrow \langle v \rangle &= \sqrt{\frac{MG}{R}} \end{aligned} \quad (2.1)$$

where $\langle T \rangle$ is the time average of the kinetic energy, $\langle U \rangle$ is the time average of the potential energy, m and $\langle v \rangle$ are respectively the observed mass and the time average of the speed of the galaxy whose velocity is experimentally measured, and M and R are respectively the observed mass and radius of the cluster of galaxies. The galaxy speed obtained using the virial theorem was much smaller than the observed one, yielding a light-to-mass ratio of the order of 500. Additionally, from Eq. 2.1, the speed of a star v should decrease outside the galactic disk as $v \propto r^{-1/2}$. However, as can be seen in Fig. 2.1, observations find that the circular velocity curve flattens out at these distances, implying that $M(r) \propto r$, suggesting the existence of a *dark* component of matter extending beyond the visible matter in the disk.

This was the first quantitative hint of the long sought missing mass inside the Universe. Since then, many different astronomers had measured galaxies rotational speed using photometry and have reached similar conclusions, as reviewed by Schwarzschild in [28].

After the Second World War, however, the case for DM became even stronger: radars used for airplanes detection were converted to radio-telescopes, providing independent and complementary measurements of the galaxies rotational speed. The red-shift of the famous 21 cm line², undetectable using optical telescopes and

¹The frequency f_s of the light emitted by stars in the galaxies is red-shifted (or blue-shifted), as a consequence of their speed v_s with respect to the observer, through the Doppler effect:

$$f_{obs} = f_s \sqrt{\frac{1 + \frac{v_s}{c}}{1 - \frac{v_s}{c}}} \sim f_s \left(1 + \frac{v_s}{c}\right),$$

where f_{obs} is the intrinsic frequency of the source and c is the speed of light.

²The 21 cm spectral line, often called *Hydrogen line* or *H I line*, is due to the transition between two hyperfine states of the $1^2S_{1/2}$ ground level of Hydrogen atoms, from a quantum state where the spin of the proton and the one of the electron are parallel, to the one in which they are anti-parallel. This transition is strongly suppressed, but since Hydrogen atoms are found in great abundance in the Universe, its associated measured rate is instead sizeable.

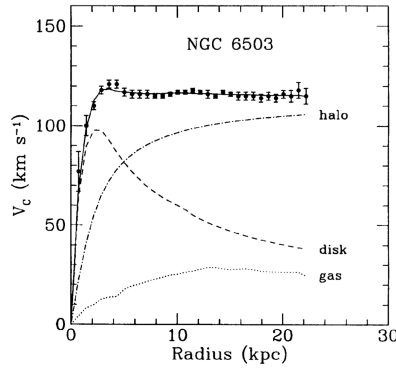


Figure 2.1. NGC 6503 galaxy rotational speed as a function of the distance from the galaxy center: measured speeds (black dots) are compared to theoretical ones due to the galactic disk (dashed line) and to the galactic gas (dotted line). The halo distribution to account for discrepancies between the measured and theoretical speeds is shown as well (dotted-dashed line). Plot from Ref. [27].

whose existence was predicted by Van de Hulst [29], was indeed used to measure the galaxy speed. Since then, also thanks to the technological advancements of photometry and spectrometry through which it was possible to extend previous measurements to larger distances with respect to the clusters center, stronger and stronger DM evidence in the form of large light-to-mass ratios were collected.

2.1.2 Cluster of galaxies: Gravitational lensing

The idea that light can be deflected by massive objects emerged for the first time from Newton [30], with the first (unpublished) calculation of such a deflection angle given by Cavendish in 1784. After 1911, with the advent of Einstein's General Relativity, it was known that the *world line*³ of a particle depends on the curvature of spacetime, which is in turn determined by the gravitational field generated by massive objects. Therefore, in calculating light deflection angles, it is necessary to take into account the additional deflection arising from the curvature of space-time around the massive object. The deflection angle θ then obtained is twice the one derived by Cavendish:

$$\theta = \frac{4GM}{c^2 b},$$

where M is the mass of the object that is generating the gravitational field, G the gravitational constant, c is the speed of light and b is the impact parameter. This effect is called *gravitational lensing* [31], as the gravitational field acts as a lens which distorts images.

The larger the matter content of the lens, the more the deflection will be sizeable, giving rise to three different kinds of lensing: the *strong lensing*, the *weak lensing* and the *micro-lensing*⁴. Since its theorisation, these lensing effects have been used to map the matter content of the Universe, to study the DM density distribution

³The world line of an object is the path that the object traces in 4-dimensional spacetime.

⁴Often lensing effects of different intensity can occur in the same astrophysical object.

and to rule out possible DM candidates.

In the following, a few examples of these studies are listed.

Strong lensing

When the mass density of the lenses is above a certain critical threshold, the lensing effect of the background source can be sizeable, either producing multiple images of the same source or magnifying it. In Fig. 2.2, the effect of the strong gravitational lensing on various galaxies, as measured by the Sloan Lens ACS (SLACS)⁵ (Advanced Camera for Surveys (ACS)) team, is shown [32].

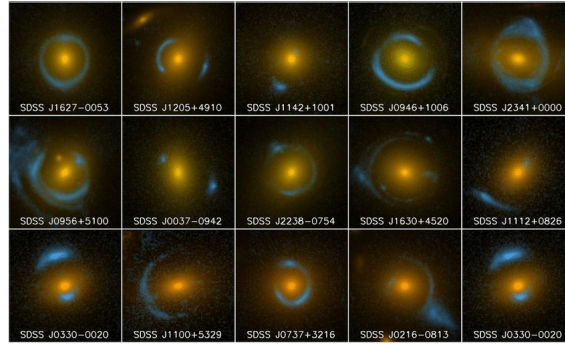


Figure 2.2. The effect of the strong gravitational lensing observed on blue-star forming galaxies (blue) due to the presence of elliptical galaxies (orange). Picture adapted from Ref. [33].

Here elliptical galaxies, compact and dense, distort the images of the background sources, which are blue star-forming galaxies. Since the red-shifts of both the lens and the background source are known, the lensing geometry defines the total mass distribution of the lens, irrespective of its brightness. The total mass distribution so obtained is spatially more extended than the one of the visible matter, hinting to the existence of DM.

Weak lensing

When the mass density of the lens lies below a critical value, multiple images cannot be produced. However, rays of light are deflected by these less dense lenses, with the distortion depending on the curvature of the lens gravitational potential.

Such a lensing effect has been observed in the cluster *1E 0657-56*, also known as Bullet Cluster, born circa 150 million of years ago after the collision of two clusters of galaxies [34]. In Fig. 2.3, the Bullet Cluster as seen from an optical telescope (left) and an X-ray telescope (right) is shown. During the collision between the galaxies, the stars, being very distant one from the other, do not interact, as it can be seen from the optical image. On the contrary, the hot gases, in the red regions in the

⁵SLACS is a project combining the large data volume of the Sloan Digital Sky Survey (SDSS) with the high-resolution imaging capability of the Hubble Space Telescope to identify and study a large number of strong gravitational lens galaxies.

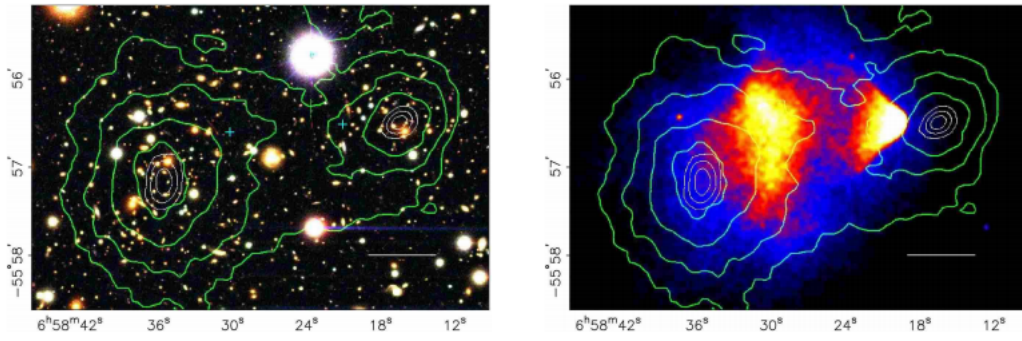


Figure 2.3. Bullet Cluster as seen with the Magellan optic telescope (left) and an X-ray telescope (right). The green lines provide the profile of the gravitational potential obtained by measuring gravitational weak lensing effects. Plot from Ref. [35].

X-rays image, interact with each other electromagnetically and so they slow down to be then confined near the collision zone. Therefore, since the majority of the ordinary matter of a galaxy is made of stellar gases, the effect of the gravitational lensing should be more intense in the collision site, where the gases are located. On the contrary, the gravitational lensing is more intense in the region where the stars are found.

The inferred mass distribution could be explained by the presence of DM in the galaxies before the collision. The Bullet cluster provides additionally information about possible DM interactions: being concentrated outside the collision site, DM is expected to have extremely low non-gravitational interactions.

Micro-lensing

When either the background source or the lens (or both) are not resolved, the deflection and distortion of the light coming from the source cannot be detected. However, a temporary brightening of the source may be observed. The intensity and the duration of the increased brightness indicate the amount of mass in the lens⁶. These effects have been used to rule out or constrain the amount of DM in the form of compact astrophysical objects (see Sec. 2.3.1).

2.1.3 Cosmological scale

A number of evidence of DM can be inferred from cosmological measurement from which cosmological parameters can be extracted.

Evolution of the Universe

The Big Bang theory is the result of decades of collection of evidence that led to the building of what is now the most complete theory of the evolution of the Universe.

⁶Obviously this kind of observations is complicated by the possibility that there exist astrophysical objects with intrinsic variable brightness, such as pulsars.

The Universe is believed to grow colder in time and to decrease its density, allowing for interactions to *freeze-out* so that structures could be formed. Such evolution is conventionally divided into three eras:

- *Radiation Era*: at the beginning (Planck epoch) all four forces are unified, whilst within the first 10^{-4} s they *freeze-out* one by one, with the Universe rapidly expanding (*inflationary phase*) and cooling down eventually to 10^9 K, where, after neutrino decoupling, Big Bang Nucleosynthesis (BBN) occurs;
- *Matter Era*: after the BBN, the nuclei thereby created bind with high energy electrons in the so-called *recombination*. Through this, photons, that are emitted from electron transitions to their ground state, freely-stream up to nowadays, producing the so-called Cosmic Microwave Background (CMB)⁷; by the end of this era, large scale structures (such as galaxies and clusters of them) and stars are formed and evolve;
- *Dark Energy (DE) Era*: DE dominates. DE existence is needed to account for the Universe expansion, which is inferred from Type Ia SuperNovae (SN) measurements. This is the Era in which the Universe is found nowadays.

Big Bang Nucleosynthesis

The BBN predicts that light elements, specifically D, ^3He , ^4He and ^7Li , are mostly produced during the first $t \sim 108$ s of the Universe evolution [36]. Heavier elements, such as C, N, O and Fe ("metals"), are instead produced in stellar reactions [37], this production often referred to as *stellar nucleosynthesis*.

Measurements of primordial abundances of light elements are among the most reliable probe of the early Universe, as BBN is based on well-understood SM physics. However, such abundances are derived now, after stellar reactions have already occurred, and they are therefore altered from their primordial values. Therefore, astrophysical sites with low metal abundances are used to measure light elements abundances that are closer to the primordial ones.

Measured abundances are compared to predicted ones, as shown in Fig. 2.5

⁷When the CMB was initially emitted it was not in the form of microwaves, but mostly visible and ultraviolet light. Over the past few billion years, the expansion of the Universe has red-shifted this radiation toward longer and longer wavelengths, so that today it appears in the microwave band.

(a). These abundances all depend on Ω_B ⁸, the fraction of *baryonic matter*⁹, that therefore can be extracted from these measurements.

Cosmic Microwave Background and Baryonic Acoustic Oscillations

The CMB provides information on the Universe composition at the *recombination epoch* and it is now observable as an excess of low energy photons. Its spectral power is the black body one, almost completely isotropic at a temperature of $T = 2.7$ K.

It was firstly measured in 1990 by the COsmic Background Explorer (COBE) satellite [40], to an accuracy of 10^{-5} in all directions. Below this level of accuracy, temperature fluctuations are observed, as afterwards measured by the Planck [41] satellite (see Fig. 2.4). Such anisotropies are recorded at both small and large scales. Small scale fluctuations are due to a cycle of compressions, due to gravitational pulls, and expansions, due to radiation pressure augmentations, which the plasma of charged particles and photons (present before the *recombination*) underwent. Large scale fluctuations are due to density fluctuations in the *recombination epoch*, since photons decoupling from denser regions lost more energy to escape from the gravitational potential.

Such fluctuations have grown with time due to gravity (denser regions attract more mass becoming even denser) and formed the present structure of the Universe. Additionally, beside impacting the temperature distribution of the CMB, they also caused sound-waves in the primordial plasma, this phenomenon being known as Baryonic Acoustic Oscillations (BAO). From measurements of both the CMB temperature power spectrum and the distribution of cluster of galaxies, both Ω_Λ and Ω_M can be constrained, as can be seen in Fig. 2.5 (b).

⁸An isotropic and homogeneous space-time can be described via the Robertson-Walker metric [38]

$$ds^2 = -dt^2 + a(t)\left(\frac{dr^2}{1 - kr^2} + r^2 d\Omega^2\right),$$

where $a(t)$ is the so-called *radius of the Universe* or *cosmic scale factor* and k is the curvature of the Universe space time, which can be either flat ($k = 0$), closed ($k = 1$) or open ($k = -1$). The evolution of the *cosmic scale factor* determines the Universe expansion, via the Friedmann equation [39]:

$$\frac{\dot{a}^2 + k}{a^2} = \frac{8\pi G_N \rho}{3},$$

where \dot{a} is the time derivative of a , G_N is the universal gravitational constant and ρ is the density.

Since the Hubble constant $H(t)$ is defined as $H(t) = \frac{\dot{a}(t)}{a(t)}$, the Friedmann equation can be rewritten as

$$\Omega - 1 = \frac{k}{a^2 H^2}, \quad (2.2)$$

where $\Omega = \frac{\rho}{\rho_{cr}} = \frac{8\pi G_N}{3H^2} \rho$. Both matter density Ω_M and DE density Ω_Λ contribute to Ω , so that $\Omega = \Omega_M + \Omega_\Lambda$. Therefore, since the Universe is now known to be flat ($k = 0$), $\Omega = 1$, and therefore $\Omega_M + \Omega_\Lambda = 1$

⁹In cosmology baryonic matter is the term used to refer to the ordinary matter as a whole.

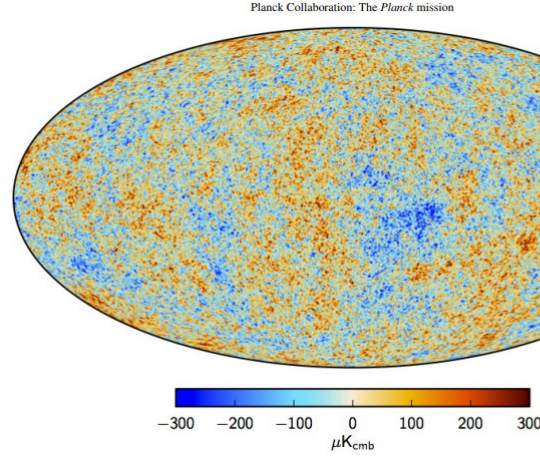


Figure 2.4. Image of the CMB temperature anisotropies measured by the Planck satellite (2015) [41]

Universe expansion and Type Ia SuperNovae measurements

Type Ia SN are produced in nuclear explosions of white dwarfs, which are extremely dense stars. When causing a type Ia SN, white dwarfs are found in a binary system and, while cooling down, they augment their mass by absorbing the companion star stellar material. When reaching the Chandrasekhar limit, i.e. when the mass of the white dwarf, m_{wd} , is $m_{wd} > 1.4 \times M_{\odot}$ (with M_{\odot} being the solar mass, $M_{\odot} = 10^{30}$ kg), the C and the O found in the star are at such high density and temperature that they can undergo nuclear reactions where ^{56}Ni is produced. The energy freed in these reactions causes the white dwarf to explode.

The luminosity of type Ia SN depends on the decay chain of ^{56}Ni thereby produced ($^{56}\text{Ni} \rightarrow ^{56}\text{Co}$, with $\tau \sim 8.8$ d, and $^{56}\text{Co} \rightarrow ^{56}\text{Fe}$, with $\tau \sim 110$ d). Type Ia SN, easily identified from such spectral features, are therefore *standard candles*, as their intrinsic luminosity depends on these processes. For this reason, they can be used to measure relative distances from which cosmological parameters, such as the Hubble parameter H_0 , the DE density Ω_{Λ} , the matter density Ω_M and the red-shift z can be extracted. If at the same time red-shift measurements are performed, Ω_{Λ} and Ω_M can be accessed. These measurements were performed by different collaborations, such as the Supernova Cosmology Project [42], whose results are shown in Fig. 2.5 (b).

Cosmological parameter constraints

From BBN measurements Ω_B is constrained to $\Omega_B \sim 0.05$, whilst from independent measurements of BAO, type Ia SN and CMB, assuming a flat Universe, Ω_M is found to be constrained to $\Omega_M \sim 0.32$. Therefore, there should exist non-baryonic matter to account for the missing matter density: the DM. From such measurements, the density of DM is extracted to be $\Omega_{\text{DM}} = 0.27$, the net majority of the matter content of the Universe.

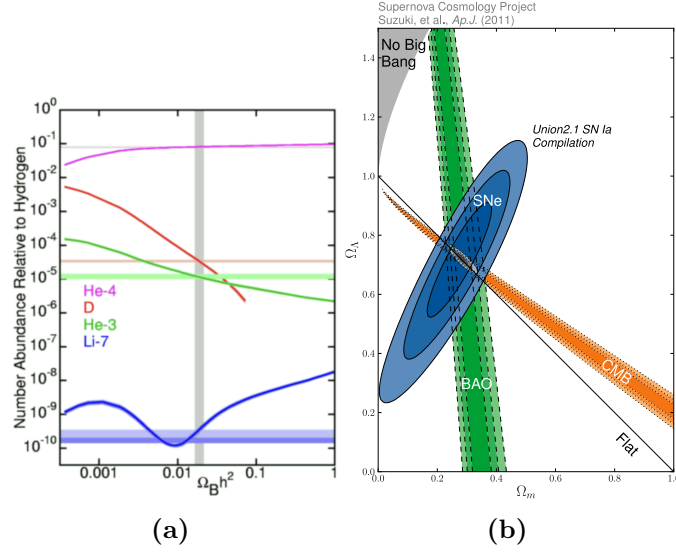


Figure 2.5. (a) light elements abundances predicted by the BBN as a function of the baryonic matter density Ω_B (darker lines) compared to measured ones (horizontal lighter lines); the vertical grey line represents the value of Ω_B which is compatible with the observations [43]; (b) constraints on Ω_Λ and Ω_m extracted from BAO (green), CMB (orange) and type Ia SN measurements (blue) [42].

2.2 Dark Matter halo

As said in Sec. 2.1.1, galactic rotational curves measurements were the first probes of the existence of a DM halo pervading the Universe, whose mass distribution can be extracted from such measurements. In order to explain the flat behaviour of the galaxies speed outside the galactic disk, from Eq. 2.1 $M_{halo} \propto r$ is obtained. Assuming a spherically distributed DM¹⁰, the density ρ_{halo} is found to be

$$\rho_{halo}(r) \propto \frac{M_{halo}(r)}{r^3} \sim \frac{1}{r^2}. \quad (2.3)$$

However, while providing an intuition, this picture is too simplistic since such a density profile predicts an infinitely massive halo. This suggests that at distances beyond current measurements, rotation curves must no longer be flat.

This notwithstanding, this derivation can be used in order to extract the order of magnitude of the DM speed and of its spatial extension. In the Milky Way the DM halo total mass is measured to be $\sim 10^{12} M_\odot$ (while the total visible mass of the Milky Way is $\sim 5 \times 10^{10} M_\odot$), from which the radius of DM halo is found to be ~ 100 kpc (while the radius of the galactic disk of the Milky Way is ~ 10 kpc), with a local density of DM of $\rho = 0.3 \text{ GeV cm}^{-3}$. Using again the virial theorem, the speed of the DM halo in the Milky Way is found to be 200 km s^{-1} .

The DM halo is therefore non-relativistic. This conclusion is corroborated as well by the results of numerical simulations, where relativistic DM (referred to as

¹⁰this assumption relies on the fact that DM self-interactions are negligible

hot DM) cannot account for the structures seen nowadays, whilst non-relativistic DM (referred to as *cold* DM) can.

2.3 Standard Dark Matter candidates

The evidence listed in Sec. 2.1 all points to the existence of DM. Modifications of general relativity that could account for these measurements, such as the MODified Newtonian Dynamics (MOND), first theorised in 1983 by Milgrom [44], have been looked for. However, a theory able to explain all the discrepancies found from the galactic to the cosmological scale is yet to be found.

For this reason it is now believed that DM does exist, and it has been looked for since its first hints. In the following, DM candidates, alongside with their experimental constraints, are illustrated.

2.3.1 Astrophysical candidates and experimental constraints

Since the first galaxy rotation measurements, physicists questioned themselves about the nature of DM. At the beginning, astronomers were looking for all varieties of astrophysical materials that were too faint to be detected with available telescopes, with candidates ranging from planets, brown dwarfs, red dwarfs, white dwarfs, neutron stars, and black holes. These objects are collectively referred to as Massive Astrophysical Compact Halo Objects (MACHO), and they have been looked for using gravitational *micro-lensing* (see Sec. 2.1.2) surveys in the Milky Way by the MACHO, Experience pour la Recherche d'Objets Sombres (EROS) and Optical Gravitational Lensing Experiment (OGLE) collaborations.

Recently, constraints on the amount of DM in form of MACHO the Milky-Way were published in a combined analysis from the EROS and MACHO collaborations in Ref. [45], while Ref. [46] shows the most recent results of the OGLE collaboration. After such measurements, an upper limit of 8% on the fraction of DM due to MACHO was found, therefore ruling out the possibility that the majority of DM could be due to these astrophysical objects.

Other astrophysical DM candidates are primordial black holes, which are black holes that formed before BBN. Such objects would have masses below the sensitivity range of *micro-lensing* surveys, with which they therefore cannot be detected. However, the observed fluctuations in the CMB (see Sec. 2.1.3) implies such a small amount of primordial black holes that they cannot be the largest DM component.

By the late 1990s, also thanks to the measurements of the light elements abundances produced in the BBN, it had become clear that baryonic DM does not constitute a large fraction of the Universe DM.

2.3.2 Particle candidates and experimental constraints

Dark Matter is now believed to be composed of particles, whose properties can be derived from the measurements listed in Sec. 2.1. In the following, particle DM

production in the early Universe is illustrated, and viable particle DM candidates are listed.

Freeze-in and freeze-out mechanism

There are numerous mechanisms through which DM could be produced in the early Universe, among which the most relevant ones are the so-called *freeze-out* and *freeze-in* mechanisms. In the following, both of them are briefly introduced. However it is typically assumed that DM was created via *freeze-out*¹¹. In the *freeze-in* mechanism, it is assumed that the initial DM abundance was negligible. Processes amongst the primordial bath of particles produced DM, but thermal equilibrium was not established. The DM yield was built gradually through these processes, that would come to an end when the Universe had cooled down and expanded enough. At that time, the residual DM abundance which is observed nowadays had *frozen-in*. In Fig. 2.6 (a) the evolution of the DM density during the *freeze-in* is shown, where it can be seen how larger DM interaction cross-sections implies larger relic abundances.

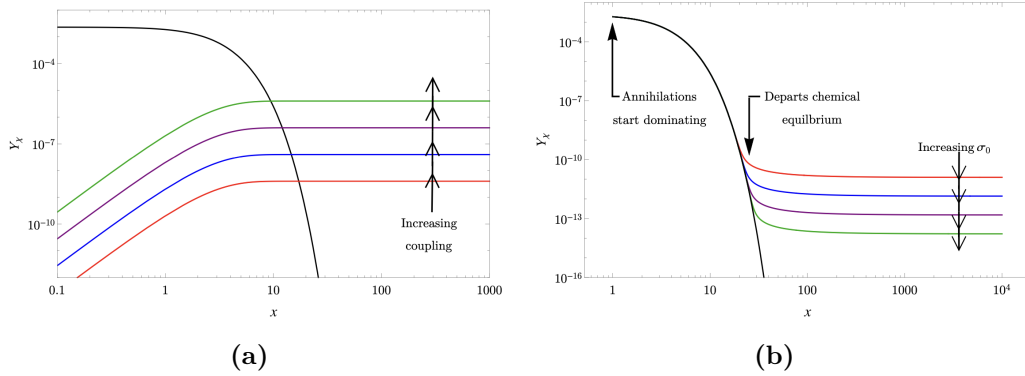


Figure 2.6. DM (χ) yield evolution (Y_χ) as a function of $x = \frac{m}{T}$, with m being the DM particle mass and T the temperature of the Universe, during the *freeze-in* (a) and the *freeze-out* (b), the black curve representing the yield in thermal equilibrium and the coloured ones representing respectively the *freeze-in* and the *freeze-out* (b) yields for various interaction strengths. Plot from Ref. [49].

In the *freeze-out* mechanism, instead, the DM was assumed to be in thermal equilibrium with the particle bath in the early Universe, where DM annihilation and creation was happening in equal rates. DM creation became suppressed when

¹¹The freeze-out mechanism is the one commonly assumed since it's the mechanism through which the baryonic matter is produced. Furthermore, through the freeze-out mechanism, DM candidates as WIMPs with the DM abundance seen today naturally arise. However, since 2009 with the article in Ref. [47], the freeze-in mechanism has started to be considered as a viable DM production mechanism. Through it, other kinds of DM candidates, such as Feebly Interactive Massive Particles (FIMPs), can be produced. This notwithstanding, since the theorisation of the freeze-in, more convoluted scenarios are being considered, for example the one in the article in Ref. [48] published in 2023, where WIMPs are produced through freeze-in via a first order transition phase in the Early Universe.

the temperature dropped below the DM mass, and therefore annihilation dominated and the abundance dropped. When the annihilation rate matched the expansion rate of the Universe, the DM particles became too far apart to annihilate and the residual amount of DM *froze-out* (this happening during the *Radiation Era*). In Fig. 2.6 (b) the evolution of the DM density during the *freeze-out* is shown, where it can be seen how larger DM interaction cross-sections implies smaller relic abundances.

2.3.3 Particle candidates and the WIMP miracle

The only DM candidate among SM particles that has a sufficiently feeble interaction with other SM particles is the neutrino ν . However, due to their small mass, ν are highly relativistic particles, therefore they could not account for the cold nature of DM (see Sec. 2.2).

The SM does not thus comprise any particle which could explain the nature of DM, which is therefore now thought to be a BSM particle, whose properties can be inferred from DM evidence collected up to now.

From measurements of the nowadays relic abundance produced during the *freeze-out*, it can be inferred that DM particles should have a life-time comparable to the age of the Universe. Additionally, the DM annihilation cross-section is found to be

$$\langle \sigma v \rangle \sim 3 \times 10^{-26} \text{ cm}^3 \text{ s}^{-1},$$

where $\langle \sigma v \rangle$ is the time-averaged product of the DM annihilation cross-section and its speed. Interestingly enough, if a DM state with Electro-Weak (EW) scale mass (multi-GeV, TeV) and coupling G_F (see Sec. 1.2) is considered, an annihilation cross-section of this order of magnitude is found.

The fact that a weak-scale DM naturally gives the correct DM density observed motivates DM to be made of Weakly Interactive Massive Particles (WIMPs) [50] — this coincidence referred to as the *WIMP miracle*. However, while *freeze-out* motivates a WIMP candidate, this is not the only viable DM hypothesis, as will be seen in Sec. 2.4.

Nonetheless, since their theorisation, WIMPs have been looked for in direct and indirect detection experiments, as well in production at colliders. Direct detection experiments look for scatterings between DM and SM particles, indirect detection experiments look for SM products of DM annihilations, while in collider searches it is looked for DM particles among particles produced in the collision. In the following, these different discovery techniques are listed, alongside with their resulting experimental constraints.

Direct detection

As said in Sec. 2.2, a DM halo is found in the Milky Way. The relative motion of the Solar System with respect to WIMPs making up the DM halo is expected to produce a flux of WIMPs impinging on the Earth. Direct detection experiments are aimed at

detecting such WIMP interactions with ordinary matter. These interactions arise from elastic or inelastic scatterings, producing either nuclear recoils (for WIMPs in the multi-GeV range) or excitation and/or ionization of the recoiled atom (for WIMPs in the sub-GeV range).

Extremely large detectors shielded from sources of additional radiation are needed in such searches, since DM particles interact extremely rarely with ordinary matter, as a consequence of the very small associated cross section, and such interactions produce extremely low energy releases, as a consequence of the cold nature of DM. To reduce possible contamination from radiation sources, these detectors are often located in underground facilities, to suppress cosmic ray background, and are built with extremely radio-pure materials. To suppress environmental radioactivity, usually rather high in underground facilities, active vetoes are often exploited. However, no evidence compatible with WIMP interactions with ordinary matter has been found up to now, this reducing the available phase-space of such WIMP models.

By way of illustration, a plot of the current bounds of the Spin-Independent (SI)¹² cross section of the WIMP-nucleon scattering for experiments looking for nuclear recoils is shown in Fig. 2.7.

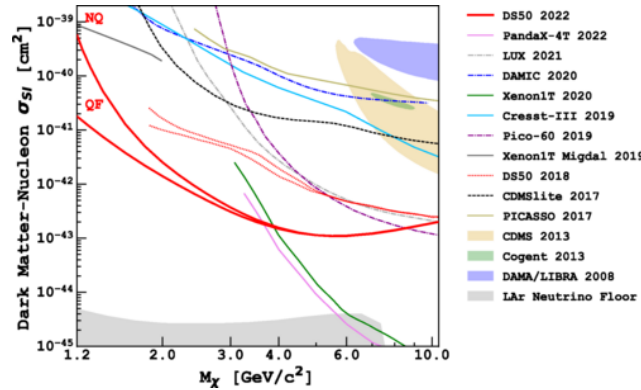


Figure 2.7. SI WIMP-nucleon cross section experimental bounds. Plot from Ref. [51].

As can be seen in this figure, the strongest limits for $m_{\text{wimp}} > 4 \text{ GeV}$ are found by Particle and Astrophysical Xenon Experiments (PandaX) [52] and XENON-1T [53] collaborations, both taking advantage of double-phase detection techniques. For lighter WIMPs, the most stringent limits are given by DarkSide-50 [54], Cryogenic Dark Matter Search low ionization threshold experiment (CDMSlite) [55] and Cryogenic Rare Event Search with Superconducting Thermometers (CRESST) [56].

The sensitivity of these searches drops drastically for small WIMP masses, as the energy released to the nuclei during the scattering is too small to produce a detectable recoil. At large WIMP masses, even though the energy released to the

¹²There exist two kinds of nucleon-WIMP coupling: the Spin-Dependent (SD) and Spin-Independent (SI) ones. The SD cross-section depends on the total spin of the nucleus, this corresponding to a scalar or vector mediator of this interaction. The Spin-Independent (SI) one is independent of the total spin of the nucleus, this corresponding to a pseudo-scalar or axial-vector interaction.

nuclei increases, the sensitivity decreases as well, since the expected WIMP flux is suppressed as $1/m_{\text{WIMP}}$.

This kind of searches are additionally bounded by the so called *neutrino floor*. Neutrinos, produced either in nuclear reactions in the Sun or in interactions between cosmic rays and the Earth atmosphere, scatter against the nuclei of the experiments targets, leading to interactions indistinguishable from the ones which might be due to WIMPs. To investigate such a phase space, directional searches looking for annual modulations of the WIMP flux are being exploited [57]. A review of such searches can be found in Ref. [58].

Indirect detection

WIMP pairs can annihilate producing pairs of SM particles. Indirect detection experiments look for excesses in the flux of SM particles which could be explained by such DM annihilation processes. Since the expected SM particles flux is proportional to the local density of DM, indirect detection experiments target high density regions of the Universe, such as the Sun or the center of different galaxies.

The IceCube [59] and the Super-Kamioka neutrino detection experiment (Super-Kamiokande) [60] collaborations look for excesses in fluxes of neutrinos, which are particularly promising DM probes as they interact only weakly with the medium they traverse before reaching the experiments. The Fermi-LAT satellite [61], instead, looks for excesses in photon or positrons fluxes, the latter being investigated by the Alpha Magnetic Spectrometer 02 (AMS-02) [62] and Payload for Antimatter Matter Exploration and Light-nuclei Astrophysics (PAMELA) [63] collaborations as well.

The three collaborations have found an excess of high energy positrons, as can be seen in Fig. 2.8, which could be explained by the existence of a WIMP with a mass of $m_{\text{WIMP}} \sim 10 \text{ GeV}$. However this finding can be explained by a variety of astrophysical phenomena, and therefore no conclusive evidence of WIMPs existence can be drawn.

Production at colliders

WIMPs searches carried out in particle colliders rely on the assumption that WIMPs can be pair-produced from SM particles interactions. In this scenario, SM particles and WIMPs interact via the exchange of a new mediator, which couples to both SM particles and WIMPs.

The resulting WIMPs would be undetectable at colliders, unless they are produced in association with SM particles. These events would yield the so-called *mono-X* signature, where a large amount of missing energy, due to the non-interacting WIMPs, is observed. Such missing energy can be sizeable when recoiling on a highly energetic X object, such as jets (see Chap. 4) or vector bosons which are produced in the initial state of the collision. Since at hadron colliders the emission of QCD Initial State Radiation (ISR) jets is favoured with respect to vector boson production, the *monojet* final state, where the missing energy is recoiling against a jet, is

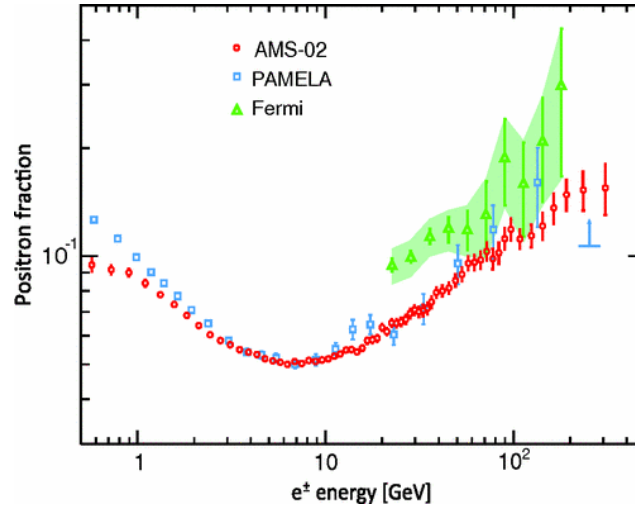


Figure 2.8. Positron to electron plus positron rate as measured by the AMS-02, the Fermi-LAT and the PAMELA collaborations as a function of the electron/positron energy itself. Figure from Ref. [64]

a golden discovery channel for WIMPs.

For this reason, this signature has been exploited to look for WIMPs by the CMS [65] and ATLAS [2] collaborations (see Chap. 3). Fig. 2.9 shows the experimental constraints on the SI WIMP cross-section obtained by the ATLAS experiment using the *monojet* signature.

As can be seen from this figure, WIMP searches at collider probe a complementary phase space with respect to direct detection ones, therefore allowing to widen the sensitivity to such BSM scenarios. The *monojet* signature is exploited in this thesis work to investigate other BSM scenarios, as will be explained in Chap. 7.

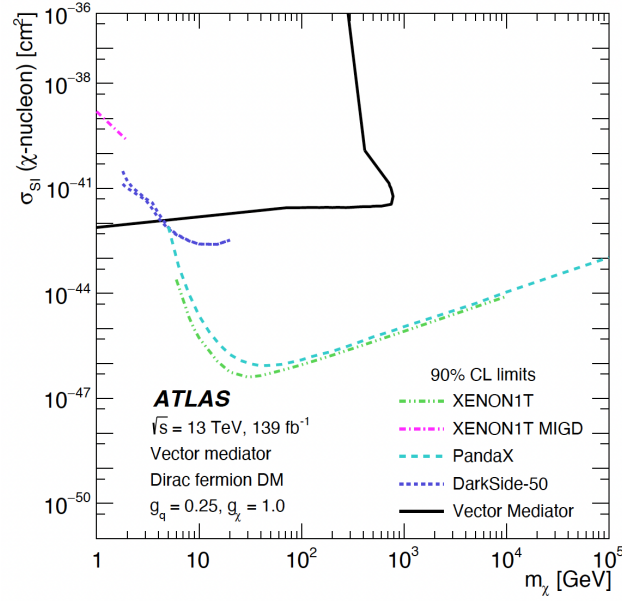


Figure 2.9. Constraints on the SI cross-section for WIMP-nucleon interactions as a function of the WIMP mass itself, m_χ . The upper limits obtained by the ATLAS collaboration using *monojet* events (black) assume a vectorial mediator for the new interaction. This interaction is also assumed to be lepto-phobic, so that the new vector mediator couples only to quarks. The mediator coupling to the quarks is set to $g_q = 0.25$ in this plot, while its coupling to the WIMP, which is assumed to be a Dirac fermion, is set to $g_\chi = 1$. Such constraints are compared to those obtained by direct detection experiments (dotted coloured lines). Figure from auxiliary material of [2].

2.4 Unconventional Dark Matter candidates: Dark Sector

The searches described in the previous section are complementary among each other, probing different WIMP mass ranges and interaction energy scales. The LHC program has put a great effort on WIMP searches, probing an extremely large phase space of WIMPs models, ranging from the EW scale up to many TeV.

Therefore, the possibility that DM is not constituted of WIMPs but of particles with masses below the EW scale, with a new interaction between SM particles and these new dark particles, has started to be investigated. In this scenario, among the most promising theories there are the so-called Dark Sector (DS) models, which assume a whole new sector of particles which are neutral under all the SM gauge groups. The particle constituting the Dark Matter is to be found among these states. Dark Sector searches are extremely interesting, as DS models have such a reduced number of free parameters (compared to other BSM scenarios, like Super SYMMetry (SUSY)), that they can be easily used as probes of SM discrepancies, allowing for an easy identification of uncovered scenarios.

Similarly to the WIMP paradigm, where WIMP particles were assumed to be weakly interacting with ordinary particles, DS models assume that interactions

between the dark and the visible sector can occur through so-called *portals*, so that DS particles could be experimentally accessible beside from their gravitational interaction. These portals have various forms and are classified according to the type and the dimension of their operators. The best motivated ones are the Vector (spin 1) portal, the Neutrino (spin 1/2) portal, the Higgs (scalar) portal and the Axion (pseudo-scalar) portal. The portal models of interest for this thesis work, namely the Vector portal and the Higgs portal, are introduced in the next sections.

2.4.1 Vector portal and Gauge sector

In the Vector portal the interaction takes place because of a kinetic mixing between one dark and one visible Abelian gauge boson (non Abelian gauge bosons do not mix). The dark gauge boson is identified with the vector boson of an extra $U(1)_d$ symmetry, and it is therefore called Dark Photon (DP), γ_d . The DP mixes with the vector boson of the $U(1)$ gauge group of electromagnetism (the SM photon γ), or, above the EW symmetry-breaking scale, of the hyper-charge. In the DP mass range considered in this thesis, the γ_d mixes with the SM photon.

The most general Lagrangian \mathcal{L}_{GS} of such a gauge sector describing the mixing between two Abelian gauge bosons A_a and A_b , associated to a $U(1)_a$ and a $U(1)_b$ group, is [66]:

$$\mathcal{L}_{GS} = -\frac{1}{4}F_{a\mu\nu}F^{a\mu\nu} - \frac{1}{4}F_{b\mu\nu}F^{b\mu\nu} - \frac{\varepsilon}{2}F_{a\mu\nu}F^{b\mu\nu},$$

where $F_{(a,b)\mu\nu} = \partial_\mu A_{(a,b)\nu} - \partial_\nu A_{(a,b)\mu}$ and ε is the kinetic mixing between the two gauge bosons. The gauge boson A_b^μ is taken to be coupled to the SM current J^μ , while the gauge boson A_a^μ is taken to be coupled to the dark one J'^μ , giving a Lagrangian \mathcal{L}_c associated to such currents

$$\mathcal{L}_c = eJ_\mu A_b^\mu + e'J'_\mu A_a^\mu,$$

with e and e' being the respective coupling constants. The gauge boson kinematic terms can be diagonalized through the fields redefinition

$$\begin{pmatrix} A_a^\mu \\ A_b^\mu \end{pmatrix} = \begin{pmatrix} \frac{1}{\sqrt{1-\varepsilon^2}} & 0 \\ -\frac{\varepsilon}{\sqrt{1-\varepsilon^2}} & 1 \end{pmatrix} \begin{pmatrix} \cos\theta & -\sin\theta \\ \sin\theta & \cos\theta \end{pmatrix} \begin{pmatrix} A^\mu \\ A'^\mu \end{pmatrix},$$

with θ being a generic angle through which the field are rotated, and A^μ and A'^μ are respectively the ordinary photon and the dark one. If the DP is massless, the choice of the rotating angle θ is arbitrary, and it is usually chosen in such a way that the SM photon couples to DS particles, other than to ordinary matter, via a coupling referred to as *milli-charge*, while the DP couples only to DS particles.

If instead the DP acquires mass through SSB (see Sec. 1.2), there is no freedom of choice of the parameter θ , which is instead locked to the value required by the

rotation of the gauge fields to the mass eigenstates. In this context, θ must satisfy the following relations:

$$\sin \theta = \frac{\delta \sqrt{1 - \varepsilon^2}}{1 - 2\delta\varepsilon + \delta^2} \quad \cos \theta = \frac{1 - \delta\varepsilon}{\sqrt{1 - 2\delta\varepsilon + \delta^2}},$$

with $\delta = M_b/M_a$. In this way, the Lagrangian \mathcal{L}_c can be rewritten as \mathcal{L}'_c

$$\begin{aligned} \mathcal{L}'_c = & \frac{1}{\sqrt{1 - 2\delta\varepsilon + \delta^2}} \left[\frac{e'(1 - \delta\varepsilon)}{\sqrt{1 - \varepsilon^2}} J'_\mu + \frac{e(\delta - \varepsilon)}{\sqrt{1 - \varepsilon^2}} J_\mu \right] A'^\mu + \\ & + \frac{1}{\sqrt{1 - 2\delta\varepsilon + \delta^2}} \left[e J_\mu - \delta e' J'_\mu \right] A^\mu. \end{aligned} \quad (2.4)$$

The Lagrangian \mathcal{L}'_c in Eq. 2.4 is the most generic Lagrangian describing both the dark and the SM currents. However, the most discussed case is the one in which the mass is given only to one of the two U(1) boson, this achieved for example by choosing $M_b = 0$. In such a way, $\delta = 0$, and \mathcal{L}'_c can be rewritten as:

$$\mathcal{L}''_c = \left[\frac{e'}{\sqrt{1 - \varepsilon^2}} J'_\mu - \frac{e\varepsilon}{\sqrt{1 - \varepsilon^2}} J_\mu \right] A'^\mu + e J_\mu A^\mu.$$

In this (commonly chosen) scenario, which is the one that will be considered in this thesis work as well, the SM photon couples only to visible sector particles, while the massive DP couples directly to the SM EM current, with a Lagrangian \mathcal{L}_{mix}

$$\mathcal{L}_{\text{mix}} \sim -e\varepsilon J^\mu A'_\mu, \quad (2.5)$$

in the limit $\varepsilon \ll 1$.

Assuming that the γ_d is the lightest state of the DS and that $m_{\gamma_d} > 2m_e \sim 1$ MeV, the γ_d can decay into SM particles thanks to its kinetic mixing with the γ . The γ_d BR into a specific pair of SM particles depends on the γ_d mass itself. An approximate estimation of the decay width of the DP into leptons l , $\Gamma_{\gamma_d \rightarrow l\bar{l}}$, is [67]

$$\Gamma_{\gamma_d \rightarrow l\bar{l}} = \frac{4}{3} \varepsilon^2 \alpha m_{\gamma_d} \sqrt{1 - 4 \frac{m_l^2}{m_{\gamma_d}^2} \left(1 + \frac{2m_l^2}{m_{\gamma_d}^2} \right)},$$

where m_l is the mass of the lepton l produced by the γ_d decay and α is the hyperfine structure constant. An approximate estimation of the decay width of the DP into hadrons, $\Gamma_{\gamma_d \rightarrow \text{hadrons}}$, is instead

$$\Gamma_{\gamma_d \rightarrow \text{hadrons}} = \frac{4}{3} \varepsilon^2 \alpha m_{\gamma_d} \sqrt{1 - 4 \frac{m_\mu^2}{m_{\gamma_d}^2} \left(1 + \frac{2m_\mu^2}{m_{\gamma_d}^2} \right)} R(s = m_{\gamma_d}^2),$$

where m_μ is the muon (μ) mass and $R(s = m_{\gamma_d}^2) = \frac{\sigma_{e^+e^- \rightarrow \text{hadrons}}(s = m_{\gamma_d}^2)}{\sigma_{e^+e^- \rightarrow \mu^+\mu^-}(s = m_{\gamma_d}^2)}$ is

the ratio of the annihilation cross sections of an electron (e^-) - positron (e^+) pair into hadrons over the one into muons, both at a centre of mass energy of $s = m_{\gamma_d}^2$.

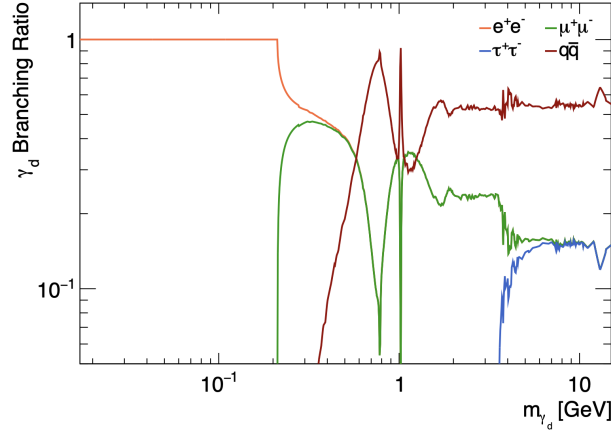


Figure 2.10. Theoretical DP BRs into electrons (orange), muons (green), taus (blue) and hadrons (red) as function of the DP mass m_{γ_d} .

DP BRs [68] into the different SM species are shown in Fig. 2.10 in the range $m_{\gamma_d} \in [0.017 \text{ GeV}, 11 \text{ GeV}]$. For $1 \text{ MeV} \sim 2m_e \leq m_{\gamma_d} < 2m_\mu \sim 210 \text{ MeV}$ the DP decays only into electrons. As a consequence of the lepton universality, when more leptonic decays are accessible their associated BRs are equal. The DP has a sizeable BRs to leptons, except in the mass range of hadronic resonances: in the mass region shown, for $m_{\gamma_d} = m_\rho \sim 776 \text{ MeV}$, $m_{\gamma_d} = m_\omega \sim 782 \text{ MeV}$ and for $m_{\gamma_d} = m_\phi \sim 1019 \text{ MeV}$ the hadronic BR is strongly enhanced, while leptonic ones are suppressed. Neutrino production is not considered since it is heavily suppressed by a factor $\frac{m_{\gamma_d}^4}{m_Z^4} \sim 10^{-8}$. The DP proper lifetime τ , expressed in seconds, is related to both ε and the DP mass, as in the approximate relation

$$\tau \propto \left(\frac{10^{-4}}{\varepsilon} \right)^2 \left(\frac{100 \text{ MeV}}{m_{\gamma_d}} \right). \quad (2.6)$$

As expected, when the coupling between the dark and the visible sector is suppressed, the γ_d acquires a non-negligible mean proper life-time, possibly becoming a Long Lived Particle (LLP) (see Sec. 7.1).

Experimental constraints

Dark Photons have been looked for since their theorisation by many different experiments, assuming that the DP is produced and decays through the vector portal. As no conclusive evidence of DPs has been found up to now in such scenarios, constraints on the free parameters of these models, namely the DP mass m_{γ_d} and its coupling to the visible sector ε , are found, as reported in Fig. 2.11. Extremely light and prompt (corresponding to large ε , see Eq. 2.6) DPs are already ruled out. Instead, heavier DP hypotheses and smaller ε , in which the DP would decay further from its production point, are not accessible with current facilities, without assuming as well the already mentioned Higgs portal, that will be described in the following section.

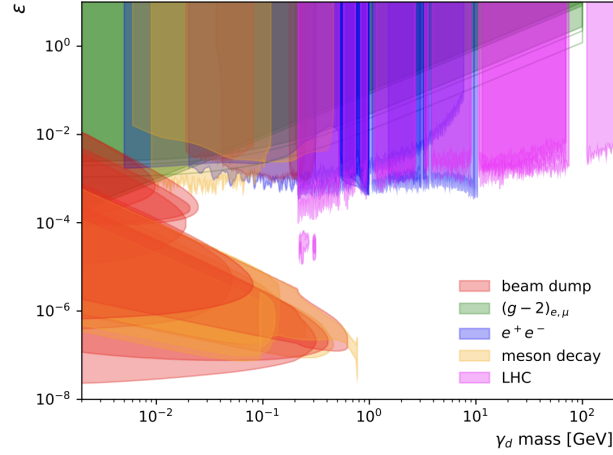


Figure 2.11. Excluded areas in the free parameter $(\varepsilon, m_{\gamma_d})$ plane, as found by beam-dump experiments (red), muon magnetic momentum measurements (green), e^+e^- colliders (blue), meson decays (yellow) and LHC (magenta). These constraints assume the vector portal only. Picture taken from [69].

2.4.2 Higgs portal and Higgs sector

When the γ_d is massless, no interaction between the γ_d and SM particles is foreseen and the visible photon couples with DS particles. If instead the γ_d acquires a mass through SSB, it couples to the visible sector via a short-range interaction. Such SSB is provided by a dark Higgs boson (referred to either as S or H_d) mechanism, analogous to the SM one described in Sec. 1.2), where the dark Higgs boson provides mass to all DS particles. The Lagrangian \mathcal{L}_{H,H_d} describing the Higgs potentials and interaction of both the dark and the visible sectors can be written as:

$$\mathcal{L}_{H,H_d}(\phi, S) = -\mu^2 |\phi|^2 + \lambda |\phi|^4 - \mu_S |S|^2 + \lambda_S |S|^4 + k |\phi|^2 |S|^2,$$

where ϕ is the Higgs boson doublet of weak-hypercharge W (see Sec. 1.2), S is the dark Higgs scalar, with μ_S and λ_S being free parameters of the theory, and k being the mixing parameter between the dark and the visible Higgs bosons. The SM Higgs boson and the dark one have to be expanded around their VEVs $\langle \phi \rangle = \left(0, \frac{v}{\sqrt{2}}\right)$ and $\langle S \rangle = \frac{v_S}{\sqrt{2}}$, so that

$$\mu = v^2 \lambda + \frac{1}{2} k v_S^2 \quad \mu_S = v_S^2 \lambda_S + \frac{1}{2} k v^2.$$

The mass matrix M_{H_0, S_0}^2 , that still does not provide the mass eigenstates, can be diagonalized in the (H_0, S_0) basis as

$$M_{H_0, S_0}^2 = \begin{pmatrix} 2v^2 \lambda & v v_S k \\ v v_S k & 2v_S^2 \lambda_S \end{pmatrix},$$

so that the mass eigenstates can be written as

$$\begin{pmatrix} H \\ S \end{pmatrix} = \begin{pmatrix} \cos \theta_h & -\sin \theta_h \\ \sin \theta_h & \cos \theta_h \end{pmatrix} \begin{pmatrix} H_0 \\ S_0 \end{pmatrix},$$

where the mixing angle θ_h is implicitly given by

$$\tan \theta_h = \frac{v^2 \lambda - v_S^2 \lambda_S - \text{sign}(v^2 \lambda - v_S^2) \sqrt{v^4 \lambda^2 + v_S^4 \lambda_S^2 + v^2 v_S^2 (k^2 - 2\lambda \lambda_S)}}{v v_S k}.$$

For small θ_h , the masses of the SM Higgs boson, m_H , and of the dark one, m_S , are

$$m_H^2 = 2\lambda v^2 + 2\sin^2 \theta_h (v^2 \lambda - \lambda_S v_S^2) \quad m_S^2 = 2\lambda_S v_S^2 + 2\sin^2 \theta_h (v^2 \lambda - \lambda_S v_S^2),$$

disregarding terms of order $\mathcal{O}(k^4)$.

The mixing between H and S generates a non-zero coupling of the SM Higgs boson to Dark Photons, allowing for the process $H \rightarrow \gamma_d \gamma_d$ to happen, when $m_H \geq 2m_{\gamma_d}$. The resulting decay width is

$$\Gamma_{H \rightarrow \gamma_d \gamma_d} = \frac{\alpha m_H^2}{8m_{\gamma_d}} \sqrt{1 - \frac{4m_{\gamma_d}^2}{m_H^2}} \left(1 - \frac{4m_{\gamma_d}^2}{m_H^2} + \frac{12m_{\gamma_d}^4}{m_H^4} \right).$$

The SM Higgs boson could in principle decay into the dark Higgs boson S too, but in this thesis S is considered sufficiently massive for this process to be kinematically forbidden.

The Higgs portal is of particular interest and often assumed in DS searches at hadron colliders (like the LHC), as they are Higgs factories and since Higgs boson exotic decays are still possible, as said in Sec. 1.3.

Experimental constraints

The ATLAS and the CMS collaborations have looked for (massive) DPs since the start of their physics program, assuming both the vector (Sec. 2.4.1) and the Higgs (Sec. 2.4.2) portals¹³. Different searches are built and optimised upon the hypotheses investigated, with the main difference being the DP life-time regime targeted. In Tab. 2.1 the most recent of such searches are listed.

Both the collaborations have not found yet any conclusive evidence of the existence of DPs, this resulting in constraints on the free parameter space of DP models,

¹³A CMS search looks for DPs using the vector portal only hypothesis, both in its decay and its production (where the Drell-Yan production mechanism is assumed) [70]. Additionally, both the ATLAS and the CMS collaborations have looked for massless γ_d , where the DP is produced via the Higgs portal and where there exist no vector portal as the DP is stable, therefore yielding missing energy. In this context, the DP is looked for using the *mono- γ* signature, where a highly energetic photon recoils on missing energy. The possibility that the Higgs boson is produced by VBF, see Sec. 1.3 (ZH, see Sec. 1.3) is investigated by both the ATLAS [71] ([72]) and the CMS [73] ([74]) collaborations. Other searches looking for γ_d in more complex scenarios, such as the ones foreseeing dark QCD as well, have been carried out by both the collaborations, with the most recent result in Ref. [75]

Signature	HP	H production	VP	τ_{γ_d}	m_{γ_d} [GeV]	Search
Displaced muons	✓	ggF	✓	Outside ID	[0.6,50]	CMS [76]
Displaced fermions		ggF+VBF+WH			[10,60]	CMS [77]
Prompt muon-pairs	✓	ggF	✓	Inside ID	[0.17,15]	ATLAS [78], ATLAS [79]
Prompt lepton-pairs					[0.3,10]	CMS [80]
					[0.2,2]	ATLAS [81]

Table 2.1. Breakdown of ATLAS and CMS DP searches, grouped according to the signature looked for. It should be noted that beside [82], which has been carried out during Run-1 (Chap. 3), all the others are Run-2 searches. Here HP and VP stands respectively for Higgs Portal and Vector Portal.

namely the DP mass, m_{γ_d} , its coupling to the visible sector, ε , and the BR of the Higgs boson decaying into DPs. The constraints found by the ATLAS collaboration prior to this thesis work are shown in Fig. 2.12.

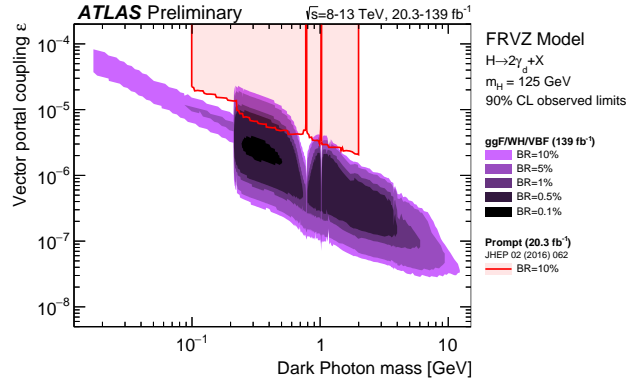


Figure 2.12. Excluded areas in the free parameter $(\varepsilon, m_{\gamma_d})$ plane, as found by the ATLAS collaboration, for different $B(H \rightarrow 2\gamma_d + X)$ hypotheses, where X stands for undetected particles. The constraints obtained in the Run-1 search looking for prompt DPs (red) [83] are compared to the ones obtained in the Run-2 displaced search (violet) [79]. These constraints assume both the vector and the Higgs portal, exploiting the so-called Falkowsky-Ruderman-Volansky- Zupan (FRVZ) benchmark signature (see Sec. 2.4.3). Plot from Ref. [79].

The hypothesis in which the coupling between the DP and the visible sector is extremely suppressed, thus yielding a DP that is so long-lived that it decays outside the ATLAS detector, is for the first time investigated in this thesis work, as explained in Chap. 7, in a reinterpretation of the *monojet* search [3].

Furthermore, the scenario where instead the γ_d decays promptly inside the innermost ATLAS detector had been investigated by the collaboration only in Run-1. This thesis work looks for the first time for this possibility using the dataset collected during Run-2, aiming at extending the sensitivity of this search to a wider m_{γ_d} range, and smaller couplings between the visible and the dark sector (both in terms of the vector portal and the Higgs portal). The latter work is presented in Chap. 5 and Chap. 6.

2.4.3 Dark Sector simplified models

So called *simplified or benchmark models* are built in such a way that their resulting signatures are representative of a wider class of models, thus allowing an easy comparison between different searches as well as an easy re-interpretation of them (as will be indeed illustrated for the search in Chap. 7). For these reasons, simplified models are often exploited in DS searches, and the ones probed in this thesis are a standard for both the CMS and ATLAS collaborations, given their simplicity.

In the analysis illustrated in Chap. 5, 6 two benchmark models involving γ_d production, the Falkowsky-Ruderman-Volansky- Zupan (FRVZ) [84, 85] and the Hidden Abelian Higgs Model (HAHM) [86], are considered. The FRVZ model is exploited in the search introduced in Chap. 7 as well, where the scenario in which the SM is extended with the addition of a single BSM scalar particle (referred to as $H \rightarrow ss$ model [87]) is considered too. For models involving the production of γ_d , the $U(1)_d$ coupling $\alpha_d = \frac{e'^2}{4\pi}$ (see Sec. 2.4.1) is assumed to be $\ll \alpha\epsilon^2$, so that additional radiation of γ_d is suppressed.

The HAHM benchmark model

A simplified model predicting decays of the Higgs boson into a pair of dark photons is the HAHM, schematically depicted in Fig. 2.13. The γ_d produced via the Higgs

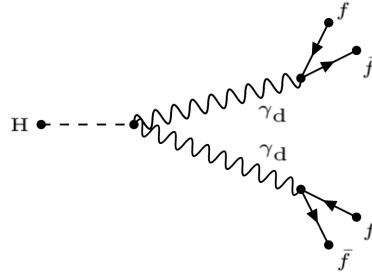


Figure 2.13. Feynman diagram of the HAHM benchmark model, where the Higgs boson H decays via the Higgs portal into a pair of dark photons γ_d , which in turn decay back to SM fermions f via the vector portal. Figure adapted from Ref. [78].

portal decay back to SM particles via the vector portal.

The FRVZ benchmark model

Another benchmark model is the FRVZ one, depicted in Fig 2.14. It has similar features of the HAHM one, though it provides a richer phenomenology, as multiple

BSM particles are produced.

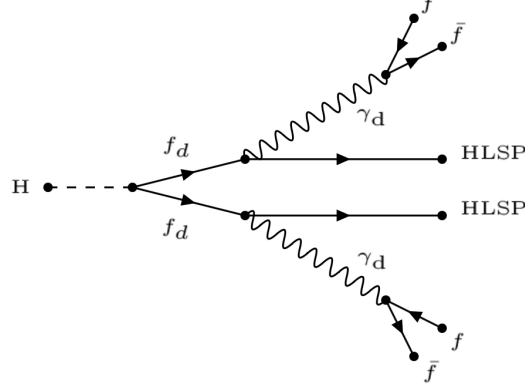


Figure 2.14. Feynman diagram of the FRVZ benchmark model, where the Higgs boson H decays via the Higgs portal into a pair of dark fermions f_d , which in turn decay into the Hidden Lightest Stable Particle (HLSP) and a γ_d , which produces a pair of SM fermions f via the vector portal. Figure adapted from Ref. [3].

A pair of dark fermions f_d are produced via the decay of the Higgs boson through the Higgs portal. Each f_d decays into the Hidden Lightest Stable Particle (HLSP) and a γ_d , which in turn decays back into a pair of SM particles through the vector portal. Being the lightest particle of the invisible sector, the HLSPs are stable and therefore undetected. The richer kinematics of this model is of particular interests in searches for BSM physics, as it can give rise to a wide variety of signatures, as well as to invisible particles. As a consequence of the presence of multiple intermediate particles, the γ_d produced in this benchmark model are less boosted than the ones in the HAHM model, as will be further discussed in Sec. 5.2.

The $H \rightarrow ss$ model

A third, even simpler model, is based on the extension of the SM with a single BSM real scalar particle. It assumes a mechanism similar to the Higgs portal, where the BSM scalar particle s acts as the Dark Higgs in the FRVZ and the HAHM models. The s particle decays into SM fermions f via a Yukawa-like coupling, as schematically depicted in Fig. 2.15. For the process to be allowed $m_s < \frac{m_H}{2}$.

The BR of the s particle into SM fermions depends on the mass of the s particle itself, as shown in Fig. 2.16.

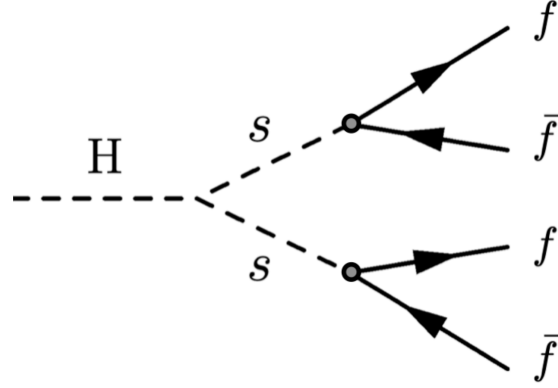


Figure 2.15. Feynman diagram of the $H \rightarrow ss$ benchmark model, where the Higgs boson H decays via the Higgs portal into a pair of dark scalars s , which in turn decay into a pair of SM fermions f that are coupled to the s particle with a Yukawa-like coupling. Figure adapted from Ref. [3].

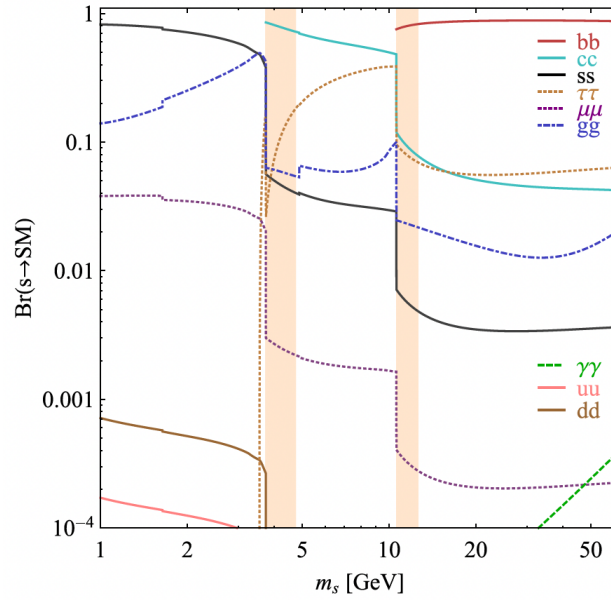


Figure 2.16. BR of the s scalar particle into SM fermions, as a function of its mass m_s . Picture taken from [69].

Chapter 3

The ATLAS experiment at the LHC

In this chapter a brief description of the Conseil Européen pour la Recherche Nucléaire (CERN) facility is given (Sec. 3.1), with particular attention on the pre-accelerators system (Sec. 3.1.1) and on the Large Hadron Collider (LHC) (Sec. 3.1.2) [88], focusing on its working conditions when the dataset exploited in this thesis work was collected. The ATLAS detector, on which the searches presented in Chap. 5, Chap. 6 and Chap. 7 are based, is described in Sec. 3.2.

3.1 The CERN facility

CERN was founded in 1954, from the realisation that high energy colliders could provide insightful information about the infinitely small, as high energy collisions act as powerful microscopes. The first large CERN accelerator, the Proton Synchrotron (PS), started its operation in 1959, shedding light upon the constituents of matter for the following years. Since then, different accelerators granting particles collisions with larger and larger energies have been built. The Super Proton Synchrotron (SPS) was built in 1976, the first proton-antiproton collider ever, and the 27 km long Large Electron Positron collider (LEP) was built in 1989. After the end of the 2000, LEP fulfilled its physics program and a proton-proton and heavy ions collider, the LHC, was built in the 27 km long tunnel previously hosting LEP. The LHC is at the moment of writing undergoing its third successful data taking. The previously built accelerators still serve their purpose, being exploited both by different experiments and as pre-accelerators of the LHC.

3.1.1 The CERN accelerator complex

An overview of the CERN accelerating complex [89] (in the conditions in which the dataset exploited in this thesis was collected) is given in Fig. 3.1. Protons produced by ionisation of Hydrogen gas are accelerated up to 450 GeV by a system of pre-accelerating elements - the LINear ACcelerator-2 (LINear ACcelerator-2), the

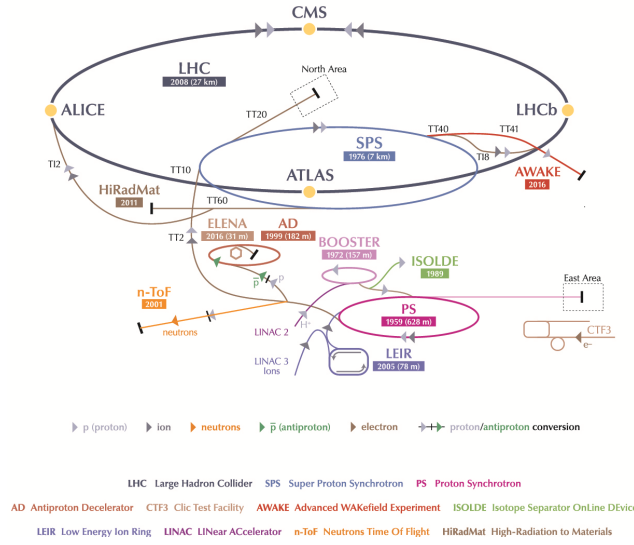


Figure 3.1. CERN Accelerator complex. The pre-accelerating elements (the LINAC-2, the PSB, the PS and the SPS) accelerate up to 450 GeV the protons, which are then injected in the LHC, reaching an energy of 6.5 TeV (during Run-2, see Sec. 3.1.2). The yellow points are the four interaction points, around which the four largest CERN experiments are built: CMS, ATLAS, ALICE and LHCb. Additional experiments built around the pre-accelerators are shown as well.

Proton Synchrotron Booster (PSB), the PS and the SPS - and then they are split into the two beam pipes of the LHC (see Sec. 3.1.2). Here the beams are accelerated to an energy of 6.5 TeV reaching a $\sqrt{s} = 13$ TeV (for Run-2, see Tab. 3.1). In the pre-accelerating phase particles are arranged into bunches, which are extremely dense and narrow packets of particles, built to maximise the chance of interactions during the collisions (therefore referred to as *bunch-crossing*). These bunches are accelerated in beam pipes where ultrahigh vacuum is granted, so to avoid any unwanted collision between the accelerated particles and the gas molecules in the beam pipe. Along the LHC ring there are four so-called IPs (Interaction Points), where the two bunches collide, around which the largest CERN experiments are located:

- A Toroidal LHC ApparatuS (ATLAS) [90] and Compact Muon Solenoid (CMS) [91], multi-purpose detectors optimised for the discovery of the Higgs Boson, for the study of its properties and for the research of new Physics;
- A Large Ion Collider Experiment (ALICE) [92], exploiting heavy ion collisions to investigate the nature of the strong interactions in the quark-gluon plasma;
- LHCb, focused on B-hadrons decays in order to study b-quark properties and the physics of Charge-Parity (CP)-violation.

3.1.2 The LHC

The LHC at the CERN is a 27 km long circular accelerator which is situated approximately 100 m underground underneath the French-Swiss border. Its planned

operation is divided into specific *Runs*, each lasting several years and separated by so-called Long Shutdown (LS), scheduled for possible repairs and upgrades. There had already been a Run-1, from 2010 to 2012, followed by the LS1, lasted until 2015, a Run-2, from 2015 to 2018, followed by the LS2, lasted until 2022, and the machine is currently in Run-3, which is planned to last until 2025.

After this Run, during the LS3, that will last until 2028, the LHC will undergo a series of major upgrades. Thanks to those, during Run-4 operations at an instantaneous luminosity (see Sec. 3.1.3) of $\mathcal{L} = 7.5 \times 10^{34} \text{ cm}^{-2}\text{s}^{-1}$, 7.5 times larger than the nominal \mathcal{L} , will be reached, in the so-called High-Luminosity (HL) phase of the LHC. More details about the HL-LHC upgrades are given in Chap. 8.

The LHC is both a proton-proton and heavy ions (lead ions) collider. Since this thesis work is based on the dataset collected during Run-2 in pp collisions, in the following this manuscript will refer to pp collisions only. A summary of the performances of the LHC during the Run-2 years of activity are compared to the design ones in Tab. 3.1. In Run-2 proton bunches were accelerated by supercon-

Parameters	2015	2016	2017	2018	Nominal
\sqrt{s} [TeV]	13	13	13	13	14
$N_p[10^{11}]$	1.1	1.2	1.2	1.2	1.15
N_B	2232	2300	2450	2500	2808
Spacing [ns]	25	25	25	25	25
\mathcal{L} [$10^{33} \text{ cm}^{-2}\text{s}^{-1}$]	5	15	20	20	10
PU	~ 13	~ 25	~ 38	~ 36	~ 25

Table 3.1. Best LHC performances during Run-2 years of activity [93] during normal physics operations, for the 25 ns filling scheme (see Sec. 3.1.3) are compared to design ones. \sqrt{s} is the centre of mass energy of the two colliding bunches, N_p is the number of proton per bunch, N_B is the number of bunches injected per revolution at the LHC, the spacing is the time interval between two consecutive injected bunches, \mathcal{L} is the instantaneous luminosity and Pile-Up (PU) determines the number of collisions happening at the same time. Details about these machine parameters are given in Sec. 3.1.3.

ducting Radio-Frequency (RF) cavities delivering 2 MV at 400 MHz, operating at a temperature of 4.5 K. The LHC has a synchrotron design, hence the accelerated particles revolution frequency¹ is kept constant by varying the magnetic field along the accelerator radius. To do so, a complex system of magnets is used, which is made up of 1232 superconducting bending dipoles forcing the particle beam to follow a circular trajectory, reaching an overall B of 8.3 T. Additional magnets, 858 quadrupoles and around 6000 correctors, are located along the ring and act on the

¹ $f = \frac{qB}{2\pi m\gamma}$, with q being the charge of the accelerated particle, B being the external magnetic field and $\gamma = \frac{1}{\sqrt{1 - \frac{v^2}{c^2}}}$.

beam characteristics, such as its focus.

3.1.3 pp collisions, bunch filling scheme, luminosity and Pile-Up

pp collisions

Charged particles accelerated in circular colliders lose part of their energy as a consequence of the synchrotron radiation produced since they are bended by magnetic fields. Such an energy loss ΔE depends on the energy E and on the mass m of the bended particle, as in

$$\Delta E \propto \frac{E^4}{m^4}.$$

If accelerated at the same energy, lighter particles lose therefore more energy for synchrotron radiation than heavier ones. As an example, the ΔE_e energy loss of an electron would be $\Delta E_e/\Delta E_p \propto m_p^4/m_e^4 \sim 10^{13}$ times larger than the energy loss ΔE_p for a proton, if both of them are accelerated at the same energy. Allowing thus to reach higher energy collisions, pp colliders are better suited as discovery machines (the discovery of the Higgs boson was the main purpose of the LHC).

Colliding hadrons (such as protons) implies however that, in events in which the transferred momentum is high (in the so called *hard scattering* events) the hadrons behave as composite particles. The colliding elements (the partons, i.e. gluons and quarks) carry only a fraction of the total momentum of the hadron, as prescribed by the Parton Distribution Function (PDF). As a result, the total longitudinal momentum of the colliding system is different from zero and cannot be determined, so that the initial state is unknown. Furthermore, colliding strongly interacting particles produces a large number of final state particles (~ 200 per pp collision in Run-2), challenging in terms of event reconstruction.

The *hard scattering* event is accompanied by emissions of soft (low-momentum) gluons from coloured particles either in the initial (ISR) or in the final state (Final State Radiation (FSR))). More than one pair of partons could interact too, (producing the so-called Multiple Partons Interaction (MPI)), resulting in a larger number of particles seen in the detectors. As a consequence of the confinement of the colour charge (see Sec. 1.1), gluons and quarks cannot be asymptotic states and they instead emit further soft gluons producing quark-antiquark pairs. Such pairs become longer lived hadrons, in the so-called *hadronisation* process, where collimated structure of hadrons are produced. A schematic view of a pp collision is given in Fig. 3.2.

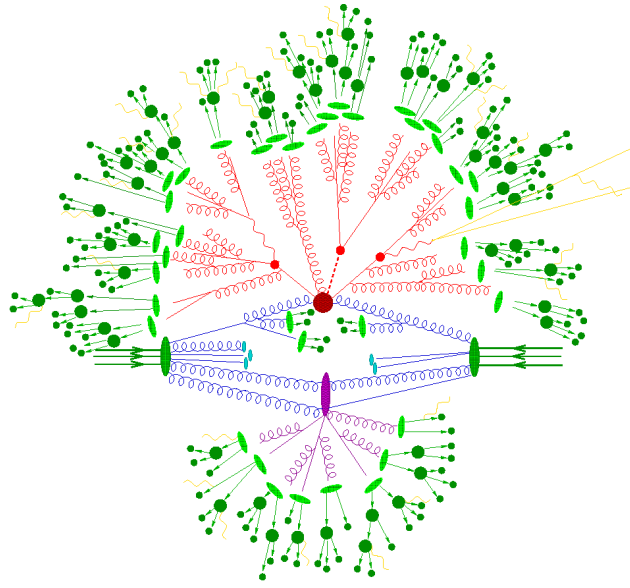


Figure 3.2. Schematic picture of a proton-proton collision. The hard process (red), the MPI (purple), the ISR, FSR and parton showering (blue), the hadronisation (green) and photon emissions (yellow) are shown as well. Plot from Ref. [94].

Bunch filling scheme

The LHC is filled with batches of bunches. After batch injections, which are composed of both *empty* and *filled* bunches (respectively bunches without and with the accelerated protons/ions), the LHC is filled with a trail of empty bunches. The number of empty and filled bunches in each batch, the number of batches before the injection of empty bunches and the number of such empty bunches defines the so-called *filling scheme*.

There are different filling schemes for the different LHC operation modes. A different scheme is exploited for pp collisions and for heavy ions ones, as well as for early operations and for nominal working conditions. During early operations, a smaller amount of filled bunches with a larger spacing between them is foreseen, while in nominal working conditions the number of filled bunches is maximised and the spacing between them is minimised, so to increase the instantaneous luminosity, as will be explained in the following section.

Each filling scheme must however satisfy requirements allowing for correct operations. These requirements are mostly due to limitations on the injection kickers, such as their rise time or their flat-top. Such characteristics affect respectively the number of empty bunches within filled ones and the maximal length of a trail of filled bunches.

In pp collisions, the nominal filling scheme for Run-2 is the 25 ns one, where the spacing between two subsequent bunches is 25 ns. In this scheme, the LHC is injected with 39 batches of bunches, for a total of 3564 bunches, of which 2808 are

filled, according to the following pattern²:

$$3564 = [2 \times (72b + 8e) + 30e] + [3 \times (72b + 8e) + 30e] + [4 \times (72b + 8e) + 31e] + \\ + 3 \times 2 \times [3 \times (72b + 8e) + 30e] + [4 \times (72b + 8e) + 31e] + 80e, \quad (3.1)$$

where e and b stand respectively for empty and filled bunches. From Eq. 3.1, a batch in this scheme is comprised of 72 filled bunches and 8 empty ones, and among different batches injections a trail of either 30 or 31 empty bunches is injected, after a consecutive injection of respectively up to three batches or four batches. After the 39 batches have been injected, the LHC is filled with 80 empty bunches, to allow for the rise time of the kickers dumping the beam (as will be explained in the following section). During 2017, this filling scheme was replaced by the so called $8b4e$ one, where batches were comprised of trails of 8 filled bunches and 4 empty ones, reducing the number of available filled bunches to 1909. Such a scheme, though, reduced the formation of electron clouds, allowing for smoother operations.-

Luminosity and Pile-Up

The number of events N_i associated to a processes i is connected to its cross section σ_i through the instantaneous luminosity \mathcal{L} as in

$$N_i = \sigma_i \int \mathcal{L} dt, \quad (3.2)$$

where \mathcal{L} is the number of interaction per unit of area and time and $\int \mathcal{L} dt$, the so-called *integrated luminosity* L , is the number of interaction per unit area occurred during the data taking. The instantaneous luminosity \mathcal{L} for circular collider experiments takes the form

$$\mathcal{L} = \frac{N_p^2 N_B f_{rev} F}{4\pi\sigma_x\sigma_y}, \quad (3.3)$$

where N_p is the number of protons per bunch (called *intensity* of the beam), N_B is the number of bunches injected in the collider per revolution, f_{rev} is the machine revolution frequency (≈ 11 kHz for the LHC), σ_x and σ_y are the horizontal (x) and vertical (y) widths of the beam, assuming Gaussian profiled beams travelling along the z direction, and $F \leq 1$ is a correction factor which takes into account the crossing angle of the two colliding beams and other intra- and extra-beam effects.

During LHC operations, the instantaneous luminosity decreases, as a consequence of the pp collisions taking place in the IPs as well as of other effects degrading the beam, such as intra-beam forces and interactions of proton bunches with residual gas molecules in the beam pipe. When the instantaneous luminosity goes below a fixed threshold, a series of magnets (*kickers*) deviates each beam trajectory

²This is exactly the pattern that was exploited during 2016. As can be seen from Tab. 3.1, in the other years of Run-2 data-taking the number of empty bunches has been reduced, allowing for a larger number of filled bunches.

from the LHC ring towards a dedicated 700 mm long extraction line (one per beam) ending in a cavern containing the so-called *dump blocks*, 8520 mm long and 722 mm wide cylindrical graphite and stainless steel blocks aimed at absorbing the residual beams energy. The latter procedure is called *beam dump*, and usually it occurs after 5 h – 10 h from the beginning of the data taking (i.e. the beginning of the run). After the beam has been dumped, in Run-2 the injection and then the ramping back from 450 GeV to 6.5 TeV took from 90 min to 120 min. A scheme of the LHC operations is given in Fig. 3.3.

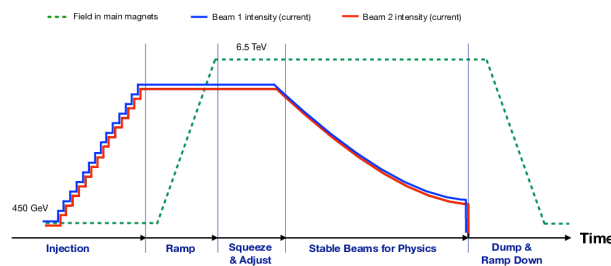


Figure 3.3. LHC operations phases, with the beam intensities (blue and red) and the magnetic field (green) profile as a function of time. From the *injection* phase, where the bunches are sent from the SPS to the LHC and the beam intensities grow over time, the magnetic field is ramped and the bunches are accelerated in the *ramp* phase. The beam quality is then improved through beam focusing and adjusting in the *squeeze and adjust* phase, and finally the *stable beam* condition is achieved, where the quality of the beams is good enough for the collisions to take place. The beam intensities decrease during the *stable beam* phase until they get too low, when the beams are dumped and the magnetic field is ramped down (*dump and ramp down* phase). Plot adapted from Ref. [95].

As a consequence of small spacing between subsequent filled bunches as well as of their high proton density (as from Tab. 3.1 $N_p \sim 10^{11}$), multiple interactions per bunch crossing can occur in the IPs. The quantifier of this phenomenon is called Pile-Up (PU) and there exist two kinds of it: the *in-time* PU and the *out-of-time* PU. The first one takes into account pp collisions occurring in the bunch crossing under study, while the second one refers to additional pp collisions occurring before or after the bunch-crossing under study, affecting the data taking for detectors that are sensitive to several bunch-crossings or that have electronics integrating over more than 25 ns.

Multiple simultaneous interactions pose a challenge for the detectors that must resolve particles from different pp collisions. Hence it is desirable to have the smallest possible PU. At the same time, increasing the number of collected events N_i is of utmost importance, even more so for searches of BSM rare phenomena such as the ones looked for in this thesis. To do so, beside increasing the duration of the data

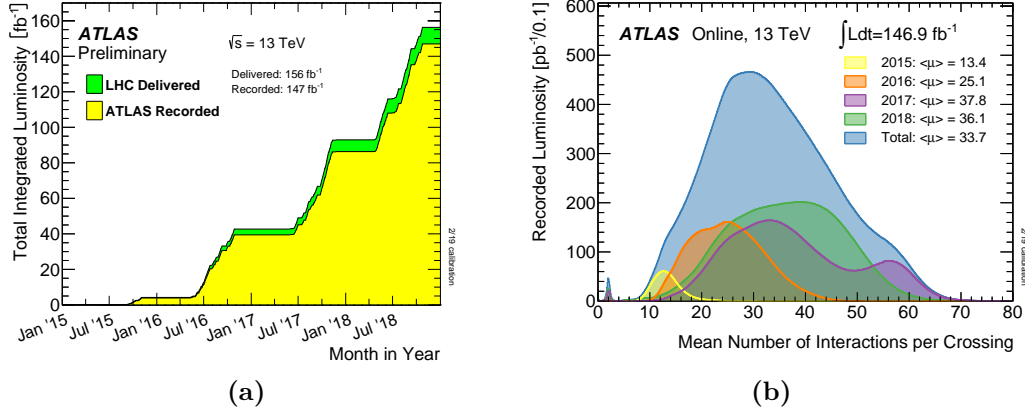


Figure 3.4. (a) Integrated delivered (yellow) and recorded by ATLAS (green) luminosity as a function of time for Run-2; (b) PU profile for different data taking years in Run-2. Plots adapted from Ref. [96].

taking, it is necessary to maximise the instantaneous luminosity \mathcal{L} (Eq. 3.2). To give an example, augmenting N_p would result in an increase of \mathcal{L} (see Eq. 3.3) but also of the *in-time* PU, since the presence of more protons in each bunch could lead more likely to multiple interactions in the same bunch crossing. On the other hand, augmenting N_B results in an increase of \mathcal{L} but also of the *out-of-time* PU, since the spacing between different bunches would decrease and then the chance of overlaps of interactions coming from different bunch crossings would grow. \mathcal{L} has thus to be increased without increasing too much the PU.

Fig. 3.4 (a) shows the integrated luminosity delivered by the LHC and recorded by ATLAS during Run-2 while Fig. 3.4 (b) depicts the ATLAS PU profile for different years of the Run-2 data-taking. The average PU in Run-2 was 33.7. The collected data usable for physics, i.e. the runs in which all ATLAS subsystems were operating at normal conditions, was firstly measured to be $L = 139 \text{ fb}^{-1}$, with an uncertainty on such measurement of 1.7%. Thanks to the study in Ref. [97] the accuracy on the luminosity measurement was improved of a factor of two, yielding $L = 140.1 \text{ fb}^{-1} \pm 1.2 \text{ fb}^{-1}$, with an uncertainty of 0.83%, the smallest ever achieved in a hadron collider. The search outlined in Chap. 5 and Chap. 6 was performed after the study of Ref. [97], and therefore its results are based on $L = 140 \text{ fb}^{-1}$. On the other hand, the search in Chap. 7 was finalised before the aforementioned study, and therefore it is based on $L = 139 \text{ fb}^{-1}$.

3.2 ATLAS detector

The aim of physics experiments is to provide measurements of physical quantities, such as cross sections, that could be compared to theoretical predictions so to prove a certain theoretical model. In particle physics, the apparatuses used to measure these quantities are the detectors, which reveal the passage of a particle through its interactions with the mean of which the detector is made of. As the energy of the interactions increases, the energy and the penetrating power of the products of

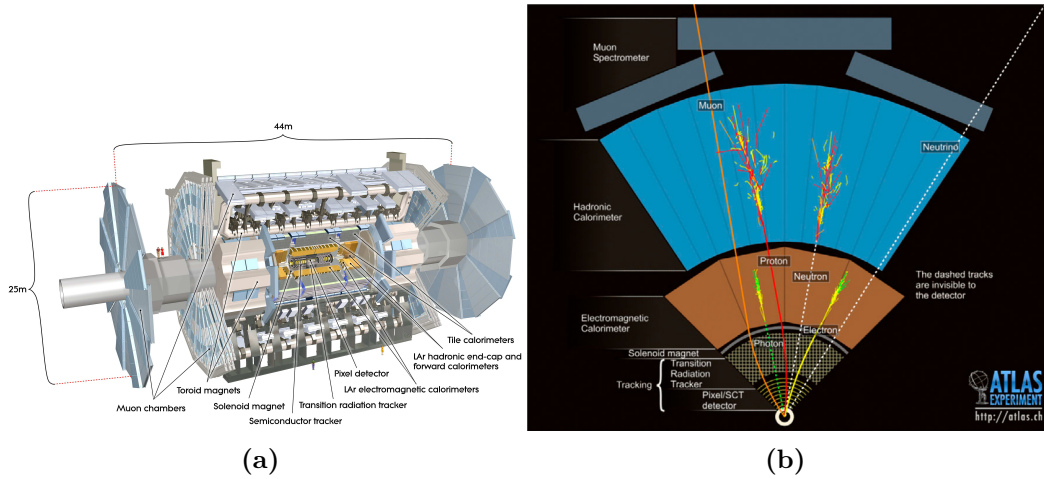


Figure 3.5. (a) ATLAS detector, plot from Ref. [98]; (b) particle interactions with different ATLAS sub-detectors. Tracks of charged particles are reconstructed in the ID (the yellow and black stripes and grid); electrons and photons leave the majority of their energy in the ECAL (brown); hadrons instead interact primarily with the HCAL (azure); muon (orange line) tracks are reconstructed in the MS (and in the ID too), while neutrinos (dashed white line) traverse the detector without interacting. Plot from Ref. [99].

such interactions also increase, implying that the detectors must be large enough to be able to identify these products. All the detectors located around the LHC IPs are therefore extremely large, to contain the very energetic particles produced in the pp collisions.

ATLAS is a barrel-shaped multi purpose detector with a forward-backward cylindrical symmetry around one of the four IPs of the LHC. It is the largest detector at the LHC, being 46 m long and 25 m wide and weighting in total approximately 7000 t. It is a so-called *general-purpose detector*, providing nearly complete and hermetic coverage of the solid angle around the IP and being made of three concentric cylindrical sub-detectors (see Fig. 3.5 (a)), each of which is optimized for the detection of specific types of particles (see Fig. 3.5 (b)). These sub-detectors, ordered in increasing radial distance from the IP, are:

- the Inner Detector (ID), reconstructing tracks of charged particles and vertices of interactions;
- the calorimeter system, measuring energy releases of particles traversing the detector; it is composed of
 - the Electromagnetic CALorimeter (ECAL), detecting EM showers;
 - the Hadronic CALorimeter (HCAL), measuring hadronic showers, jets and Missing Energy Transverse (MET) E_T^{miss} ;
- the Muon Spectrometer (MS), reconstructing muon tracks.

3.2.1 Coordinate system

In order to uniquely describe the topology of events occurring in the ATLAS detector, a right-handed cartesian coordinate system is defined (see Fig. 3.6), with its origin matching the IP.

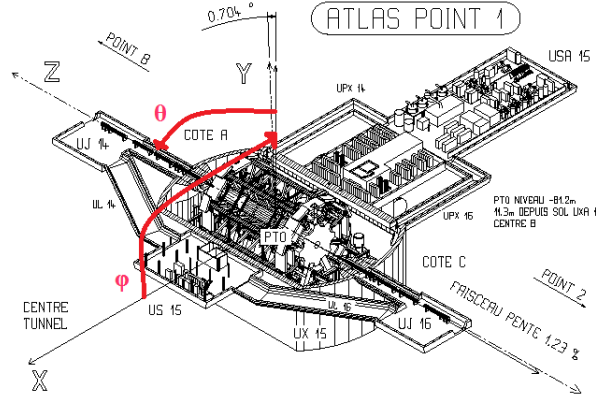


Figure 3.6. Coordinate system for the ATLAS detector. Both the right-handed cartesian coordinate system and the cylindrical one are shown. Plot adapted from Ref. [100].

The z axis coincides with the beam line, the y axis points upwards and the x axis points towards the centre of the LHC. The area of the detector at positive z is referred to as *side A*, while the one at negative z is referred to as *side C*.

Cylindrical coordinates (r, ϕ) are used as well (with $\phi \in (-\pi, \pi]$ and $\phi = 0$ in the direction of the positive x axis) to exploit the cylindrical symmetry of the detector. The polar angle θ is used too, with $\theta \in [0, \pi]$, where $\theta = 0$ is the direction of the positive z axis.

As said in Sec. 3.1.3, since protons behave as composite particles at high energies, the collisions occur between partons, carrying an unknown (but governed by the PDF) fraction of the total momentum of the proton. The longitudinal momentum in the initial state is thus unknown. Physical observables invariant under Lorentz boosts along the z axis are therefore used to describe events:

- the azimuthal angle ϕ ;
- the transverse momentum $p_T := \sqrt{p_x^2 + p_y^2}$ (with p_x and p_y being the momentum of the particle along respectively the x and the y axis), that is the projection of the particle momentum on the plane transverse to the beam axis;
- rapidities differences Δy , where $y = \frac{1}{2} \ln \frac{E + p_z}{E - p_z}$ (with E and p_z respectively the particle energy and its momentum along the z axis); for relativistic particles, the rapidity coincides with the pseudorapidity $\eta = -\ln \tan \frac{\theta}{2}$. $\eta = 0$ corresponds to the y axis while $\eta = \pm \inf$ corresponds to the z axis. The region of the detector at high η is often referred to as the *forward region*, and in general detectors coverage is often expressed in terms of η ;

- the angular distance between two objects $\Delta R = \sqrt{\Delta\eta^2 + \Delta\phi^2}$;
- the MET E_T^{miss} , quantifying a momentum imbalance in the transverse plane (a more accurate definition of the E_T^{miss} is given in Sec. 4.3).

The central cylindrical section of the detector, closer to the IP, is called *barrel*, while the regions positioned at the ends of the detector, away from the IP, are called *endcaps*.

In the following, the different ATLAS sub-detectors systems are described.

3.2.2 Magnet system

A charged particle moving in a plane transverse to a magnetic field B is bended with a curvature radius r depending on its momentum P and on the magnetic field, as in³

$$P[\text{GeV}] = 0.3B[\text{T}]r[\text{m}].$$

Detectors measuring the momentum of charged particles are therefore located in magnetic fields, that need to be rather high for measuring high- p_T particles. The ATLAS detector, measuring the momentum of charged particles both in the ID and in the MS, features a superconducting magnet system (see Fig. 3.7), providing a magnetic field over a volume of approximately 12 000 m³ of the whole detector [101]. The ID is located inside a solenoid generating a 2 T magnetic field parallel to the

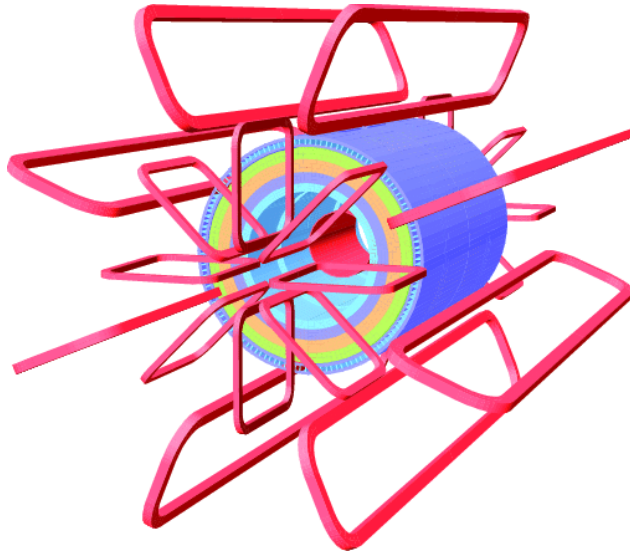


Figure 3.7. Schematic view of the magnet system of the ATLAS detector. Plot adapted from Ref. [90].

beam line, so that charged particles are bended in the $(r - \phi)$ plane. Such solenoid

³in this derivation it is assumed that the particle has a unitary electric charge (in terms of the electron charge). Furthermore, here only the magnitude of the momentum is given, since to understand its orientation one should take into account both the orientation of the magnetic field and the sign of the charge of the particle.

is 5.9 m long with an internal diameter of 2.46 m and an external one of 2.56 m. The barrel (endcap) MS is instead located in a 0.5 T (1 T) toroidal magnetic field, bending charged particles in the $(r - z)$ plane in the barrel (endcap) region of the MS. The barrel (endcap) toroid air-core system is composed of 8 (8 per side) 25.3 m (5 m) long coils forming a cylinder with an internal diameter of 9.4 m (1.65 m) and an external diameter of 20.1 m (10.7 m).

3.2.3 Inner Detector

The ID [102], schematically depicted in Fig. 3.8, is the detector closest to the beam line and it reconstructs the tracks left by charged particles and their production vertices. Since its proximity to the IP, the ID operates in a high density environment

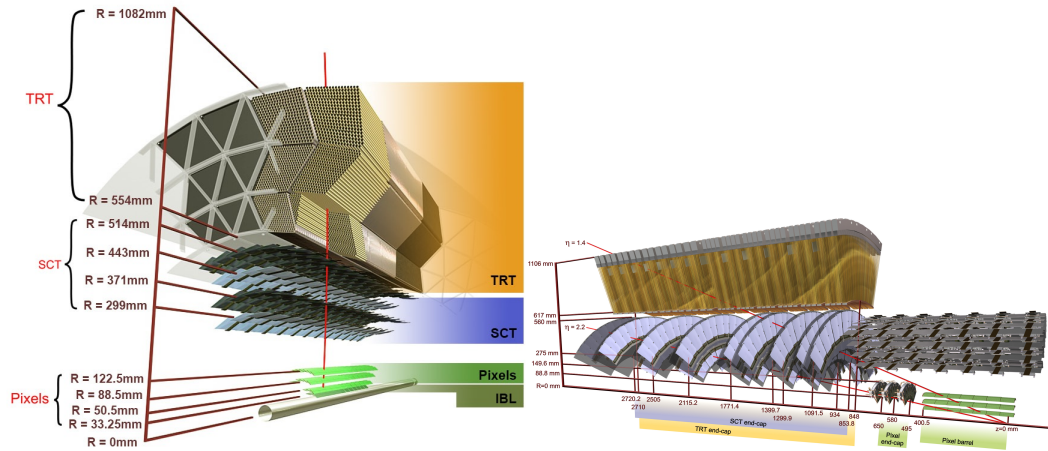


Figure 3.8. ID in the (r, ϕ) plane in the barrel [103] (left) and endcap [104] (right). The radial distances covered by the barrel detectors as well as longitudinal and radial ones by the endcap detectors are shown. The paths of two particles with $\eta = 2.2$ and $\eta = 1.1$ are depicted as an example.

and is therefore the ATLAS sub-detector with the finest granularity. It extends from 33 mm to 1082 mm in radial distance from the IP, it is 6.2 m long in the longitudinal direction and it covers the pseudorapidity range of $|\eta| \leq 2.5$. It consists of three types of tracking systems that, ordered in increasing radial distance from the IP, are: the Pixel Detector (PD), the Semi-Conductor Tracker (SCT) and the Transition Radiation Tracker (TRT).

The total resolution on the measurement of the p_T of charged particles traversing the ID is

$$\frac{\sigma_{p_T}}{p_T} = 0.5\% p_T [\text{GeV}] \oplus 1\%.$$

The p_T resolution thus decreases as a function of the p_T itself, as the curvature radius increases, this resulting in a smaller number of hits left in the ID.

Pixel Detector

Being the detector closest to the IP, the PD has finest granularity of all the ID sub-detectors. It is composed of three (three) layers in the barrel (endcap) region, located at radial r (longitudinal z) distances respectively of 50.5 mm ($|z| = 495$ mm), 88.5 mm ($|z| = 580$ mm) and 122.5 mm ($|z| = 149.6$ mm), covering a longitudinal (radial) distance of 400.5 mm (88.8 mm $< r < 149.6$ mm) in total. It is made of 1744 sensors with 46080 read-out silicon pixels each, for a total of roughly 80 million read-out channels. Each has a dimension of $400 \times 50 \mu\text{m}^2$, with a resolution of $10 \mu\text{m}$ in the (r, ϕ) plane and of $115 \mu\text{m}$ in the z direction. After the LS1, the Insertable B-Layer (IBL) has been inserted at a radius of $r = 33.25$ mm, providing an improvement on primary and secondary vertices reconstruction (see Sec. 4.1) and enabling the identification of high p_T tracks.

Semi-Conductor Tracker

The SCT provides a high precision measurement of the tracks impact parameters⁴ and p_T . In the barrel, it comprises four layers, located at radial distances of 299 mm, 371 mm, 443 mm and 514 mm, covering a longitudinal distance $|z|$ of 749 mm. In both the endcap regions there are nine disks located at different longitudinal distances z , the first one at $|z| = 839$ mm (per side) and the last one at $|z| = 2735$ mm (per side), covering the area between the radial distances from 275 mm to 560 mm. The reconstruction resolution is $17 \mu\text{m}$ in the plane (r, ϕ) and $580 \mu\text{m}$ in z .

Transition Radiation Tracker

Being the outermost ID detector, the TRT is the ID sub-detector with the coarser granularity. It is composed of 4 mm diameter drift tubes, that in the barrel (endcap) region are parallel to z (r) and arranged in 73 (160) layers, which are located at different radial (longitudinal) distances r (z), the first being at 563 mm ($|z| = 848$ mm) and the last at 1066 mm ($|z| = 2710$ mm), covering a longitudinal (radial) distance of 712 mm (400 mm, from $r = 644$ mm to $r = 1004$ mm). Measurements are performed in the (z, ϕ) plane, with a resolution of $130 \mu\text{m}$. The TRT straws are filled with a gaseous mixture of 70% Xe, 27% CO_2 and 3%O, that is ionized when charged particles traverse it.

Furthermore, Transition Radiation (TR) signals can be used to distinguish among different kinds of particles. Ultra-relativistic particles traversing media with different dielectric and/or magnetic properties emit a number of TR photons which is proportional to the γ of the particle itself. If travelling with the same p_T , lighter particles thus produce more TR photons than heavier ones. These photons would be absorbed by the gas mixture, producing high energy hits. From the amount of

⁴in this context, the impact parameters refers to the perpendicular distance between the trajectory of a particle and the nominal IP at the point of closest approach, which is the point where the particle is closest to the IP. More details about impact parameters evaluation will be given in Chap. 4.1.

such hits, electrons are distinguished from pions with $1 \text{ GeV} < E_T < 100 \text{ GeV}$ with a 99% efficiency.

3.2.4 Calorimeter system

The calorimeter system is the apparatus measuring the energy left by photons, electrons and hadrons as well as the MET. It is made of two different sub-detectors, that, ordered in increasing radial distances from the IP, are: the ECAL [105] and the HCAL [106]-[107]. The ECAL measures energy releases left by photons and electrons coming from EM showers, which are cascades of secondary particles produced from EM interactions of high-energy particles with the matter. Its dimensions are thus given in terms of radiation lengths⁵ X_0 . The HCAL detects instead the energy left by hadrons producing hadronic showers, which are cascades of secondary hadrons produced from strong interactions of hadrons with the matter. Its size is thus given in terms of the interaction lengths⁶ λ . Both the ECAL and the HCAL are sampling calorimeters, in which absorber and active layers are combined, allowing for more compact detectors with respect to homogeneous calorimeters, which however provide a better energy resolution being made only of active materials. A scheme of the calorimeter system is shown in Fig. 3.9.

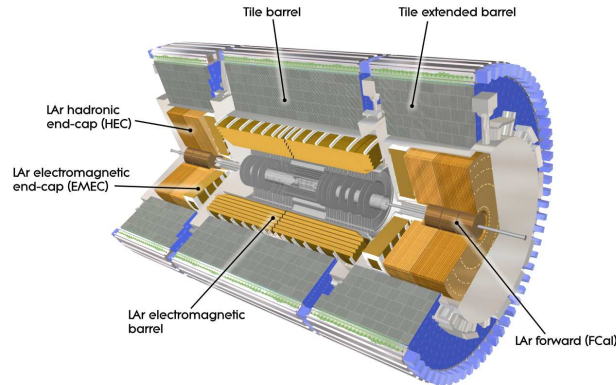


Figure 3.9. Schematic view of the calorimeter system. Plot from Ref. [90].

Electromagnetic CALorimeter

The ECAL is $22 X_0$ long in the barrel and $24 X_0$ long in the endcaps. The absorber layers are made up of lead while the active ones are made up of Liquid Argon (LAr). The structure is accordion-shaped in order to provide a fast reconstruction of signals

⁵the radiation length is the distance travelled by a beam of particles in a certain mean, before the number of such particles is reduced of a factor $1/e$, as a consequence of their EM interactions with the mean itself.

⁶the interaction length is the distance travelled by a beam of hadrons in a certain mean, before the number of such hadrons is reduced of a factor $1/e$ as a consequence of their strong interactions with the mean itself

and an almost complete coverage in ϕ , maximising the number of particle interactions with the different active layers and avoiding possible dead zones. In between two consecutive lead layers, electrodes detect the signal produced by electrons and photons that release their energy in the LAr.

To provide a high granularity, the ECAL is divided in 3 separate sections:

- the EM barrel, covering the pseudorapidity range $|\eta| \leq 1.475$, an r from 1.41 m to 1.96 m and a z of $z = \pm 3.21$ m;
- the two EMECs (ElectronMagnetic EndCaps), covering the pseudorapidity range $1.37 \leq |\eta| \leq 3.2$ and a z from $z = \pm 3.70$ m to $z = \pm 4.25$ m

In the region $|\eta| < 1.8$ an additional calorimeter with finely segmented layers of LAr and lead is located close to the beam-pipe. This addition allows to correct the energy measured in the barrel by adding the energy released before it. The separation region between the barrel and the endcaps, in the range $1.37 < |\eta| < 1.52$, is called *crack-region* and is typically vetoed in the reconstruction of electrons or photons since it contains a large amount of inactive material.

The overall energy resolution of the ECAL is

$$\frac{\Delta E}{E[\text{GeV}]} = \frac{10\%}{\sqrt{E[\text{GeV}]}} \oplus 0.7\%.$$

Hadronic CALorimeter

The HCAL is 9.7λ long in the barrel and 10λ long in the end-caps. This size allows to contain almost completely hadronic showers, preventing leakages to the MS and guaranteeing a reliable E_T^{miss} reconstruction. The HCAL is divided into six regions, each of which has a different sampling technique depending on the different radiation environments:

- the tile and the two extended barrels, which surround the ECAL, from $r = 2.28$ m to $r = 4.25$ m. The tile barrel covers the region $|\eta| \leq 1.0$ and extends up to $z = \pm 5.8$ m, while the two extended barrels cover the region $0.8 \leq |\eta| \leq 1.7$ from $z = \pm 5.8$ m to $z = \pm 8.4$ m. The active material is made up of scintillating tiles, while the steel is used as passive material. The tile calorimeter energy resolution is

$$\frac{\Delta E}{E} = \frac{50\%}{\sqrt{E[\text{GeV}]}} \oplus 3\%;$$

- the two Hadronic EndCaps (HECs), composed of two wheels of radius 2.03 m, both covering the range $1.5 \leq |\eta| \leq 3.2$. Here LAr is used as active material and copper plates as absorbers, as the amount of radiation in the end-caps is greater than the one in the barrel. Each HEC has an energy resolution of

$$\frac{\Delta E}{E} = \frac{50\%}{\sqrt{E[\text{GeV}]}} \oplus 3\%;$$

- the Forward Calorimeter (FCal) is placed very close to the beam pipe, covering the pseudorapidity range $3.1 \leq |\eta| \leq 4.9$, where the particle density is extremely high. It is composed of three layers: LAr as active material, and copper and tungsten as absorbers for respectively the innermost and the external layers. The FCal has an energy resolution of

$$\frac{\Delta E}{E} = \frac{100\%}{\sqrt{E[\text{GeV}]}} \oplus 10\%.$$

3.2.5 Muon Spectrometer

The MS [108] is located in the outermost part of the ATLAS detector and it reconstructs tracks of muons with $p_T > 3 \text{ GeV}$ in the region $|\eta| \leq 2.7$. It provides almost complete coverage in such η region, except for an opening in the central ($r\phi$) plane ($\eta = 0$) for the passage of cables and services of the ID, of the central solenoid and of the calorimeters. In addition, the MS can also provide the trigger (see Sec. 3.2.6) for events where muons are found with $|\eta| \leq 2.4$. Magnetic bending is provided by the large barrel toroid (small endcap toroids) for $|\eta| \leq 1.4$ ($1.6 \leq |\eta| \leq 2.7$) (see Sec. 3.2.2). In the region $1.4 \leq |\eta| \leq 1.6$, called transition region, the bending is provided by a combination of the barrel and the endcap magnetic fields.

In the barrel (endcap) region at $|\eta| \leq 1.05$ ($1.05 \leq |\eta| \leq 2.7$), three cylindrical layers, referred to as stations (muon wheels), are situated around (perpendicular to) the beam axis, at radial (longitudinal) distances r (z) of $r \sim 5 \text{ m}$ ($|z| = 7.5 \text{ m}$, the small wheel), $r \sim 7.5 \text{ m}$ ($|z| = 13 \text{ m}$, the innermost big wheel) and $r \sim 10 \text{ m}$ ($|z| = 22 \text{ m}$, the outermost big wheel). The three barrel (endcap) layers are called, in increasing distance from the IP, Barrel Inner (BI) (Endcap Inner (EI)), Barrel Middle (BM) (Endcap Middle (EM)) and Barrel Outer (BO) (Endcap Outer (EO)). Each layer is further divided in the azimuthal plane into 16 stations, eight large (L) and eight small (S), covering respectively 28° and 17° . Large sectors are located in between the eight barrel toroid coils, and small sectors overlap in ϕ with the coils. Sectors are numbered starting from $\phi = 0^\circ$, with Sector 1 being a Large sector. A schematic view of the MS is given in Fig. 3.10.

The overall momentum resolution for low- p_T muons is $\sigma_{p_T}/p_T \sim 2 - 3\%$, while for high- p_T ones is $\sigma_{p_T}/p_T \sim 10\%$.

The MS exploits two different types of so-called *muon chambers* in the different MS regions, to maximise the performances of the detector. The MS high precision chambers are used for precise measurements of the muon tracks p_T , while the MS trigger chambers are exploited by the trigger system. Being exploited in the trigger system, trigger chambers are much faster, but less precise, than precision chambers.

Precision chambers

The two types of MS high precision chambers are:

- the Monitored Drift Tubes (MDTs): used in the barrel region and in the endcap up to $|\eta| \leq 2$ for high precision track measurement, they are composed

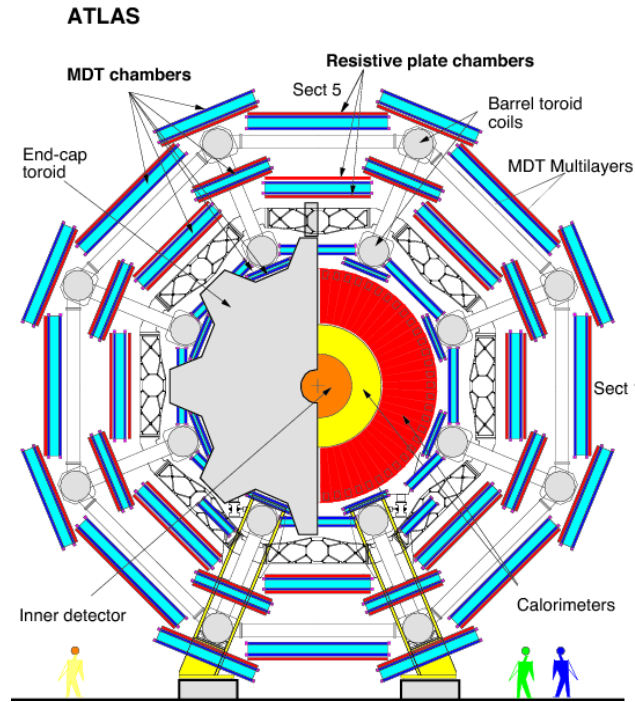


Figure 3.10. View of the ATLAS detector in the (r, ϕ) plane; the components of the MS are highlighted. Plot from Ref. [108].

of two multi-layers of aluminum drift tubes, each $400\text{ }\mu\text{m}$ thick and with a diameter of 30 mm , filled with a gas mixture of Ar and CO_2 at a pressure of 3 bar. The charge produced by the ionization of the gas is collected by a Tungsten-Rhenium wire placed in the center of the tube, providing a resolution on the sagitta of $35\text{ }\mu\text{m}$. MDTs are installed in all the aforementioned barrel and endcap stations, apart from the small wheel;

- the Cathode Strip Chambers (CSCs): used in the small wheel in the forward region $2 \leq |\eta| \leq 2.7$, they are more robust than MDTs since they are subject to a higher particles flux. CSC cathodes are filled with a gas mixture of Ar and CO_2 and are segmented in orthogonal strip wires, allowing a measurement in both (r, ϕ) coordinates, with a resolution of $60\text{ }\mu\text{m}$ in r , of 5 mm in ϕ and of 7 ns in time t .

Trigger chambers

The two types of MS trigger chambers are:

- Resistive Plate Chambers (RPCs): exploited in the barrel up to $|\eta| < 1.05$, they are arranged into two-layered stations, referred to as *doublets*, of which two are found in the BM and one in the BO. Each RPC consists of two bakelite plates separated by a 2 mm gap filled with a gas mixture of 97% tetrafluoroethane ($\text{C}_2\text{H}_2\text{F}_4$) and 3% isobutane (C_4H_{10}). A high electric field of 4.5 kVmm^{-1} is maintained between the two plates to amplify the primary

ionization of charged particles crossing the detector. The signal so produced is collected on metallic strips located in the outer sides of the bakelite plates. The track reconstruction resolution is 10 mm in z , 10 mm in ϕ and 1.5 ns in time t ;

- Thin Gap Chambers (TGCs): exploited in the end-caps, they are very thin multi-wire chambers designed to have the anode-cathode spacing smaller than the anode-anode spacing, for a very short drift time of 20 ns (smaller than bunch spacing, see Tab. 3.1), providing a fast signal which is crucial for the trigger system. The chambers are filled with a gas mixture of CO₂ and n-pentane (C₅H₁₂) operating in saturation mode. The track reconstruction resolution is 2 – 6 mm in r , 3 – 7 mm in ϕ and 4 ns in time t .

Besides trigger information, MS trigger chambers measure as well the muon coordinate in the orthogonal direction to the one provided by the precision tracking chambers.

3.2.6 Trigger system

During Run-2 proton bunches in the LHC collided every 25 ns, corresponding to a collision rate of 40 MHz. Considering that per each event 1.5 MB of data are written, if all the events were recorded 60 TB of data per second would have been produced. Since such a large data rate is incompatible with modern technology for data storage and since most of the events produced are not interesting for the ATLAS physics program since they originate from low- p_T inelastic and diffractive pp collisions, a preliminary selection based on physics signatures, such as the presence of energetic leptons, photons, jets or missing energy, is performed before the event is recorded. This selection is made by the ATLAS two-levels Trigger System [109, 110]: the Level-1 (L1) trigger, with dedicated electronics exploiting basic information from the detectors, and the High Level Trigger (HLT), with software algorithms performing a preliminary reconstruction of the event.

L1 trigger

The L1 trigger is based only on electronics and it elaborates information from the Muon System (L1Muon), the Calorimeter System (L1Calo) and the L1 Topological Processor (L1Topo). The L1Muon trigger takes as input information from the RPCs in the barrel and from the TGCs in the endcap, the latter being combined with information from the Tile Calorimeter to reduce the rate of fake triggers in the region $1.05 < |\eta| < 1.3$. The L1Calo trigger takes information from the calorimeters and sends it to the Cluster Processor (CP) and the Jet/Energy-sum Processor (JEP), reconstructing respectively electrons/photons/ τ -leptons candidates and jets/ E_T^{miss} . The L1Topo provides a decision based on combined L1Calo and L1Muon items, including their relative position and energy thresholds, combined mass and corrections due to the E_T^{miss} .

The final decision on whether accepting the event at the L1 trigger can be

based either on the number of muons above a certain p_T threshold, on the total energy measured in portions of the calorimeters or not reconstructed in the whole detector, as for the E_T^{miss} triggers, and it is made by the so-called Central Trigger Processor (CTP), to which information from the L1Calo, L1Muon, L1Topo and from additional control sub-systems are sent. The rate of accepted events is reduced from the CTP down to 100 kHz, with a fixed maximum latency of 2.5 μs .

High Level Trigger

Once an event is accepted by the L1 trigger, Region Of Interests (ROIs), defined in the (η, ϕ) plane, are identified and data coming from them are transferred via the Read-Out Driver (RODs) from the Front End (FE) boards of the sub-detectors to the Read-Out System (ROS), which are interfaced with a farm of Central Processing Units (CPUs) where the software-based HLT is run. The HLT system performs a decision in hundreds of milliseconds, with an output rate of 1.2 kHz, with a typical disk writing rate of $\sim 1.2 \text{ GBs}^{-1}$. Data selected by the L1+HLT trigger system are stored permanently.

Trigger menus and data streams

An event must have fired a so-called *trigger chain*, a combination of a L1 and a HLT trigger algorithm, in order to be selected. Such combination applies kinematic selections on the preliminary reconstructed objects, selecting events with candidate leptons, photons, jets with specific characteristics, such as a given p_T . Such chains are typically used by multiple analysis groups in the ATLAS collaboration, and are stored in the so-called *trigger menu*. The trigger menu evolved during Run-2 to cope with the increase of instantaneous luminosity. To further reduce the event rate associated to a given trigger chain, a prescaling factor of N can be applied to the trigger chain, so that only $1/N$ events of the total passing the trigger chain are stored. Usually ATLAS searches rely on the so-called *lowest un-prescaled* triggers, with minimum p_T thresholds and no prescale applied. In the searches introduced in Chap. 5, 6 and 7 the same choice is made.

In ATLAS, six so-called *data-streams* identified with different trigger chains are exploited:

- the *physics stream*: used in standard physics analyses, it stores the information from the full detector, with a typical event size of $\sim 1 \text{ MB}$;
- the *Trigger-Level Analysis (TLA) stream*: used in physics analyses using information reconstructed only at the HLT level, it stores only partial detector information and specific physics objects, allowing for looser trigger constraints thanks to the smaller event size, which is typically of $\sim 6.5 \text{ kB}$;
- the *debug stream*: used to fully recover events for which the HLT failed to be fully ran, as a consequence of processing times exceeding limitations, data transfer errors or similar issues;

- the *calibration stream*: used for detector calibration purposes, it collects data from specific sub-detectors;
- the *express stream*: used for data quality monitoring, it collects a restrained amount of data from the physics stream and applies offline reconstruction;
- the *monitoring stream*: used to control the status of ATLAS sub-detectors, it does not foresee any data storage.

3.2.7 Event simulation

While the cross section of hard scatter events can be calculated perturbatively thanks to the asymptotic freedom of QCD⁷, the same cannot be done for soft processes. The vast amount of non-perturbative processes at particle colliders makes thus comparing theoretical predictions to experimental measurements difficult. Studying the large number of samples produced by Monte Carlo (MC) simulations could be a useful way to overcome these difficulties, producing the possible outcomes by randomly sampling the underlying (assumed or measured) PDFs. Since hard and soft processes can be factorised, the simulation can be done in two steps, at the *parton level* and at the *particle level*. A third simulation step, referred to as *detector level* simulation, taking into account particles interactions with the detector elements, is then performed as well.

Parton level simulation

The simulation of the hard process is done, in the perturbative regime at a fixed order in perturbation theory, taking into account the PDFs of the partons and their available phase space. The outcome of this simulation contains also coloured partons and is said to be done at the *parton level*. In this thesis the MADGRAPH event generator [111] has been used for matrix element calculations of the hard processes at Next-to-Leading-Order (NLO) accuracy for signal samples used in both the searches presented, as explained in Chap. 5 and Chap. 7, and it is interfaced with PYTHIA [112] (see next section) for the second step of the simulation.

Particle level simulation

At this stage of the simulation, the (still perturbative) parton showering, the decay of unstable particles, the (non perturbative) hadronisation and the *underlying event* are included. The latter contains all the (soft) particles that in an event are not coming from the hard process, resulting from the beam remnants, MPI, ISR and FSR. The impact of such processes (contributing to the PU, as explained in Sec. 3.1.3) is evaluated from studies on *minimum bias* events, resulting from *pp* collisions where extremely loose trigger requirements are asked (hence the definition *minimum bias*). After such a study, these multiple interactions are simulated with PYTHIA8.210 with the A3 set of tuned parameters (tune) [113] and the

⁷The strong coupling constant α_s decreases with the increase of the energy scale.

NNPDF2.31o set of PDFs [114]. In this thesis, the PYTHIA generator was used as well for the second step of the signal samples simulations as well as interfaced [115] with POSITIVE WEIGHT HARDEST EMISSION GENERATOR (POWHEG) [116] for the generation of $t\bar{t}$ and single- t samples, while the SIMULATION OF HIGH-ENERGY REACTIONS OF PARTICLES (SHERPA) generator [117] is instead used standalone for the generations of the other SM background processes beside for V + jets with an EW production of the V boson, where HADRON EMISSION REACTIONS WITH INTERFERING GLUONS (HERWIG) (++) [118] is used. PYTHIA, SHERPA and HERWIG++ provide a full event generation taking into account the soft and the hard processes. While the first one, being a LO generator, is usually interfaced with matrix-element generators with higher accuracy, the latter two, providing a better accuracy, are used standalone, as they cannot be interfaced with any other generator. POWHEG provides instead a method for generating NLO accurate parton-level events, particularly useful for simulating processes where NLO corrections are important, such as top quark production, and it has to be interfaced with parton showering simulators, such as PYTHIA.

Detector level simulation

Particle interactions with detector elements have to be taken into account as well in order to compare simulations results with measurements. Detector effects, such as sensitivities, geometrical acceptances and resolutions, are considered too. The outputs of the entire simulations, directly compared to measurements, are called *detector level* distributions and the particles present at this stage are called *reconstructed particles*. In this stage of the simulation, detector noise is considered as well and the simulated signal hits are overlaid with cavern background events hits and with additional hits from soft QCD events to simulate the effect of PU. The detector level simulation is performed in ATLAS by GEOMETRY AND TRACKING (GEANT)4 [119, 120], a toolkit widely used in high energy physics.

MC weights

Simulated MC events have an associated weight taking into account different aspects of the simulation:

- calculation order of perturbation theory: events that are generated beyond LO have a MC weight correcting the cross-section distribution so to reproduce the one at the correct order in perturbation theory;
- form factor: each event has a weight taking into account the form factor associated to QCD emissions;
- PU: an event weight is also derived to correct the distribution of the PU per bunch crossing, so that the simulation distribution matches the one in data. MC simulations are indeed usually produced before the PU profile per run has been evaluated.

In order to correctly reproduce the expected number of events, such MC weight should be normalised to the total number of weighted events. Since different PU profiles are observed for the different Run-2 data takings (as in Fig. 3.4 (b)), such normalisation procedure should be performed independently for the four data-taking years. Therefore, the expected number of events N associated to a process with cross section σ is obtained via:

$$N = \sigma \sum_j^{2015-2018} L_j \sum_i^{N_j} \frac{w_i^j}{w_{tot}^j},$$

with j spanning over the Run-2 data-taking years, L_j , N_j and w_{tot}^j being respectively the integrated luminosity, the number of generated MC events and the sum of the events weights (taking into account the PU weight) associated to the j data-taking year and w_i^j being i -th event MC weight, which takes into account the PU weight associated to the PU profile of the j -th data taking year.

A set of corrections related to the measurement procedure needs to be taken into account as well in the event weight. These corrections are called Scale Factors (SFs) and they are exploited so that the performances of the various reconstruction and trigger algorithms obtained in MC simulations match those in data.

Blinded searches

MC simulations are widely used in searches of BSM physics, as the ones described in this thesis work. The new physics process looked for is simulated, along with possible background processes that could mimic signal events. The analysis strategy is then obtained exploiting such simulations, by defining selection cuts reducing the background while retaining as much signal efficiency as possible. At this stage, the analysis is said to be *blinded*. Once the selections and the background estimation techniques have been fixed, the analysis is carried out onto the collected dataset, with this procedure being called *unblinding*. The analysis is performed onto real data only once it has been finalised to avoid any possible bias.

While the search in Chap. 7 at the moment of writing is already published and therefore the results here presented are unblinded ones, the search in Chap. 5, 6 is still under internal review of the ATLAS collaboration and only one out of three analysis channels has been unblinded.

Chapter 4

Physics objects reconstruction in ATLAS

Once an event is accepted by the ATLAS Trigger System (Sec. 3.2.6), the electronic signals produced by each sub-detector described in Sec. 3.2 are permanently stored. The raw signals collected from the different detectors are converted into meaningful information through a set of techniques and algorithms, finding candidates for electrons, muons, photons, jets, etc., in a step that is called *physics objects reconstruction*. Such candidates are found along with their properties, such as their momenta, energy or charge. The two building blocks used as input for this reconstruction are tracks built from hits in the ID and in the MS and clusters reconstructed from energy deposits in the calorimeters. Different objects definition, based on different reconstruction algorithms, can be used, with this choice being driven by the specific search interest. Furthermore, standard object definitions are usually recommended by the ATLAS collaboration, but further optimisation can be done at the analysis level to improve selections and maximise the sensitivity. In the following, a description of how detector signatures are reconstructed as physics objects is given. Specific selections imposed on the physics objects exploited which are aimed at improving the sensitivity of the search in Chap. 5 and Chap. 6 are here introduced but discussed in the relevant chapters. Such selections are also here outlined for the search in Chap. 7, but the reader is referred to Ref. [2] for further details, since their associated optimisation are not carried out in the context of this thesis work.

4.1 Tracks and vertices

The ID is immersed in a solenoid producing a magnetic field whose axis is parallel to the beam line, as explained in Sec. 3.2.2. Charged particles are therefore bended in the ID in the plane transverse to the beam axis, travelling with a helical trajectory defined by 5 parameters: η and ϕ , as defined in Sec. 3.2.1, q/p , the ratio of the charge of the particle over its momentum, and the impact parameters z_0 and d_0 , the points of closest approach between the track and the nominal IP respectively in

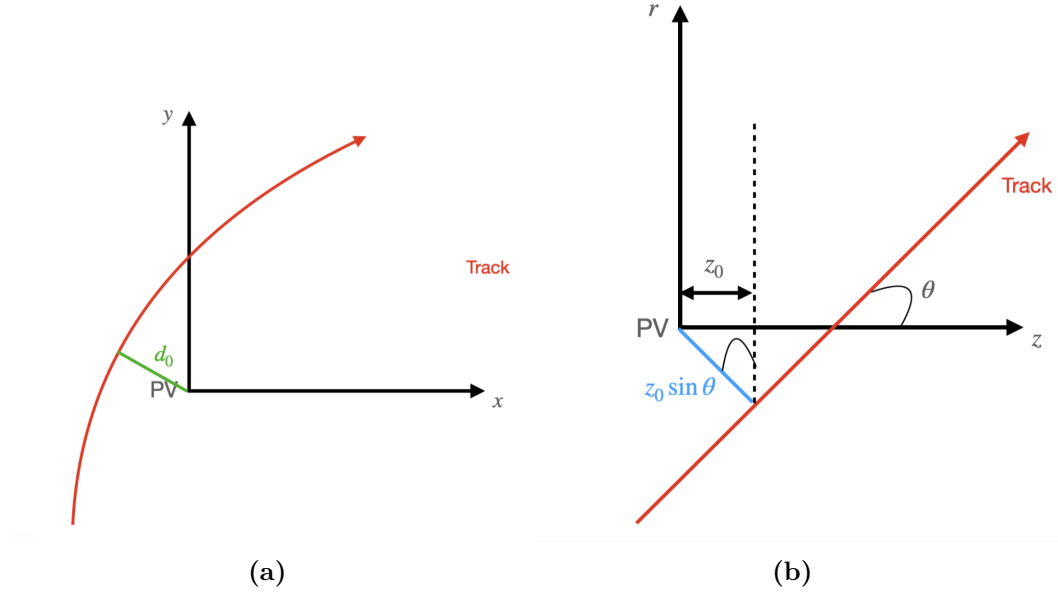


Figure 4.1. (a) d_0 variable in the (x, y) plane; (b) z_0 variable in the (r, z) plane. These impact parameters are evaluated with respect to the nominal IP, here identified with the so-called Primary Vertex (PV). More details about the PV identification can be found in the text.

the (r, z) and the (x, y) planes. A schematic picture of the two impact parameter variables is given in Fig. 4.1. The track reconstruction algorithm can be summarised in the following four consecutive steps:

- *initial clustering*: hits in the PD and in the SCTs are clustered together, forming so-called *space-points*;
- *seeding and track finding*: *track seeds* are built from groups of at least three space-points; through a combinatorial *Kalman Filter (KF)* [121] other compatible hits are added to the track seeds, to form *track candidates*;
- *ambiguity solving*: since different tracks might share the same space-points, an ambiguity-solving algorithm is run, assigning a score to tracks according to the χ^2 of the track fit, its p_T and the number of holes in the track, i.e. the number of hits missing from an ID layer¹. If a PD (two SCTs) cluster(s) is (are) shared by more than two tracks or if two tracks share more than two clusters, the tracks with the lowest ambiguity score are rejected;
- *TRTs extrapolation*: track candidates satisfying in addition either the **Loose** or the **Tight Primary** identification Working Point (WP) (see Tab. 4.1) are then extrapolated to the TRTs and their parameters are updated after performing a high-resolution fit of their trajectory.

¹A hole is defined as an intersection with a detector sensitive element where the expected matching cluster is missing. Inactive regions or sensors are not included in the hole definition.

Loose WP	Tight Primary WP
$p_T > 0.5 \text{ GeV}$	All the Loose requirements
$ \eta < 2.5$	≥ 9 hits in PD/SCTs detectors for $ \eta \leq 1.65$
≥ 7 clusters in PD/SCTs detectors	≥ 11 hits in PD/SCTs detectors for $ \eta > 1.65$
≤ 2 holes in the PD/SCTs detectors	1 hit in the IBL or in the innermost PD layer
≤ 1 hole in the PD	No PD holes
$ d_0 < 2 \text{ mm}$	-
$ z_0 \sin \theta < 3 \text{ mm}$	-

Table 4.1. Summary of Loose (left) and Tight Primary (right) identification WPs requirements for tracks.

In the analysis outlined in Chap. 5, 6 tracks satisfying the Loose WP are exploited, while in the search in Chap. 7 tracks are not required to satisfy any specific requirements since they are not specifically exploited.

Multiple pp interactions occur per bunch-crossing (Sec. 3.1.3), but usually there is only one hard-scatter event per collision, which is associated to a vertex which is referred to as the *Primary Vertex (PV)*. To look for such PV, ID tracks reconstructed as previously outlined are exploited. Each track is extrapolated to the beam line, with the resulting intersection being a vertex seed. Additional tracks are associated to the vertex if compatible with it, taking into account their relative positions and the track parameters. If the track is not compatible with another track vertex, it is extrapolated to the beam line, with the intersection forming a new vertex seed. This procedure is repeated until no track is left un-associated. Being the hard scatter event the one associated to the largest energy transfer, the PV is defined as the vertex with the largest $\sum p_{T^2}$ of its associated tracks. More details about the track reconstruction algorithm, its performance and about the PV reconstruction can be found in Ref. [122, 123].

4.2 Jets

Hadronic jets are the final product of the hadronisation of quarks or gluons and are therefore composed of a multitude of collimated hadrons. In the following, details about jet reconstruction, calibration and identification are given.

4.2.1 Jets reconstruction

Jets reconstruction starts from calorimeter cells with the following steps:

- *proto-clusters formation*: calorimeter cells with $\xi = E_{\text{cell}}^{\text{EM}} / \sigma_{\text{noise,cell}}^{\text{EM}} > 4$ are *topo-clusters seed*, where $E_{\text{cell}}^{\text{EM}}$ and $\sigma_{\text{noise,cell}}^{\text{EM}}$ are respectively the measured energy and the (expected) noise associated to a calorimeter cell. The EM superscript refers to the fact that these energies are at the so-called EM scale, meaning that they correctly reproduce energy deposits for electrons and pho-

tons, while corrections to accurately reproduce hadrons energy releases are applied at a later stage, as described in the following. If cells with $\xi > 2$ are found in the same layer adjacent to a topo-cluster seed or in an adjacent layer but (partially) overlapping in (η, ϕ) , they are added to the topo-cluster seed. Finally, all adjacent cells (in the same layer) with $\xi > 0$ are added to the same topo-cluster seed. The clusters so formed are referred to as *proto-clusters*;

- *proto-clusters splitting and topo-clusters formation*: proto-clusters can be too large to provide a good measurement of the energy flow from the particles generated in the recorded event. Therefore, proto-clusters with two or more local maxima are split into smaller sized clusters: each local maxima with $E_{\text{cell}} > 500 \text{ MeV}$ with at least 4 neighbours with smaller signals is split. If a cell is shared among two different proto-clusters, it is associated to the highest energy one. *Topo-clusters* are then formed, with a correction based on their pseudorapidity and position in the calorimeter, to take into account the position of the PV. Their properties, such as their four-momentum and their position, are evaluated for both the full topo-cluster and the different calorimeter layers. More details about topo-clusters formation can be found in Ref. [124];
- *Jet formation*: topo-clusters are then clustered using a clustering algorithm exploiting the metric

$$d_{i,j} = \min(p_{T,i}^{2p}, p_{T,j}^{2p}) \frac{\Delta^2 R_{i,j}}{R^2} \quad (4.1)$$

with i, j spanning over the topo-clusters, $p_{T,i}$ and $p_{T,j}$ being the p_T of respectively the i -th and the j -th topo-cluster, $\Delta R_{i,j}$ being the solid angle between the two topo-clusters and R the clustering size, that for conventional jets in ATLAS is set to $R = 0.4$. The value of the p parameter defines different kinds of clustering algorithms: $p = 1$ refers to the so-called k_t algorithm [125], $p = 0$ to the Cambridge-Aachen one [126] and $p = -1$ to the anti- k_t algorithm [127], which is the one conventionally used in ATLAS for jet clustering. The metric in Eq. 4.1 (with $R = 0.4$ and $p = -1$) is exploited to assess whether two different topo-clusters should be merged into one: given the highest energy topo-cluster i , $d_{i,j}$ is evaluated for all the other j topo-clusters, ordered in decreasing energy, and if $d_{i,j} < d_{i,B} = 1/p_{T,i}^2$ the two topo-clusters are merged and the j -th topo-cluster is removed from the collection. As soon as $d_{i,j} > d_{i,B} = 1/p_{T,i}^2$, the jet clustering for the jet seeded by the i -th topo-cluster is considered as completed, the first jet is formed and the j -th topo-cluster becomes a new jet-seed. The clustering is completed when all the topo-clusters are part of a jet (or are a jet themselves).

The jets built with this procedure are referred to as *EMTopo jets*. These are the jets exploited in the search outlined in Chap. 7 (while no jets are used in the search outlined in Chap. 5, 6). There exist however other kinds of jets: the *Particle-Flow (PFlow)-jets* [128], the *large- R jets* [129] and the *variable radius track jets* [130].

The *Particle-Flow (PFlow)-jets* are reconstructed by subtracting to topo-clusters the expected energy deposition due to ID tracks (with p_T below 100 GeV) matched

to them, this resulting in a better energy resolution. The physics objects built after these subtractions are referred to as *PFlow objects*, that consists of charged PFlow objects, the ID tracks, and neutral PFlow objects, the energy-modified topo-cluster to which an associated ID track was found and the energy unmodified topo-clusters to which no associated ID track was found.

The *large- R jets* [129], where EMTopo jets are clustered once again, using the anti- k_t algorithm with $R = 1$.

The *variable radius track jets* [130], where the anti- k_t algorithm is run unto both topo-clusters and ID tracks with a variable radius depending on the constituent p_T as well, clustering with a smaller cone more boosted objects.

4.2.2 Jets calibration

The jet energy is obtained from its constituents, whose energies, as mentioned above, are measured at the EM scale and corrected for the position of the PV. A set of additional corrections (calibrations) are applied to take into account the Pile-Up, the jet properties (such as its flavour composition), the Jet Energy Scale (JES) and the (potential) mis-modelling of the MC simulations exploited to implement the other corrections.

The PU calibration is needed since additional collisions beside the hard-scatter one modifies the jets energy: this correction is performed firstly by subtracting from the jet energy the observed energy density due to PU, considering the area of the jet itself, and then by matching the reconstructed jet energy to the truth one, to account for residual discrepancies present after the first step. This matching procedure comes with an uncertainty that is translated onto jets observables.

The JES calibration takes instead into account energy losses due to hadrons interactions with the passive layers of the sampling calorimeters, using as for the PU a matching between the truth and the reconstructed jet energies, this yielding an uncertainty as well. The flavour composition of the jets as well as the nature of the parton initiating the hadronisation are accounted for too, with an improvement of the 30% in the energy resolution.

Finally, the calibration taking into account the mis-modelling of the MC simulations is performed. Such calibration comprises the mis-modelling of the hard-scatter processes, of the underlying event and of the jet formation as well as of the different technologies and granularities of the calorimeter system and the different detector response to various hadrons as a function of their p_T .

An additional source of systematic uncertainty arises from the Jet Energy Resolution (JER), quantifying the width of the Gaussian jet response distribution. The JER uncertainty takes into account many different effects from the stochastic nature of hadronic showers to electronic noise. The breakdown of the JER and JES uncertainties, split for the different outlined contributions and as a function of the jet p_T , are shown in Fig. 4.2.

More details about these calibrations, the measurement of the JES and the JER and of their relative uncertainties can be found in Refs. [132, 131].

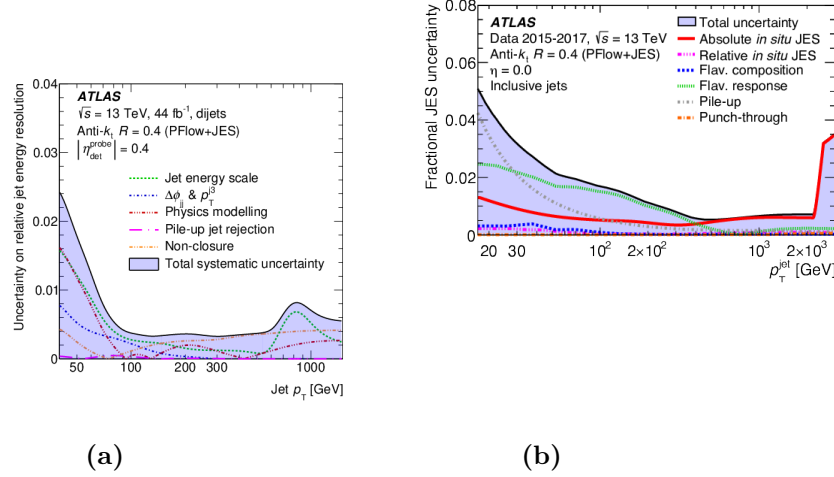


Figure 4.2. Total uncertainty on the JES (a) and JER (b) determination and its sub-components shown as a function of the jet p_T . Plots from Ref. [131].

4.2.3 Jets identification

Jets from pp collisions have to be distinguished from the ones originating from large noise bursts into the calorimeters, from PU or from the Non Collisional Background (NCB), the latter being due to either cosmic-rays crossing the calorimeter or remnants of interactions of protons in the beam with components of the accelerator, such as dipoles and collimators (Beam Induced Background (BIB)). In order to suppress these *fake* jets, identification WPs are exploited and are here introduced. Jets arising from PU are further discriminated using a PU tagger, introduced in the next section.

Selections aimed at distinguishing jets due to noise bursts exploit information from the pulse shape in calorimeter cells, by comparing, per each calorimeter cell, the theoretically expected shape to the measured one. The per-cell variable obtained, $Q^{\text{LAr}_{\text{cell}}}$, is exploited in per-jet variables, namely:

- $\langle Q \rangle$, which is the weighted average of $Q^{\text{LAr}_{\text{cell}}}$, which is normalised in such a way that $\langle Q \rangle \in [0, 1]$;
- $f_Q^{\text{LAr}} (f_Q^{\text{HEC}})$, which is the ratio of the energy released in the LAr calorimeter (HEC, see Sec. 3.2.4) cells with a bad pulse shape, over the total energy released in all the calorimeter cells with a bad pulse shape.

The variable $|E_{\text{neg}}|$, which is the absolute sum of the energies of all the cells where a negative energy has been measured, is used to suppress jets due to large noise bursts.

Jets due to noise or NCB are more likely to be localised longitudinally. Such jets are identified using the fraction of the total energy of the jets over the one left in the ECAL (f_{EM}), in the HEC (f_{HEC}), and in one layer of the calorimeter (f_{max}).

The jet charged energy fraction (f_{ch}), evaluated as the sum of the p_{T} of the tracks associated to the PV and to the jet over the p_{T} of the jet itself, is divided for f_{max} and is used to select *real* jets, since they are expected to contain a large number of charged hadrons.

Two identification WPs exploiting the listed variables are used to suppress *fake* jets: the **LooseBad** WP and the **TightBad** WP. The former exploits a combination of requirements onto the mentioned variables beside $f_{\text{ch}}/f_{\text{max}}$, the most discriminating one. The **TightBad** WP includes all the selections of the **LooseBad** WP and adds a requirement on $f_{\text{ch}}/f_{\text{max}}$ too. Jets failing the **LooseBad** (**TightBad**) WP are considered as **Loose** (**Tight**).

The **Loose** WP provides an efficiency of selecting jets from pp collisions above 99.5% (99.5%) for $p_{\text{T}} > 20(100)$ GeV, while the **Tight** WP, to be used by searches heavily affected by NCB, selects jets with an efficiency of 95% (99.5%) for $p_{\text{T}} > 20(100)$ GeV.

The jets in the search in Chaps. 5, Chap. 6 must satisfy the **Loose** WP, as the search is not significantly affected by the NCB and jets are only exploited to reduce the $t\bar{t}$ background. The search in Chap. 5, on the other hand, is fully based on jets and might be more affected by the NCB. For this reason, in each event while sub-leading jets must satisfy the **Loose** WP, the leading one must satisfy the **Tight** WP.

Pile-Up jets rejection

The PU calibration corrects the jet energy by removing energy contributions due to PU. However, jets purely due to PU can be reconstructed as well. In order to suppress PU jets, the so called Jet Vertex Tagger (JVT) variable [133], a likelihood discriminator, is used. Such variable is based on:

- the corrected Jet Vertex Fraction (corrJVF):

$$\text{corrJVF} = \frac{\sum_k |p_{\text{T},k}^{\text{trk-jet}}(\text{PV})|}{\sum_k |p_{\text{T},k}^{\text{trk-jet}}(\text{PV})| + \frac{\sum_n \sum_k |p_{\text{T},k}^{\text{trk-jet}}(V_n)|}{f(n^{\text{pu-trk}})}}$$

where $\sum_k |p_{\text{T},k}^{\text{trk-jet}}(\text{PV})|$ is the scalar sum of the p_{T} of all the tracks associated to a jet and coming from the PV, $\sum_n \sum_k |p_{\text{T},k}^{\text{trk-jet}}(V_n)|$ is the scalar sum of the p_{T} of all the tracks associated to a jet and coming from all the V_n vertices beside the PV and $f(n^{\text{pu-trk}})$ is a linear function of the number of all PU tracks in the event². This variable represents thus the fractional p_{T} of the jet due to tracks coming from the PV compared to the one due to tracks coming from PU vertices, the latter term being penalized if many PU tracks are found in the event by the term $f(n^{\text{pu-trk}})$. Smaller values of CorrJVF are therefore hint of PU jets;

²The number PU tracks in the event is determined as the number of tracks not associated to the PV. $f(n^{\text{pu-trk}})$ is $k \cdot n^{\text{pu-trk}}$, with $k = 0.01$ being the slope of $\langle p_{\text{T}}^{\text{pu}} \rangle$ as a function of $n^{\text{pu-trk}}$. The discrimination power of corrJVF is however stable against different choices of k .

- $R_{p_T} = \frac{\sum_k |p_{T,k}^{trk-jet}(PV)|}{|p_T^{jet}|}$, with $\sum_k |p_{T,k}^{trk-jet}(PV)|$ being the scalar sum of the p_T of all the tracks associated to a jet and coming from the PV, while $|p_T^{jet}|$ is the p_T of the jet itself. R_{p_T} is expected to be smaller for PU jets than for genuine ones, as PU jets are expected to have a small p_T coming from the tracks associated to the PV.

The JVT variable is exploited in both the search outlined in Chap. 5 and Chap. 6 and the one in Chap. 7 to remove PU jets.

Jets flavour tagging

Since jets can be originated from different particles, they are distinguished in different categories: b -jets and c -jets are originating respectively from b and c quarks, τ -jets from hadronically decaying τ and *light*-jets from the lightest quarks (u, d, s)³. A tagging technique, referred to as b -tagging, is aimed at distinguishing b -jets from the other ones, relying on the specific characteristics of such jets: being the b -hadrons long-lived (with a lifetime of the order of picoseconds), they produce secondary vertices with multiple tracks. Different b -tagging techniques are used, relying on 4 different low-level taggers:

- *IP2D and IP3D* [134]: likelihood ratio discriminants which are based respectively on the transverse ($\frac{d_0}{\sigma_{d_0}}$) and on the longitudinal ($\frac{z_0}{\sigma_{z_0}}$) impact parameters significance;
- *SV1* [135]: reconstructing secondary vertices in the jets, it outputs eight variables, such as the mass of the vertices or the significance of the decay length;
- *JetFitter* [136]: reconstructing the full b and c -hadrons decay chains, it outputs eight discriminating variables as well, mainly related to the track multiplicity associated to each vertex;
- *RNNIP* [137]: Recursive Neural Network (RNN) taking as input different variables, such as the impact parameters significance, it outputs 4 scores related to the probability of being a certain type of jet (b -jet, c -jet, τ -jet or *light*-jet).

These different low-level taggers are combined to create 3 different high-level taggers [134, 138]:

- *MV2c10*: a Boosted Decision Tree (BDT) using as inputs the outputs of all the previous low-level taggers beside the RNNIP one. It is used in the search in Chap. 7 for the definition of the CR enriched in $t\bar{t}$ and single- t events, where jets are produced from the hadronisation of b -quarks originating from the t quark decay;

³the top-quark does not hadronise since it is too heavy and it instead decays weakly primarily into a W boson and a b -quark.

- DL1: a Deep Neural Network (DNN) using the same inputs as MV2c10, with additional information about the production of tertiary vertices extracted from JetFitter;
- DL1r: an extension of DL1, exploits its same inputs with the addition of the outputs of RNNIP.

4.3 Missing Energy Transverse

The Missing Energy Transverse (MET) \vec{E}_T^{miss} is a 2D vector defined in the transverse plane of the collisions and it is a proxy of the production of non-interacting particles. It is therefore a key discriminant variable for all WIMP searches, and it is exploited in the search in Chap. 7, where it is looked for LLPs escaping ATLAS undetected. It is defined as:

$$\vec{E}_T^{\text{miss}} = - \sum_{k=\text{hard objects}} \vec{p}_{T,k} - \sum_{j=\text{soft objects}} \vec{p}_{T,j},$$

that is the negative vector sum of the p_T of all the so-called *hard objects*, i.e. the reconstructed objects (such as muon, electrons etc.), and of all the so-called *soft objects*, which are instead referring to contributions not associated to fully-reconstructed objects. The objects entering the definition of the E_T^{miss} are independent from each other and therefore an ambiguity solving procedure is exploited to avoid the double-counting of detector signals.

The so-called *soft term*, which is associated to the E_T^{miss} term arising from the soft objects, can include either ID tracks coming from the PV, as in the search in Chap. 7, and in this case is referred to as the *Track Soft Term (TST)*, or calorimeter deposits, and in this case is referred to as the *Calorimeter Soft Term (CST)*. The TST is PU insensitive and has a better resolution with respect to the CST, as the ID has a better p_T resolution than the energy resolution of the calorimeter system. The CST has instead a larger-scale response of the MET, since it takes instead into account contributions from neutral particles too, differently from the TST, and can exploit the coverage of the calorimeter system up to $|\eta| < 4.5$, while the TST is bounded to $|\eta| < 2.5$ by the ID acceptance.

A detailed description of the E_T^{miss} definition and performance can be found in Ref. [139].

4.4 Electrons and Photons

Electromagnetic showers developed by electrons⁴ and photons in the LAr calorimeter have a similar signature and so their reconstruction proceeds simultaneously. In the following, the reconstruction procedure as well the identification and the isolation requirements of electrons and photons is outlined. More details can be found in Ref. [140].

⁴where not stated otherwise, the term electron refers to both electrons and positrons

4.4.1 Reconstruction

Photons undergoing pair production before reaching the calorimeters are called *converted photons*, while photons reaching the calorimeter are called *unconverted photons*. Different particle hypotheses are made according to the signature observed in the detectors. A cluster matched to a track is identified as an electron, a cluster matched to a conversion vertex is identified as a converted photon and a cluster matched nor to a track nor to a conversion vertex is identified as an unconverted photon. Electrons and photons reconstruction is performed in five consecutive steps, here listed:

- *topo-clusters building*: topo-clusters are built as explained in Sec. 4.2.1. The topo-clusters considered for electrons and photons building are only the ones where the energy at the EM scale reconstructed in the ECAL is larger than 400 MeV;
- *tracks reconstruction*: tracks are built as explained in Sec. 4.1, where, however, instead of using the KF a non linear generalisation of it, called *Gaussian Sum Filter (GSF)* [141], is exploited. The latter, differently from the KF, takes into account the potentially large energy losses of electrons when travelling in the ID (while hadrons are expected to have minimal interactions when traversing the ID and therefore the KF can be exploited in the reconstruction of hadrons-associated tracks);
- *track to topo-cluster matching*: GSF tracks are extrapolated to the second layer of the ECAL and are attempted to be matched to topo-clusters. Tracks are matched to topo-clusters if $\eta_{clus} - \eta_{trk} < 0.05$ and $-0.1 < q(\phi_{trk} - \phi_{clus}) < 0.05^5$, either with the measured p_T of the track or with a corrected p_T , taking into account the measured calorimeter energy. If more than one track is associated to the same topo-cluster, tracks are ranked according to their characteristics. Tracks with hits in the PD are preferred with respect to tracks having hits in the SCT only. Among these categories, tracks with the best ΔR match with the topo-clusters are preferred. If the differences in the matching, both with the measured or rescaled track p_T , are small (< 0.01), the track with the larger number of hits is preferred. In the building of electrons, the best-matched track is the one giving properties to the electron itself. Such loosely matched tracks are used as well to build conversion vertices, that can be reconstructed with either one or two tracks and with tracks with hits in the Silicon detectors (the PD and the SCT), denoted as *Si tracks*, or in the TRT only, denoted as *TRT tracks*. Double-track conversion vertices are reconstructed from a pair of oppositely charged tracks with an invariant mass compatible with 0, since they arise from photons which are massless. Single-track conversion vertices are instead usually reconstructed from tracks without hits in the innermost layers of the ID, since these are usually due to late conversions. The requirements to build conversion vertices are looser for

⁵the asymmetric requirement is due to the fact that tracks could lose some energy from radiated photons that instead clusters will measure

Si tracks than for *TRT* ones and are tighter for single-track conversion vertices than for double-tracks ones;

- *super-clusters building*: *super-clusters* are built from so-called *seed clusters* and *satellite clusters*. Topo-clusters along with their matched tracks are ordered in decreasing E_T . Topo-clusters are tested as seed for *electron super-clusters* if they have $E_T > 1$ GeV and if they have an associated track with at least 4 hits in the Silicon detectors, while they are tested as seed for *photon super-clusters* if they have $E_T > 1.5$ GeV, with no requirements on the associated tracks and vertices. For both electrons and photons, satellite clusters are added if they lie within $\delta\eta \times \delta\phi = 0.075 \times 0.125$. For *electron super-clusters*, the matching requirement is loosened to $\delta\eta \times \delta\phi = 0.125 \times 0.3$ if the satellite cluster has the same best-matched track of the seed cluster. For *photon super-clusters*, satellite clusters are added, regardless of the (η, ϕ) matching, if their associated conversion vertices are made only of *Si tracks* and their best matched track belongs to the conversion vertex of the seed cluster;
- *electron and photon objects building*: an energy and position calibration is applied to the super-clusters, tracks are matched to electron super-clusters and conversion vertices to photon ones, with the same matching procedure used for the matching of topo-clusters to tracks and conversion vertices. Since an electron super-cluster can be a photon super-cluster as well, the procedure outlined in Fig. 4.3 to finally identify electrons and photons is carried out. In this way, if a super-cluster with no conversion vertex but associated tracks is found, an electron is built, while if a super-cluster with no track but a conversion vertex is found, a photon is built. In the other scenarios, the super-cluster is reconstructed both as an electron and as a photon, that are therefore marked as ambiguous. An additional calibration, object specific, is performed after this matching. Finally, shower shapes and other discriminating variables are evaluated for further electron and photon identification, as explained in the following.

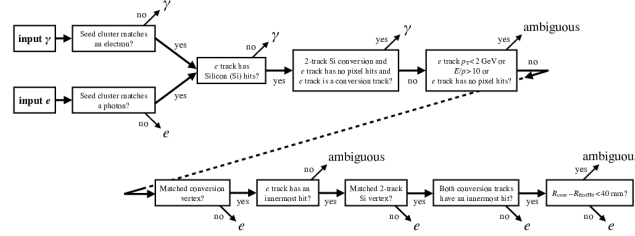


Figure 4.3. Flowchart showing the logic of the ambiguity resolution for particles initially reconstructed both as electrons and photons. Plot from Ref. [140].

4.4.2 Identification and isolation

Electrons

A likelihood discriminant, taking as input the aforementioned distributions of the electron candidates, is adopted to define three mutually inclusive *identification Working Points* (**Loose**, **Medium**, **Tight**), helping in discriminating prompt electrons from ones produced in photon conversion or from the decay of heavy flavour hadrons. All these WPs require at least seven hits in the Silicon detectors, of which two should be in the PD, to discriminate against photon conversions. The search outlined in Chap. 5, 6 exploits the **Medium** WP. The search in Chap. 7 exploits for the electron veto the **Loose&Blayer** one, defined requiring an hit in the IBL (defined in Sec. 3.2.3), and the **Tight** WP for electrons reconstructed in the $1e$ CR.

Electrons arising from prompt decays of the W , the Z and the H bosons are characterized by an activity around them which is smaller than the one associated to electrons produced from semi-leptonic decays of heavy-flavoured hadrons. An observable quantifying such activity and aimed at identifying prompt electrons is referred to as *isolation*. This isolation can be either track-based or calorimeter based, being evaluated as the amount of activity surrounding the candidate, respectively in the ID and in the calorimeter system. The track-based isolation is PU independent and provides a better p_T scale and resolution for individual soft hadrons. The calorimeter-based isolation provides information about neutral particles, which are ignored by track-based isolation, as well as information about objects whose associated tracks are either below the ID p_T threshold or outside the ID η coverage. For this reason, calorimeter-based and track-based isolation are combined to define the two *isolation Working Points* listed in Tab. 4.2. $E_T^{\text{topoetcone20}}$, a calorimeter-based isolation, is the sum of the transverse energy E_T of the topological cell clusters in a cone of size $\Delta R = 0.2$ around the electron, subtracting the energy deposits associated both to the electron itself and to the PU. $p_T^{\text{varcone30}}$, a track-based isolation,

Isolation WP	$E_T^{\text{topoetcone20}}$	$p_T^{\text{varcone30}}$
Loose_VarRad	$\frac{E_T^{\text{topoetcone20}}}{p_T^e} < 0.2$	$\frac{p_T^{\text{varcone30}}}{p_T} < 0.15$
Tight_VarRad	$\frac{E_T^{\text{topoetcone20}}}{p_T^e} < 0.06$	$\frac{p_T^{\text{varcone30}}}{p_T^e} < 0.06$

Table 4.2. Summary of Loose_VarRad and Tight_VarRad isolation WPs requirements for electrons.

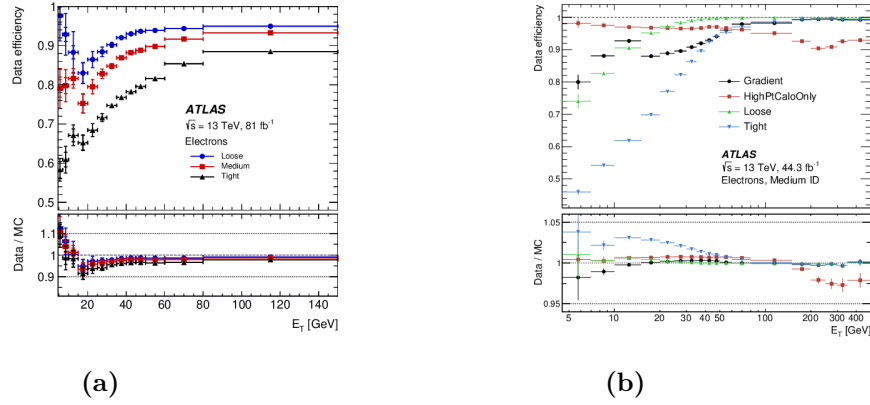


Figure 4.4. Electron identification (a) and isolation (b) efficiency as a function of their transverse energy. In the bottom pad the ratio between the efficiency measured in data and in the MC simulations is reported. Plot from Ref. [140].

is the sum of the p_T of the tracks inside a cone of size $\Delta R = \min(\frac{10 \text{ GeV}}{p_T^e}, 0.3)$ (a variable size, depending on the electron p_T) around the electron track, excluding the electron track itself. Such isolation variables are required to be small compared to the electron p_T itself, as listed in Tab. 4.2. The analysis outlined in Chap. 5, 6 exploits the Loose_VarRad WP, while the search described in Chap. 7 exploits the Medium_VarRad one. The efficiency of the identification and isolation WPs are measured in data and in MC simulations with the tag & probe (T&P) method using $J\Psi \rightarrow e^+e^-$ ($Z \rightarrow e^+e^-$) for electrons with $E_T < 20$ GeV ($E_T > 15$ GeV). Such efficiencies are shown in Fig. 4.4 as a function of the electron E_T . Discrepancies observed are due to a mis-modellings in the MC simulations, and they are corrected with *data to MC SFs*, that will be affected by uncertainties whose impact is discussed on the relevant chapters in this thesis.

Photons

Since converted photons tend to have wider energy deposits than electrons, as the initial opening angle between the produced electron-positron pair is amplified by the presence of the magnetic field, the photon identification criteria are based on

variables related to the shape of their associated EM showers, and they define three *identification WPs* (**Loose**, **Medium**, **Tight**). While the search described in Chap. 5, 6 does not rely on photon reconstruction, the one in Chap. 7 does and exploits the **Tight** identification WP. Similar isolation criteria to the ones introduced for the electrons are defined for photons, but since no isolation requirement is applied to photons in the analysis in Chap. 7, the reader is referred to Ref. [142] for further details. The identification and isolation efficiencies are measured in data and compared to MC simulations in $Z \rightarrow l^+l^-\gamma$ and $Z \rightarrow e^+e^-$ events, with mis-modelling covered by SFs, as for electrons.

4.5 Muons

Muons produced at the IP in pp collisions are usually Minimum Ionizing Particles (MIPs). They therefore traverse the full ATLAS detector losing a small fraction of their energy, reaching finally the MS. They can thus be reconstructed with a standalone measurement in the MS, but the rejection of fake muons can be improved by requiring a matching track in the ID. The calorimeter information can be used for improving the determination of track parameters, to account for larger energy losses and to aid in the muon reconstruction not exploiting the ID. In the following, the algorithms aimed at reconstructing muons are outlined, along with the identification and isolation requirements aimed at rejecting fake muons while retaining a large reconstruction efficiency. Further details can be found in Ref. [143].

4.5.1 Reconstruction

There are different kinds of muon reconstruction algorithms exploiting different sub-detector systems. Such algorithms combine information from the ID, from the calorimeter system and from the MS. Tracks in the ID are reconstructed as outlined in Sec. 4.1, while the tracks reconstruction technique in the MS is described in the following.

MS tracks reconstruction

MS segments are reconstructed as short straight-line local track segments from hits in individual MS stations. MS segments in MDT/CSC stations are combined into track candidates via a parabolic fit (representing a first-order approximation of the particle bending inside a magnetic field) constrained to the IP. The ϕ coordinate recovered through RPC/TGC is used to form 3D track candidates. A fit of the muon trajectory in the magnetic field is then performed, taking into account interaction with MS detector material and misalignments between chambers. Using the fitted trajectory, outlier hits are removed and hits lying in the obtained trajectory that were not previously considered are added. A track fit is then performed again with the hits obtained in the previous step. Among the tracks sharing large fractions of

hits, the ones with a better quality are retained and the others are discarded⁶. The fit is again performed with a loose constraint on the IP and taking into account energy losses in the calorimeter system. The p_T of the MS track so obtained is then expressed at the IP.

Muon types

Six muon types are defined in ATLAS, based on the detectors and on the techniques used to perform their reconstruction:

- *ComBined (CB) muons*: reconstructed using full ID and MS tracks. Starting from MS tracks built as explained previously, it is looked for matching tracks in the ID. Since this muon reconstruction exploits a full track reconstructed in the ID, CB muons are reconstructed up to $|\eta| < 2.5$;
- *Silicon Forward (SiF) muons*: reconstructed, like CB muons, starting from MS tracks and then looking for matches backwards in the ID. However, in order to recover efficiency in the region with $2.5 < |\eta| < 2.7$, MS tracks are matched with ID segments rather than full ID tracks;
- *CaloTagged (CT) muons*: reconstructed using ID tracks that are extrapolated to the calorimeter system looking for energy deposits compatible with the ones left by MIPs;
- *Inside-Out (IO) muons*: reconstructed using ID tracks extrapolated to the MS, looking for at least three loosely aligned hits in the MS;
- *Segmented Tagged (ST) muons*: reconstructed from ID tracks that are extrapolated to the MS, looking for MS segments, rather than three hits as for IO muons, matching the ID tracks;
- *StandAlone (SA)/MS Extrapolated (ME) muons*: reconstructed from MS tracks only, since no ID track is found to be matching the extrapolated MS track.

To correct for energy losses inside the calorimeter system and to correctly correlate the tracks in the MS to the ones in the ID (when available), muons energy losses are estimated by combining an analytical parameterisations of the energy loss with the calorimeter measurement, reaching a precision on the energy loss of 30 MeV for 50 GeV muons.

Both the search in Chap. 5, 6 and the one in Chap. 7 exploits CB muons.

4.5.2 Identification and isolation

Identification

After reconstruction, muon candidates are selected according to a set of requirements on the number of hits in the different sub-detectors, on the track fit prop-

⁶Both tracks are kept if they are identical only in the first two stations but have different hits outward.

erties, and on variables assessing the compatibility of the individual measurements in the ID and in the MS (when both are available). Such variables are the q/p compatibility⁷, whose expression can be found in Eq. 4.2, and ρ' , given in Eq. 4.3:

$$q/p \text{ compatibility} = \frac{|q/p_{\text{ID}} - q/p_{\text{MS}}|}{\sqrt{\sigma^2(q/p_{\text{ID}}) + \sigma^2(q/p_{\text{MS}})}}, \quad (4.2)$$

with q/p being the ratio between the measured charge and momentum of the muon, $\sigma(q/p)$ the uncertainty on the measured q/p and the subscripts MS and ID standing for measurements in the MS or in the ID respectively;

$$\rho' = \frac{p_{\text{T,ID}} - p_{\text{T,MS}}}{p_{\text{T,CB}}} \quad (4.3)$$

with $p_{\text{T,ID}}$, $p_{\text{T,MS}}$ and $p_{\text{T,CB}}$ being the p_{T} measured respectively in the ID, in MS, and in a combined measurement exploiting both sub-detectors.

Three mutually inclusive identification WPs (**Tight**, **Medium** and **Loose**) are based on these and other variables. The **Tight** WP requires muons to be only CB or IO, with additional requirements, optimised for different p_{T} and η bins, on both the q/p compatibility and ρ' . Furthermore, **Tight** muons must have a normalised χ^2 of the combined track fit smaller than 8, rejecting tracks due to hadron decays in flight. Finally, **Tight** muons are required to have at least two *precision stations*, MS stations in which the muon has at least three hits in the CSC or MDT detectors.

The **Medium** WP accepts CB and IO muons with a flat q/p compatibility requirement, that should be smaller than 7. The number of precision stations is reduced to one for muons with $|\eta| < 0.1$ and at most one *precision hole station* has to be reconstructed. The latter is a MS station where the muon has less than three hits and is missing⁸ at least three hits that are expected given its trajectory and the detector layout and operational status. This WP accepts as well SiF and ME muons in the $2.5 < |\eta| < 2.7$ region, to extend the η coverage of the **Tight** identification WP.

The **Loose** WP accepts all the muons passing the **Medium** WP. It includes CT and ST muons in the $|\eta| < 0.1$ region, to recover inefficiencies due to the gap in the MS coverage. If IO muons have $|\eta| < 1.3$ and $p_{\text{T}} < 7 \text{ GeV}$, they are accepted even with one precision station only if they are reconstructed as ST muons as well, to increase the efficiency to low p_{T} muons.

Two additional WPs are optimised for selecting low p_{T} muons, the **Low-pT** WP, or high p_{T} ones, the **High-pT** WP. Muons satisfying the **High-pT** WP are IO and CB **Medium** muons, with however three precision stations (instead of two as for the **Medium** WP) and with some additional requirements mitigating the impact of potential misalignments between the different detector elements.

The **Low-pT** WP is introduced to recover efficiencies for muons with $p_{\text{T}} < 10 \text{ GeV}$. This WP selects CB and IO muons, the latter being reconstructed as ST

⁷The q/p variable is directly proportional to the sagitta s of the track.

⁸a missing hit is counted where the muon trajectory crosses an active sensor that does not register a hit

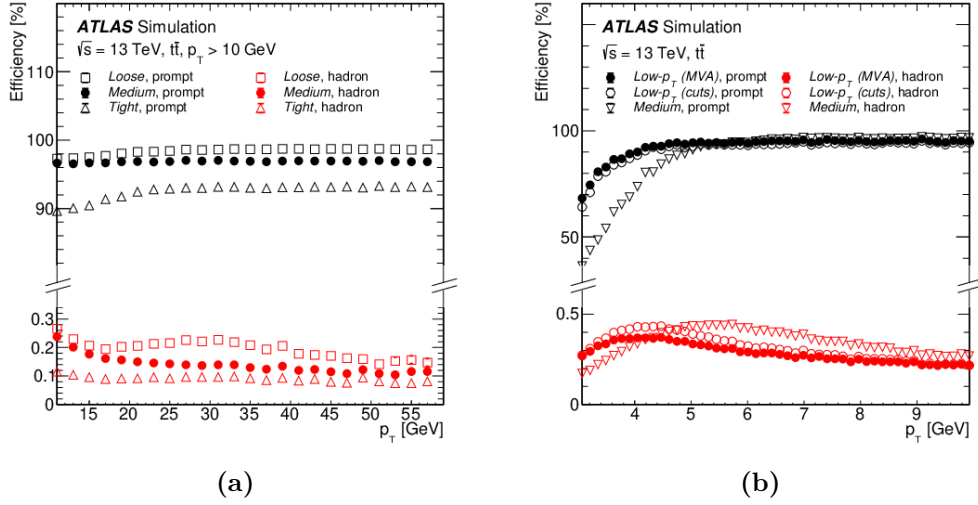


Figure 4.5. Muon identification efficiencies for different WPs, as a function of the muon p_T itself. (a) shows the comparison of the Loose, Medium and Tight WPs while (b) shows a comparison of the Medium and the Low- p_T WPs. Two versions of the Low- p_T WP are shown, a cut based one (white dots) and a Multi-Variate Analysis (MVA) one (black dots). Plot from Ref. [143].

muons with the same requirements as for Loose ST muons, beside the $p_T < 7$ GeV cut. Fake low p_T muons due to the decay of light hadrons are rejected exploiting further requirements. For $p_T > 18$ GeV the Low- p_T WP is defined to be identical to the Medium one.

Identification efficiencies are measured using the same T&P method exploited for electrons and photons, in $Z \rightarrow \mu^+\mu^-$ ($J\Psi \rightarrow \mu^+\mu^-$) events for $p_T > 20$ GeV ($p_T \leq 20$ GeV) and mis-matches between MC simulations and data are accounted for exploiting SFs, affected by uncertainties which are propagated to all muon candidates. Identification efficiencies for the Tight, Medium and Loose WPs are shown as a function of the muon p_T in Fig. 4.5 (a), while Fig. 4.5 (b) compares the efficiency of the Low- p_T WP to the Medium one. Muons reconstructed in the analysis in Chap. 5, 6 are required to satisfy the Loose WP, while the ones exploited in the search outlined in Chap. 7 are required to satisfy the Medium WP.

Isolation

Prompt muons, like prompt electrons, are characterized by an activity around them which is smaller than the one associated to muons produced from semi-leptonic decays of heavy-flavoured hadrons. For this reason, track-based and calorimeter based isolation variables are evaluated for muons as well, and they are combined to create a different set of WPs. The ones of particular interest for this thesis work are summarised in Tab. 4.3.

While the track-based isolation is the same one exploited for the electron isolation WP, the calorimeter-based isolation exploited for muons is different: $E_T^{\text{neflowiso20}}$

Isolation WP	Definition	Track p_T [GeV]
PFlow_Loose	$p_T^{\text{varcone30}} + 0.4E_T^{\text{neflowiso20}} < 0.16p_T^\mu$	> 0.5
PFlow_Tight	$p_T^{\text{varcone30}} + 0.4E_T^{\text{neflowiso20}} < 0.045p_T^\mu$	-

Table 4.3. Summary of PFlow_Loose and PFlow_Tight isolation WPs requirements for muons. While the tracks used for the track-based isolation in the PFlow_Loose WP must have $p_T > 0.5$ GeV, no p_T requirements is asked on the tracks used for the track-based isolation computation in the PFlow_Tight WP.

is the sum of the transverse energy E_T of the topological cell clusters in a cone of size $\Delta R = 0.2$ around the muon, subtracting not only the muon and the PU energy deposits, but all energy deposits matched to tracks in the ID. This isolation variable allows for a less correlated relation between the calorimeter and the track-based isolation, since energy deposits due to charged particles (already accounted for in the ID) are removed. This isolation WP is referred to as PFlow.

The search described in Chap. 5, 6 exploits muons satisfying a modified version of the PFlow_Loose isolation WP (see Sec. 5.3.1), while no isolation requirement is asked for muons in the search outlined in Chap. 7. Isolation efficiencies are evaluated in the same way as identification ones, with mis-modelling that are corrected with data to MC SFs, affected by uncertainties whose impact is discussed on the relevant chapters in this thesis.

4.6 Overlap Removal

In ATLAS, the various physics objects are reconstructed in separate steps, as explained in the previous sections, using the same detector information. Therefore, the same detector signals could be used to reconstruct different objects. As an example, the same energy deposited in a region of the calorimeters could be reconstructed as an electron or photon, a hadronic jet, and a tau lepton⁹ at the same time. Furthermore, an extremely boosted topology could cause some issues in assigning these detector signals to different objects as well. This ambiguity in object reconstruction is problematic for analyses, since it can easily lead to counting the same energy deposits multiple times.

ATLAS analyses use thus a procedure of so-called *Overlap Removal (OR)* to resolve this issue. This procedure compares two types of objects at a time and if there is geometric overlap (defined using for example a ΔR matching or the association to the same ID track), one object or the other is removed, depending on a pre-defined priority. Each object pair is compared sequentially, resulting in a complete set of objects without any ambiguity.

The electron-jet OR removes reconstructed jets that are identical to reconstructed prompt electron candidates, while preserving heavy-flavour jets with semi-

⁹Details about τ leptons reconstruction are not given in this thesis. The reader is referred to Refs. [144, 145].

leptonic decays and light-flavour jets faking a loose electron. Additionally, it removes events (or objects) where a close-by prompt electron and a hadronic jet might bias each other's position or energy reconstruction.

The muon-jet OR is used either to separate prompt muons from muons originating from the decay of hadrons within a jet or to remove jets originating from FSR or Bremsstrahlung photons. Collinear FSR produces indeed a photon which is close-by to the muon ID track that will be combined with calorimeter deposits, so that the combined object will be reconstructed both as an electron and a jet. Very energetic muons loose their energy due to Bremsstrahlung, with this energy loss being larger in high density means. Such muons would loose the majority of this Bremsstrahlung energy in the calorimeter system, thus producing deposits that would be reconstructed as jets.

The electron-muon OR is used to reject electrons reconstructed when a muon radiates a hard photon, as already introduced in the muon-jet OR procedure. In this case, the muon and the electron would either share an ID track or be at $\Delta R < 0.1$.

Usually such OR procedures are performed sequentially, starting from the muon-electron OR, than to the electron-jet one and then finally to the muon-jet one. Additional OR requirements are applied to distinguish among photons and taus and all the other objects. However, since such ORs are not relevant for this work they are not further discussed.

The physics objects retained after the OR are the only ones that are used in physics analyses. Depending on the aim of the physics search, certain OR procedures could be applied or different priorities from the ones here outlined could be exploited. The OR procedures applied for the search of prompt DPs in described in Sec. 5.3.3, while for the ones employed by the search for detector stable LLPs the reader is referred to Ref. [2].

Chapter 5

Prompt Dark Photon signatures at the ATLAS experiment

A search for Dark Photons decaying promptly in the ATLAS innermost detector is presented in this and in the following chapter. This search is for the first time performed using the full Run-2 dataset, and it aims at extending the sensitivity of the prompt DPs search carried out during Run-1 [81]. This chapter illustrates the relevant signatures through which DPs decaying promptly in the ATLAS ID are reconstructed. In Sec. 5.1, the dataset and the MC simulations used for this DPs search are listed. In Sec. 5.2, truth level kinematics of the studied benchmark models (see Sec. 2.4.3) are shown. In Sec. 5.3, how the collimation of the γ_d decay products impact their reconstruction is shown. In Sec. 5.4, the algorithm reconstructing the γ_d decay products into the so-called *prompt Lepton-Jets* (pLJs) is described, and its associated reconstruction efficiencies are shown. Particular focus is given to the reconstruction of the pLJ invariant mass, as the latter is used in the background estimation in two of the three channels of this search (see Sec. 6.2.1). Finally, in Sec. 5.5 the trigger strategy used in this search is introduced.

5.1 Data and simulated event samples

The search here presented is based on the full Run-2 dataset (see Sec. 3). Monte Carlo simulations (Sec. 3.2.7) of the benchmark models investigated (Sec. 2.4.3) are exploited in order to optimize selection criteria to maximize the sensitivity to signal-like events. As will be explained in the following, the signature looked for is quite different from usual SM-like processes. For this reason, SM MC simulations cannot be used to assess background contributions in the region of interest. The background estimation for this search is thus completely data-driven (see Sec. 6.2). Nonetheless, MC simulations of SM processes are used in order to understand features of background processes that might affect, at a larger level with respect to what could be inferred from MC simulations only, this search.

5.1.1 Full Run-2 dataset

Data were collected during 2015-2018 in pp collisions at a center-of-mass energy of $\sqrt{s} = 13$ TeV (see Tab. 3.1), with a total integrated luminosity of $L = 140 \text{ fb}^{-1}$ (see Sec. 3.1.3)

5.1.2 MC samples

Generated events undergo the full simulation chain outlined in Sec. 3.2.7. While signal and background MC simulations all rely on GEANT4 for simulating the full detector geometry and response, they rely on different MC generators for the simulation of the hard scatter event, the parton showering and the hadronisation. All these simulations include as well effects due to the *in time* and the *out of time* Pile-Up (see Sec. 3.1.3), as explained in Sec. 3.2.7. Further details about these MC simulations are given in the following.

Signal samples

The benchmark models exploited in this search are the FRVZ and the HAHM ones, presented in Sec. 2.4.3. These models foresee both the vector and the Higgs portal, where the SM Higgs boson is here assumed to be generated via the ggF production mechanism (see Sec. 1.3). The MG5_aMC@NLO v2.2.3 generator, linked together with the PYTHIA8 generator v8.186, is used for ggF production of the Higgs boson and its subsequent decay to dark-sector particles. More details about these generators can be found in Sec. 3.2.7.

Multiple signal samples are produced, with DP masses ranging between 17 MeV and 40 GeV. The mass range is chosen in accordance with the ATLAS Run-2 search looking for displaced DPs [79] and to extend the boundaries of the previous ATLAS prompt search [81], below the di-muon production threshold and above 2 GeV. Since this search targets a signature arising from prompt DP decays, the DP mean lifetime τ_{γ_d} is set to 0. The masses of the additional particles foreseen in the FRVZ benchmark model, namely f_d and HLSP, are chosen (as for the ATLAS Run-2 displaced search) to be small relative to the Higgs boson one, and far from the kinematic threshold at $m_{\text{HLSP}} + m_{\gamma_d} = m_{f_d}$, so that the two Dark Photons produced are boosted and well separated in the transverse plane, as will be seen in Sec. 5.2. The set of parameters used to generate the signal MC is listed in Tab. 5.1 (a) for the FRVZ process, and in Tab. 5.1 (b) for the HAHM one.

SM background processes

The main source of background in this analysis comes from (virtual) vector bosons decaying into lepton pairs and highly energetic low-mass mesons decaying into lepton pairs. As already said, these backgrounds are not reproduced by MC simulations in the phase space of interest of this search. Other SM processes that could lead to potential sources of background include W +jets, Z +jets, $t\bar{t}$, single-top-quark, WW ,

m_{γ_d} [GeV]	m_{HLSP} [GeV]	m_{f_d} [GeV]	
0.017	2	5	
0.03	2	5	
0.06	2	5	
0.1	2	5	
0.24	2	5	
0.4	2	5	
0.9	2	5	
2	2	10	
6	4	25	
10	6	35	
15	10	45	
25	10	45	
40	7	55	

m_{γ_d} [GeV]
0.017
0.01
0.4
2
10
15
25
40

(a) Parameters used for the MC simulations of the process $H \rightarrow 2\gamma_d + X$, according to the FRVZ model. For the definition of the different particles see Fig. 2.14.

(b) Parameters used for the MC simulations of the process $H \rightarrow 2\gamma_d$, according to the HAHM model.

Table 5.1. Parameters used for the MC simulations of the FRVZ (a) and HAHM processes. Each generated dataset consists of 390000 MC events.

WZ, and ZZ production events. Simulation of the W +jets, Z +jets, WW , WZ , and ZZ events are generated using SHERPA 2.2.1 [117] with the NNPDF 3.0 NNLO [146] Parton Distribution Function (PDF) set. Single top and $t\bar{t}$ MC samples are generated using POWHEG-BOX 1.2856 [116] and PYTHIA 6.428 [115] with the Perugia2012 [147] tune for parton showering and hadronisation, and CT10/CTEQ6L1 [148, 149] PDF sets.

5.2 Signal MC truth-level kinematics

In Fig. 5.1, distributions of the Dark Photon p_T (a), of the ΔR between the γ_d decay products (b) and of the $\Delta\phi$ between the two γ_d produced (c) are shown, for different γ_d mass hypotheses, where γ_d are produced via the FRVZ benchmark model.

While for light γ_d the p_T distribution (Fig. 5.1 (a)) are similar among different mass hypotheses, for heavier Dark Photons their mass starts to be non-negligible compared to the average p_T of the f_d , this impacting the γ_d p_T distributions.

The ΔR distributions show how, for $m_{\gamma_d} < 2\text{ GeV}$, the γ_d decay products lie inside a cone of radius $\Delta R = 0.4$. For this reason, as will be explained in Sec. 5.4, γ_d decay products are collectively reconstructed as a single object referred to as *prompt Lepton-Jet*, that is a collimated bundle of leptons reconstructed within a $\Delta R = 0.4$ cone. For heavier γ_d , the sensitivity of the search is then expected to drop, as γ_d decay products are less collimated. Similar plots are shown for the

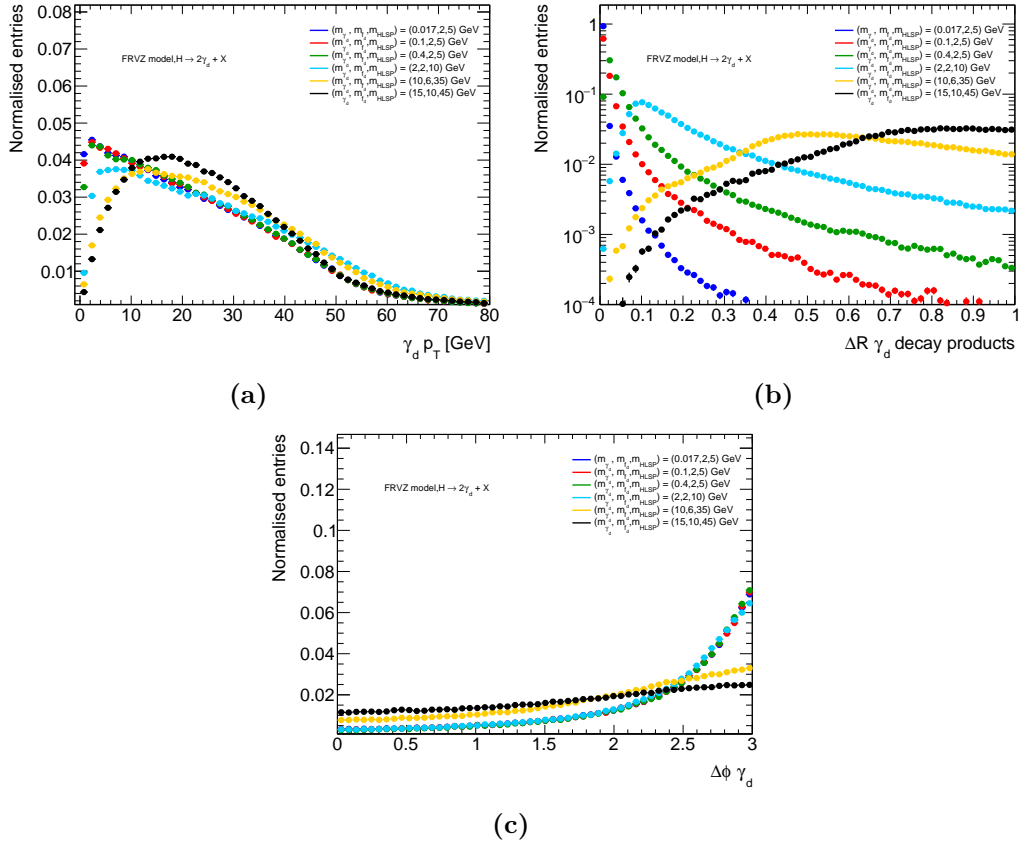


Figure 5.1. Transverse momentum (a), ΔR opening of the two decay products (b) and azimuthal separation (c) for different DP masses generated according to the FRVZ model. The full set of MC parameters for the FRVZ model is defined in Tab. 5.1 (a).

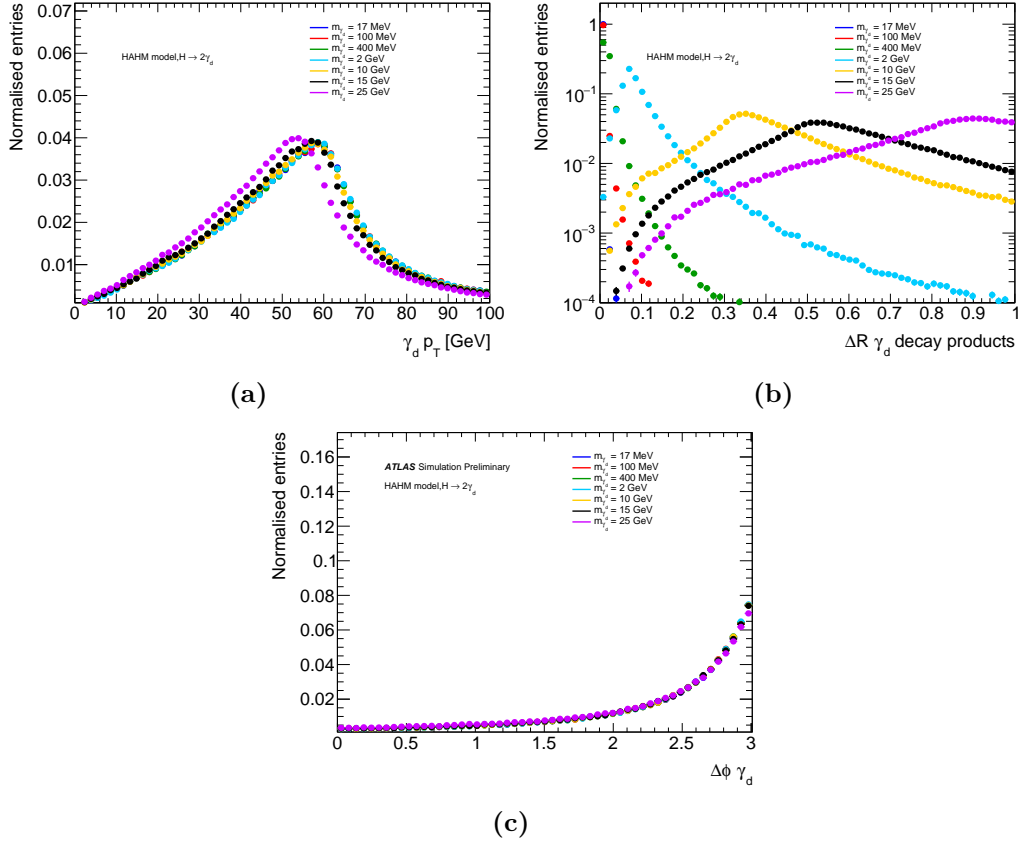


Figure 5.2. Transverse momentum (a), ΔR opening of the two decay products (b) and azimuthal separation (c) for different DP masses generated according to the HAHM model. The full set of MC parameters for the HAHM is defined in Tab. 5.1 (b).

HAHM model in Fig. 5.2. In this case, the p_T distribution is almost identical between the various mass points, due to the reduced complexity of the model. The differences between these truth-level distributions in the FRVZ and HAHM models are highlighted in Fig. 5.3. The $\gamma_d p_T$ distributions and the ΔR distributions between γ_d decay products are compared for a γ_d with a $m_{\gamma_d} = 0.4$ GeV, respectively in Fig. 5.3 (a) and Fig. 5.3 (b). The absence of intermediate hidden fermions in the HAHM model results clearly into a larger average p_T of the γ_d and, consequently, to more collimated decay products. For these reasons, this search is more sensitive to the HAHM model rather than to the FRVZ one.

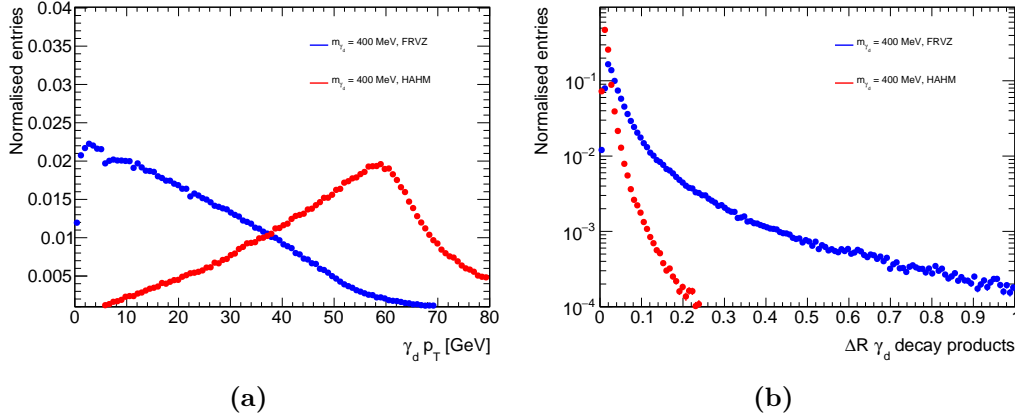


Figure 5.3. Comparison between the $\gamma_d p_T$ distributions (a) and the γ_d decay products opening angle ΔR (b) in the FRVZ (blue) and HAHM (red) models, for a γ_d with mass $m_{\gamma_d} = 0.4$ GeV. The full set of MC parameters for both models is defined in Tab. 5.1.

5.3 Muons and electron reconstruction

Dark Photons can decay into different SM particles, as shown in Fig. 2.10 in Sec. 2.4.1. This notwithstanding, only γ_d decays into muons and electrons are considered in this search, as the products of other decay modes would be completely indistinguishable from the overwhelming QCD background. Electrons and muons are reconstructed using the standard reconstruction algorithms introduced respectively in Sec. 4.4 and Sec. 4.5. Requirements on the reconstruction of such objects are summarised in Tab. 5.2.

Object	p_T [GeV]	$ \eta $	Identification	Isolation
Electron	> 4.5	$< 2.5^*$	Medium	Loose_VarRad
Muon	> 3	< 2.5	CB Loose	PFlowLoose_VarRad**

Table 5.2. Summary of requirements for muon and electron reconstructed objects. Details about these requirements can be found in Sec. 4.4 for electrons and Sec. 4.5 for muons.

* The so-called *crack-region* ($1.37 < |\eta| < 1.52$), the non-instrumented region between the barrel and the endcap of the calorimeter system, is excluded.

** The nominal PFlowLoose_VarRad isolation WP is modified, as explained in Sec. 5.3.1.

The η requirement is due to the ID coverage, while the p_T one is the minimal p_T to allow for the reconstruction of these objects to be reliable (see Chap. 4). The identification WPs are instead chosen in order to maximize the sensitivity. As will be explained in Sec. 6.1, signal-like events involving electrons have a less clean signature with respect to the ones involving muons, and therefore a tighter identification WP is chosen for the electron reconstruction. Leptons arising from hadron decays (also denoted as non-prompt leptons) constitute a background for this search. To further reduce the contribution of such non-prompt leptons, the isolation requirements specified Tab. 5.2 are applied on each lepton candidate, since they are expected to be surrounded by additional particles. Details about these

standard requirements can be found in Chap. 4.

As a consequence of the muons collimation (see Sec. 5.2), however, a modified version of the standard muon isolation WP is used, as explained in Sec. 5.3.1. Differently from muons, standard requirements on isolation can be instead applied for electrons without a significant impact on the signal acceptance, as explained in Sec. 5.3.2. Electrons and muons are in addition required to have a valid track which has to be reconstructed in the ID. This requirement, along with the fact that muons should be of the ComBined type, efficiently selects leptons produced from promptly decaying DPs. Requirements on these associated tracks are summarised in Tab. 5.3.

Associated Track	p_T [GeV]	$ \eta $	Quality	d_0/σ_{d_0}	$z_0 \sin \theta$ [mm]
Electron-track	> 0.5	< 2.5	Loose	5	0.5
Muon-track	> 0.5	< 2.5	Loose	3	0.5

Table 5.3. Summary of requirements for muon/electron-associated tracks. Further details about those can be found in Sec. 4.1.

The η requirement is due to the ID coverage while the p_T one is the minimal p_T to allow for the reconstruction of the tracks to be reliable. The track-quality requirement allows for a second fitting step in the track reconstruction, ensuring a better-quality ID track, as explained in Sec. 4.1. The d_0 and z_0 variables are computed with respect to the PV, that is identified as the vertex with the largest associated $\sum p_T^2$. The tight requirements on such variables, collectively referred to as *Track-To-Vertex Association* (TTVA), further suppress backgrounds due to non-prompt leptons. Details about all these standard requirements can be found in Sec. 4.1.

5.3.1 Isolation for collimated muons

As previously said, the muon isolation (introduced in Sec. 4.5) quantifies the activity surrounding a muon candidate. A high isolation variable's value is usually associated to non-prompt muons arising from hadron decays. Therefore, isolation WPs aim at rejecting muon candidates arising from hadron decays by requiring a small isolation (compared to the p_T of the muon itself). However, in boosted topologies, where prompt muons are found close to each other, a high isolation can be recovered even for prompt muons. This high isolation is however not due to any hadronic activity, but is instead due to the additional muons found within the isolation cone.

In this search, muons produced by the γ_d decay in both the FRVZ and HAHM model are usually very collimated, as can be seen by Fig. 5.1 (b) and Fig. 5.2 (b), and therefore their associated isolation is often rather high. The (charged) track-based isolation $p_T^{\text{varcone30}}$, in the following referred to as **ptvarcone30**, is employed in the **PFlowLoose_VarRad** WP (see Sec. 4.5). The distributions of this variable for the leading and the sub-leading muons found in a $\Delta R = 0.4$ cone are shown in Fig. 5.4 for muons produced by a $m_{\gamma_d} = 2 \text{ GeV}$ γ_d decay in the FRVZ model.

This track-based isolation is much larger (of the order of several tens of GeV) than the typical one for prompt muons (few MeV), and essentially corresponds to

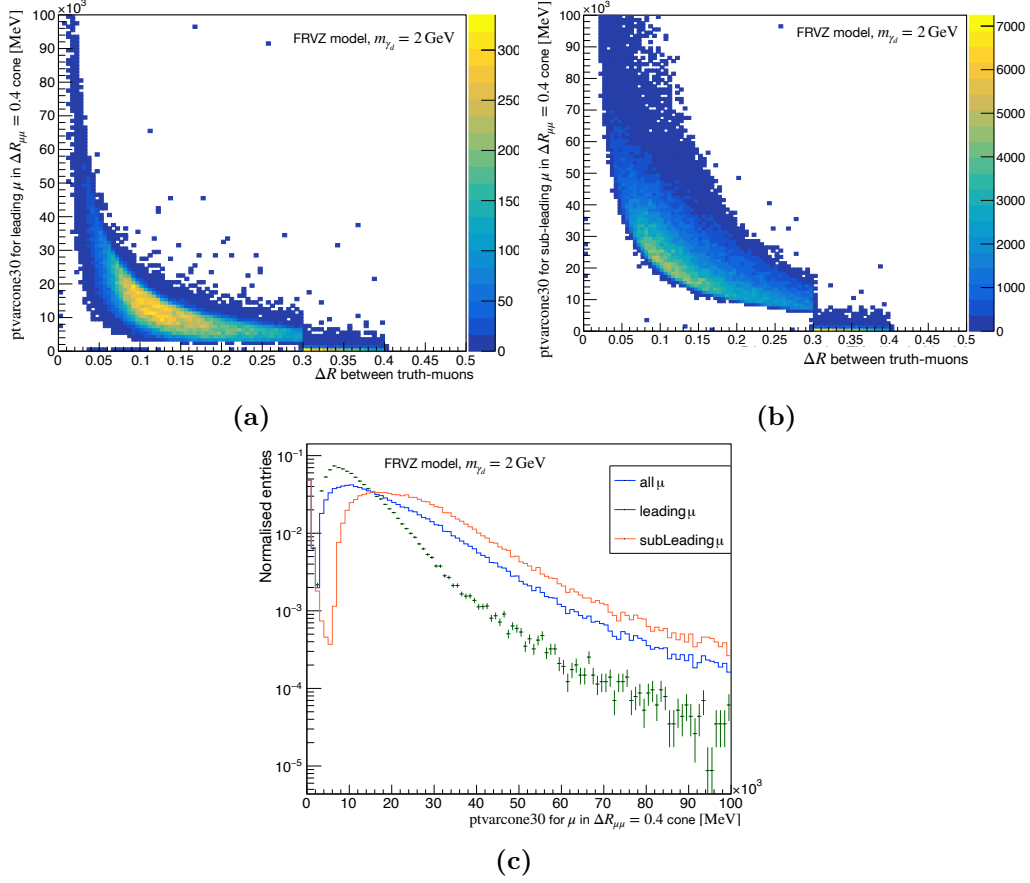


Figure 5.4. ptvarcone30 distribution for the leading muon (a) and the sub-leading muon (b) in a muon pair with $\Delta R_{\mu\mu} = 0.4$, as a function of the truth $\Delta R_{\mu\mu}$ itself. (c) shows instead the normalised ptvarcone30 distribution for both the muons found in the cone (green), for the leading one (blue) and for the sub-leading one (red). Muons are produced in γ_d decays, where the γ_d is produced via the FRVZ benchmark model and has a mass of $m_{\gamma_d} = 2 \text{ GeV}$.

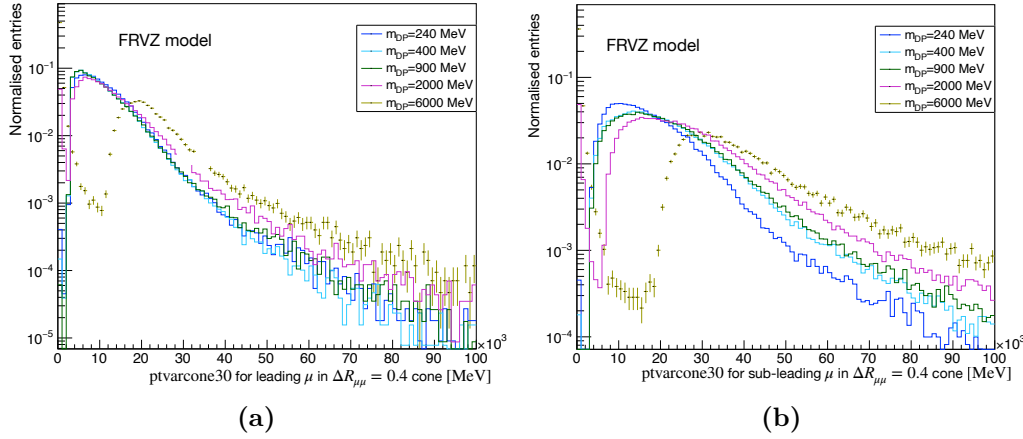


Figure 5.5. Normalised `ptvarcone30` distribution for the leading muon (a) and for the sub-leading muon (b) in a muon pair with $\Delta R_{\mu\mu} = 0.4$, as a function of the truth $\Delta R_{\mu\mu}$ itself. Muons are produced in γ_d decays, where the γ_d is produced via the FRVZ benchmark model and different m_{γ_d} are hypothesised.

the transverse momentum of the nearby muon, since the standard computation of the track isolation energy includes any track that is found within the isolation cone. Comparing the `ptvarcone30` distribution for the leading muons to the one of sub-leading muons, it's clear how indeed the `ptvarcone30` of the sub-leading muon is the p_T of the leading one, and vice-versa. When the γ_d is sufficiently massive, the two muons sometimes fall outside outside the isolation cone of the other. In this case, the `ptvarcone30` is negligible (as it's clear by looking at the `ptvarcone30` distribution for Fig. 5.4 (a) and (b) for $\Delta R_{\mu\mu} \geq 0.3$).

When the DP is heavier, it has to be more boosted for the produced muons to be reconstructed within the same cone. Therefore, the average p_T of the muons is larger, this resulting in larger isolation energies. This can be seen in Fig. 5.5, where the `ptvarcone30` distribution for the leading and for the sub-leading muon found inside a $\Delta R = 0.4$ cone are shown for muons produced by γ_d decays, for different m_{γ_d} hypotheses, in the FRVZ benchmark model.

The (neutral) calorimeter-based isolation $E_T^{\text{neflowiso20}}$, in the following referred to as `neflowiso120`, is employed as well in the `PFlowLoose_VarRad` WP. The distributions of this variable for the leading and the sub-leading muons found in a $\Delta R = 0.4$ cone are shown in Fig. 5.6 for muons produced by a $m_{\gamma_d} = 2 \text{ GeV}$ γ_d decay in the FRVZ model. The shape observed here, differently from the charged component of the isolation, is the typical one for prompt muons. This is due to the fact that the energy deposit in the calorimeter is small for low-energy muons (a couple of GeV) and to the fact that topo-clusters (see Sec. 4.2.1) associated to muon tracks are not considered as neutral and therefore are not accounted for in the `neflowiso20` computation.

For these reasons, both charged and neutral isolation variables are corrected by subtracting the `PFlow` objects (see Sec. 4.2.1) found around a muon candidate, if they are associated to another muon. Such muons are required to pass the same requirements as the one explained in Sec. 5.2. Fig. 5.7 (a) shows the track isolation

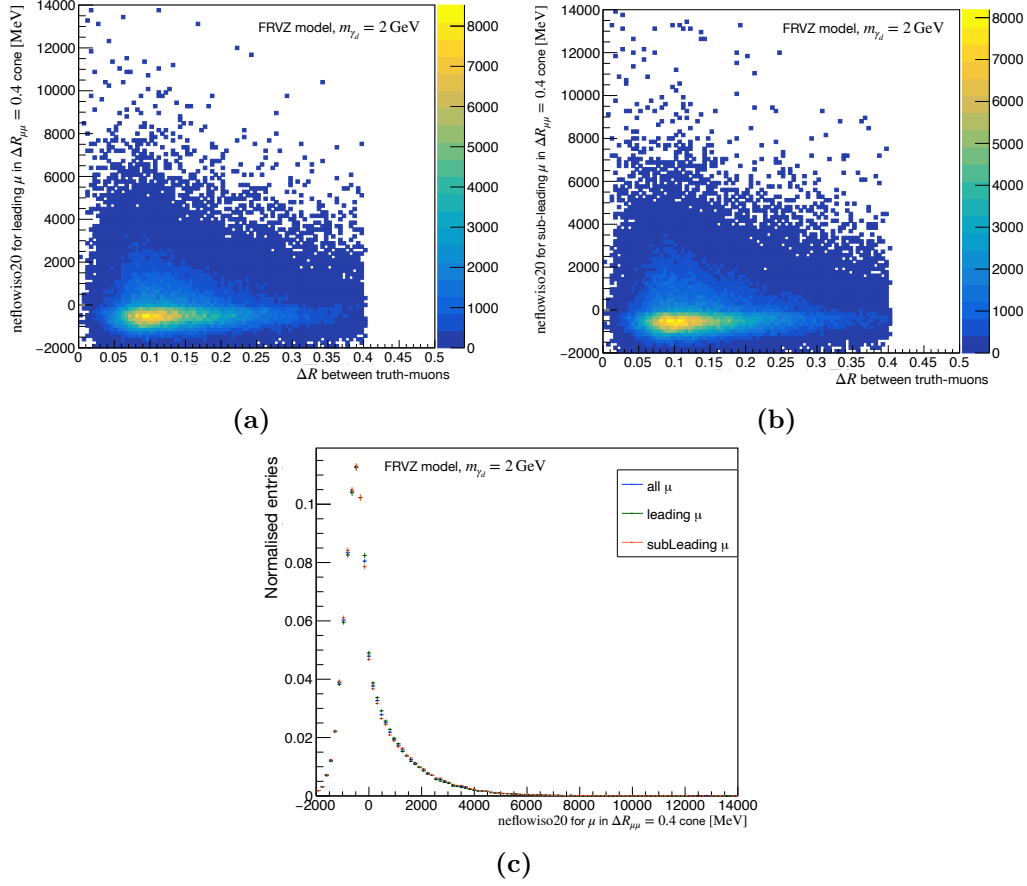


Figure 5.6. neflowiso120 distribution for the leading muon (a) and for the sub-leading muon (b) in a muon pair with $\Delta R_{\mu\mu} = 0.4$, as a function of the truth $\Delta R_{\mu\mu}$ itself. (c) shows instead the normalised neflowiso120 distribution for both the muons found in the cone (green), for the leading one (blue) and for the sub-leading one (red). Muons are produced in γ_d decays, where the γ_d is produced via the FRVZ benchmark model and has a mass of $m_{\gamma_d} = 2 \text{ GeV}$.

distribution before and after such correction, recovering the expected behaviour for prompt muons, where thus the majority of the muon candidates have a null isolation energy.

The per-muon candidate efficiency of the `PFlowLoose_VarRad` WP for the standard and the corrected isolation is shown in Fig. 5.7 (b). While for the nominal isolation WP the vast majority of the muon candidates are rejected for the different m_{γ_d} hypotheses, the per-candidate corrected isolation WP efficiency is larger than the 90% for all the investigated scenarios.

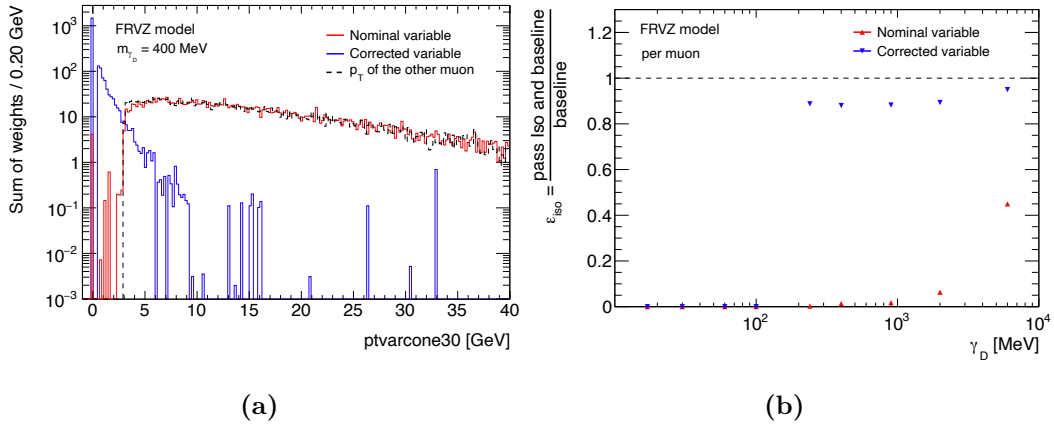


Figure 5.7. (a) Track isolation distribution `ptvarcone30` before (in red) and after (in blue) the isolation correction, for muon candidates arising from the decay of a Dark Photon with mass $m_{\gamma_d} = 400$ MeV and produced via the FRVZ benchmark model. The transverse momentum of the nearby muon is shown in dashed black. (b) Per-muon efficiency as a function of the γ_d mass for the isolation variables before (red) and after (blue) the isolation correction. Also in this case the γ_d is produced via the FRVZ benchmark model.

Given the large improvements due to this modification, further studies, illustrated in Sec. 6.3 are performed.

5.3.2 Collimated electrons

Electrons are reconstructed when at least one GSF track is matched to a topo-cluster, as described in detail in Sec. 4.4. Such matching is also known as *association* between tracks and electrons. In the topology investigated, electrons arising from γ_d decays are usually so close-by that their EM showers are overlapped and therefore they are reconstructed as a single topo-cluster with two associated tracks. This overlap happens in 90–95% of $\gamma_d \rightarrow ee$ decays when $m_{\gamma_d} < 2$ GeV for both the FRVZ and the HAHM model. This percentage decreases for increasing DP masses. In Fig. 5.8, the number of reconstructed topo-clusters (a) and their associated tracks (b) is shown as a function of the truth ΔR between the electrons, for a 0.1 GeV γ_d decaying into electrons and produced via the FRVZ benchmark model.

This has some implications on the isolation criteria that has to be adopted. Differently from muons, standard isolation requirements can be applied without having

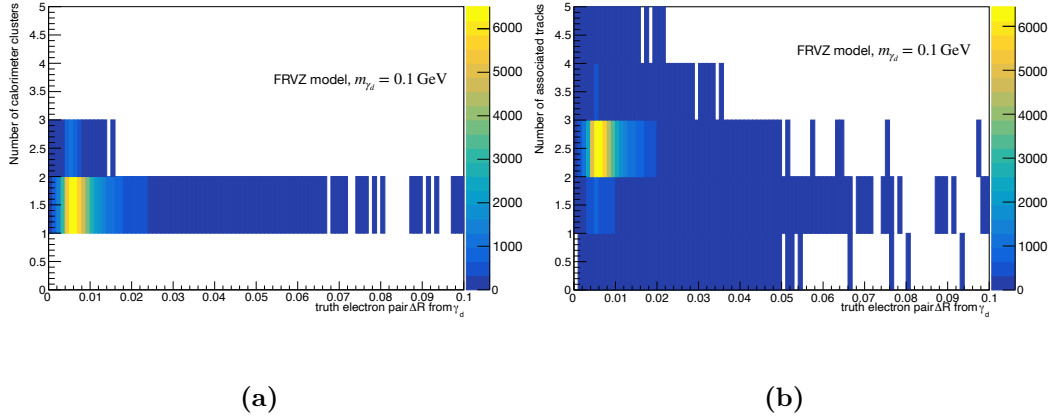


Figure 5.8. Number of topo-clusters (a) and their associated tracks (b) as a function of ΔR between truth electrons produced by γ_d decays. The γ_d is produced via the FRVZ benchmark model and has a mass of 0.1 GeV.

a significant impact on the signal acceptance. This is due to the fact that, since the two topo-clusters are often merged, the energy of both electrons is comprised within a single electron, therefore not impacting the isolation computation. For this reason, no ad-hoc isolation modification has been used for electrons. The calorimeter and track-based isolation energies requirements for electrons are comprised in the Loose_VarRad isolation WP, detailed in Sec. 4.4.

5.3.3 Overlap removal

The reconstruction of the same energy deposits as multiple objects is resolved using the Overlap Removal procedure, outlined in Sec. 4.6. Here, as summarised in Tab. 5.4, if a CT muon (see Sec. 4.5) overlaps with an electron and they share an ID track, the muon is rejected and the electron is retained. If instead the muon is not of the CT type but it still shares an ID track with the electron, the electron is discarded and the muon is retained. If an electron is found within $\Delta R = 0.2$ of an electron, the jet is discarded and the electron is retained. Then, all the electrons found in a cone $\Delta R = 0.4$ around a jet are discarded and the jet is retained. Only

Reject	Against	Criteria
Muon	Electron	is CT and shared ID track
Electron	Muon	shared ID track
Electron	Jet	$\Delta R < 0.2$
Jet	Electron	$\Delta R < 0.4$

Table 5.4. Overlap removal selection criteria.

objects passing the overlap removal requirements are used in the analysis. The impact of the OR on the signal efficiency is observed to be negligible.

5.4 Prompt Lepton-Jets reconstruction

As said in Sec. 5.2, γ_d decay products are so collimated that they are reconstructed as a single object, the *prompt Lepton-Jet*.

Lepton-Jets are reconstructed using the Cambridge–Aachen clustering algorithm (see Sec. 4.2). The algorithm starts from the highest p_T lepton and looks for additional leptons of the same type within a $\Delta R = 0.4$ cone around the initial lepton-associated track’s momentum vector. If a second lepton of the same type is found in the cone, the axis of the cone is rotated to the vector sum of the momenta of the two lepton-associated tracks. This procedure is repeated until no additional lepton of the same type is found in the cone. There is no upper limit on the number of leptons in the Lepton-Jet, so to be sensitive to scenarios with additional γ_d radiations too, resulting in more leptons found within the same pLJ cone.

Lepton-Jets are classified, as schematically depicted in Fig. 5.9, according to the number of muons and electrons found within their cone:

- **muonic-LJ (μ LJ)**: at least two muons and no electrons are found in the cone;
- **electronic-LJ (e LJ)**: at least one electron with at least two associated tracks is found in the cone, while no muon is reconstructed within the same cone.

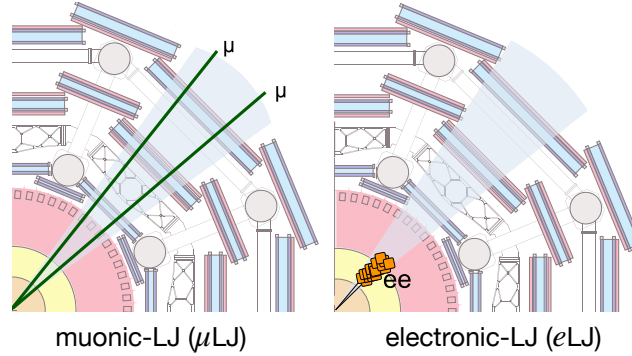


Figure 5.9. Schematic drawing of the two types of reconstructed LJs: μ LJ (left) and e LJ (right).

Differently from μ LJs, e LJs are reconstructed even when only one electron (with two associated tracks) is found, since, as said in Sec. 5.3.2, in the investigated topology electrons are often so collimated that they are reconstructed as a single object. The fraction of events where two electrons are found within the same e LJ is negligible for $m_{\gamma_d} < 2 \text{ GeV}$ in both the FRVZ and the HAHM benchmark models.

Since e LJs are discarded if a muon is found within their cone, and μ LJs are discarded if an electron is found within their cone, the two LJs categories are mutually exclusive.

The analysis looks for events in which at least two LJs are reconstructed, in order to reduce the background contributions. Therefore three different *search channels* are defined:

- the **muonic channel** ($\mu\text{LJ}-\mu\text{LJ}$), where the leading and the furthest LJs are both muonic;
- the **mixed channel** ($\mu\text{LJ}-e\text{LJ}$), where the leading and the furthest LJs are of different type (one muonic and one electronic);
- the **electronic channel** ($e\text{LJ}-e\text{LJ}$), where the leading and the furthest LJs are both electronic.

The orthogonality between the channels is ensured by considering the type of the leading LJ and the type of the farthest one in azimuthal angle, since the two LJs are expected to be almost back-to-back.

Further details on the characteristics of these two LJ types are given in the following sections.

5.4.1 Muonic Lepton-Jets reconstruction efficiencies

The μLJ reconstruction efficiency is shown in Fig. 5.10 as a function of the γ_d transverse momentum, η and opening angle between its decay products, for a DP produced via the FRVZ benchmark model, for different DP mass hypotheses. The same distributions are shown for a DP produced via the HAHM benchmark model in Fig. 5.11. These efficiencies are obtained considering only γ_d decays into muons and looking for a μLJ matching such γ_d in a $\Delta R = 0.4$ cone.

Fig. 5.10 (a) and Fig. 5.11 (a) show how for light γ_d the reconstruction efficiency drops for very high $\gamma_d p_T$. This is due to the fact that very boosted (light) γ_d produce extremely boosted muons, whose reconstruction resolution deteriorates for extremely large p_T . Additionally, it can be seen how the LJ reconstruction efficiency is correlated with the mass and the $\gamma_d p_T$, since the heavier the γ_d the more boosted it should be for muons to be reconstructed within a μLJ .

Fig. 5.10 (b) and Fig. 5.11 (b) show that the reconstruction efficiency is flat in η , with a drop in the $|\eta| < 0.1$ region. This is due to the fact that muons are required to be of the ComBined type and therefore they need to be reconstructed both in the ID and in the MS and the MS has a hole in the coverage in $|\eta| < 0.1$. The drop in the $|\eta| > 2.5$ region is instead due to the ID acceptance. From these plots, it can also be seen how the average LJ reconstruction efficiency drops drastically for heavier mass DPs, as a consequence of their smaller boost, resulting into less collimated decay products. It can also be seen how the average reconstruction efficiency is larger for γ_d produced via the HAHM model with respect to the ones produced via the FRVZ one, as a consequence of the larger boost of the γ_d produced in the former model.

Fig. 5.10 (c) and Fig. 5.11 (c) show instead how, as expected, reconstruction efficiencies are flat as a function of ΔR for heavy γ_d , while for light γ_d this is not the case. This is due to the dependency of the μLJs reconstruction efficiency on the $\gamma_d p_T$. As can be seen from Fig. 5.10 (a) and Fig. 5.11 (a), for light γ_d μLJs can be reconstructed even when γ_d have a small p_T . When DPs have a very small p_T , the produced muons will have a small p_T as well and thus they will be more bended by the magnetic field in which the ID is immersed. Furthermore, muons

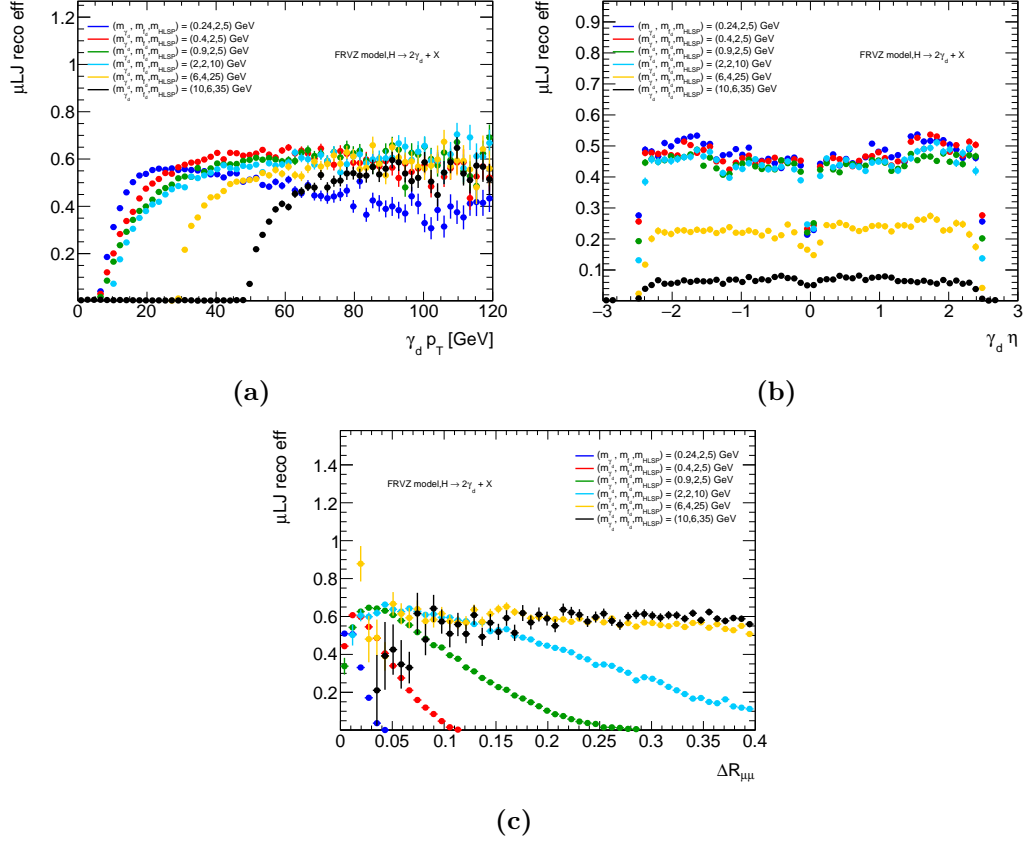


Figure 5.10. Reconstruction efficiencies for μ LJs produced by the decay of γ_d according to the FRVZ model. (a) shows the reconstruction efficiency as a function of the transverse momentum p_T of the DP; (b) shows the reconstruction efficiency as a function of the $\gamma_d \eta$; (c) shows the reconstruction efficiency as a function of the opening angle ΔR between the γ_d decay products. A μ LJ is considered to be reconstructed if it is found within a $\Delta R = 0.4$ cone around a γ_d decaying into muons.

that are extremely soft ($p_T \lesssim 5 \text{ GeV}$) are reconstructed less efficiently than higher energy ones. The μ LJ reconstruction efficiency thus decreases as a function of ΔR for lighter DPs, where very soft muons can be reconstructed as a μ LJ.

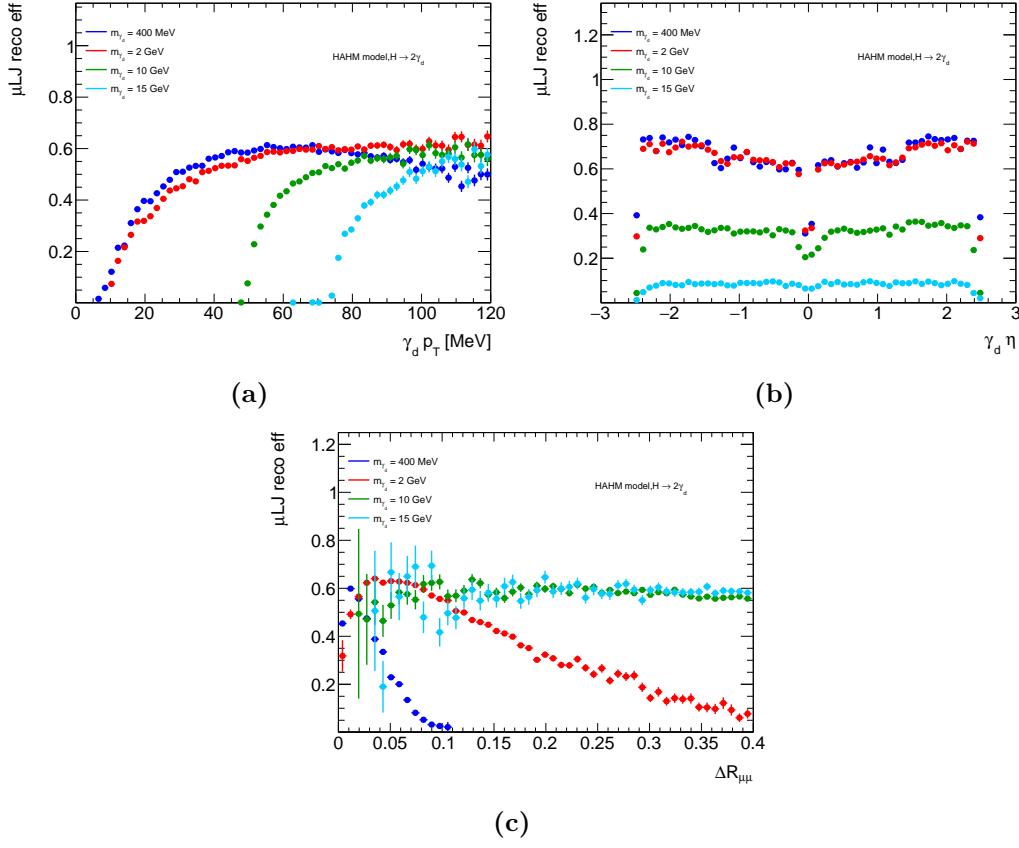


Figure 5.11. Reconstruction efficiencies for μ LJs produced by the decay of γ_d according to the HAHM model. (a) shows the reconstruction efficiency as a function of the transverse momentum p_T of the DP; (b) shows the reconstruction efficiency as a function of the $\gamma_d \eta$, while (c) shows the reconstruction efficiency as a function of the opening angle ΔR between the γ_d decay products. A μ LJ is considered to be reconstructed if it is found within a $\Delta R = 0.4$ cone around a γ_d decaying into muons.

5.4.2 Electronic Lepton-Jets reconstruction efficiencies

The e LJ reconstruction efficiency is shown in Fig. 5.12 as a function of the γ_d transverse momentum, η and opening angle (ΔR) between its decay products, for a DP produced via the FRVZ benchmark model, for different DP mass hypotheses.

These efficiencies are obtained considering only γ_d decays into electrons and looking for a e LJ matching such γ_d in a $\Delta R = 0.4$ cone.

As said in Sec. 5.4, e LJs can be reconstructed either with one topo-cluster with at least two associated tracks (i.e. one single electron) or with at least two topo-clusters matched to tracks (i.e. at least two electrons), with the latter possibility becoming relevant for heavy DPs. Therefore, in such a scenario, the e LJ reconstruction efficiencies are populated with these two kinds of e LJs. The plots in Fig. 5.12 are thus shown in Fig. 5.13, Fig. 5.14 and Fig. 5.15 separately for e LJs reconstructed with only one electron (a) and e LJs reconstructed with two electrons (b).

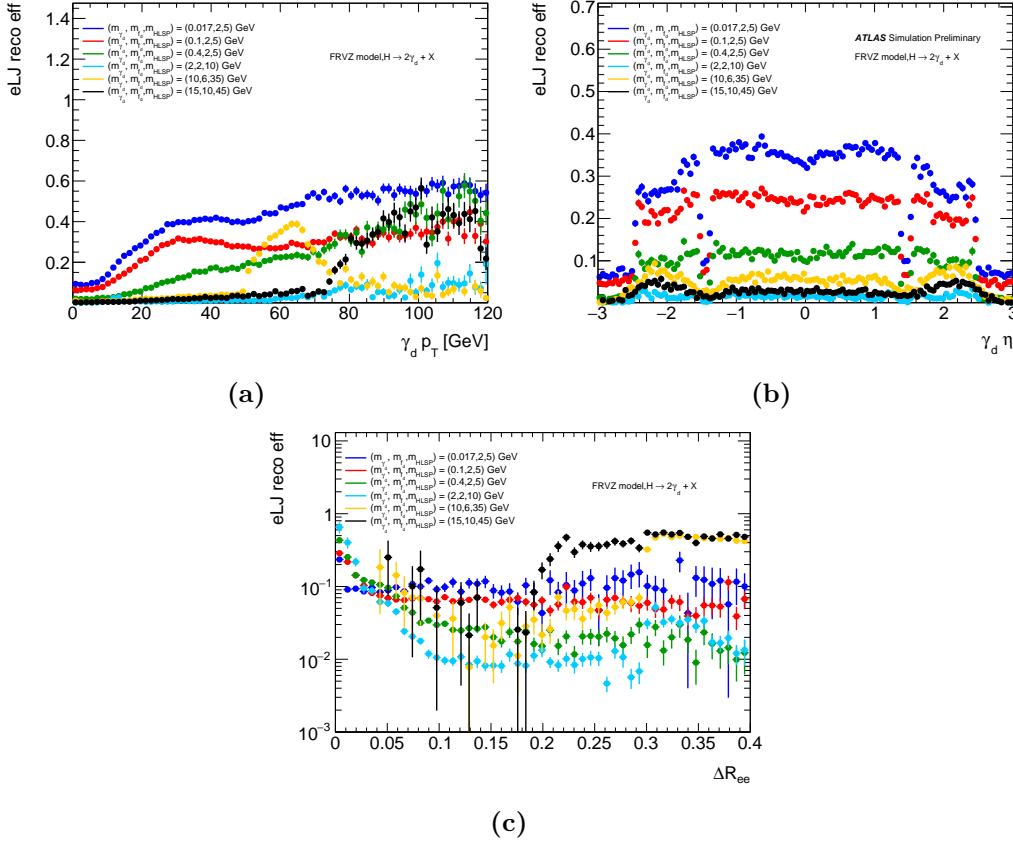


Figure 5.12. Reconstruction efficiencies for eLJ s produced by the decay of γ_d according to the FRVZ model. (a) shows the reconstruction efficiency as a function of the transverse momentum p_T of the DP; (b) shows the reconstruction efficiency as a function of the γ_d η ; (c) shows the reconstruction efficiency as a function of the opening angle ΔR between the γ_d decay products. An eLJ is considered to be reconstructed if it is found within a $\Delta R = 0.4$ cone around a γ_d decaying into electrons.

For $m_{\gamma_d} \geq 10$ GeV, eLJ s with one electron are almost never reconstructed, as can be seen from all the efficiency plots. In this mass range, eLJ s with two electrons are reconstructed only within a certain p_T window, as can be seen from Fig. 5.13 (b). Dark Photons with p_T smaller than the lower bound of such window produce too open electrons, that are not reconstructed within the same LJ. DPs with instead a p_T larger than the upper bound of such window produce extremely collimated electrons, that are thus reconstructed as one-electron eLJ s.

As can be seen from Fig. 5.14, the eLJ reconstruction efficiency at small η is larger for eLJ s reconstructed with two electrons (b) rather than for eLJ s reconstructed with one (a) as a consequence of the better resolution in that η region, where the two collimated electrons are more likely to be resolved.

The eLJ reconstruction efficiency decreases as a function of ΔR for eLJ s reconstructed with only one electron (Fig. 5.14 (a)) and is instead flat as a function of ΔR , for $m_{\gamma_d} \leq 10$ GeV, for eLJ s reconstructed with two electrons (Fig. 5.14 (b)). In the region with $m_{\gamma_d} \geq 10$ GeV, the reconstruction efficiency drops for $\Delta R < 0.2$, as,

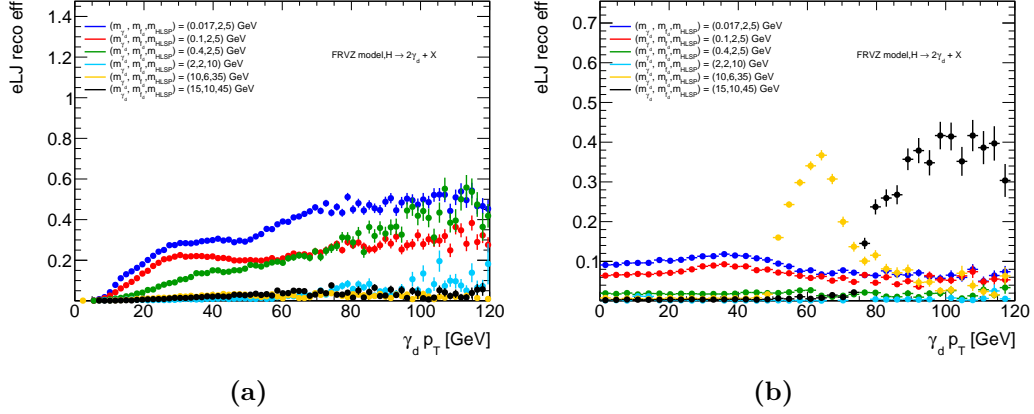


Figure 5.13. Reconstruction efficiencies for eLJ s composed of only one electron (a) or two electrons (b) as a function of the $\gamma_d p_T$, where the γ_d is produced according to the FRVZ model. An eLJ is considered to be reconstructed if it is found within a $\Delta R = 0.4$ cone around a γ_d decaying into electrons.

given the average p_T of the electrons, they would be too collimated for being reconstructed as one-electron eLJ s. In $0.2 < \Delta R < 0.3$, electrons are resolved as their clusters do not overlap, but they might fail isolation as they lie within the cone of the other. For this reason, the average eLJ reconstruction efficiency is larger in $0.3 < \Delta R < 0.4$ than in $0.2 < \Delta R < 0.3$.

The same distributions are shown for a DP produced via the HAHM benchmark model in Fig. 5.16.

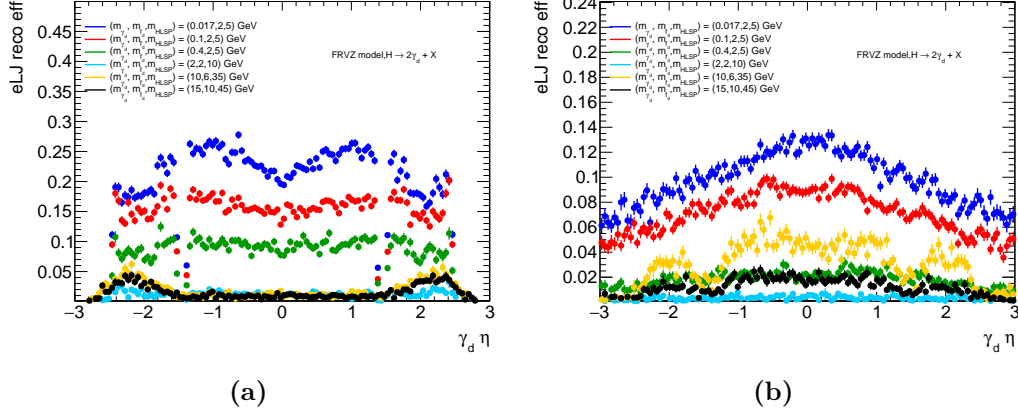


Figure 5.14. Reconstruction efficiencies for eLJs composed of only one electron (a) or two electrons (b) as a function of the γ_d η , where the γ_d is produced according to the FRVZ model. An eLJ is considered to be reconstructed if it is found within a $\Delta R = 0.4$ cone around a γ_d decaying into electrons.

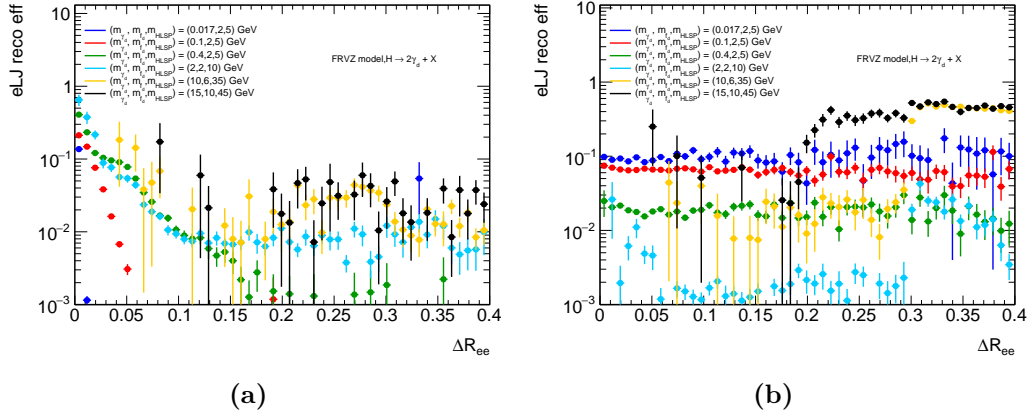


Figure 5.15. Reconstruction efficiencies for eLJs composed of only one electron (a) or two electrons (b) as a function of the opening angle ΔR between the γ_d decay products, where the γ_d is produced according to the FRVZ model. An eLJ is considered to be reconstructed if it is found within a $\Delta R = 0.4$ cone around a γ_d decaying into electrons.

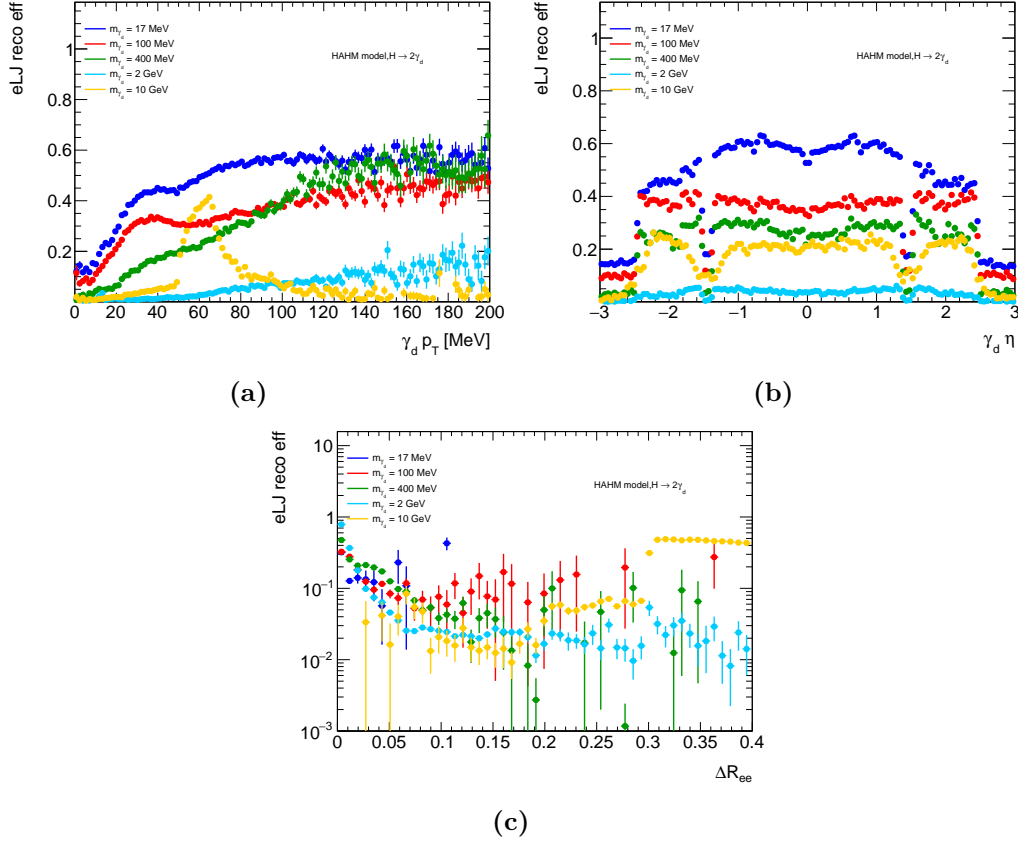


Figure 5.16. Reconstruction efficiencies for eLJ s produced by the decay of γ_d according to the HAHM model. (a) shows the reconstruction efficiency as a function of the transverse momentum p_T of the DP; (b) shows the reconstruction efficiency as a function of the $\gamma_d \eta$, while (c) shows the reconstruction efficiency as a function of the opening angle ΔR between the γ_d decay products. An eLJ is considered to be reconstructed if it is found within a $\Delta R = 0.4$ cone around a γ_d decaying into electrons.

5.4.3 Selection criteria for Lepton-Jets

As said in Sec. 5.4, e LJs are reconstructed with either one topo-cluster with at least two ID tracks associated to it, or with at least two separate electrons. Therefore, when defining LJ-level variables, whilst for μ LJ the full muon objects are used, for e LJ either full electron or electron-associated ID tracks are used. Specifically, when the e LJ is reconstructed with two electrons, the full electron object is considered. When only one electron is reconstructed, the electron-associated ID track having the same charge of the electron, being closest to the full-electron axis and having the largest p_T is considered as first track, and in the following is going to be referred to as *leading track*. The second track considered is the electron-associated ID track that has opposite charge with respect to the electron and that has the largest p_T , and in the following is going to be referred to as *sub-leading track*. The following variables are then used during the event selection and are defined for each LJ:

- LJ mass: reconstructed as the invariant mass of the muons/electrons/ID tracks in a μ LJ / e LJ with two electrons / e LJ with one electron. The LJ mass is expected to peak around the mass of the γ_d . Further details about the LJ invariant mass calculation are given in Sec. 5.4.4;
- p_T imbalance (p_T^{imb}): defined as

$$p_T^{\text{imb}} = \frac{p_T^{\text{lead}} - p_T^{\text{sub-lead}}}{p_T^{\text{lead}} + p_T^{\text{sub-lead}}}$$

where p_T^{lead} and $p_T^{\text{sub-lead}}$ refer respectively to the leading and the sub-leading muon/electron/ID track found in a μ LJ / e LJ with two electrons / e LJ with one electron. LJs from a γ_d decay are expected to be balanced in p_T ;

- q_{LJ} , that is the sum of the charges of muons/electrons/ID tracks in a μ LJ / e LJ with two electrons / e LJ with one electron. LJs originating from neutral particle decays are expected to have a zero sum of charges.

The following event-level variables are also defined:

- Azimuthal distance between LJs, $\Delta\phi(\text{LJ}, \text{LJ})$, where signal LJs are expected to be back-to-back in the transverse plane (since they are the result of a two-body decay of a Higgs boson generated at rest), hence a cut on $\Delta\phi$ reduces the background without significantly affecting the signal efficiency;
- LJ mass imbalance (m^{imb}), defined as the absolute value of the difference, divided by the sum, of the masses of the two selected LJs in the event. The distribution of this variable, for LJs originating from a γ_d decay, is expected to have its maximum around 0.

How these listed variables are employed in discriminating the different sources of backgrounds affecting the various search channels is described in detail in Sec. 6.1.

5.4.4 Invariant mass reconstruction

The LJ invariant mass is among the variables that are used in this search, and is built as explained in Sec. 5.4.3. This quantity can be in principle extremely powerful in discriminating potential sources of background, as the LJs should have an invariant mass compatible with the γ_d mass. The distributions of the invariant mass for μ LJs and for e LJs are shown for the FRVZ benchmark model respectively in Fig. 5.17 (a) and Fig. 5.17 (b) and for the HAHM model respectively in Fig. 5.17 (c) and Fig. 5.17 (d).

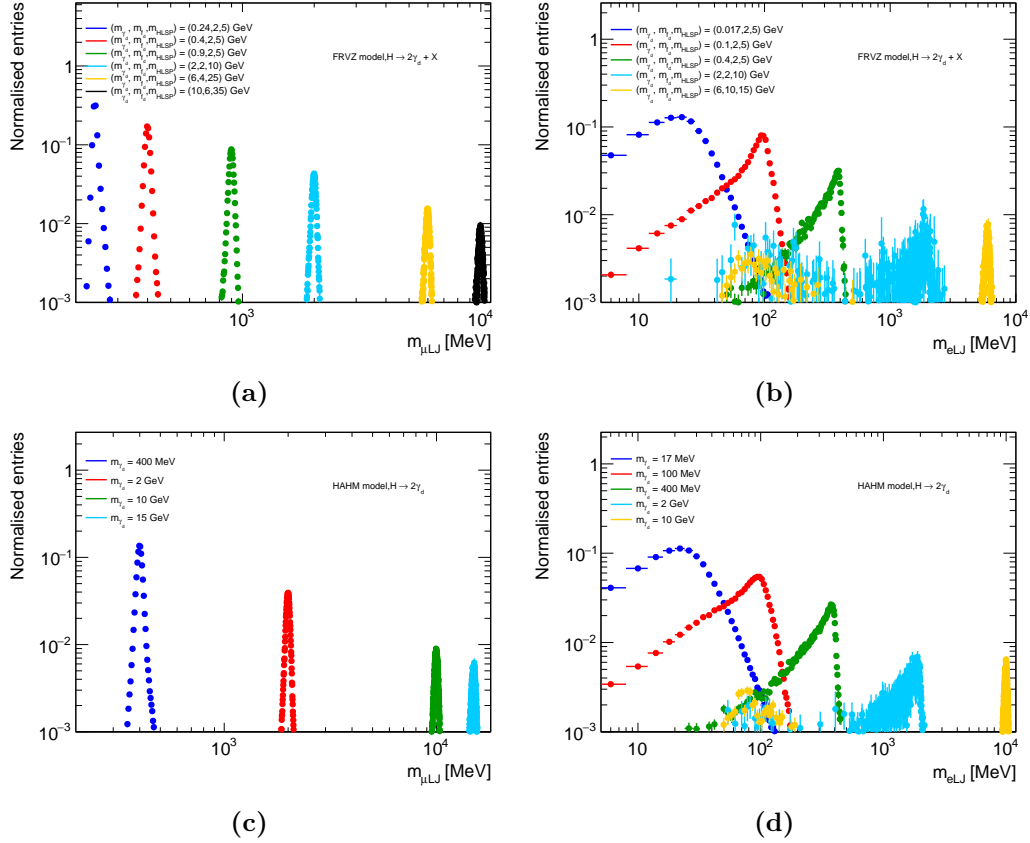


Figure 5.17. Reconstructed invariant mass of μ LJ (e LJ) for the FRVZ (a) ((b)) and the HAHM model (c) ((d)), for different m_{γ_d} hypotheses.

From these pictures it's clear how, while the resolution on the μ LJ invariant mass is very good (in the range of 10 MeV – 100 MeV for the investigated m_{γ_d} range), with the μ LJ invariant mass peaking at the γ_d mass, the e LJ invariant mass reconstruction shows a pathological behaviour.

To further investigate this feature, the e LJ invariant mass distributions are studied in Fig. 5.18 for the FRVZ model ((a),(b)) and the HAHM one ((c),(d)), separately for the scenario in which the e LJ is comprised of two electrons ((a),(c)) and for the scenario in which it is comprised of only one electron ((b),(d)). These distributions show how the pathological reconstruction arises in e LJs comprised of

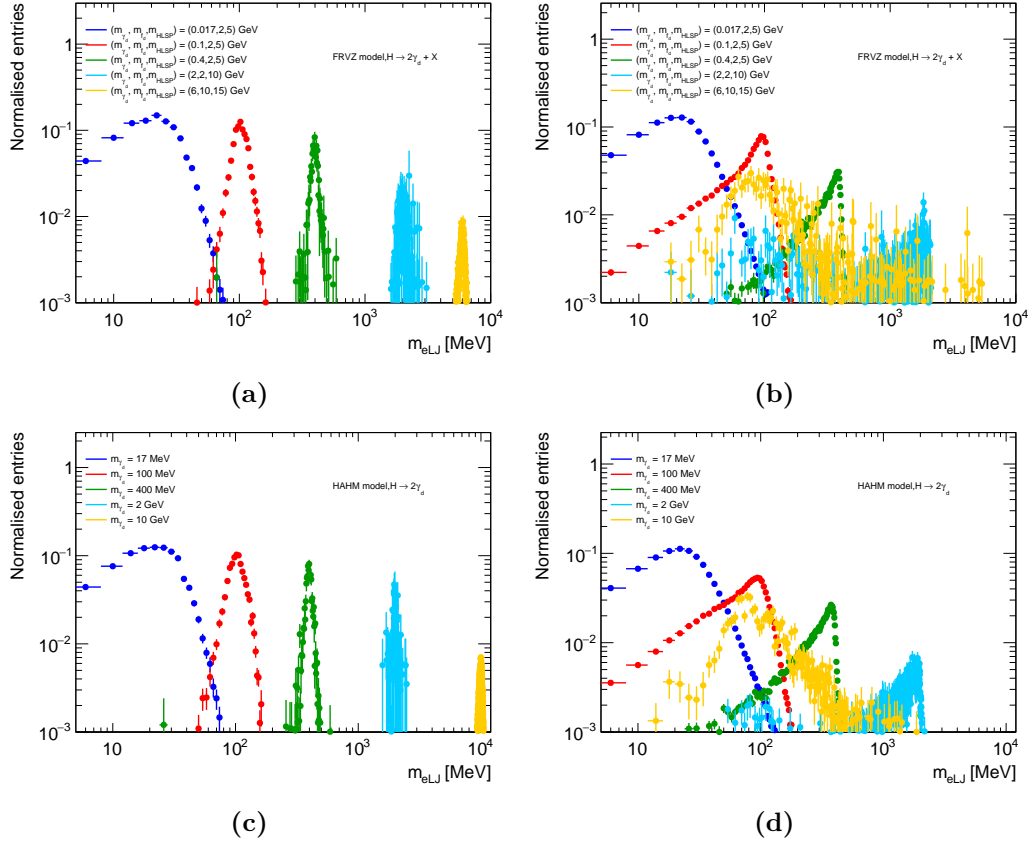


Figure 5.18. Reconstructed eLJ invariant mass for eLJ comprised of two electrons in the FRVZ model (a) and in the HAHM model (c), and for eLJ built with only one electron, in the FRVZ model (b) and in the HAHM model (d).

only one electron. In Fig. 5.18 (b) and (d) a poorer resolution is observed, since in this case the eLJ invariant mass is reconstructed only with ID tracks rather than with the electron objects, as in Fig. 5.18 (a) and (c). Furthermore, for heavy DPs, eLJ s can be mistakenly reconstructed even when the electrons do not fall within the $\Delta R = 0.4$ LJ cone. The latter happens when a random track (i.e. not coming from a genuine electron) is associated to the topo-cluster found in the eLJ . In this case, a random, generally smaller, eLJ invariant mass is reconstructed. Therefore, the μLJ invariant mass is used in this search in both the muonic and the mixed channel as main discriminating variable against the background, whilst some loose requirements on the eLJ invariant mass are used in this search only in order to suppress some sources of background in the electronic and mixed channel.

5.5 Triggers

Data were collected using a combination of single and multi-lepton triggers (see Sec. 3.2.6). The trigger strategy for each channel (the muonic, the electronic and the mixed one) is here introduced. All the triggers used in this analysis are un-

prescaled (see Sec. 3.2.6) during the relative data-taking periods.

5.5.1 Muonic channel triggers

The topology of the $\mu\text{LJ}-\mu\text{LJ}$ channel suggests the use of muon triggers. Single muon triggers require either high- p_T or isolated muons. Standard isolation requirements are found to significantly reduce the efficiency on selecting signal μLJs , as said in Sec. 5.3.1, regardless of the p_T threshold. Moreover, since the muons produced by the γ_d decays are rather soft, non-isolated single-muon triggers are found to be less effective than multi-muons ones (for all the scenarios investigated), given their higher p_T thresholds. For these reasons, single-muon triggers are discarded in favour of di-muon and tri-muon triggers. The list of adopted triggers, built from the lowest un-prescaled triggers available in different data-taking periods, is reported in Tab. 5.5.

Type	Data-taking periods	Trigger
di-muon	2015	HLT_mu18_mu8noL1
	2015 - 2016 A	HLT_2mu10
	2016 A	HLT_2mu10_nomucomb
	2016 A-D3	HLT_mu20_mu8noL1
	2016 B-end - 2017 - 2018	HLT_2mu14
	2016 B-D3	HLT_2mu14_nomucomb
	2016 D4-end - 2017 - 2018	HLT_mu22_mu8noL1
tri-muon	2015 - 2016 B-D3 - 2017 - 2018	HLT_3mu6
	2015-2018 - all periods	HLT_3mu6_msonly

Table 5.5. List of muon triggers used in the $\mu\text{LJ}-\mu\text{LJ}$ channel for the corresponding data-taking periods. The suffix **noL1** appearing in asymmetric di-muon triggers (i.e. triggers having two different p_T requirements for the two muons) refers to the fact that the muon triggering the **mu8** leg doesn't pass the L1 trigger. The suffix **nomucomb** implies that the HLT muon is reconstructed using the MS only.

Trigger matching

As explained in Sec. 3.2.6, the trigger system performs a quick first online selection of potentially interesting events. Since the event reconstruction at the trigger-level is necessarily less accurate than the full offline reconstruction, in order to confirm HLT physics objects, it is looked for close-by offline ones which must satisfy the requirements specified in the triggers (in this case, the requirements are only p_T -related ones). Therefore, the following criteria are used for considering an offline muon to be matched to a HLT object:

1. the offline muon must have a p_T above the HLT threshold of at least 1 GeV;
2. the ΔR between the offline muon and its closest HLT object should be at most 0.2.

A consistent number of offline muons are required to be trigger matched (e.g. the 2mu10 trigger is considered valid if, when fired, per each HLT muon there is one offline muon within $\Delta R = 0.2$ and with $p_T > 11$ GeV).

Additionally, it is required that all HLT muons should be matched to offline muons reconstructed within a μLJ and that at least one muon per each μLJ should be trigger-matched.

Trigger Scale Factors and trigger bucketing

Per event triggers SFs need to be applied in order for the trigger efficiencies evaluated via MC simulations to match the ones observed in data. To do so, efficiencies are evaluated per each muon reconstructed at the trigger level, referred to as *trigger-leg*. Such efficiencies per trigger leg are then combined to form the total trigger efficiency, this combination being simplified thanks to the inclusive definition of single-leg triggers, so that the muons selected by tighter triggers legs are always a subset of the muons selected by looser triggers legs.

As an example, the trigger SF computation for the logical OR of the two di-muon triggers exploited in 2015 is outlined in the following.

Calling A an event where the symmetric di-muon trigger 2mu10 trigger is fired and B an event where the asymmetric di-muon trigger mu18_mu8noL1 trigger is fired, Fig. 5.19 shows where these events belong in the phase space of the leading and the sub-leading muons found in the event.

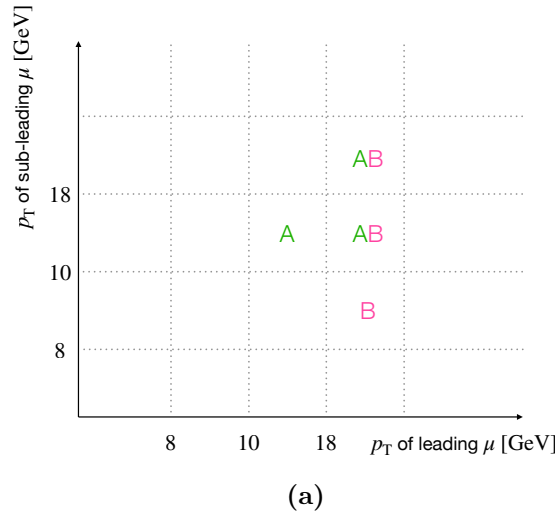


Figure 5.19. Events where the 2mu10 trigger is fired (A) or the mu18_mu8noL1 (B) is fired as a function of the p_T of the leading (x -axis) and sub-leading muon (y -axis) found in the event.

From this table it's clear how there are certain events (the ones in which the leading muon has $p_T > 18$ GeV and the sub-leading one has $p_T > 10$ GeV) in which both triggers are fired. This should be accounted for, so not to over-estimate the total trigger efficiency. The probability for the 2mu10 trigger to be fired can be

evaluated via:

$$p(2\mu 10) = p_{\mu_1}(\mu 10)p_{\mu_2}(\mu 10),$$

where μ_1 and μ_2 refers to respectively the leading and the sub-leading muons and $p_{\mu_{1,2}}(\mu 10)$ being the probability for the relative muon to fire the **mu10** trigger leg. The probability for the **mu18_mu8noL1** trigger to be fired can be evaluated via:

$$p(\mu 18_mu 8noL1) = p_{\mu_1}(\mu 18)p_{\mu_2}(\mu 8) + p_{\mu_1}(\mu 8)p_{\mu_2}(\mu 18) - p_{\mu_1}(\mu 18)p_{\mu_2}(\mu 18),$$

with $p_{\mu_{1,2}}(\mu 8)$ and $p_{\mu_{1,2}}(\mu 18)$ being the probability for the relative muon to fire respectively the **mu8** and the **mu18** trigger leg. The term $p_{\mu_1}(\mu 18)p_{\mu_2}(\mu 18)$ refers to the probability that both muons have fired the **mu18** trigger leg, and this term has to be subtracted to avoid double-counting. The efficiency of the logical **OR** of such triggers is

$$\begin{aligned} p(2\mu 10 || \mu 18_mu 8noL1) &= p(2\mu 10) + p(\mu 18_mu 8noL1) + \\ &\quad - p_{\mu_1}(\mu 10)p_{\mu_2}(\mu 18) + \\ &\quad - p_{\mu_1}(\mu 18)p_{\mu_2}(\mu 10), \end{aligned} \tag{5.1}$$

where the two last terms are needed to account for the scenario in which the muons trigger both the **2mu10** and the **mu18_mu8noL1** triggers. The event trigger SF is then computed by evaluating such $p_{\mu_i}(j)$ probabilities (with $i = 1, 2$ respectively for the leading and the sub-leading muon and j being each trigger leg), one term at a time, both in MC and in data, and combining them as prescribed by Eq. 5.1.

The trigger strategy chosen for this channel includes the **3mu6** trigger as well, thus complicating exponentially the SF calculation procedure, to account for all the different combinations rising when three muons and four muon legs (**mu6**, **mu8**, **mu10**, **mu18** for 2015) are considered. For this reason, an alternative strategy has been chosen, this strategy being referred to as *trigger bucketing*.

The idea behind it is to find two orthogonal regions (*buckets*) which are expected to be populated by events that are triggered either only by the di-muon triggers or only by the **3mu6** trigger. Such regions can be identified by looking at the p_T of the reconstructed muons. If the leading muon of each μLJ have a p_T smaller than the di-muon trigger thresholds, the di-muon trigger cannot be fired. Such events could potentially fire the **3mu6** trigger, given the lower p_T of the reconstructed muons. Thus, two orthogonal fiducial region are defined as:

- **high- p_T region:** the leading muons of each μLJ satisfy the di-muon triggers p_T threshold requirements (that are always higher than those of the **3mu6** trigger);
- **low- p_T region:** the leading muons of each μLJ do not satisfy the di-muon triggers p_T thresholds.

As an example, in 2015 the two regions are defined as:

- **high- p_T region:** events where $p_T(\mu_1) > 10 \text{ GeV}$ and $p_T(\mu_2) > 10 \text{ GeV}$, or $p_T(\mu_1) > 8 \text{ GeV}$ and $p_T(\mu_2) > 18 \text{ GeV}$, or $p_T(\mu_1) > 18 \text{ GeV}$ and $p_T(\mu_2) > 8 \text{ GeV}$ (with $\mu_{1,2}$ being the leading muons of respectively the leading μLJ and the farthest one);

- low- p_T region: events not satisfying the high- p_T region requirements.

This categorization is adopted for the sole purpose of computing the correct trigger SF in each event. The SFs computation for the combination of the trigger in the high- p_T SR is standard and provided by the collaboration as explained in Ref. [150]. The SFs (and their associated systematics) computation for the 3 μ 6 SF exploited in the low- p_T SR is carried out in Ref. [151].

Being orthogonal, the high- p_T and the low- p_T regions are combined to form a unique μ LJ- μ LJ channel SR.

Trigger efficiency

The di-muon and tri-muon trigger efficiencies are shown respectively in Fig. 5.20 and Fig. 5.21 as a function of the leading γ_d p_T (a) and η (b), for a γ_d produced in the FRVZ benchmark model and for different m_{γ_d} hypotheses. In order to evaluate these efficiencies, the events have been pre-selected requiring that both γ_d decay at the truth-level into a pair of muons. The different p_T turn-on curves that can be seen in Fig. 5.20 (a) and Fig. 5.21 (a) are due to the different trigger thresholds, whilst the loss in efficiency at $|\eta| > 2.5$ that can be seen in Fig. 5.20 (b) and Fig. 5.21 (b) is due to the ID coverage.

The trigger efficiency in the regions defined in the trigger bucket strategy is shown for both the di-muon and 3 μ 6 triggers in Fig. 5.22. These efficiencies are presented as a function of the leading γ_d p_T , for a DP with a mass of $m_{\gamma_d} = 0.24$ GeV and produced via the FRVZ model. In order to evaluate these efficiencies, the events have been pre-selected requiring that both γ_d decay into a pair of muons.

The usage of only the di-muon triggers in both the high- p_T and the low- p_T regions would cause a null efficiency for the scenario in which γ_d are less boosted, while the usage of 3 μ 6 only, though allowing additional sensitivity to the scenario in which γ_d are soft, would imply a smaller average trigger efficiency. Therefore, exploiting di-muon triggers only in the high- p_T region and the 3 μ 6 one only in the low- p_T one maximizes the trigger efficiency in the full γ_d p_T range.

In such a way, for light γ_d produced in the FRVZ model, the trigger efficiency is increased by more than the 50%. For heavier γ_d hypotheses, the impact of the addition of the 3 μ 6 trigger is negligible, since in order for μ LJs to be reconstructed γ_d have to be more boosted (see Sec. 5.4.1), and therefore events always lie in the high p_T category.

This is the case also for γ_d produced via the HAHM model, where the average γ_d p_T is larger (see Sec. 5.2).

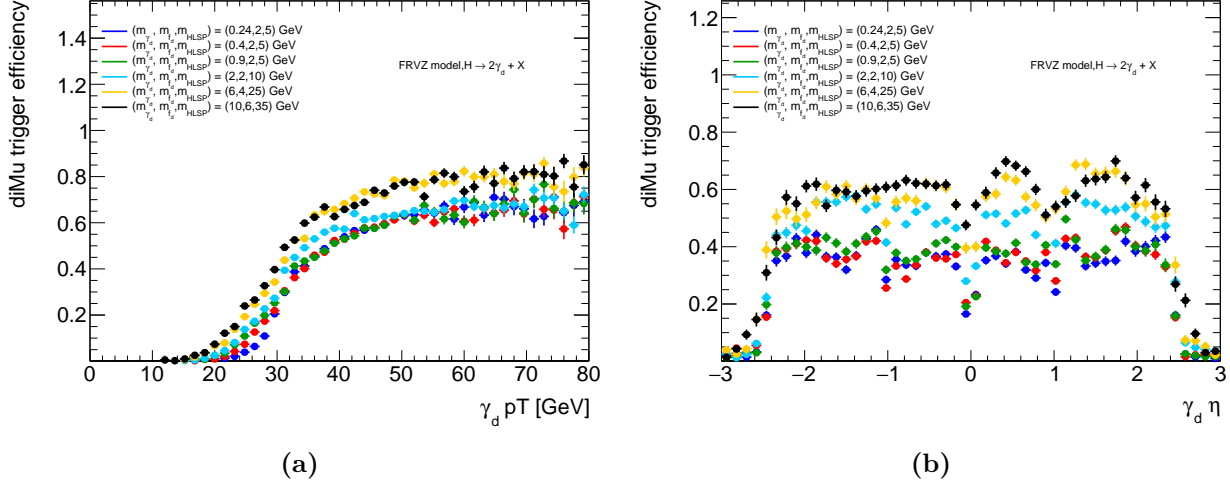


Figure 5.20. Di-muon trigger efficiencies for the FRVZ signal model, shown for different mass points and as a function of the $\gamma_d p_T$ (a) and η (b). Events are pre-selected requiring that both γ_d decay into a pair of muons.

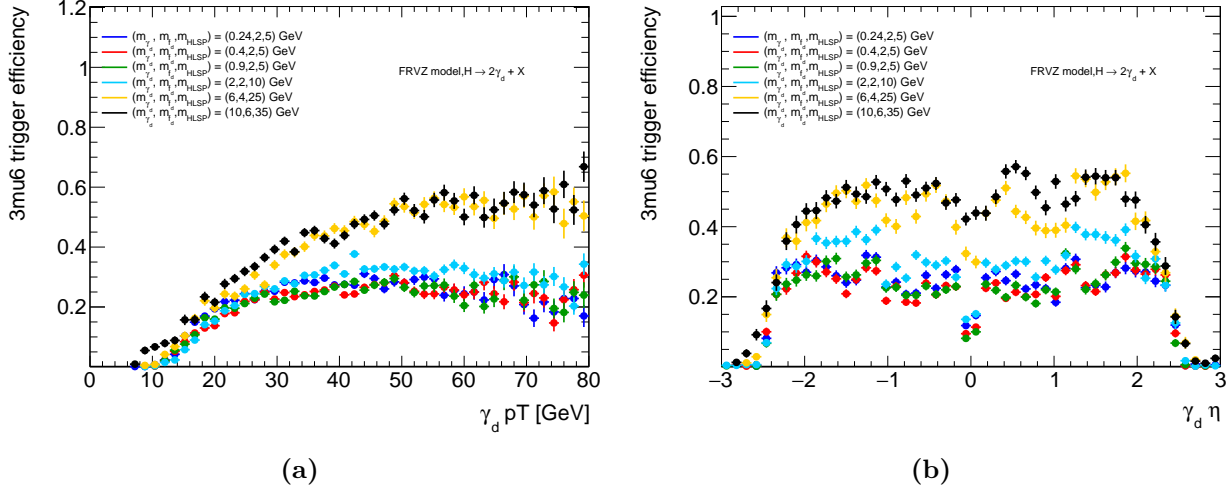


Figure 5.21. 3mu6(_msonly) trigger efficiencies for the FRVZ signal model, shown for different mass points and as a function of the leading $\gamma_d p_T$ (a) and η (b). Events are pre-selected requiring that both γ_d decay into a pair of muons.

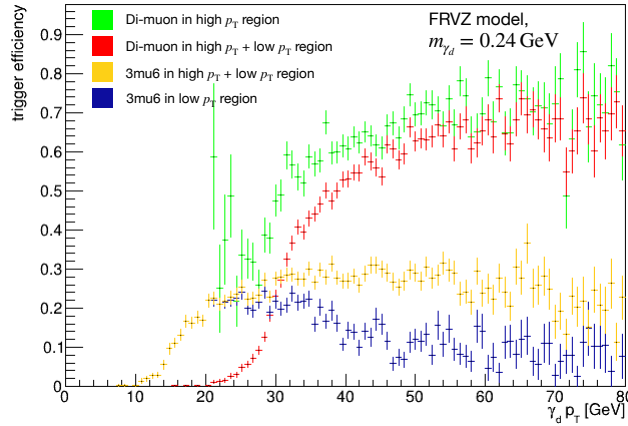


Figure 5.22. Trigger efficiency as a function of the leading $\gamma_d p_T$, for a γ_d with $m_{\gamma_d} = 0.24$ GeV, where the γ_d is produced via the FRVZ benchmark model. Events are pre-selected requiring that both γ_d decay into a pair of muons. The di-muon trigger efficiency (red) is compared to the efficiency of the same trigger for events in the high- p_T region (green). The 3mu6 trigger efficiency (yellow) is compared to the efficiency of the same trigger for events in the low- p_T region (blue).

5.5.2 Electronic channel triggers

The signature of the $eLJ-eLJ$ channel suggests to use single-electron and di-electron triggers. Here tri-electron triggers are not used since most-often only one electron is reconstructed per each eLJ . Additionally, since isolation requirements does not impact the signal efficiency, single electron triggers including isolation requirements are used as well. The list of adopted triggers, built from the lowest un-prescaled triggers available in different data-taking periods, is reported in Tab. 5.6 and Tab. 5.7 for single-electron and di-electron triggers respectively.

Periods	Single-electron triggers
2015	HLT_e24_lhmedium_L1EM20VH
	HLT_e60_lhmedium
	HLT_e120_lhloose
2016-2018	HLT_e26_lhtight_nod0_ivarloose
	HLT_e60_lhmedium_nod0
	HLT_e140_lhloose_nod0

Table 5.6. List of single-electron triggers used in the $eLJ-eLJ$ channel for the corresponding data-taking periods. The suffixes **lhtight**, **lhmedium**, **lhloose** appearing in all the electron triggers indicate that the electron firing the trigger must satisfy the specified identification WP. The **ivarloose** suffix means instead that the HLT electron must satisfy an HLT track-based isolation, while the **nod0** suffix implies that no transverse impact parameter (d_0) cuts are required on the online electron. The **L1EM20VH** means that an EM cluster is reconstructed at the L1 trigger, passing an E_T cut of 20 GeV and a HCAL based isolation requirement.

Periods	Di-electron triggers
2015	HLT_2e12_lhvloose_L12EM10VH
2016	HLT_2e17_lhvloose_nod0
2017 (only B5-B8)	HLT_2e24_lhvloose_nod0
2017 (except B5-B8) - 2018	HLT_2e17_lhvloose_nod0_L12EM15VHI
	HLT_2e24_lhvloose_nod0

Table 5.7. List of di-electron triggers used in the $eLJ-eLJ$ channel for the corresponding data-taking periods. During the accidentally prescaled periods B5-B8 (runs 326834-328393 with an effective reduction of 0.6fb^{-1}), `HLT_2e24_lhvloose_nod0` is used instead of `HLT_2e17_lhvloose_nod0_L12EM15VHI`. The suffixes `lhtight`, `lhmedium`, `lhloose` appearing in all the electron triggers indicate that the electrons firing the trigger must satisfy the specified identification WP. The `nod0` suffix implies that no transverse impact parameter (d_0) cuts are required on the online electron. The `L1E2M10VH` (`L12EM15VHI`) suffix means that two EM clusters are reconstructed at the L1 trigger, passing an E_T cut of 10 GeV (15 GeV) and calorimeter based isolation requirements.

Trigger matching

The following criteria are used to consider an offline electron to be matched to an HLT trigger object:

1. the offline electron must have a p_T above the HLT threshold of at least ≥ 1 GeV;
2. the ΔR between the offline electron and its closest HLT trigger object should be at most 0.2.

A consistent number of offline electrons are required to be trigger matched. Additionally, it is required that all HLT electrons should be matched to offline electrons reconstructed within a eLJ . In events selected by di-electron triggers, the two trigger items are required to match electrons found in different reconstructed $eLJs$.

Trigger efficiency

The single-electron and di-electron trigger efficiencies are shown respectively in Fig. 5.23 and Fig. 5.24 as a function of the $\gamma_d p_T$ (a) and η (b), for a γ_d produced in the FRVZ benchmark model. In order to evaluate these efficiencies, the events have been pre-selected requiring that at the truth-level both γ_d decay into a pair of electrons.

The different p_T turn-on curves that can be seen in Fig. 5.23 (a) Fig. 5.24 (a) are due to the different trigger thresholds. The differences in the η distribution for the single electron, Fig. 5.23 (b), and the di-electron, Fig. 5.24 (b), trigger efficiency is due to the fact that the electron reconstruction efficiency degrades with increasing η (see Sec. 4.4). Therefore, collimated electrons are more-likely to be correctly

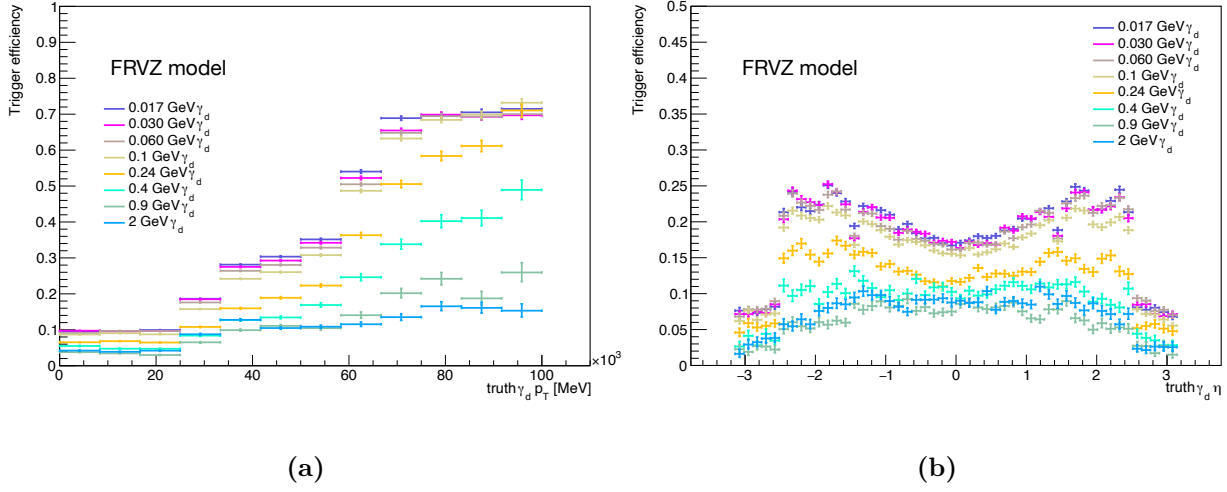


Figure 5.23. Single-electron triggers efficiencies for the FRVZ signal model, shown for different mass points and as a function of the leading $\gamma_d p_T$ (a) and η (b). Events are pre-selected requiring that both γ_d decay into a pair of electrons.

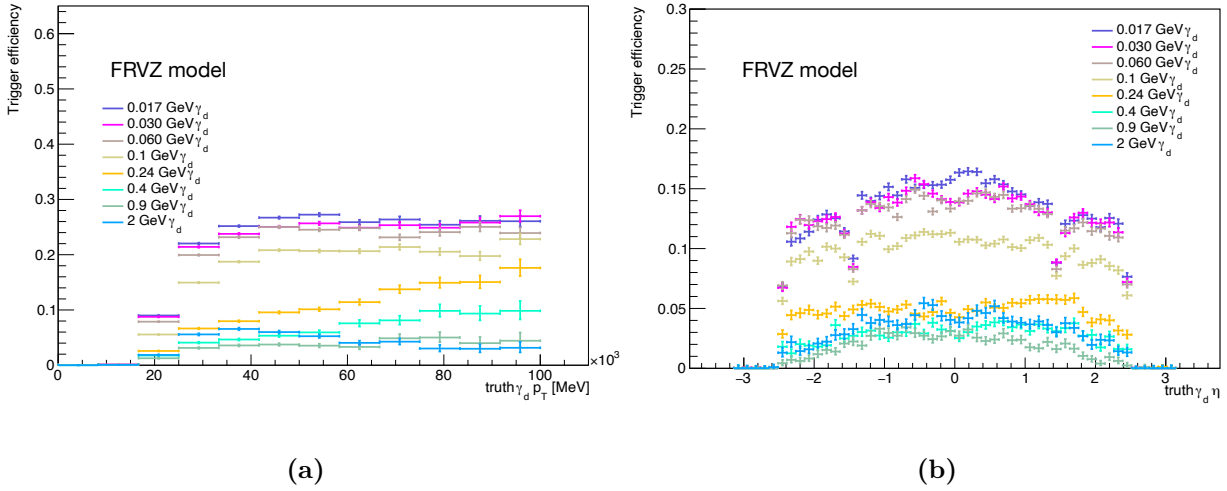


Figure 5.24. Di-electron trigger efficiencies for the FRVZ signal model, shown for different mass points and as a function of the leading $\gamma_d p_T$ (a) and η (b). Events are pre-selected requiring that both γ_d decay into a pair of electrons.

reconstructed as two electrons in the small η region rather than in the high η one.

5.5.3 Mixed channel triggers

The signature of the $\mu\text{LJ}-e\text{LJ}$ channel suggests to use di-muon triggers, single-electron triggers and mixed-flavour triggers, the latter requiring the reconstruction of both electron and muon objects at the online level. As for the $\mu\text{LJ}-\mu\text{LJ}$ channel, the efficiency of single muon triggers is negligible as a consequence of their associated high p_T thresholds or tight isolation requirements. The list of adopted triggers is reported in Tab. 5.8. The usage of the mixed flavour triggers allows to recover

Type	Data-taking periods	Trigger
Single-electron	2015	HLT_e24_lhmedium_L1EM20VH
		HLT_e60_lhmedium
		HLT_e120_lhloose
	2016 A-end	HLT_e26_lhtight_nod0_ivarloose
		HLT_e60_lhmedium_nod0
		HLT_e140_lhloose_nod0
Di-muon	2015	HLT_mu18_mu8noL1
	2015 - 2016 A	HLT_2mu10
	2016 A - E	HLT_mu20_mu8noL1
	2016 B - end - 2017 - 2018	HLT_2mu14
	2016 F - end - 2017 -2018	HLT_mu22_mu8noL1
Mixed flavour	2015	HLT_e7_lhmedium_mu24
	2015	HLT_e17_lhloose_mu14
	2016 A	HLT_e24_lhmedium_nod0_L1EM20VHI_mu8noL1
	2016 B-E	HLT_e7_lhmedium_nod0_mu24
	2016 F - end	HLT_e26_lhmedium_nod0_L1EM22VHI_mu8noL1
	2016 A - end - 2017 - 2018	HLT_e17_lhloose_nod0_mu14
	2017 - 2018	HLT_e26_lhmedium_nod0_mu8noL1

Table 5.8. List of single-electron, di-muon and di-lepton mixed flavour triggers used in the $e\text{LJ}-\mu\text{LJ}$ channel for the corresponding data-taking periods. For the meaning of the different suffixes the reader is referred to the caption of Tabs. 5.5, 5.6, 5.7.

sensitivities to electrons too soft to fire the single-electron triggers and to muons too collimated for firing the di-muon triggers, which are not able to seed multiple muons found within the same ROI of $\Delta\eta \times \Delta\phi = 0.2 \times 0.2$ (see Sec. 3.2.6).

Trigger matching

The trigger matching per trigger follows the same requirements as the one specified in the previous sections. If a di-lepton trigger is fired, both the HLT objects need to be trigger-matched to an offline reconstructed lepton.

Trigger efficiency

The mixed-flavour trigger efficiencies are shown in Fig. 5.25 as a function of the γ_d p_T (a) and η (b), for a γ_d produced in the FRVZ benchmark model. In order to

evaluate these efficiencies, the events have been pre-selected requiring that at the truth-level one γ_d decay into a pair of electrons and the other one into a pair of muons.

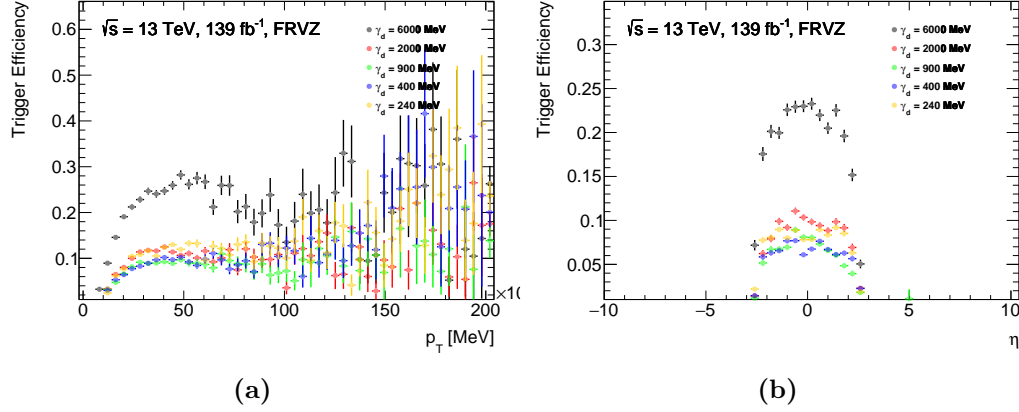


Figure 5.25. Mixed triggers efficiencies for the FRVZ signal model, shown for different mass points and as a function of the leading γ_d p_T (a) and η (b). Events are pre-selected requiring that one γ_d decay into a pair of electrons and the other one into a pair of muons.

5.5.4 Benchmark samples trigger efficiency

The resulting trigger acceptance for the different signal hypotheses foreseen by the two benchmark models exploited in this search are shown in Tab. 5.9 and Tab. 5.10 for respectively the FRVZ and the HAHM models. The trigger acceptance is defined as the ratio between the number of triggered events and the total number of MC generated ones.

Triggers	FRVZ $m_{\gamma_d} = 17$ MeV	FRVZ $m_{\gamma_d} = 30$ MeV	FRVZ $m_{\gamma_d} = 60$ MeV	FRVZ $m_{\gamma_d} = 0.1$ GeV	FRVZ $m_{\gamma_d} = 0.24$ GeV	FRVZ $m_{\gamma_d} = 0.4$ GeV	FRVZ $m_{\gamma_d} = 0.9$ GeV	FRVZ $m_{\gamma_d} = 2.0$ GeV	FRVZ $m_{\gamma_d} = 6.0$ GeV
Single-electron	18%	18%	16%	16%	12%	9.3%	6.4%	7.7%	22%
Di-electron	12%	11%	11%	8.4%	4.1%	2.5%	1.7%	3.0%	11%
Single- OR di-electron	24%	24%	23%	21%	14%	10%	7.4%	9.5%	26%
Di-muon	-	-	-	-	12%	13%	11%	8.8%	6.7%
3_MU6 OR 3_MU6_msonly	-	-	-	-	3.6%	4.0%	3.4%	1.8%	1.3%
Mixed flavour di-lepton	-	-	-	-	4.4%	3.3%	3.2%	4.8%	5.5%

Table 5.9. Efficiencies (in %) of the analysis triggers for each MC signal FRVZ process.

For $m_{\gamma_d} < 2m_\mu$ the muonic triggers and the mixed-flavour triggers are by construction not effective, as γ_d decays into muons are kinematically forbidden.

As expected, the trigger efficiencies are much larger for the HAHM model than for the FRVZ one, as a consequence of the larger average boost of the γ_d in the former model (see Sec. 5.2). It should be noted that, since no requirement is made on the γ_d decay mode, these efficiencies also depend on the $BR(\gamma_d \rightarrow l\bar{l})$ shown in Fig. 2.10, with l being the leptons into which the γ_d has decayed.

Triggers	HAHM $m_{\gamma_d} = 17 \text{ MeV}$	HAHM $m_{\gamma_d} = 0.1 \text{ GeV}$	HAHM $m_{\gamma_d} = 0.4 \text{ GeV}$	HAHM $m_{\gamma_d} = 2 \text{ GeV}$	HAHM $m_{\gamma_d} = 10 \text{ GeV}$	HAHM $m_{\gamma_d} = 15 \text{ GeV}$	HAHM $m_{\gamma_d} = 25 \text{ GeV}$	HAHM $m_{\gamma_d} = 40 \text{ GeV}$
Single-electron	58%	56%	34%	12%	67%	72%	73%	75%
Di-electron	52%	46%	18%	5%	56%	63%	66%	69%
Single- OR di-electron	70%	67%	39%	15%	74%	78%	80%	83%
Di-muon	-	-	34%	32%	31%	31%	30%	31%
3_MU6 OR 3_MU6_msonly	-	-	5.7%	6.3%	7.1%	7.1%	6.9%	6.7%
Mixed flavour di-lepton	-	-	10%	7.0%	15%	15%	16%	15%

Table 5.10. Efficiencies (in %) of the analysis triggers for each MC signal HAHM process.

For $m_{\gamma_d} < 2m_\mu$ the muonic and the mixed-flavour triggers are by construction not effective, as γ_d decays into muons are kinematically forbidden.

Chapter 6

ATLAS full Run-2 search for prompt Lepton-Jets

This chapter describes the strategy and the results of the search for prompt Lepton-Jets based on the dataset collected by the ATLAS experiment during the whole Run-2. Sec. 6.1 describes the selections aimed at retaining high signal yields while reducing the contributions of background processes. The procedures to estimate the residual backgrounds are outlined in Sec. 6.2. How systematic uncertainties are estimated and how they impact the result of the search is introduced in Sec. 6.3. Sec. 6.4 and Sec. 6.5 present the results of this search respectively for the electronic channel and for the mixed and the muonic ones. Finally, in Sec. 6.6 a comparison between this search and the one carried out during Run-1 by the ATLAS collaboration [81] is given.

6.1 Events selection

The following requirements are applied to each event:

- the event must be in the *Good Run List*, a set of runs where the ATLAS detector was known to be working in nominal conditions;
- the event must be accepted by the logical OR of the triggers mentioned in Sec. 5.5;
- the event must have at least one good Primary Vertex (see Sec. 4.1) (the vertex with the highest $\sum p_T^2$ and at least two tracks associated to it);
- at least two LJs must be reconstructed in the event.

As already said, if more than two LJs are identified in an event, the analysis is performed on the leading LJ and its farthest in $|\Delta\phi|$. As explained in Sec. 5.4, according to the type of the two LJs identified in the event, the analysis is categorized in the $\mu\text{LJ}-\mu\text{LJ}$, $e\text{LJ}-e\text{LJ}$ and $\mu\text{LJ}-e\text{LJ}$ search channels. Each channel is affected by different sources of backgrounds, that are here briefly outlined.

Pairs of mis-identified LJs can be found in SM events where two collimated pairs of muons or electrons are produced. One of the processes contributing to this background is the production of boosted light mesons pairs decaying into leptons (e.g. di- J/ψ events). Another contribution originates from events where virtual vector bosons (γ^*/Z^*) decay to leptons, leading to a non-resonant background.

Other contributions, arising from $V + \text{jets}$, $t\bar{t}$, single-top, di-boson and multi-jets events have also been considered. e LJs can be reconstructed in such processes, as an e LJ can consist of an electron (arising, for example, from a Z and a W decay) crossed by a random track. On the contrary, being reconstructed with two muons satisfying the quality criteria in Sec. 5.2, μ LJs are not expected to be found in these kinds of background processes, beside the (unlikely) scenario in which Z boson decays into extremely boosted muons. e LJs can also be produced in $\gamma + \text{jets}$ events, where the photon converts into a collimated electron-positron pair (see Sec. 4.4). Therefore, in order to suppress the background contributions that affect differently the three channels, the event selection has been separately optimised for the muonic (Sec. 6.1.1), the electronic (Sec. 6.1.2) and the mixed (Sec. 6.1.3) channel. These requirements define the three Signal Regions (SRs), the regions maximizing the signal sensitivity, described in the following.

The electronic channel SR is optimised for being sensitive to the region with low m_{γ_d} , while the mixed and the muonic channel SRs, being populated by construction only when $m_{\gamma_d} > 2m_\mu$, are designed in such a way to be sensitive to larger m_{γ_d} hypotheses.

6.1.1 Muonic channel

Events identified in the μ LJ- μ LJ channel are required to satisfy the following conditions:

- the event must fire the `3mu6(_msonly)` trigger if it belongs to the low p_T region (as defined in Sec. 5.5.1) or it must fire a di-muon trigger if it is identified in the high- p_T region;
- all the online HLT seeds, of at least one of the triggers fired in the event, must be matched to an offline reconstructed muon inside the μ LJ. The matching is performed according to Sec. 5.5.1, with the requirement that at least two matched muons belong to different μ LJs;
- the q_{LJ} of both μ LJs must be equal to zero.

These requirements were found to be sufficient to reduce to 0 the available statistics of the simulated MC samples representing the different SM background processes previously outlined. In the following, the effect of this selection on the signal MC samples is reported.

Signal yields

The event yields in the $\mu\text{LJ}-\mu\text{LJ}$ channel are shown in Tab. 6.1 and Tab. 6.2, for the FRVZ and the HAHM model, respectively.

m_{γ_d} [GeV]	0.24	0.4	0.9	2	6	10	15
None	33780 \pm 70	33780 \pm 70	33780 \pm 70	33140 \pm 110	34930 \pm 100	33780 \pm 70	33770 \pm 70
2 μLJ	876 \pm 10	1102 \pm 12	865 \pm 10	330 \pm 4	42.2 \pm 1.2	14.5 \pm 1.4	4.0 \pm 0.7
Triggers	508 \pm 8	670 \pm 9	523 \pm 8	248.2 \pm 3.3	40.0 \pm 1.2	13.9 \pm 1.3	4.0 \pm 0.7
Trigger Matching	346 \pm 6	456 \pm 7	358 \pm 7	183.9 \pm 2.9	34.4 \pm 1.1	13.7 \pm 1.3	3.7 \pm 0.7
$q_{\mu\text{LJ}} = 0$	346 \pm 6	456 \pm 7	358 \pm 7	183.9 \pm 2.9	34.4 \pm 1.1	13.7 \pm 1.3	3.0 \pm 0.6

Table 6.1. Signal (weighted) events yield after each selection applied in the $\mu\text{LJ}-\mu\text{LJ}$ channel. Events are generated according to the FRVZ model and are normalised assuming a branching ratio $B(H \rightarrow 2\gamma_d + X) = 0.5\%$, with $L = 140 \text{ fb}^{-1}$ and $\sigma = \sigma_{\text{ggF}}$.

The associated uncertainty per each event yield is evaluated as $\sqrt{\sum_i^{N_{\text{raw}}} w_i^2}$, with N_{raw} being the number of un-weighted MC events and w_i being the per event weight.

m_{γ_d} [GeV]	0.4	2	10	15	25
None	33780 \pm 70	33780 \pm 70	33770 \pm 70	33770 \pm 70	33780 \pm 70
2 μLJ	2239 \pm 17	1978 \pm 16	349 \pm 7	29.7 \pm 2.0	5.2 \pm 0.8
Triggers	1992 \pm 16	1785 \pm 15	344 \pm 7	29.4 \pm 2.0	5.2 \pm 0.8
Trigger Matching	1739 \pm 15	1561 \pm 14	335 \pm 7	28.9 \pm 1.9	5.0 \pm 0.8
$q_{\mu\text{LJ}} = 0$	1738 \pm 15	1561 \pm 14	335 \pm 7	28.9 \pm 1.9	5.0 \pm 0.8

Table 6.2. Signal (weighted) events yield after each selection applied in the $\mu\text{LJ}-\mu\text{LJ}$ channel. Events are generated according to the HAHM model and are normalised assuming a branching ratio $B(H \rightarrow 2\gamma_d) = 0.5\%$, with $L = 140 \text{ fb}^{-1}$ and $\sigma = \sigma_{\text{ggF}}$.

The associated uncertainty per each event yield is evaluated as $\sqrt{\sum_i^{N_{\text{raw}}} w_i^2}$, with N_{raw} being the number of un-weighted MC events and w_i being the per event weight.

Events are weighted and normalised as explained Sec. 3.2.7, with $L = 140 \text{ fb}^{-1}$, $\sigma_{pp \rightarrow 2\gamma_d(+X)} = \sigma_{\text{ggF}} \times BR(H \rightarrow 2\gamma_d(+X))$, with $BR(H \rightarrow 2\gamma_d(+X)) = 0.5\%$ (and σ_{ggF} as in Sec. 1.3.1). The associated uncertainty per each event yield is evaluated as $\sqrt{\sum_i^{N_{\text{raw}}} w_i^2}$, with N_{raw} being the number of un-weighted MC events and w_i being the per event weight. The number of residual events after the selection decreases for larger γ_d masses, since the γ_d are less boosted, this resulting in smaller trigger and LJs reconstruction efficiencies. The event yields are shown for each model up to the heaviest γ_d to which the selection is sensitive.

6.1.2 Electronic channel

Events identified in the $e\text{LJ}-e\text{LJ}$ channel are required to satisfy the following conditions:

- the event must fire any of the trigger specified in Sec. 5.5.2;

- all the online HLT seeds, of at least one of the triggers fired in the event, must be matched to an offline reconstructed electron inside the eLJ . The matching is performed according to Sec. 5.5.2, with the requirement that, if a di-electron trigger is fired, the two matched electrons must belong to different $eLJs$;
- the angular separation in the transverse plane between the two $eLJs$ must be $|\Delta\phi(eLJ, eLJ)| > 2.5$;
- the leading eLJ must have $|\eta| < 1.37$;
- the invariant mass of the eLJ pair must be outside the Z -mass window, i.e. $m_{eLJ} \notin [81, 101] \text{ GeV}$;
- the imbalance between the invariant masses of the $eLJs$ must satisfy $m_{eLJ}^{\text{imb}} < 0.8$;
- the q_{LJ} of both $eLJs$ must be zero;
- the $eLJs$ must be reconstructed with exactly one electron (and two tracks associated to it, as explained in Sec. 5.4);
- no jets with $p_T > 40 \text{ GeV}$ has to be reconstructed;
- the leading track of each eLJ must have $p_T > 5 \text{ GeV}$.

In the μLJ – μLJ channel, simply requiring $2\mu LJ$ to be reconstructed (other than trigger and trigger-matching requirements) reduces to a negligible level, within the MC statistics, the yields associated to the different sources of backgrounds previously outlined. The same is not true for the eLJ – eLJ channel, where additional criteria are needed to suppress such background events.

$eLJs$ can be reconstructed in $V + \text{jets}$ processes, with electrons produced by vector boson decays being crossed by random tracks. Such $eLJs$ are expected to be both less back-to-back and more in the forward, high $|\eta|$, region, with respect to signal-like ones (see Sec. 5.2). The distributions of these variables are shown in Fig. 6.1 for the SM background processes and for $eLJs$ produced by γ_d decays in the FRVZ benchmark model, where the γ_d has a mass of $m_{\gamma_d} = 0.1 \text{ GeV}$.

Even though the eLJ invariant mass has a poorer resolution with respect to the μLJ one, particularly for $eLJs$ comprised of only one electron, Fig. 6.2 (a) shows how the invariant mass of the di- eLJ system is a powerful variable in discriminating the $Z(\rightarrow ee) + \text{jets}$ background, where each electron produced by the Z decay is reconstructed as an eLJ , if it is crossed by a random track. In these events, the invariant mass of the di- eLJ system thus peaks around the Z mass.

$eLJs$ originating from γ_d decays are expected to have a small m^{imb} . A selection on the $eLJs$ m^{imb} therefore is discriminating against combinatorial SM backgrounds, which have a flat distribution of m^{imb} . The distribution of the $eLJs$ m^{imb} reconstructed from γ_d decays, where the γ_d is produced in the FRVZ benchmark model and has a mass of $m_{\gamma_d} = 0.1 \text{ GeV}$, is compared in Fig. 6.2 (b) to the distributions for $eLJs$ arising in different SM background processes.

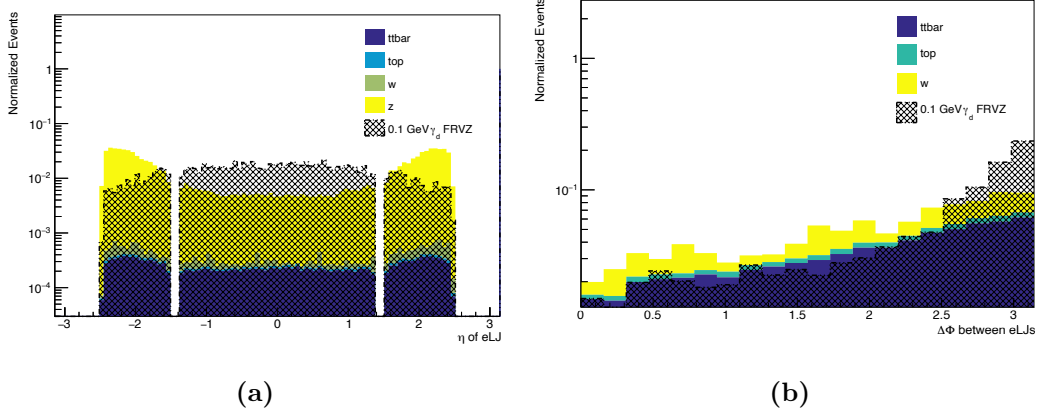


Figure 6.1. eLJ s $|\eta|$ distribution (a) and $|\Delta\phi|$ between two eLJ s (b) for signal MC events (dashed), where the eLJ s are reconstructed from a $m_{\gamma_d} = 0.1 \text{ GeV}$ γ_d produced in the FRVZ benchmark model, and background MC events (solid).

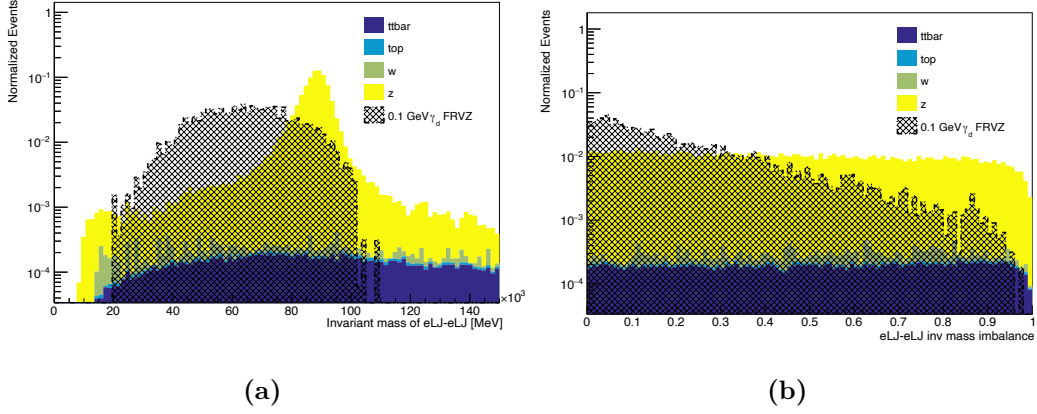


Figure 6.2. (a) invariant mass and (b) mass imbalance m^{imb} of the di- eLJ system for signal MC events (dashed), where the eLJ s are reconstructed from a $m_{\gamma_d} = 0.1 \text{ GeV}$ γ_d produced in the FRVZ benchmark model, and background MC events (solid).

eLJ s originating from neutral particle decays are expected to have zero sum of charge. A selection on the eLJ charge q_{LJ} therefore reduces combinatorial backgrounds from all SM background processes where one of the eLJ associated track is a random track. The distribution of the q_{LJ} for eLJ s reconstructed from γ_d decays, where the γ_d is produced in the FRVZ benchmark model and has a mass $m_{\gamma_d} = 0.1 \text{ GeV}$, is compared in Fig. 6.3 to the distributions for eLJ s arising in different SM background processes. An eLJ is reconstructed per each electron produced by the Z boson decay. To be reconstructed as an eLJ , the electron produced by the Z decay has a topo-cluster with an associated random track. This results into the q_{LJ} distribution having the two peaks at $q_{LJ} = \pm 2$.

Since the eLJ - eLJ channel is tailored to be sensitive to the lighter m_{γ_d} hypotheses, eLJ s are required to be reconstructed with only one electron. This requirement simplifies the background composition and it does not affect the signal efficiency in the

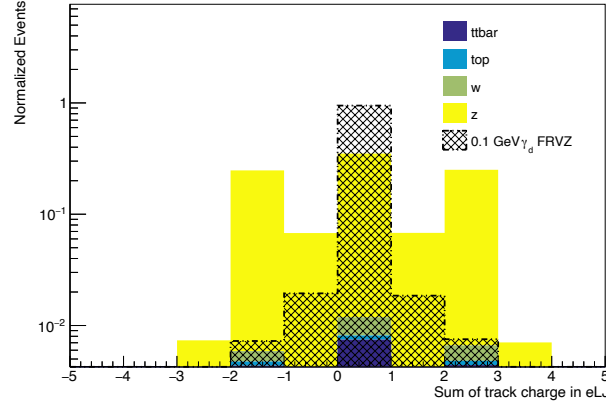


Figure 6.3. q_{LJ} of eLJs for signal MC events (dashed), where the eLJs are reconstructed from a $m_{\gamma_d} = 0.1 \text{ GeV}$ γ_d produced in the FRVZ benchmark model, and background MC events (solid).

desired mass range.

Finally, in order to suppress events where jets are mis-reconstructed as eLJs, high energy jets (with $p_T > 40 \text{ GeV}$) are vetoed. This selection efficiently reduces events associated to the $t\bar{t}$ background, as can be seen from Fig. 6.4.

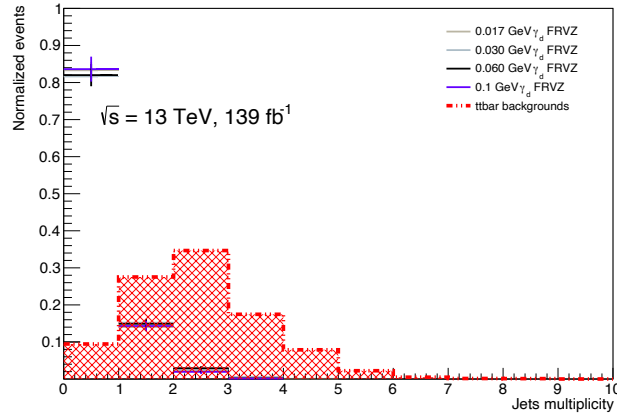


Figure 6.4. Jets with $p_T > 40 \text{ GeV}$ multiplicity for signal events with different m_{γ_d} hypotheses (solid lines), and background MC $t\bar{t}$ events (dashed).

Signal and SM MC background yields

The event yields in the eLJ-eLJ channel are shown in Tab. 6.3 and Tab. 6.4, for the FRVZ and the HAHM model, respectively.

As for the $\mu\text{LJ}-\mu\text{LJ}$ channel, events are weighted and normalised as explained Sec. 3.2.7, with $L = 140 \text{ fb}^{-1}$, $\sigma_{pp \rightarrow 2\gamma_d(+X)} = \sigma_{\text{ggF}} \times BR(H \rightarrow 2\gamma_d(+X))$, with

m_{γ_d} [GeV]	0.017	0.03	0.06	0.1	0.24	0.4	0.9	2	6
2 eLJ s	950 \pm 11	770 \pm 9.8	560 \pm 8.4	410 \pm 7.1	110 \pm 3.6	27 \pm 1.8	4.3 \pm 0.7	0.59 \pm 0.25	6.6 \pm 0.86
Trigger Matching	830 \pm 10	650 \pm 9	480 \pm 7.7	360 \pm 6.7	100 \pm 3.5	27 \pm 1.8	4.3 \pm 0.7	0.59 \pm 0.25	6.4 \pm 0.84
Leading track $p_T > 5$ GeV	830 \pm 10	650 \pm 9	480 \pm 7.7	360 \pm 6.7	100 \pm 3.5	27 \pm 1.8	4.3 \pm 0.7	0.59 \pm 0.25	6.4 \pm 0.84
$eLJ \eta < 1.37$	540 \pm 8.2	410 \pm 7.2	310 \pm 6.2	210 \pm 5.1	64 \pm 2.8	18 \pm 1.5	2.8 \pm 0.57	0.19 \pm 0.14	4.5 \pm 0.71
$ \Delta\Phi(eLJ, eLJ) > 2.5$	290 \pm 5.9	220 \pm 5.2	160 \pm 4.6	130 \pm 4	30 \pm 1.9	7.6 \pm 0.96	1.4 \pm 0.41	/	2.8 \pm 0.56
Z mass veto	230 \pm 5.3	180 \pm 4.7	130 \pm 4.1	100 \pm 3.5	23 \pm 1.7	4.9 \pm 0.76	1.1 \pm 0.36	/	1.7 \pm 0.43
$q_{eLJ} = 0$	230 \pm 5.3	180 \pm 4.7	130 \pm 4.1	100 \pm 3.5	23 \pm 1.7	4.9 \pm 0.76	1.1 \pm 0.36	/	1.7 \pm 0.43
No jet with $p_T > 40$ GeV	200 \pm 4.9	150 \pm 4.3	110 \pm 3.7	86 \pm 3.2	19 \pm 1.5	4.7 \pm 0.75	0.95 \pm 0.33	/	1.4 \pm 0.4
1 electron in eLJ	170 \pm 4.6	130 \pm 4	95 \pm 3.4	75 \pm 3	18 \pm 1.5	4.5 \pm 0.74	0.95 \pm 0.33	/	/
$ m_{eLJ}^{imb} < 0.8$	170 \pm 4.5	130 \pm 3.9	94 \pm 3.4	74 \pm 3	18 \pm 1.5	4.4 \pm 0.73	0.72 \pm 0.28	/	/

Table 6.3. Signal (weighted) events yield after each selection applied in the eLJ – eLJ channel. Events are generated according to the FRVZ model and are normalised assuming a branching ratio $B(H \rightarrow 2\gamma_d + X) = 0.5\%$, with $L = 140 \text{ fb}^{-1}$ and $\sigma = \sigma_{\text{ggF}}$.

The associated uncertainty per each event yield is evaluated as $\sqrt{\sum_i^{N_{\text{raw}}} w_i^2}$, with N_{raw} being the number of un-weighted MC events and w_i being the per event weight.

m_{γ_d} [GeV]	0.017	0.1	0.4	2	10	15	25
2 eLJ s	4200 \pm 23	1600 \pm 14	230 \pm 5.5	4.2 \pm 0.69	110 \pm 3.6	24 \pm 1.7	11 \pm 1.1
Trigger Matching	4100 \pm 23	1600 \pm 14	230 \pm 5.4	4.2 \pm 0.69	110 \pm 3.6	23 \pm 1.6	10 \pm 1.1
Leading track $p_T > 5$ GeV	4100 \pm 23	1600 \pm 14	230 \pm 5.4	4.2 \pm 0.69	110 \pm 3.6	23 \pm 1.6	10 \pm 1.1
$eLJ \eta < 1.37$	2700 \pm 19	840 \pm 10	140 \pm 4.2	2.9 \pm 0.57	65 \pm 2.8	10 \pm 1.1	3.7 \pm 0.64
$ \Delta\Phi(eLJ, eLJ) > 2.5$	1800 \pm 15	510 \pm 8	69 \pm 2.9	0.56 \pm 0.26	55 \pm 2.5	1.2 \pm 0.35	0.19 \pm 0.13
Z mass veto	1700 \pm 15	470 \pm 7.7	66 \pm 2.9	0.56 \pm 0.26	53 \pm 2.5	0.75 \pm 0.27	0.19 \pm 0.13
$q_{eLJ} = 0$	1700 \pm 15	470 \pm 7.7	66 \pm 2.9	0.56 \pm 0.26	53 \pm 2.5	0.67 \pm 0.26	0.19 \pm 0.13
No jet with $p_T > 40$ GeV	1400 \pm 13	380 \pm 7	54 \pm 2.5	0.56 \pm 0.26	49 \pm 2.4	0.47 \pm 0.22	0.12 \pm 0.12
1 electron in eLJ	1300 \pm 13	340 \pm 6.6	50 \pm 2.4	0.56 \pm 0.26	/	0.062 \pm 0.062	0.12 \pm 0.12
$ m_{eLJ}^{imb} < 0.8$	1300 \pm 13	340 \pm 6.6	50 \pm 2.4	0.56 \pm 0.26	/	0.062 \pm 0.062	0.12 \pm 0.12

Table 6.4. Signal (weighted) events yield after each selection applied in the eLJ – eLJ channel. Events are generated according to the HAHM model and are normalised assuming a branching ratio $B(H \rightarrow 2\gamma_d) = 0.5\%$, with $L = 140 \text{ fb}^{-1}$ and $\sigma = \sigma_{\text{ggF}}$.

The associated uncertainty per each event yield is evaluated as $\sqrt{\sum_i^{N_{\text{raw}}} w_i^2}$, with N_{raw} being the number of un-weighted MC events and w_i being the per event weight.

$BR(H \rightarrow 2\gamma_d(+X)) = 0.5\%$. The associated uncertainty per each event yield is evaluated as $\sqrt{\sum_i^{N_{\text{raw}}} w_i^2}$, with N_{raw} being the number of un-weighted MC events and w_i being the per event weight.

The number of residual events decreases for larger γ_d masses, since the γ_d are less boosted, this resulting in smaller trigger and 1-electron eLJ s reconstruction efficiencies.

The number of events selected in the eLJ – eLJ channel are shown in Tab. 6.5 for the $t\bar{t}$, single-top, Z + jets, W + jets and QCD multi-jet MC. Also in this case, events are normalised and weighted as explained in Sec. 3.2.7, with $L = 140 \text{ fb}^{-1}$ and their relative associated cross-section.

After the requirements previously described, the residual background is dominated by Z + jets events. All the other SM backgrounds that are not reported in this table have a negligible statistics after requiring two eLJ s to be reconstructed.

	$t\bar{t}$	single-top	Z +jets	W +jets	QCD multi-jet
2 e LJs	2600 ± 17	240 ± 5.8	130000 ± 780	1100 ± 100	1500 ± 1200
Trigger Matching	2600 ± 17	240 ± 5.8	130000 ± 770	1100 ± 93	1500 ± 1200
Leading track $p_T > 5$ GeV	2600 ± 17	240 ± 5.8	130000 ± 770	1100 ± 93	1500 ± 1200
e LJ $ \eta < 1.37$	690 ± 8.5	52 ± 2.6	13000 ± 240	140 ± 35	100 ± 43
$ \Delta\Phi(e\text{LJ}, e\text{LJ}) > 2.5$	250 ± 5.1	20 ± 1.7	10000 ± 230	38 ± 7.6	29 ± 4.9
Z mass veto	230 ± 4.9	18 ± 1.6	2000 ± 94	39 ± 7.5	29 ± 4.9
$q_{e\text{LJ}} = 0$	160 ± 4	12 ± 1.3	1300 ± 75	28 ± 6.9	21 ± 4.3
No jet with $pt > 40$ GeV	15 ± 1.3	2.2 ± 0.53	1100 ± 73	17 ± 6.3	5.5 ± 2.1
1 electron in e LJ	15 ± 1.3	2.2 ± 0.53	1100 ± 73	17 ± 6.3	5.5 ± 2.1
$ m_{e\text{LJ}}^{\text{imb}} < 0.8$	12 ± 1.1	1.8 ± 0.48	920 ± 66	16 ± 6.2	5.2 ± 2.1

Table 6.5. SM background (weighted) events yield after each selection applied in the $e\text{LJ}$ – $e\text{LJ}$ channel. Events are normalised to 140 fb^{-1} . The associated uncertainty per each event yield is evaluated as $\sqrt{\sum_i^{N_{\text{raw}}} w_i^2}$, with N_{raw} being the number of un-weighted MC events and w_i being the per event weight.

6.1.3 Mixed channel

Events identified in the μLJ – $e\text{LJ}$ channel are required to satisfy the following conditions:

- the event must fire any of the trigger specified in Sec. 5.5.3;
- all the online HLT seeds, of at least one of the triggers fired in the event, must be matched to an offline reconstructed muon/electron inside the $\mu\text{LJ}/e\text{LJ}$. The matching is performed according to Sec. 5.5.3;
- the angular separation in the transverse plane between the $e\text{LJ}$ and the μLJ must be $|\Delta\phi(e\text{LJ}, \mu\text{LJ})| > 2$;
- the $e\text{LJ}$ must have $|\eta| < 1.37$;
- the q_{LJ} of both the μLJ and the $e\text{LJ}$ must be equal to zero;
- the $e\text{LJ } p_T^{\text{imb}}$ (see Sec. 5.4.3) must be $p_{T,e\text{LJ}}^{\text{imb}} < 0.8$;
- the $e\text{LJ}$ leading track must have $p_T > 5$ GeV.

The requirements on the $\Delta\phi(e\text{LJ}, \mu\text{LJ})$ and on the $e\text{LJ } |\eta|$ suppress all the SM backgrounds as explained in Sec. 6.1.2. The Z -mass window is here not vetoed, differently from the $e\text{LJ}$ – $e\text{LJ}$ channel, as LJs of different type cannot be produced in such a background process.

The requirement on the m^{imb} used in the electronic channel to reduce the combinatorial background is here not applied, since the very different invariant mass resolution for $e\text{LJs}$ and the μLJs result in mass-unbalanced LJs in this channel. Such a requirement would thus reduce too much the signal yields.

The $e\text{LJ } p_T^{\text{imb}}$ is instead a powerful variable in suppressing the combinatorial backgrounds without reducing too much the signal acceptance, as signal $e\text{LJs}$ are expected to be more balanced in p_T than background ones. The distribution of the

eLJ s p_T^{imb} reconstructed from γ_d decays, where the γ_d is produced in the FRVZ benchmark model and has a mass $m_{\gamma_d} = 0.1 \text{ GeV}$, is compared in Fig. 6.5 to the distributions for eLJ s arising in different SM background processes.

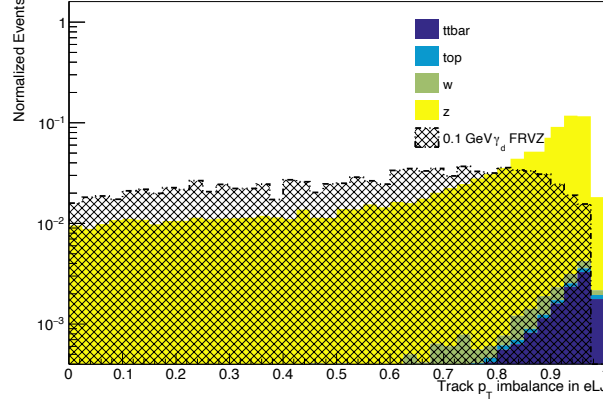


Figure 6.5. eLJ p_T^{imb} for signal MC events (dashed), where the eLJ s are reconstructed from a $m_{\gamma_d} = 0.1 \text{ GeV}$ γ_d produced in the FRVZ benchmark model, and background MC events (solid).

As can be seen from this plot, eLJ s produced in events associated to different SM background processes have a larger p_T^{imb} than signal eLJ s, and this is particularly evident for the $Z + \text{jets}$ background.

These requirements were found to be sufficient to reduce to zero the available statistics of the simulated MC samples representing the different SM background processes previously outlined. In the following, the effect of this selection on the signal MC samples is reported.

Signal yields

The number of events selected in the μLJ – eLJ channel are shown in Tab. 6.6 and Tab. 6.7, for the FRVZ and the HAHM model, respectively.

As for the other channels, events are weighted and normalised as explained Sec. 3.2.7, with $L = 140 \text{ fb}^{-1}$, $\sigma_{pp \rightarrow 2\gamma_d(+X)} = \sigma_{\text{ggF}} \times BR(H \rightarrow 2\gamma_d(+X))$, with $BR(H \rightarrow 2\gamma_d(+X)) = 0.5\%$. The associated uncertainty per each event yield is evaluated as $\sqrt{\sum_i^{N_{\text{raw}}} w_i^2}$, with N_{raw} being the number of un-weighted MC events and w_i being the per event weight.

Differently from the other two search channels, the number of residual events after the selection decreases as a function of m_{γ_d} for $m_{\gamma_d} \leq 2 \text{ GeV}$, it increases for $2 \text{ GeV} < m_{\gamma_d} \leq 6 \text{ GeV}$ and $2 \text{ GeV} < m_{\gamma_d} \leq 10 \text{ GeV}$ respectively for the FRVZ and HAHM model, and then it decreases again. This is due to the collimation of the electrons inside the eLJ s: the loss in efficiency at the 2 GeV mass point is due to the fact that truth electrons are not enough collimated to be reconstructed as a single electron, but they are sufficiently collimated to fall within the isolation

m_{γ_d} [GeV]	0.24	0.4	0.9	2	6	10
None	33790 \pm 70	33790 \pm 70	33790 \pm 70	33790 \pm 70	33790 \pm 70	33780 \pm 70
Triggers	4421 \pm 24	4115 \pm 23	3508 \pm 21	4538 \pm 24	4968 \pm 25	3735b \pm 29
1 μ LJ, 1 e LJ	388 \pm 7	247 \pm 5	83.4 \pm 3.2	33.1 \pm 2.0	71.1 \pm 2.9	18.4 \pm 1.5
Trigger Matching	365 \pm 7	237 \pm 5	80.2 \pm 3.1	32.4 \pm 2.0	69.8 \pm 2.9	18.0 \pm 1.5
e LJ leading track $p_T > 5$ GeV	363 \pm 7	234 \pm 5	79.5 \pm 3.1	31.5 \pm 2.0	68.9 \pm 2.8	10.2 \pm 1.1
e LJ $ \eta < 1.37$	250 \pm 6	167 \pm 5	61.3 \pm 2.7	20.3 \pm 1.6	51.4 \pm 2.5	1.4 \pm 0.4
$ \Delta\phi(\mu\text{LJ}, e\text{LJ}) > 2$	175 \pm 5	108 \pm 4	35.4 \pm 2.1	10.0 \pm 1.1	36.9 \pm 2.1	1.4 \pm 0.4
$q_{\mu\text{LJ}} = 0$	175 \pm 5	108 \pm 4	35.4 \pm 2.1	10.0 \pm 1.1	36.9 \pm 2.1	0.82 \pm 0.29
$q_{e\text{LJ}} = 0$	170 \pm 5	107 \pm 4	34.1 \pm 2.1	8.8 \pm 1.0	35.0 \pm 2.0	0.35 \pm 0.18
$ p_{T,e\text{LJ}}^{\text{imb}} < 0.8$	132 \pm 4	79.3 \pm 3.1	27.5 \pm 1.9	5.4 \pm 0.8	33.2 \pm 2.0	0.35 \pm 0.18

Table 6.6. Signal (weighted) events yield after each selection applied in the μLJ – $e\text{LJ}$ channel. Events are generated according to the FRVZ model and are normalised assuming a branching ratio $B(H \rightarrow 2\gamma_d + X) = 0.5\%$, with $L = 140 \text{ fb}^{-1}$ and $\sigma = \sigma_{\text{ggF}}$.

The associated uncertainty per each event yield is evaluated as $\sqrt{\sum_i^{N_{\text{raw}}} w_i^2}$, with N_{raw} being the number of un-weighted MC events and w_i being the per event weight.

m_{γ_d} [GeV]	0.4	2	10	15
None	33780 \pm 70	33780 \pm 70	33760 \pm 70	33760 \pm 70
Triggers	12660 \pm 40	9857 \pm 35	15010 \pm 40	15960 \pm 50
1 μ LJ, 1 e LJ	1240 \pm 12	150 \pm 4	371 \pm 7	38.6 \pm 2.2
Trigger Matching	1231 \pm 12	148 \pm 4	370 \pm 7	38.6 \pm 2.2
e LJ leading track $p_T > 5$ GeV	1227 \pm 12	147 \pm 4	367 \pm 7	25.4 \pm 1.8
e LJ $ \eta < 1.37$	884 \pm 11	108 \pm 4	269 \pm 6	3.2 \pm 0.8
$ \Delta\phi(\mu\text{LJ}, e\text{LJ}) > 2$	681 \pm 9	62.5 \pm 2.7	234 \pm 5	3.2 \pm 0.8
$q_{\mu\text{LJ}} = 0$	681 \pm 9	62.5 \pm 2.7	234 \pm 5	2.2 \pm 0.7
$q_{e\text{LJ}} = 0$	663 \pm 9	58.1 \pm 2.6	227 \pm 5	0.46 \pm 0.23
$ p_{T,e\text{LJ}}^{\text{imb}} < 0.8$	547 \pm 8	42.5 \pm 2.2	220 \pm 5	0.46 \pm 0.23

Table 6.7. Signal (weighted) events yield after each selection applied in the μLJ – $e\text{LJ}$ channel. Events are generated according to the HAHM model and are normalised assuming a branching ratio $B(H \rightarrow 2\gamma_d) = 0.5\%$, with $L = 140 \text{ fb}^{-1}$ and $\sigma = \sigma_{\text{ggF}}$.

The associated uncertainty per each event yield is evaluated as $\sqrt{\sum_i^{N_{\text{raw}}} w_i^2}$, with N_{raw} being the number of un-weighted MC events and w_i being the per event weight.

cone of the other, so that isolation requirements are failed, this resulting in a worse $e\text{LJ}$ reconstruction efficiency.

As for the other channel, the event yields are shown for each model up to the heavier γ_d to which the selection is sensitive.

6.2 Background estimation

In the μLJ – μLJ and μLJ – $e\text{LJ}$ analysis channels, the residual SM background contributions after the requirements detailed in Sec. 6.1.1 and Sec. 6.1.3 are the ones arising from decays of virtual vector bosons, mimicking both μLJs and $e\text{LJs}$, and low-mass resonances decaying into muon pairs, mimicking μLJs .

In the $e\text{LJ}$ – $e\text{LJ}$ channel, instead, after the selection criteria outlined in Sec. 6.1.2,

background events are mainly composed of $Z + \text{jets}$ events, where the electrons produced by the Z boson decay that are randomly crossed by an ID track are reconstructed as $e\text{LJs}$.

However, since there are no MC simulations reproducing these background processes in the phase space investigated, the background estimation cannot rely on such MC simulations. Therefore, the background estimation for all the three channels is fully data-driven. These channels exploit however two different background estimation techniques.

Thanks to the very good resolution of the μLJ invariant mass, both the $\mu\text{LJ}-\mu\text{LJ}$ and the $\mu\text{LJ}-e\text{LJ}$ channels rely on the so-called *bump-hunt* method, where it is looked for local excesses (*bumps*) compatible with the γ_d mass in the μLJs invariant mass spectrum in data.

As a consequence of the poorer resolution of the $e\text{LJ}$ invariant mass, the $e\text{LJ}-e\text{LJ}$ channel exploits instead the so-called *ABCD* based likelihood method [152], where the background is divided into 4 sub-regions (A , B , C and D) via the usage of two uncorrelated variables and the background contribution in A , where the majority of the signal is expected, can be extrapolated from the other regions.

In Sec. 6.2.1, the background estimation for the $\mu\text{LJ}-\mu\text{LJ}$ and the $\mu\text{LJ}-e\text{LJ}$ channels via the *bump-hunt* technique is outlined. In Sec. 6.2.2 the background estimation for the $e\text{LJ}-e\text{LJ}$ channel via the *ABCD* method is described.

6.2.1 Bump-hunt for muonic Lepton-Jets

The two analysis channels foreseeing the reconstruction of μLJs , the muonic and the mixed channel, rely on an un-binned likelihood fit on the μLJs invariant mass spectrum, where it is looked for *bumps*, i.e. localised excesses, compatible with different γ_d mass hypotheses. A schematic picture of the bump-hunt technique is given in Fig. 6.6. One of the advantages of this method is that is less model dependent than the *ABCD* one, which is usually used for this kind of searches [79, 78, 81]. Furthermore, since a shape fit is exploited, additional information regarding such a shape are used, thus yielding a better sensitivity.

Given the background sources contributing to these channels, as outlined in the previous section, the background invariant mass spectrum is expected to be comprised of an exponentially decreasing component, related to the combinatorial non-resonant background due to decays of off-shell vector bosons, and a resonant component, due to boosted low mass resonances decaying into collimated muon pairs. The most general background template is therefore described by the sum of two exponentials for the non-resonant background (to account for potentially different exponential slopes at large and small invariant masses), with Gaussians parameterising the resonances (such as the J/ψ , the $\phi(1020)$ and $\psi(2S)$). Such background template is hence described by the Probability Density Function (PDF)

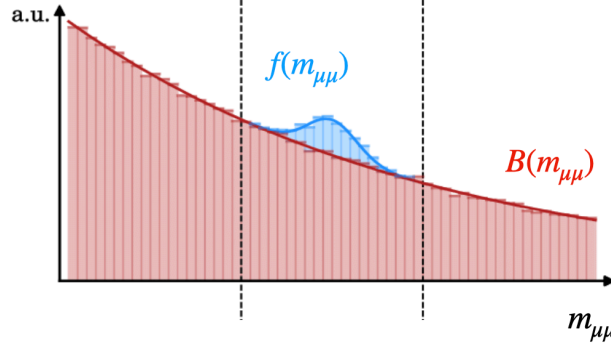


Figure 6.6. Schematic picture of the bump-hunt technique. The red distribution is the background one, in this case described by the PDF $B(m_{\mu\mu})$ in Eq. 6.1, extracted from a CR (see the following sections) and whose normalisation is instead extracted from data. The blue distribution is instead the signal one, whose PDF is the one in Eq. 6.2 and whose normalisation is parameterised via Eq. 6.4 and Eq. 6.6 for respectively the $\mu\text{LJ}-\mu\text{LJ}$ and the $e\text{LJ}-\mu\text{LJ}$ channels.

$B(m_{\mu\mu})$:

$$B(m_{\mu\mu}) = \left(1 - f_{\text{exp}} - f_{\text{J}/\psi} - f_{\phi(1020)} - f_{\psi(2S)}\right) e^{-m_{\mu\mu}/\tau_2} + f_{\text{exp}} e^{-m_{\mu\mu}/\tau} + f_{\text{J}/\psi} e^{-\left(\frac{m_{\mu\mu} - \mu_{\text{J}/\psi}}{\sigma_{\text{J}/\psi}}\right)^2} + f_{\psi(2S)} e^{-\left(\frac{m_{\mu\mu} - \mu_{\psi(2S)}}{\sigma_{\psi(2S)}}\right)^2} + f_{\phi(1020)} e^{-\left(\frac{m_{\mu\mu} - \mu_{\phi(1020)}}{\sigma_{\phi(1020)}}\right)^2}, \quad (6.1)$$

where f_i , with $i = \text{exp}, \text{J}/\psi, \phi(1020), \psi(2S)$, is the fraction of events associated to the i -th background process, with respect to the total number of background events; τ and τ_2 are the arguments of the two exponentials and μ_{res} and σ_{res} , with $\text{res} = \text{J}/\psi, \phi(1020), \psi(2S)$, are respectively the mean and standard deviation of the gaussians describing the resonances shape. The parameter μ_ϕ is fixed to 1.02 GeV, σ_ϕ to 0.02 GeV and σ_ψ is set to 0.05 GeV, as taken from [153], while m_Ψ , $m_{\text{J}\Psi}$ and $\sigma_{\text{J}/\psi}$ are free to float.

Such background modelling is tested in two orthogonal CRs, one defined for the muonic channel and one for the mixed channel. The fitted parameters extracted from such CRs are not expected to be equal to the ones extracted in the relative SRs, since differences in such regions could impact, for example, the p_T profile of the μLJ , potentially modifying the μLJ s invariant mass spectrum. These CRs are thus only exploited to check whether the functional form used to model the background is flexible enough to describe the μLJ invariant mass in different regions.

The normalisation of the background template is extracted, after *unblinding* (see Sec. 3.2.7), from the SRs described in Sec. 6.1.1 and Sec. 6.1.3.

A modelling of the expected signal μLJ s invariant mass spectrum is needed as well, both in terms of its functional form, in the following referred to as *shape-modelling*, and overall normalisation, referred to as *acceptance \times efficiency modelling*. Such a modelling is needed in order to test different m_{γ_d} hypotheses with

respect to the ones that were assumed in the MC samples generation. The definition of the CRs and the evaluation of the signal shape and acceptance \times efficiency modelling for both the muonic and the mixed channel are described in the last part of this section.

Control Region for the muonic channel

In order to test the flexibility of the background functional form in Eq. 6.1, a dedicated CR has been defined in the $\mu\text{LJ}-\mu\text{LJ}$ channel.

This CR is built in such a way to be as close as possible to the $\mu\text{LJ}-\mu\text{LJ}$ SR. In this way, if the functional form in Eq. 6.1 describes the μLJ invariant mass spectrum in the $\mu\text{LJ}-\mu\text{LJ}$ CR, the same is expected to be true in the $\mu\text{LJ}-\mu\text{LJ}$ SR.

It is required for exactly one μLJ and an additional pair of open muons to be reconstructed. These additional muons must satisfy the same requirements that muons in μLJs satisfy, so to have a CR which is as similar as possible to the SR.

The triggers that the events must fire are the ones listed in Sec. 5.5.1, and a similar trigger matching scheme is asked as well, requiring that at least one muon from the μLJ and one of the two additional muons must be matched to an HLT object.

The presence of $e\text{LJs}$ is vetoed, ensuring orthogonality with the $\mu\text{LJ}-e\text{LJ}$ channel SR. In addition, the presence of electrons satisfying the same requirements of the electrons in $e\text{LJs}$ is vetoed.

With these requirements, the signal events populating this CR are only the ones where both γ_d decay into muons that are too far apart to be reconstructed as a μLJ . Muons coming from heavier γ_d are less collimated, and therefore they are not reconstructed as μLJs . To avoid signal contamination for larger m_{γ_d} hypotheses, a minimum angular separation between the two additional muons $\Delta R_{\mu\mu}$ is asked ($\Delta R_{\mu\mu} \geq 1.8$).

For the heaviest m_{γ_d} hypotheses the signal leakage is still non-negligible, as can be seen in Fig. 6.7. For this reason, a large m^{imb} is imposed ($|m^{\text{imb}}| > 0.2$), as the μLJ and the additional μ -pair are coming from the same γ_d and therefore they should be balanced in mass. This requirement is not effective in reducing the signal leakage of the larger mass hypotheses of the FRVZ benchmark model (Fig. 6.8 (a)). In such a scenario, the two γ_d produced in the event are less back to back (see Sec. 5.2) and muons coming from different γ_d may be picked-up by the same μLJ (μ -pair). μLJs built in such a way have an invariant mass different from m_{γ_d} , as clear from Fig. 6.8 (b), (c).

In the HAHM model, however, the larger boost of the DPs implies that they are more often back to back, so that, even for heavy γ_d hypothesis, the probability of reconstructing μLJs with muons arising from different γ_d is negligible. This notwithstanding, a requirement on the opening angle between the μLJ and the additional μ -pair ($|\Delta\phi_{\mu\text{LJ}-\mu\mu}| > 2.8$) is imposed to reduce the signal leakage of the heavier γ_d hypotheses in the FRVZ benchmark model.

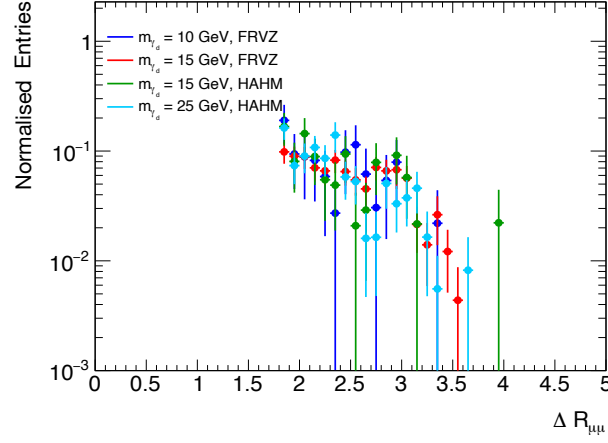


Figure 6.7. Opening angle between additional μ -pair with $\Delta R_{\mu\mu} > 1.8$, for different m_{γ_d} hypotheses in both the HAHM and FRVZ benchmark models.

Finally, the charge of the μ LJ is required to be 0. After all these requirements, a negligible signal leakage is obtained for both benchmark models and for all hypothesised m_{γ_d} .

Details on the expected number of events are given in Tab. 6.8 and Tab. 6.9 for respectively the FRVZ and the HAHM models.

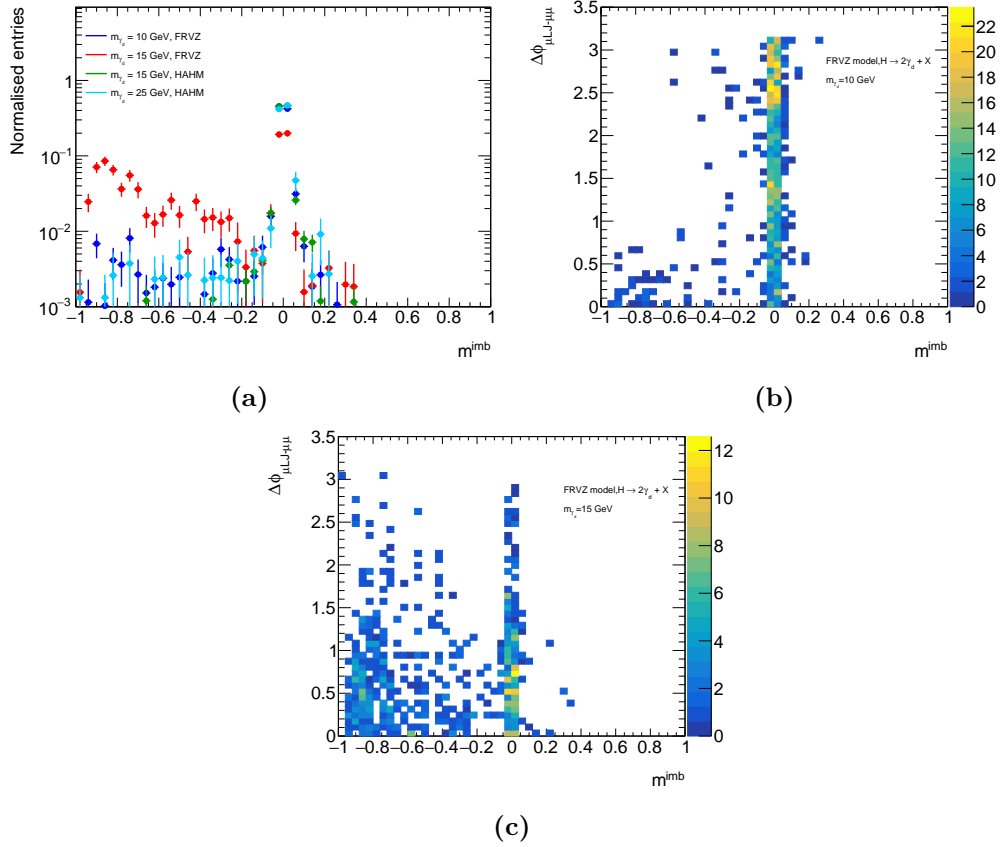


Figure 6.8. (a) m^{imb} between the additional μ -pair and the μLJ for different m_{γ_d} hypotheses in both the HAHM and FRVZ benchmark models; (b) m^{imb} as a function of the opening angle $\Delta\phi_{\mu\text{LJ}-\mu}$ for $m_{\gamma_d} = 10$ GeV in the FRVZ benchmark model; (c) m^{imb} as a function of the opening angle $\Delta\phi_{\mu\text{LJ}-\mu}$ for $m_{\gamma_d} = 15$ GeV in the FRVZ benchmark model. The events included in the plot are the ones after the cut on $\Delta R_{\mu\mu}$.

m_{γ_d} [GeV]	0.24	0.4	0.9	2	6	10	15
None	33780 \pm 70	33780 \pm 70	33780 \pm 70	33140 \pm 110	34930 \pm 100	33780 \pm 70	33770 \pm 70
$1\mu\text{LJ} + 0e\text{LJ}$	7738 \pm 31	8948 \pm 34	8317 \pm 33	5584 \pm 27	2157 \pm 15	1253 \pm 13	375 \pm 7
Triggers	497 \pm 8	655 \pm 9	652 \pm 9	333 \pm 4	227.3 \pm 3.5	322 \pm 6	151 \pm 4
Trigger Matching	58.5 \pm 2.7	198 \pm 5	281 \pm 6	151.5 \pm 2.6	137.2 \pm 2.4	243 \pm 6	117 \pm 4
Electron veto	58.1 \pm 2.7	196 \pm 5	280 \pm 6	150.8 \pm 2.6	136.1 \pm 2.3	241 \pm 6	117 \pm 4
2 signal muons	0.25 \pm 0.18	0.27 \pm 0.16	0.30 \pm 0.18	0.26 \pm 0.11	55.8 \pm 1.4	119 \pm 4	65.5 \pm 2.8
$\Delta R_{\mu\mu} > 1.8$	0.25 \pm 0.18	0.19 \pm 0.14	0.13 \pm 0.13	0.11 \pm 0.06	0.06 \pm 0.04	3.9 \pm 0.7	24.0 \pm 1.6
$ m^{\text{imb}} > 0.2$	0.25 \pm 0.18	0.19 \pm 0.14	0.13 \pm 0.13	0.11 \pm 0.06	0.06 \pm 0.04	2.8 \pm 0.6	19.6 \pm 1.5
$ \Delta\phi_{\mu\text{LJ}-\mu} > 2.8$	0.13 \pm 0.13	/	0.13 \pm 0.13	0.04 \pm 0.04	0.027 \pm 0.027	0.08 \pm 0.08	/
$q_{\mu\text{LJ}} = 0$	/	/	0.13 \pm 0.13	/	0.027 \pm 0.027	/	/

Table 6.8. Signal (weighted) events remaining after each selection applied in the CR of the $\mu\text{LJ}-\mu\text{LJ}$ channel. Events are generated according to the FRVZ model and are normalised assuming a branching ratio $B(H \rightarrow 2\gamma_d + X) = 0.5\%$, with $L = 140 \text{ fb}^{-1}$ and $\sigma = \sigma_{\text{ggF}}$. The associated uncertainty per each event yield is evaluated as $\sqrt{\sum_i N_{\text{raw}} w_i^2}$, with N_{raw} being the number of un-weighted MC events and w_i being the per event weight.

m_{γ_d} [GeV]	0.4	2	10	15	25
None	33780 \pm 70	33780 \pm 70	33770 \pm 70	33770 \pm 70	33780 \pm 70
1 μ LJ + 0 e LJ	10770 \pm 40	11550 \pm 40	5391 \pm 26	1648 \pm 15	338 \pm 7
Trigger	906 \pm 11	995 \pm 11	1277 \pm 13	480 \pm 8	107 \pm 4
Trigger Matching	313 \pm 6	430 \pm 7	1028 \pm 11	410 \pm 7	87.5 \pm 3.4
Electron veto	313 \pm 6	429 \pm 7	1022 \pm 11	408 \pm 7	87.0 \pm 3.3
2 signal muons	0.34 \pm 0.20	0.62 \pm 0.26	573 \pm 8	250 \pm 6	50.5 \pm 2.5
$\Delta R_{\mu\mu} > 1.8$	0.23 \pm 0.16	0.35 \pm 0.20	0.89 \pm 0.30	5.8 \pm 0.8	14.4 \pm 1.3
$ m^{\text{imb}} > 0.2$	0.23 \pm 0.16	0.35 \pm 0.20	0.58 \pm 0.24	0.23 \pm 0.16	0.33 \pm 0.17
$ \Delta\phi_{\mu\text{LJ}-\mu\mu} > 2.8$	0.13 \pm 0.13	0.25 \pm 0.18	0.48 \pm 0.22	0.10 \pm 0.10	/
$q_{\mu\text{LJ}} = 0$	/	/	/	0.10 \pm 0.10	/

Table 6.9. Signal (weighted) events remaining after each selection applied in the CR of the $\mu\text{LJ}-\mu\text{LJ}$ channel. Events are generated according to the HAHM model and are normalised assuming a branching ratio $B(H \rightarrow 2\gamma_d) = 0.5\%$, with $L = 140 \text{ fb}^{-1}$ and $\sigma = \sigma_{\text{ggF}}$. The associated uncertainty per each event yield is evaluated as $\sqrt{\sum_i^{N_{\text{raw}}} w_i^2}$, with N_{raw} being the number of un-weighted MC events and w_i being the per event weight.

Since requiring only the two additional muons pair to be open effectively suppresses the signal leakage for both the HAHM and the FRVZ model for $m_{\gamma_d} < 6 \text{ GeV}$, the region with 1 μLJ , no $e\text{LJ}$ and two additional open muons is used, with a cut on the μLJ mass ($m_{\mu\text{LJ}} < 5 \text{ GeV}$), as Validation Region (VR). A summary of the requirements used to define the SR, the CR and the VR is reported in Tab. 6.10.

Fig. 6.9 shows the distribution of the invariant mass of the μLJ in the $\mu\text{LJ}-\mu\text{LJ}$ CR in data, obtained by processing the full Run-2 dataset, with the $B(m_{\mu\mu})$ fitted (via an un-binned likelihood fit) PDF (see Eq. 6.1) overlaid on such a spectrum.

The fitted parameters values are shown in Tab. 6.11. The reduced chi-square of

	SR	CR	VR
requirement	2 μLJ	1 μLJ + 2 μ ($\Delta R > 1.8$)	1 μLJ + 2 μ ($\Delta R > 1.8$)
veto	/	electrons, $e\text{LJ}$	electrons, $e\text{LJ}$
HLT matching	two muons from two μLJ	one muon from μLJ and one additional μ	one muon from μLJ and one additional μ
m^{imb}	/	> 0.2	
$m_{\mu\text{LJ}}^{\text{cut}}$	/	/	$< 5 \text{ GeV}$

Table 6.10. Breakdown of the selections applied in the definition of the $\mu\text{LJ}-\mu\text{LJ}$ SR and the corresponding CR and VR.

the fit performed is $\tilde{\chi}_\nu^2 = 0.64^1$.

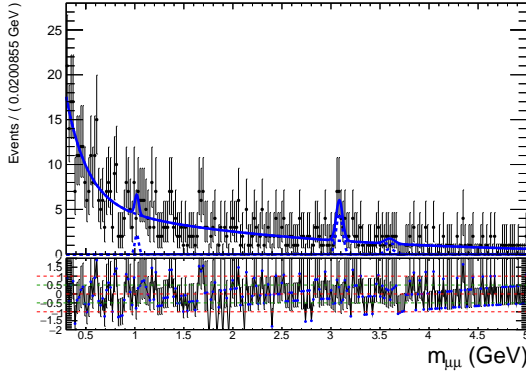


Figure 6.9. Fitted background PDF describing the background distribution in the μLJ mass spectrum (blue line) overlaid to the data points (black dots) in the $\mu\text{LJ}-\mu\text{LJ}$ channel CR.

The $B(m_{\mu\mu})$ PDF is fitted on the VR defined in Tab. 6.10 as well, as shown in Fig. 6.10, whilst the fitted parameters values are shown in Tab. 6.12. The reduced chi-square of the fit performed is $\tilde{\chi}_\nu^2 = 0.50^2$.

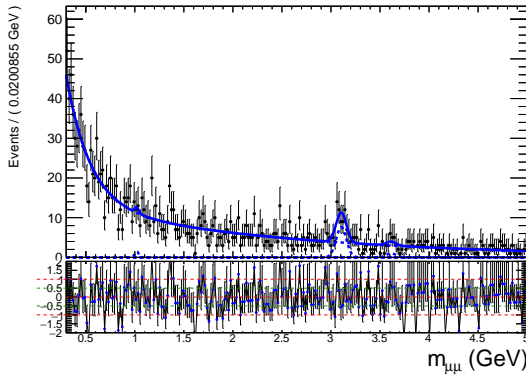


Figure 6.10. Fitted background PDF describing the background distribution in the μLJ mass spectrum (blue line) overlaid to the data points (black dots) in the $\mu\text{LJ}-\mu\text{LJ}$ channel VR.

By comparing the fitted parameters in Tab. 6.11 and Tab. 6.12 it can be seen how the additional requirements on μLJ s asked in the CR do not induce any sizeable difference in the μLJ invariant mass spectrum.

Parameter	Fitted value
f_{exp}	0.88 ± 0.05
$f_{\text{J}/\psi}$	0.032 ± 0.009
$f_{\psi(2S)}$	0.006 ± 0.005
$f_{\phi(1020)}$	0.008 ± 0.008
$\mu_{\text{J}/\psi}$	$(3.086 \pm 0.014) \text{ GeV}$
$\sigma_{\text{J}/\psi}$	$(0.033 \pm 0.013) \text{ GeV}$
$\mu_{\psi(2S)}$	$(3.61 \pm 0.05) \text{ GeV}$
τ	$(0.22 \pm 0.07) \text{ GeV}$
τ_2	$(2.09 \pm 0.28) \text{ GeV}$

Table 6.11. Fitted parameters of $B(m_{\mu\mu})$ PDF (see Eq. 6.1) with their relative uncertainty.

Parameter	Fitted value
f_{exp}	0.817 ± 0.025
$f_{\text{J}/\psi}$	0.031 ± 0.009
$f_{\psi(2S)}$	0.004 ± 0.003
$f_{\phi(1020)}$	0.002 ± 0.004
$\mu_{\text{J}/\psi}$	$(3.105 \pm 0.012) \text{ GeV}$
$\sigma_{\text{J}/\psi}$	$(0.052 \pm 0.016) \text{ GeV}$
$\mu_{\psi(2S)}$	$(3.61 \pm 0.05) \text{ GeV}$
τ	$(0.24 \pm 0.04) \text{ GeV}$
τ_2	$(2.22 \pm 0.20) \text{ GeV}$

Table 6.12. Fitted parameters of $B(m_{\mu\mu})$ PDF (see Eq. 6.1) with their relative uncertainty.

¹Such a chi-square is obtained by binning the distribution according to the binning specified by the y-axis of the plot in Fig. 6.9

²Such a chi-square is obtained by binning the distribution according to the binning specified by the y-axis of the plot in Fig. 6.10

Nonetheless, since the SR μLJ spectrum could be potentially different in terms of fitted parameters with respect to the CR ones, the background template needs only to be flexible enough to be able to describe the SR spectrum as well. In order to assess an uncertainty on the choice of the background functional form, a so-called *spurious signal test* is performed, as described in Sec. 6.3.

Control Region for the mixed channel

In order to test the flexibility of the background functional form in Eq. 6.1, a dedicated CR has been defined in the $e\text{LJ}-\mu\text{LJ}$ channel as well.

This CR is built in such a way to be as close as possible to the $e\text{LJ}-\mu\text{LJ}$ SR. In this way, if the functional form in Eq. 6.1 describes the μLJ invariant mass spectrum in the $e\text{LJ}-\mu\text{LJ}$ CR, the same is expected to be true in the $e\text{LJ}-\mu\text{LJ}$ SR.

It is required for exactly one μLJ , no $e\text{LJ}$ s and an additional pair of open electrons to be reconstructed. These additional electrons must satisfy the same requirements of the ones making up $e\text{LJ}$ s, in order to have a CR which is as similar as possible to the SR.

The triggers that the events must fire are the ones listed in Sec. 5.5.3 and a similar trigger matching scheme is asked as well, considering muons in the μLJ and electrons in the electron-pair.

The presence of the electron-pair in addition to the μLJ ensures orthogonality with the $\mu\text{LJ}-\mu\text{LJ}$ channel. Thus, signal events populating the CR are only the ones where one γ_d decays into muons and is reconstructed as μLJ and one γ_d decays into electrons that are too far apart to be reconstructed as an $e\text{LJ}$.

All CR requirements are the same as the ones for the SR, with the exception of the selections on the $|\eta|$, $p_{\text{T}}^{\text{imb}}$ and q of the electron-pair. After these requirements, a small signal leakage is still present, so an additional cut on the mass imbalance m^{imb} between the μLJ and the di-electron pair ($|m^{\text{imb}}| > 0.6$) is applied.

Details on the expected number of signal events are given in Tab. 6.13 and Tab. 6.14 for respectively the FRVZ and HAHM models.

m_{γ_d} [GeV]	0.24	0.4	0.9	2	6	10
None	337900 \pm 700	337900 \pm 700	337900 \pm 700	337900 \pm 700	337900 \pm 700	337800 \pm 700
Triggers	4421 \pm 24	4115 \pm 23	3508 \pm 21	4538 \pm 24	4968 \pm 25	67350 \pm 29
1 μLJ , 0 $e\text{LJ}$, 0 μ , $e \geq 2$	0.95 \pm 0.34	0.55 \pm 0.25	1.2 \pm 0.4	2.1 \pm 0.5	65.0 \pm 2.8	59.7 \pm 2.6
Trigger Matching	0.61 \pm 0.27	0.34 \pm 0.20	0.70 \pm 0.29	1.7 \pm 0.4	57.9 \pm 2.6	57.9 \pm 2.6
Leading electron $p_{\text{T}} > 5$ GeV	0.61 \pm 0.27	0.34 \pm 0.20	0.70 \pm 0.29	1.5 \pm 0.4	57.9 \pm 2.6	57.6 \pm 2.6
$ \Delta\phi(\mu\text{LJ}, ee) > 2$	0.24 \pm 0.17	0.22 \pm 0.16	0.24 \pm 0.17	1.12 \pm 0.35	43.3 \pm 2.2	27.8 \pm 1.8
$q_{\mu\text{LJ}} = 0$	0.24 \pm 0.17	0.22 \pm 0.16	0.24 \pm 0.17	1.12 \pm 0.35	43.3 \pm 2.2	27.8 \pm 1.8
$m^{\text{imb}} >$	0.24 \pm 0.17	0.22 \pm 0.16	0.24 \pm 0.17	0.64 \pm 0.26	0.13 \pm 0.09	0.06 \pm 0.06

Table 6.13. Signal (weighted) events remaining after each selection applied in the CR of the $\mu\text{LJ}-e\text{LJ}$ channel. Events are generated according to the FRVZ model and are normalised assuming a branching ratio $B(H \rightarrow 2\gamma_d + X) = 0.5\%$, with $L = 140 \text{ fb}^{-1}$ and $\sigma = \sigma_{\text{ggF}}$. The associated uncertainty per each event yield is evaluated as $\sqrt{\sum_i^{N_{\text{raw}}} w_i^2}$, with N_{raw} being the number of un-weighted MC events and w_i being the per event weight.

m_{γ_d} [GeV]	0.4	2	10	15
None	337800 ± 700	337800 ± 700	337600 ± 700	337600 ± 700
Triggers	12660 ± 40	9857 ± 35	15010 ± 40	15960 ± 50
1 μ LJ, 0 eLJ, 0 μ , $e \geq 2$	2.3 ± 0.5	1.4 ± 0.4	332 ± 6	131 ± 4
Trigger Matching	2.2 ± 0.5	1.02 ± 0.34	325 ± 6	129 ± 4
Leading electron $p_T > 5$ GeV	2.2 ± 0.5	1.02 ± 0.34	325 ± 6	129 ± 4
$ \Delta\phi(\mu\text{LJ}, ee) > 2$	1.8 ± 0.5	0.44 ± 0.22	273 ± 6	63.4 ± 2.8
$q_{\mu\text{LJ}} = 0$	1.8 ± 0.5	0.44 ± 0.22	273 ± 6	63.4 ± 2.8
$m^{\text{imb}} > 0.6$	1.2 ± 0.4	0.44 ± 0.22	0.39 ± 0.21	0.12 ± 0.12

Table 6.14. Signal (weighted) events remaining after each selection applied in the CR of the μLJ – $e\text{LJ}$ channel. Events are generated according to the HAHM model and are normalised assuming a branching ratio $B(H \rightarrow 2\gamma_d) = 0.5\%$, with $L = 140 \text{ fb}^{-1}$ and $\sigma = \sigma_{\text{ggF}}$. The associated uncertainty per each event yield is evaluated as $\sqrt{\sum_i^{N_{\text{raw}}} w_i^2}$, with N_{raw} being the number of un-weighted MC events and w_i being the per event weight.

Fig. 6.11 shows the distribution of the invariant mass of the μLJ in the μLJ – $e\text{LJ}$ CR in data, obtained by processing the full Run-2 dataset, with the $B(m_{\mu\mu})$ fitted (via an unbinned likelihood fit) PDF (see Eq. 6.1) overlaid on such a spectrum. The reduced chi-square of the fit performed is $\tilde{\chi}_\nu^2 = 0.50^3$. The fitted parameters values are shown in Tab. 6.15.

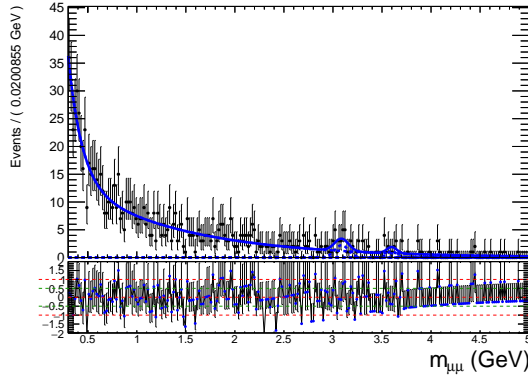


Figure 6.11. Fitted background PDF describing the background distribution in the μLJ mass spectrum (blue line) overlaid to the data points (black dots) in the μLJ – $e\text{LJ}$ channel CR.

Parameter	Fitted value
f_{exp}	0.08 ± 0.05
$f_{J/\psi}$	0.021 ± 0.008
$f_{\phi(1020)}$	0.000 ± 0.005
$f_{\psi(2S)}$	0.008 ± 0.004
$\mu_{J/\psi}$	$(3.088 \pm 0.029) \text{ GeV}$
$\mu_{\psi(2S)}$	$(3.60 \pm 0.10) \text{ GeV}$
$\sigma_{J/\psi}$	$(0.071 \pm 0.032) \text{ GeV}$
τ	$(1.15 \pm 0.08) \text{ GeV}$
τ_2	$(0.14 \pm 0.04) \text{ GeV}$

Table 6.15. Fitted parameters of $B(m_{\mu\mu})$ PDF (see Eq. 6.1) with their relative uncertainty.

Signal shape modelling

The signal-shape modelling is performed separately for the muonic and the mixed channel, since the different trigger strategies exploited in these channels could lead

³Such a chi-square is obtained by binning the distribution according to the binning specified by the y-axis of the plot in Fig. 6.11

in principle to non-negligible differences in the p_T spectrum of the muons in the μ LJs, therefore potentially impacting the μ LJ mass spectrum.

The μ LJs invariant mass distribution expected for the signal is modelled in both the channels via a Double-Sided Crystal Ball (DSCB) function, with a Gaussian core with power-law end tails, defined as:

$$N \cdot \begin{cases} e^{-t^2/2} & \text{if } -\alpha_{\text{low}} \leq t \leq \alpha_{\text{high}} \\ \frac{e^{-0.5\alpha_{\text{low}}^2}}{\left[\frac{\alpha_{\text{low}}}{n_{\text{low}}} \left(\frac{n_{\text{low}}}{\alpha_{\text{low}}} - \alpha_{\text{low}} - t\right)\right]^{n_{\text{low}}}} & \text{if } t < -\alpha_{\text{low}} \\ \frac{e^{-0.5\alpha_{\text{high}}^2}}{\left[\frac{\alpha_{\text{high}}}{n_{\text{high}}} \left(\frac{n_{\text{high}}}{\alpha_{\text{high}}} - \alpha_{\text{high}} + t\right)\right]^{n_{\text{high}}}} & \text{if } t > \alpha_{\text{high}}, \end{cases} \quad (6.2)$$

where $t = (m_{\mu\mu} - \mu_{\text{CB}})/\sigma_{\text{CB}}$ with μ_{CB} and σ_{CB} respectively the peak and the width of the Gaussian core of the PDF; N is a normalisation parameter; α_{low} (α_{high}) is the position of the junction between the Gaussian and power law on the low (high) mass tail in units of t and n_{low} (n_{high}) is the exponent of this power law.

The DSCB parameters are extracted for the different γ_d mass hypotheses of the generated MC samples from an un-binned likelihood fit on the reconstructed μ LJs invariant mass, using the PDF in Eq. 6.2. The n_{high} and n_{low} parameters are fixed, in order to improve the fit stability, given their large correlation with α_{high} and α_{low} , respectively.

The reconstructed μ LJ invariant mass distribution for the generated MC samples in the FRVZ model, along with the fitted DSCB PDF, are shown in Fig. 6.12 and in Fig. 6.13 respectively for the muonic and the mixed channels.

Fig. 6.14 and Fig. 6.15 show instead the fitted DSCB parameters for the different m_{γ_d} hypotheses respectively for the μ LJ- μ LJ and the μ LJ- e LJ channels.

In order to extract the invariant mass shape for different signal hypotheses with respect to the generated ones, the PDF free parameters are parameterised as a function of m_{γ_d} using analytical functions of different complexity. Given the large range in energy spanned, covering several orders of magnitude, special care is given to the low di-muon masses (1 GeV) scenarios, to provide a better parameterisation for the lowest mass points. Therefore, the analytical functions are essentially built with a first order polynomial, combined for some of the parameters of the DSCB with a Fermi-Dirac function. The fitted parameters extracted from low-statistics MC samples (such as the one in Fig. 6.12 (g)) are not used in the interpolation.

The models used to interpolate between the FRVZ generated mass points are described in Tab. 6.16 and Tab. 6.17.

In Fig. 6.12 and Fig. 6.13 the DSCB PDF obtained using the extrapolated parameters is shown as well, showing an excellent agreement with both the data points and the fitted PDF, therefore corroborating the validity of the extrapolation technique. The points at $m_{\gamma_d} = 15$ GeV and $m_{\gamma_d} = 2$ GeV for respectively the μ LJ- μ LJ and the μ LJ- e LJ channel show a worse agreement with the modelling, as a consequence of a loss of statistics for the relative signal points (as can be seen respectively from Tab. 6.1 and Tab. 6.6). For this reason, these signal points are excluded from the interpolation of the DSCB fitter parameters.

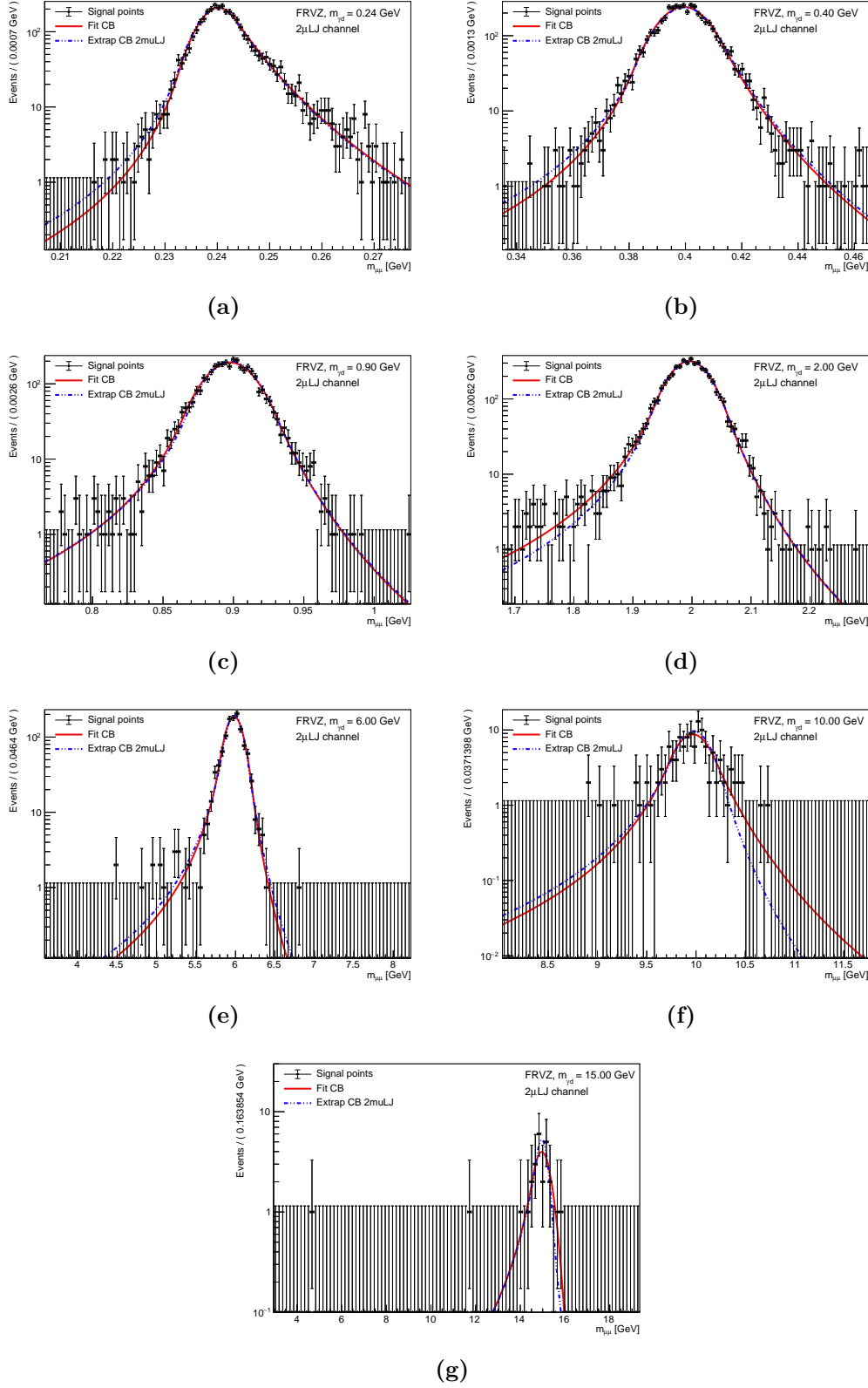


Figure 6.12. μLJ invariant mass distribution for the FRVZ model, in the μLJ – μLJ channel (dots), shown for different γ_d mass: (a) 0.24 GeV, (b) 0.4 GeV, (c) 0.9 GeV, (d) 2 GeV, (e) 6 GeV, (f) 10 GeV and (g) 15 GeV. The fitted PDF (red) is compared to the extrapolated one (blue) (see text).

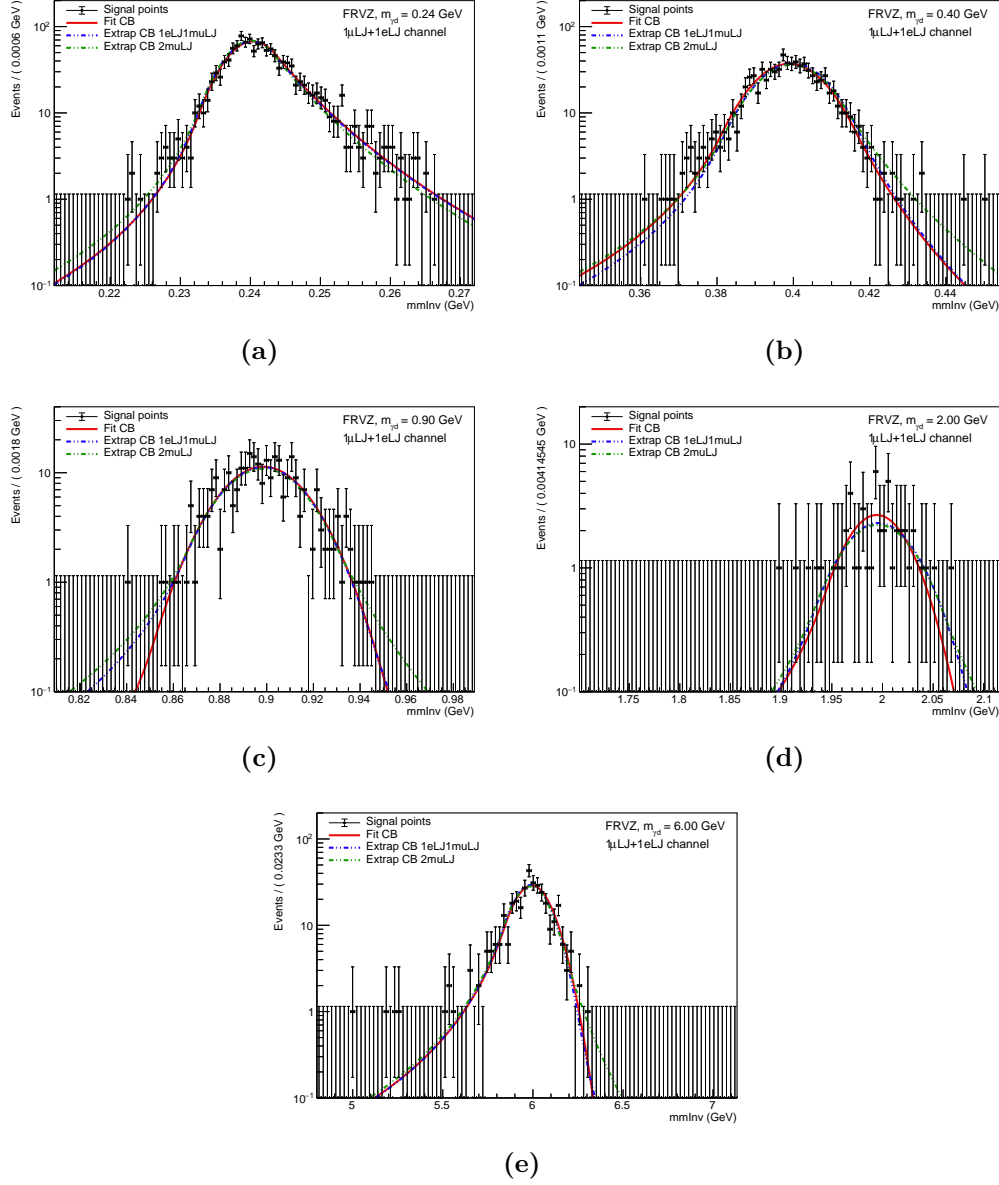


Figure 6.13. μLJ invariant mass distribution for the FRVZ model, in the $e\text{LJ}-\mu\text{LJ}$ channel (dots), shown for different γ_d mass: (a) 0.24 GeV, (b) 0.4 GeV, (c) 0.9 GeV, (d) 2 GeV, (e) 6 GeV. The fitted PDF (red) is compared to the one extrapolated both from this channel (blue) and from the muonic one (green) (see text).

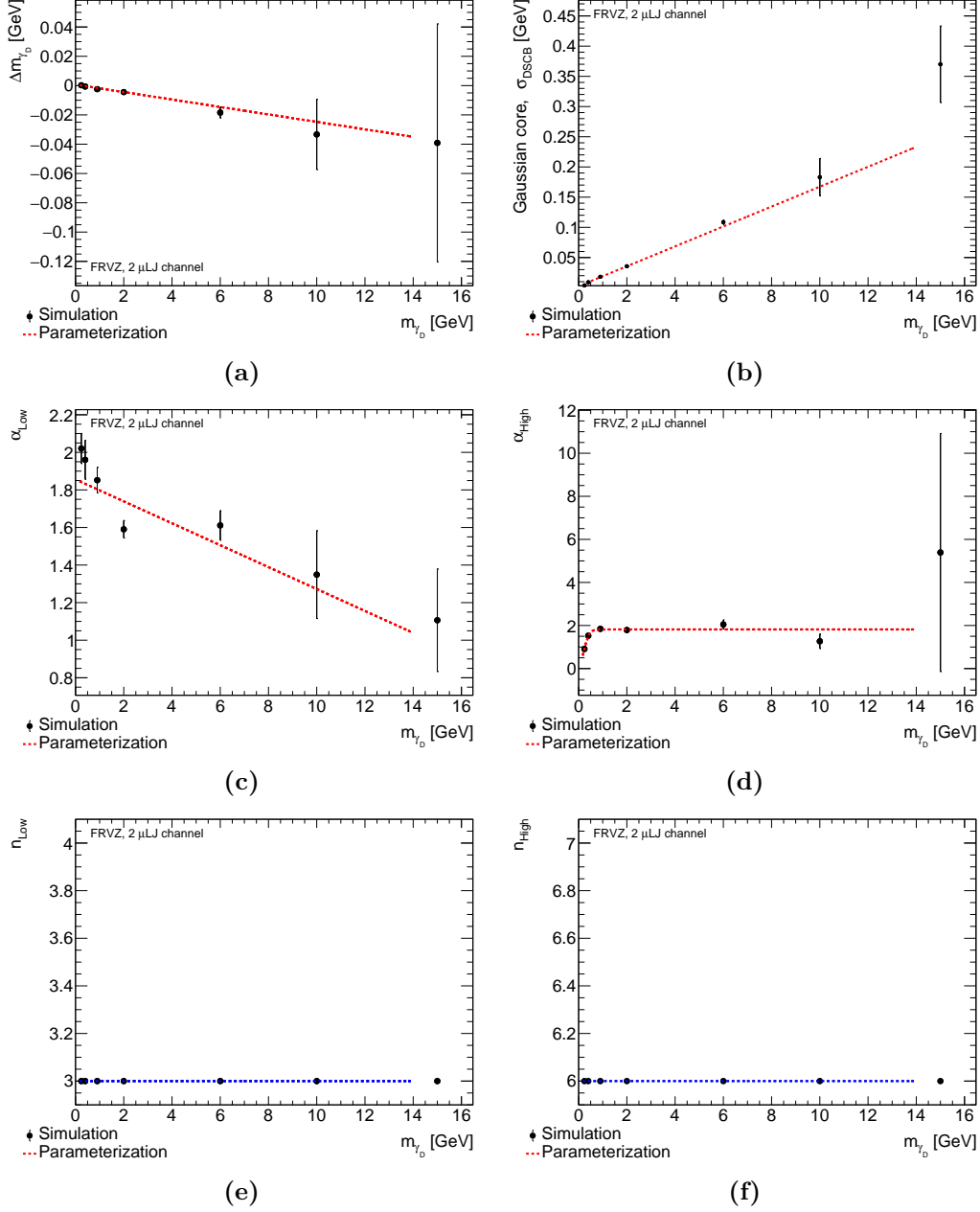


Figure 6.14. Fitted parameters of the DSCB as a function of the different m_{γ_d} for the FRVZ benchmark model in the $\mu\text{LJ}-\mu\text{LJ}$ channel, showing (a) $\Delta m_{\gamma_d} = \mu_{\text{CB}} - m_{\gamma_d}$, with m_{γ_d} being the generated MC mass, (b) σ_{CB} , (c) α_{Low} , (d) α_{High} , (e) n_{Low} and (e) n_{High} . The dotted lines show the fitted interpolation. Each parameter is in addition shown with its associated error bar, resulting from the DSCB fit itself. The fitted parameters extracted from low-statistics MC samples are not used in the interpolation.

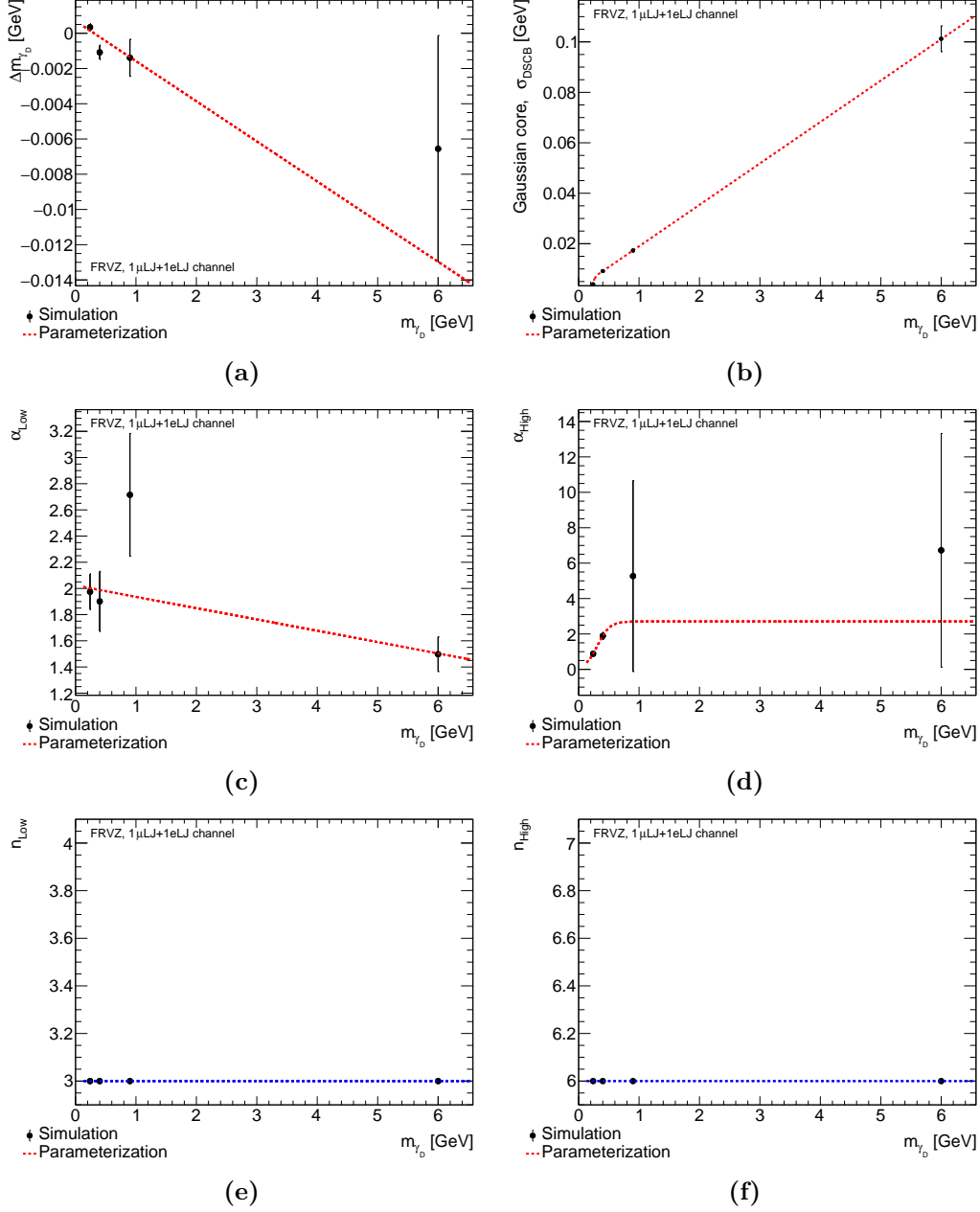


Figure 6.15. Fitted parameters of the DSCB as a function of the different m_{γ_d} for the FRVZ benchmark model in the $\mu\text{LJ}-e\text{LJ}$ channel, showing (a) $\Delta m_{\gamma_d} = \mu_{\text{CB}} - m_{\gamma_d}$, with m_{γ_d} being the generated MC mass, (b) σ_{CB} , (c) α_{Low} , (d) α_{High} , (e) n_{Low} and (e) n_{High} . The dotted lines show the fitted interpolation. Each parameter is in addition shown with its associated error bar, resulting from the DSCB fit itself. The fitted parameters extracted from low-statistics MC samples are not used in the interpolation.

Table 6.16. Parameterisations of the DSCB parameters describing the signal shape, as a function of the DP mass, for the $\mu\text{LJ}-\mu\text{LJ}$ channel in the FRVZ benchmark model.

Parameter	Parameterisation	a	b	c	d
Δm_{γ_d}	$a + bm_{\gamma_d}$	$0.66 \pm 0.013 \text{ MeV}$	$2.54 \pm 0.06 \text{ MeV/GeV}$	-	-
σ_{CB}	$\frac{a+bm_{\gamma_d}}{1+\exp(-(m_{\gamma_d}-c)/d)}$	$2.6 \pm 0.3 \text{ MeV}$	$16.47 \pm 0.14 \text{ MeV/GeV}$	$239.94 \pm 0.18 \text{ MeV}$	$46 \pm 28 \text{ MeV}$
α_{low}	$a + bm_{\gamma_d}$	1.86 ± 0.04	$-5.8 \pm 1.5 \text{ GeV}^{-1}$	-	-
α_{high}	$\frac{a}{1+\exp(-(m_{\gamma_d}-c)/d)}$	1.82 ± 0.04	-	$238.9 \pm 01.0 \text{ MeV}$	$100 \pm 2 \text{ MeV}$
n_{low}	a	2	-	-	-
n_{high}	a	6	-	-	-

Table 6.17. Parameterisations of the DSCB parameters describing the signal shape, as a function of the DP mass, for the $e\text{LJ}-\mu\text{LJ}$ channel in the FRVZ benchmark model.

Parameter	parameterisation	a	b	c	d
Δm_{γ_d}	$a + bm_{\gamma_d}$	$0.7 \pm 0.3 \text{ MeV}$	$2.4 \pm 0.9 \text{ MeV/GeV}$	-	-
σ_{CB}	$\frac{a+bm_{\gamma_d}}{1+\exp(-(m_{\gamma_d}-c)/d)}$	$2.6 \pm 0.6 \text{ MeV}$	$16.4 \pm 0.08 \text{ MeV/GeV}$	$240 \pm 50 \text{ MeV}$	$12.6 \pm 1.1 \text{ MeV}$
α_{low}	$a + bm_{\gamma_d}$	2.02 ± 0.012	$-9 \pm 3 \text{ GeV}^{-1}$	-	-
α_{high}	$\frac{a}{1+\exp(-(m_{\gamma_d}-c)/d)}$	2.7 ± 0.5	-	$310 \pm 30 \text{ MeV}$	$100 \pm 2 \text{ MeV}$
n_{low}	a	2	-	-	-
n_{high}	a	6	-	-	-

In Fig. 6.13 the PDF extracted from the $\mu\text{LJ}-\mu\text{LJ}$ SR is shown too, from which it can be seen how PDFs extracted from the $\mu\text{LJ}-\mu\text{LJ}$ channel accurately describes the μLJ invariant mass spectrum in the $\mu\text{LJ}-e\text{LJ}$ channel, for the different m_{γ_d} hypotheses. For this reason, the $\mu\text{LJ}-\mu\text{LJ}$ modelling is used for both the channels, since the muonic channel has a larger statistics for all the signal points investigated.

The same study is performed for the HAHM model as well. The reconstructed μLJ invariant mass distribution for the generated MC samples in this model, along with the fitted DSCB and extrapolated PDFs, are shown in Fig. 6.16 and in Fig. 6.17 respectively for the muonic and the mixed channels. Fig. 6.18 and Fig. 6.19 show instead the fitted DSCB parameters for the different m_{γ_d} hypotheses respectively for the $\mu\text{LJ}-\mu\text{LJ}$ and the $\mu\text{LJ}-e\text{LJ}$ channels. The models used to interpolate between the FRVZ generated mass points is described in Tab. 6.18 and Tab. 6.19.

Table 6.18. Parameterisations of the DSCB parameters describing the signal shape, as a function of the DP mass, for the $\mu\text{LJ}-\mu\text{LJ}$ channel in the HAHM benchmark model.

Parameter	Parameterisation	a	b	c	d
Δm_{γ_d}	$a + bm_{\gamma_d}$	$0.23 \pm 0.16 \text{ MeV}$	$-1.59 \pm 0.23 \text{ MeV/GeV}$	-	-
σ_{CB}	$a + bm_{\gamma_d}$	$4.10 \pm 0.17 \text{ MeV}$	$17.912 \pm 0.026 \text{ MeV/GeV}$	-	-
α_{low}	$a + bm_{\gamma_d}$	1.88 ± 0.03	$-0.0040 \pm 0.0006 \text{ GeV}^{-1}$	-	-
α_{high}	$\frac{a}{1+\exp(-(m_{\gamma_d}-c)/d)}$	1.90 ± 0.06	-	$326 \pm 11 \text{ MeV}$	$100 \pm 2 \text{ MeV}$
n_{low}	a	2	-	-	-
n_{high}	a	6	-	-	-

In this scenario as well an excellent agreement between the extrapolated DSCB PDF and both the data points and the fitted PDF is observed. Furthermore, no striking difference is observed between the two channels μLJ invariant mass spectrum in this benchmark model too. The point at $m_{\gamma_d} = 25 \text{ GeV}$ for the $\mu\text{LJ}-\mu\text{LJ}$ shows a worse agreement with the modelling, as a consequence of a loss of statistics for the relative signal point (as can be seen from Tab. 6.2). For this reason, this signal point is excluded from the interpolation of the DSCB fitter parameters.

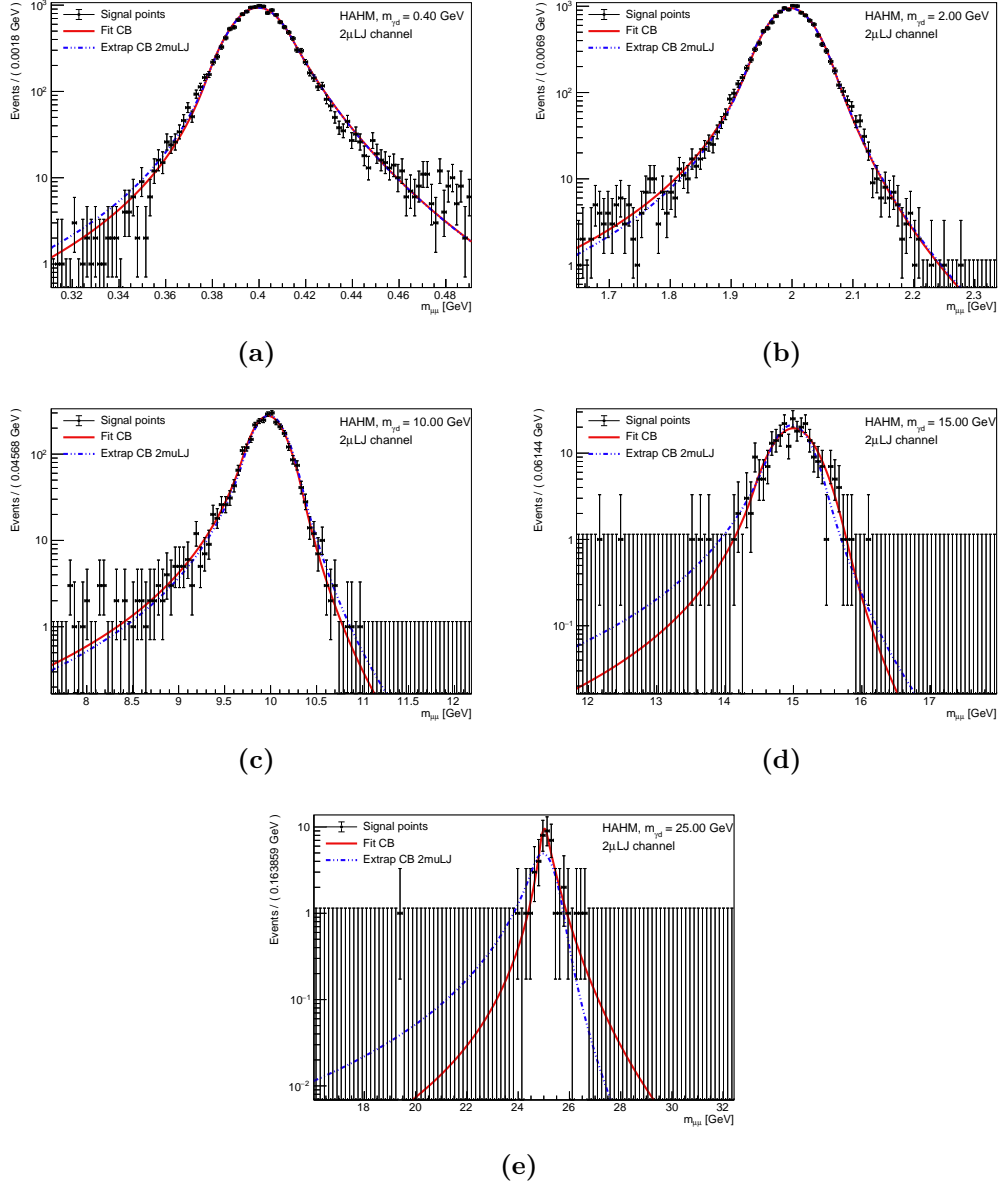


Figure 6.16. μLJ invariant mass distribution for the HAHM model, in the μLJ – μLJ channel (dots), shown for different γ_d mass: (a) 0.4 GeV, (b) 2 GeV, (c) 10 GeV, (d) 15 GeV and (e) 25 GeV. The fitted PDF (red) is compared to the extrapolated one (blue) (see text).

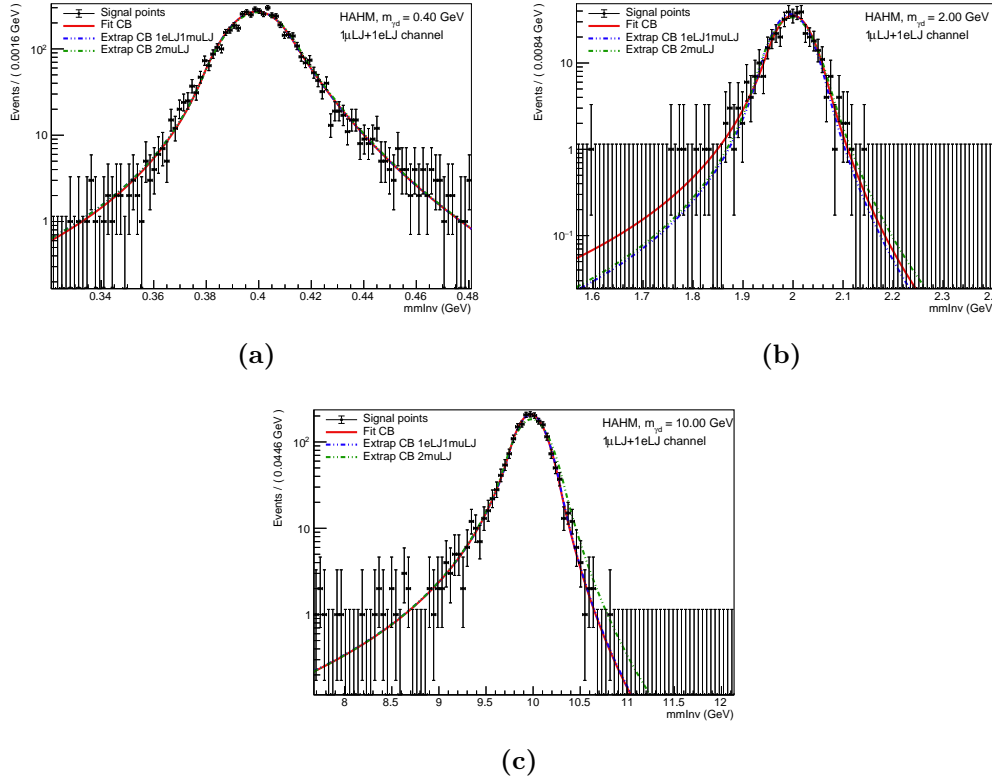


Figure 6.17. μLJ invariant mass distribution for the HAHM model, in the $\mu\text{LJ}-e\text{LJ}$ channel (dots), shown for different γ_d mass: (a) 0.4 GeV, (b) 2 GeV and (c) 10 GeV. The fitted PDF (red) is compared to the one extrapolated both from this channel (blue) and from the muonic one (green) (see text).

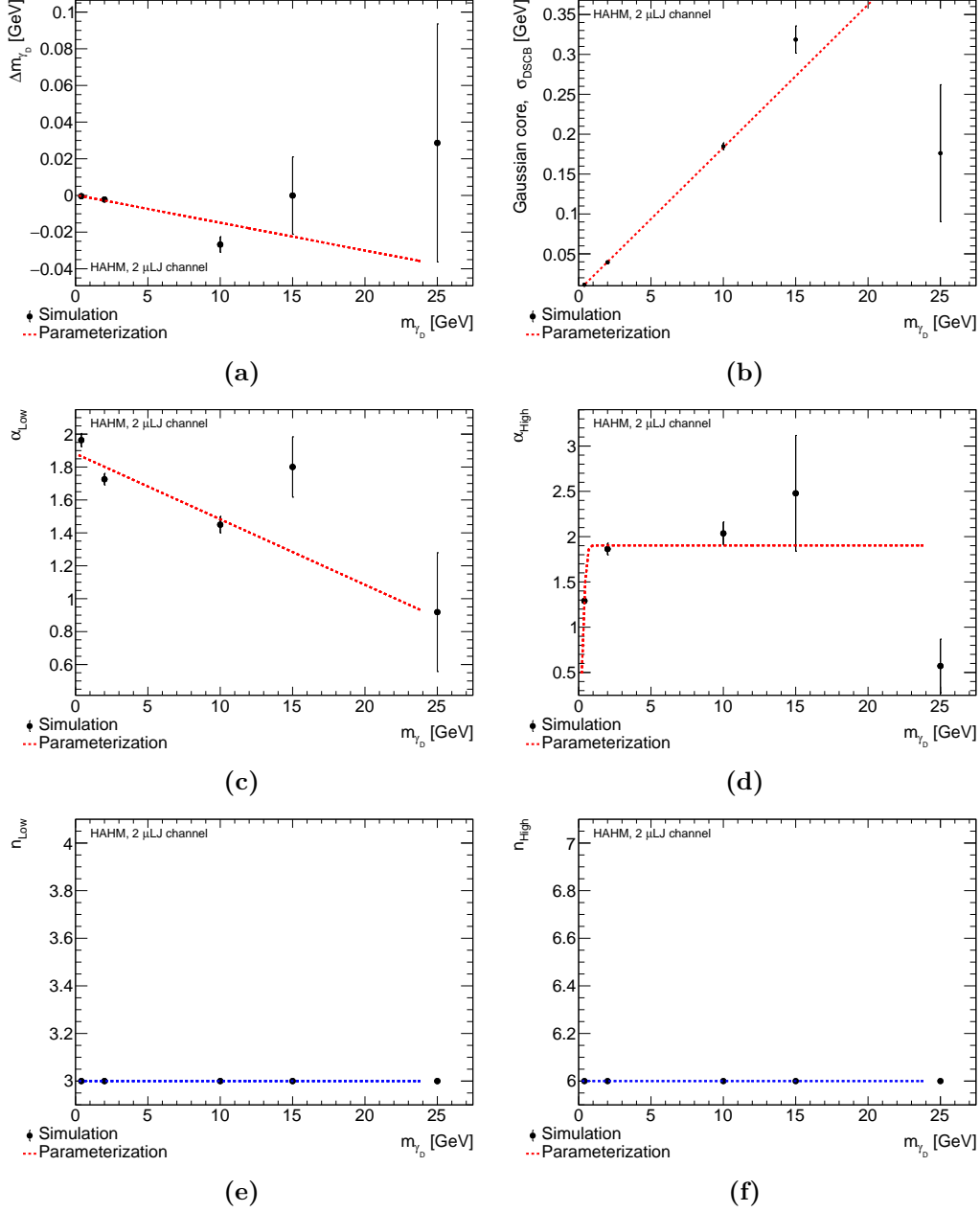


Figure 6.18. Fitted parameters of the DSCB as a function of the different m_{γ_d} for the FRVZ benchmark model in the $\mu\text{LJ}-\mu\text{LJ}$ channel, showing (a) $\Delta m_{\gamma_d} = \mu_{\text{CB}} - m_{\gamma_d}$, with m_{γ_d} being the generated MC mass, (b) σ_{CB} , (c) α_{Low} , (d) α_{High} , (e) n_{Low} and (e) n_{High} . The dotted lines show the fitted interpolation. Each parameter is in addition shown with its associated error bar, resulting from the DSCB fit itself. The fitted parameters extracted from low-statistics MC samples are not used in the interpolation.

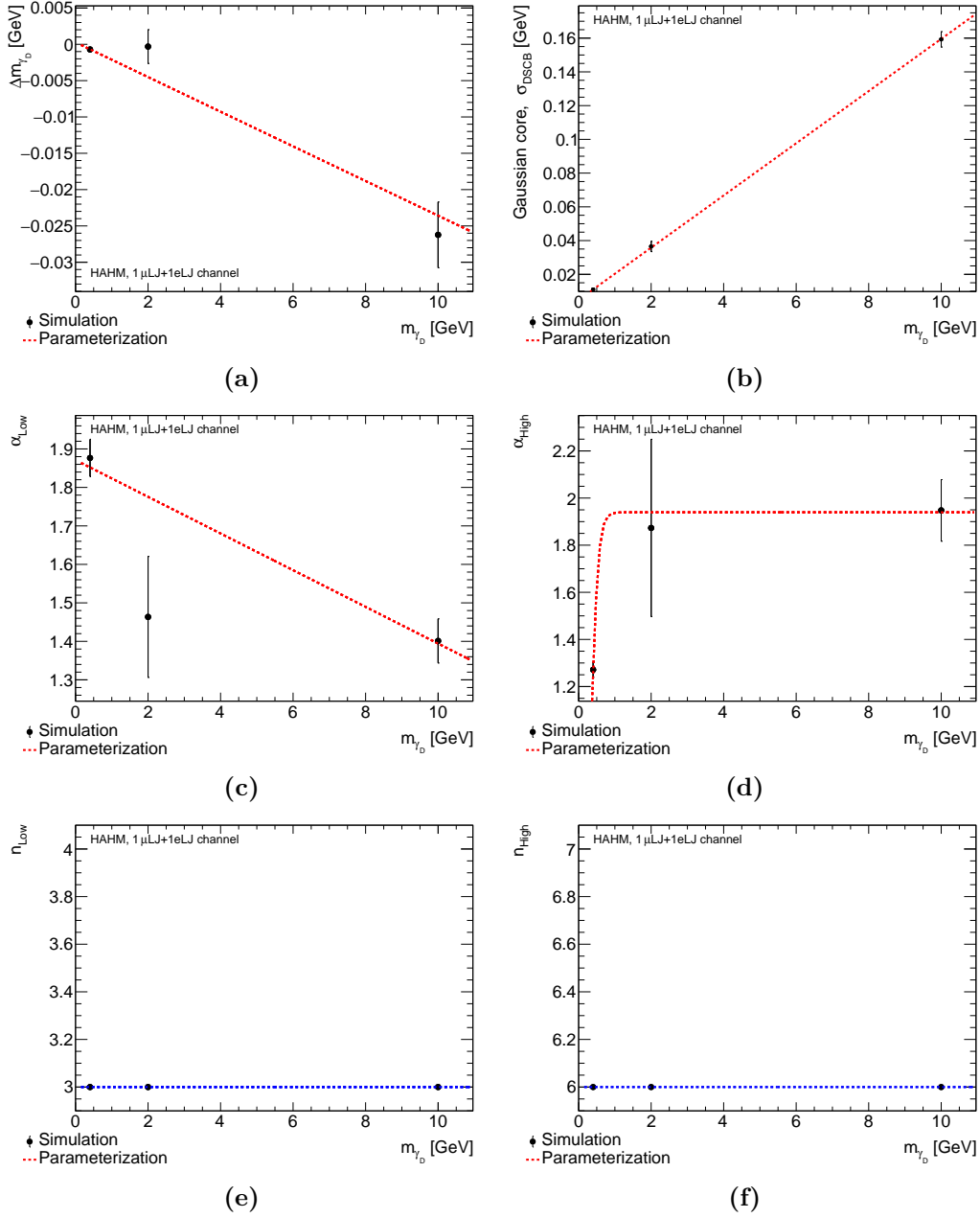


Figure 6.19. Fitted parameters of the DSCB as a function of the different m_{γ_d} for the FRVZ benchmark model in the μ LJ- e LJ channel, showing (a) $\Delta m_{\gamma_d} = \mu_{\text{CB}} - m_{\gamma_d}$, with m_{γ_d} being the generated MC mass, (b) σ_{CB} , (c) α_{Low} , (d) α_{High} , (e) n_{Low} and (e) n_{High} . The dotted lines show the fitted interpolation. Each parameter is in addition shown with its associated error bar, resulting from the DSCB fit itself. The fitted parameters extracted from low-statistics MC samples are not used in the interpolation.

Table 6.19. Parameterisations of the DSCB parameters describing the signal shape, as a function of the DP mass, for the eLJ – μLJ channel in the HAHM benchmark model.

Parameter	Parameterisation	a	b	c	d
Δm_{γ_d}	$a + bm_{\gamma_d}$	0.26 ± 0.23 MeV	2.4 ± 0.5 MeV/GeV	-	-
σ_{CB}	$a + bm_{\gamma_d}$	4.9 ± 0.3 MeV	15.4 ± 0.5 MeV/GeV	-	-
α_{low}	$a + bm_{\gamma_d}$	1.87 ± 0.05	$-0.048 \pm 0.008 \text{GeV}^{-1}$	-	-
α_{high}	$\frac{a}{1 + \exp(-(m_{\gamma_d} - c)/d)}$	1.94 ± 0.12	-	336 ± 20 MeV	100 ± 2 MeV
n_{low}	a	2	-	-	-
n_{high}	a	6	-	-	-

It can be observed however how in the HAHM model the invariant mass resolution (σ_{cb}) is slightly worse than the one of the FRVZ model. As an example, for a γ_d with $m_{\gamma_d} = 2$ GeV in the FRVZ benchmark model, a resolution of ~ 30 MeV is observed (Fig. 6.14 (b)), while for the same γ_d hypothesis a resolution of ~ 40 MeV is observed for the HAHM benchmark model. This is due to the fact that muons in the HAHM model are more boosted, this resulting in a worse resolution.

In Fig. 6.17 both the PDF extracted for the μLJ – eLJ and the one extracted for the μLJ – μLJ channels are depicted, showing (as in the FRVZ benchmark model) that the PDFs extracted from the μLJ – μLJ SR accurately describes the μLJ invariant mass spectrum in the μLJ – eLJ SR, for the different m_{γ_d} hypotheses.

For this reason, the μLJ – μLJ modelling is used for both the channels for both the FRVZ and the HAHM models.

The uncertainty on the signal shape modelling is evaluated, for both the channels, as explained in Sec. 6.3.2.

Signal acceptance \times efficiency modelling

The acceptance \times efficiency ($\mathcal{A} \times \epsilon|_{\text{channel}}$) of the μLJ – μLJ and eLJ – μLJ channels is modelled as a function of m_{γ_d} . The γ_d mass determines both the BRs of the γ_d into SM particles and the boost of the γ_d . In order to factor out the γ_d BR into muons from $\mathcal{A} \times \epsilon|_{\text{channel}}$ for the muonic channel, $\mathcal{A} \times \epsilon|_{\gamma_d \rightarrow \mu\mu, \gamma_d \rightarrow \mu\mu}$ is evaluated, requiring that both γ_d decay at the truth level into muons, as in

$$\mathcal{A} \times \epsilon|_{\gamma_d \rightarrow \mu\mu, \gamma_d \rightarrow \mu\mu} = \frac{SR^{2\mu LJ}(\gamma_d \rightarrow \mu\mu, \gamma_d \rightarrow \mu\mu)}{In(\gamma_d \rightarrow \mu\mu, \gamma_d \rightarrow \mu\mu)}, \quad (6.3)$$

where $SR^{2\mu LJ}(\gamma_d \rightarrow \mu\mu, \gamma_d \rightarrow \mu\mu)$ is the number of events in the μLJ – μLJ channel SR where both γ_d decay into muons and $In(\gamma_d \rightarrow \mu\mu, \gamma_d \rightarrow \mu\mu)$ is the initial number of events where both γ_d decay into muons. By dividing and multiplying by the total number of initial events, In , Eq. 6.3 becomes:

$$\begin{aligned} \mathcal{A} \times \epsilon|_{\gamma_d \rightarrow \mu\mu, \gamma_d \rightarrow \mu\mu} &= \frac{SR^{2\mu LJ}(\gamma_d \rightarrow \mu\mu, \gamma_d \rightarrow \mu\mu)}{In} \times \frac{In}{In(\gamma_d \rightarrow \mu\mu, \gamma_d \rightarrow \mu\mu)} = \\ &= \mathcal{A} \times \epsilon|_{\mu LJ-\mu LJ} \times \frac{1}{BR(\gamma_d \rightarrow \mu\mu)^2}, \end{aligned}$$

where $\frac{In(\gamma_d \rightarrow \mu\mu, \gamma_d \rightarrow \mu\mu)}{In} = BR(\gamma_d \rightarrow \mu\mu)^2$ has been used and where the last equality holds true only if $SR^{2\mu LJ}(\gamma_d \rightarrow \mu\mu, \gamma_d \rightarrow \mu\mu) = SR^{2\mu LJ}$, that is only if the

$\mu\text{LJ}-\mu\text{LJ}$ SR is populated at the truth level only of events where both DPs decay into muons. If this is the case, then $\mathcal{A} \times \epsilon|_{\mu\text{LJ}-\mu\text{LJ channel}}$ can be written as

$$\mathcal{A} \times \epsilon|_{\mu\text{LJ}-\mu\text{LJ channel}} = \mathcal{A} \times \epsilon|_{\gamma_d \rightarrow \mu\mu, \gamma_d \rightarrow \mu\mu} BR(\gamma_d \rightarrow \mu\mu)^2, \quad (6.4)$$

For the mixed channel, $\mathcal{A} \times \epsilon|_{\gamma_d \rightarrow \mu\mu, \gamma_d \rightarrow ee}$ is instead computed, requiring that one γ_d decays at the truth level into electrons and the other one into muons, as in

$$\mathcal{A} \times \epsilon|_{\gamma_d \rightarrow \mu\mu, \gamma_d \rightarrow ee} = \frac{SR^{1\mu\text{LJ}+1e\text{LJ}}(\gamma_d \rightarrow \mu\mu, \gamma_d \rightarrow ee)}{In(\gamma_d \rightarrow \mu\mu, \gamma_d \rightarrow ee)}, \quad (6.5)$$

where $SR^{1\mu\text{LJ}+1e\text{LJ}}(\gamma_d \rightarrow \mu\mu, \gamma_d \rightarrow ee)$ is the number of events in the $\mu\text{LJ}-e\text{LJ}$ channel SR where one γ_d decays into muons and the other one into electrons and $In(\gamma_d \rightarrow \mu\mu, \gamma_d \rightarrow ee)$ is the initial number of events where one γ_d decays into muons and the other one into electrons. By dividing and multiplying by the total number of initial events, In , Eq. 6.5 becomes:

$$\begin{aligned} \mathcal{A} \times \epsilon|_{\gamma_d \rightarrow \mu\mu, \gamma_d \rightarrow ee} &= \frac{SR^{1\mu\text{LJ}+1e\text{LJ}}(\gamma_d \rightarrow \mu\mu, \gamma_d \rightarrow ee)}{In} \times \frac{In}{In(\gamma_d \rightarrow \mu\mu, \gamma_d \rightarrow ee)} = \\ &= \mathcal{A} \times \epsilon|_{\mu\text{LJ}-e\text{LJ}} \times \frac{1}{2 \times BR(\gamma_d \rightarrow \mu\mu)BR(\gamma_d \rightarrow ee)}, \end{aligned}$$

where $\frac{In(\gamma_d \rightarrow ee, \gamma_d \rightarrow \mu\mu)}{In} = 2 \times BR(\gamma_d \rightarrow \mu\mu)BR(\gamma_d \rightarrow ee)$ has been used and where the last equality holds true only if $SR^{1\mu\text{LJ}+1e\text{LJ}}(\gamma_d \rightarrow \mu\mu, \gamma_d \rightarrow ee) = SR^{1\mu\text{LJ}-1e\text{LJ}}$, that is only if the $\mu\text{LJ}-e\text{LJ}$ SR is populated at the truth level only of events where on DPs decays into muons and the other one into electrons. If this is the case, then $\mathcal{A} \times \epsilon|_{\mu\text{LJ}-e\text{LJ channel}}$ is evaluated as:

$$\mathcal{A} \times \epsilon|_{\mu\text{LJ}-e\text{LJ channel}} = \mathcal{A} \times \epsilon|_{\gamma_d \rightarrow \mu\mu, \gamma_d \rightarrow ee} BR(\gamma_d \rightarrow \mu\mu)BR(\gamma_d \rightarrow ee) \times 2. \quad (6.6)$$

Fig. 6.20 (a) and (b) show respectively $\mathcal{A} \times \epsilon|_{\gamma_d \rightarrow \mu\mu, \gamma_d \rightarrow \mu\mu}$ and $\mathcal{A} \times \epsilon|_{\gamma_d \rightarrow \mu\mu, \gamma_d \rightarrow ee}$ for both the HAHM and the FRVZ model.

The acceptance of the $\mu\text{LJ}-\mu\text{LJ}$ channel is constant for light γ_d and the decreases for heavier γ_d hypotheses. For increasing m_{γ_d} the γ_d is less boosted, the muons are less collimated and they would fall inside the same LJ cone less likely.

The acceptance of the $e\text{LJ}-\mu\text{LJ}$ channel shows instead a different behaviour: while for light γ_d $\mathcal{A} \times \epsilon$ decreases, reaching a minimum for $m_{\gamma_d} = 2 \text{ GeV}$, for intermediate γ_d masses it increases and then decreases again for the heaviest γ_d hypothesis to which this channel is sensitive.

This is due to the $e\text{LJs}$ reconstruction efficiencies and can be better understood by looking at Fig. 6.21, showing the acceptance times efficiency for $e\text{LJs}$ made of only one electron (a) and $e\text{LJs}$ built with two separate electrons (b).

The $\mathcal{A} \times \epsilon$ for $e\text{LJs}$ made of only one electron, sizeable only for light γ_d , decreases as a function of the γ_d mass since it gets less likely to have two electrons that are so-collimated to be reconstructed as a single one. Conversely, the $\mathcal{A} \times \epsilon$ for $e\text{LJs}$ built with two electrons, sizeable only for heavy γ_d , increases as a function of m_{γ_d} , as vice-versa it becomes more likely to find electrons that are sufficiently open to be resolved. For the heaviest γ_d mass hypotheses, the two resolved electrons are too open to be reconstructed within the same $e\text{LJ}$ cone.

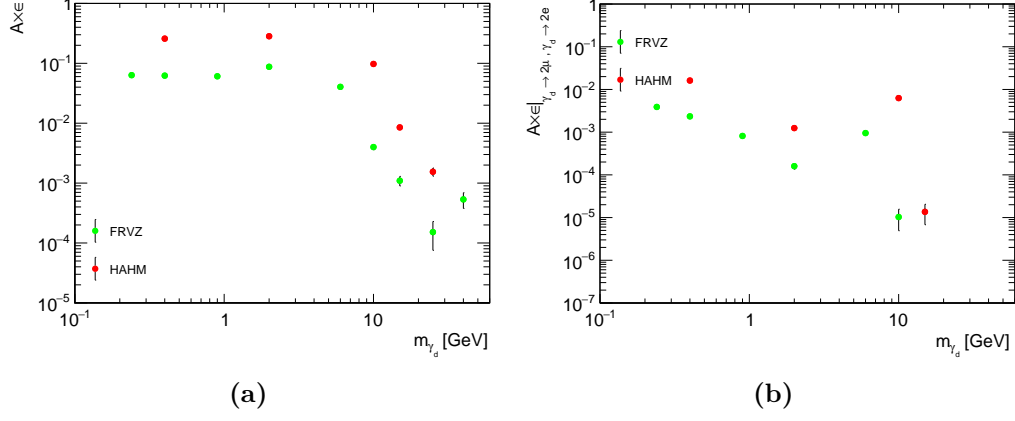


Figure 6.20. (a) $\mathcal{A} \times \epsilon|_{\gamma_d \rightarrow \mu\mu, \gamma_d \rightarrow \mu\mu}$ for the FRVZ (green) and the HAHM (red) model, (b) $\mathcal{A} \times \epsilon|_{\gamma_d \rightarrow \mu\mu, \gamma_d \rightarrow ee}$ for the FRVZ (green) and the HAHM (red) model.

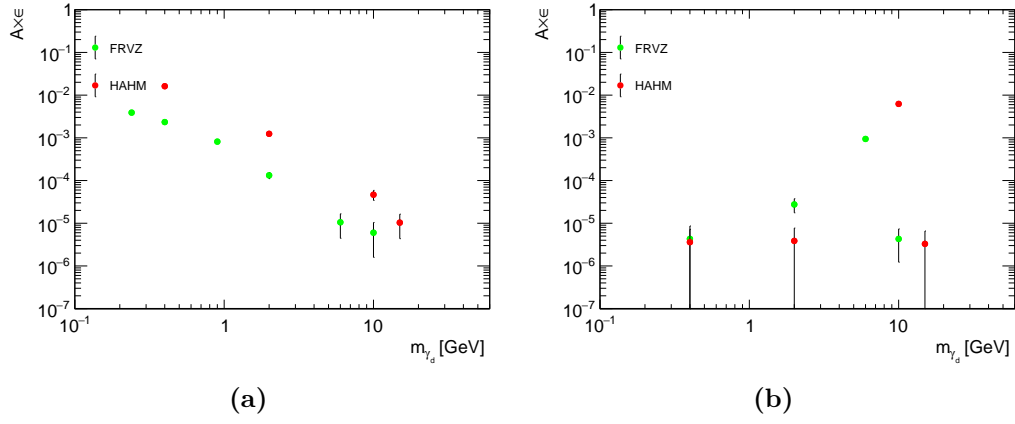


Figure 6.21. $\mathcal{A} \times \epsilon|_{\gamma_d \rightarrow \mu\mu, \gamma_d \rightarrow ee}$ for eLJs reconstructed with only one electron (a) and for eLJs reconstructed with two electrons (b), for the FRVZ (green) and the HAHM (red) models.

6.2.2 ABCD method for the electronic channel

After selection, the main background source for the $e\text{LJ}-e\text{LJ}$ channel is mainly composed of $Z + \gamma/\text{jets}$ events with a e/γ showering, mimicking a signal $e\text{LJ}$. This remaining contribution is estimated with the *ABCD method*.

The method requires that the SR (usually identified with the region A) is defined in terms of a selection on two variables, namely x and y , and that three CRs (usually identified with the regions B , C and D) can be obtained by inverting the selection on these two variables. The two variables exploited are preferentially continuous, allowing for a smooth transition between the different regions.

Therefore the different regions are defined, in terms of the variables x, y , as:

$$\begin{aligned} A &: x_1 \leq x < x_2 ; y_1 \leq y < y_2 \\ B &: x_1 \leq x < x_2 ; y_2 \leq y < y_3 \\ C &: x_2 \leq x < x_3 ; y_1 \leq y < y_2 \\ D &: x_2 \leq x < x_3 ; y_2 \leq y < y_3 \end{aligned}$$

A schematic picture of an ABCD plane, in terms of the x and y variables, is given in Fig. 6.22.

If the signal is well contained in region A and the background is uniformly distributed in the plane defined by the four regions, the number of expected events in region A , N_A , can be extrapolated from the observed number of events in the three CRs (N_B, N_C, N_D) as in:

$$N_A = \frac{N_C}{N_D} N_B. \quad (6.7)$$

If different sources of backgrounds populate the ABCD plane, the background estimation in region A is still reliable as long as such sources of backgrounds have still a uniform distribution in the plane. However, if some non-uniformity of the background distribution in the plane is observed, the method is still valid as long as Eq. 6.7 holds true. Since the latter equality cannot be verified as it is without looking at the events yield in SR, this check is performed either in sub-planes of the ABCD plane (like the BD or the DC regions) or in additional VRs where the same ABCD plane is defined. Such checks are performed in this search and they are described in the following section.

Furthermore, if signal events are expected to populate the CRs, the method should properly take into account such events, so not to bias the background estimation in region A . To account for this possible signal leakages and for additional sources of backgrounds (that can be in principle simply subtracted arithmetically, if an estimation for such events is available), a likelihood-based approach is exploited, where, instead of using Eq. 6.7, a four-bin statistical model is built, taking into account the underlying relationship between the background in the different regions. This method is more robust against CRs with small number of events and takes into account possible small signal contaminations in the CRs. Details about the fitting technique can be found in Sec. 6.5.1.

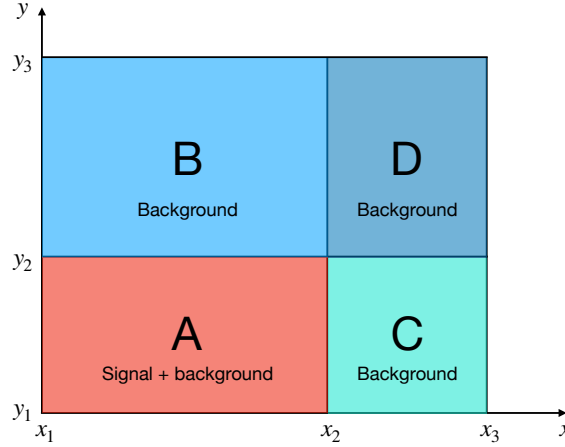


Figure 6.22. Schematic representation of an ABCD plane, in terms of the x, y variables, where the A region is the SR, populated by both signal and background events, and the B, C and D are instead CRs.

The two variables used to define the ABCD plane are the leading $eLJ p_T^{\text{imb}}$ and the farthest $eLJ R_\phi$. The variable R_ϕ is the ratio of 3×3 to 3×7 ($\eta \times \phi$) cell energies of the ECAL middle layer. The R_ϕ distribution is expected to be broader for electrons in $eLJs$ originating from γ_d decays than for electrons in $eLJs$ reconstructed in SM events, as in the former case the EM cluster is wide, as most often two neighboring EM showers are merged together into a single cluster.

Both the leading $eLJ p_T^{\text{imb}}$ and the farthest $eLJ R_\phi$ are good discriminants between signal and background, as can be seen respectively in Fig. 6.5 (a) and Fig. 6.23. These variables are highly uncorrelated in background events, since they refer to different objects and they exploit information from different ATLAS sub-detectors, being R_ϕ reconstructed from the calorimeter and p_T^{imb} from the ID. Fig. 6.23 (b) shows the data to MC comparison of the R_ϕ of the leading electron in an eLJ in events where $m_{eLJ-eLJ} \in [81, 101] \text{ GeV}$, showing how this variable is correctly modelled in the full spectrum.

The threshold values for the leading $eLJ p_T^{\text{imb}}$ and for the farthest $eLJ R_\phi$ are determined by maximising the signal to background sensitivity, denominated significance $S/\sqrt{B_{exp}}$ (with S being the signal yields and B_{exp} being the expected background yield), while keeping the signal leakage in the regions $B/C/D$ to below the 10%. Fig. 6.24 shows the ratio between the number of signal events, for the $m_{\gamma_d} = 17 \text{ MeV}$ mass sample in the FRVZ model, in regions B, C and D over the number of expected data events in these regions for different values of the leading $eLJ p_T^{\text{imb}}$ and of the farthest $eLJ R_\phi$.

Fig. 6.25 shows $S/\sqrt{B_{exp}}$ in SR A for different values of the leading $eLJ p_T^{\text{imb}}$ and of the farthest $eLJ R_\phi$.

Regions A, B, C and D are thus defined as in Tab. 6.20.

Fig. 6.26 shows this ABCD plane for (a) the FRVZ benchmark model with $m_{\gamma_d} = 0.1 \text{ GeV}$ and (b) the full Run-2 dataset.

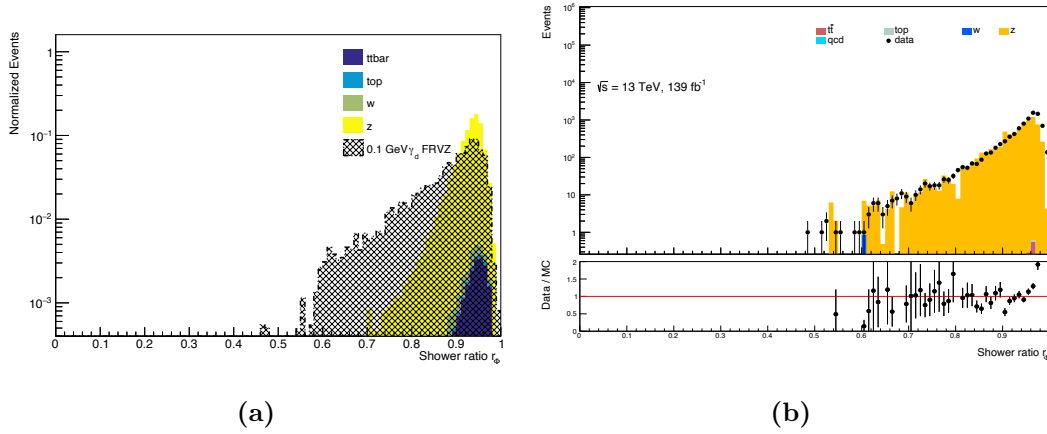


Figure 6.23. eLJ leading electron shower ratio R_ϕ (a) distribution for MC signal and background events and (b) data to MC comparison.

Table 6.20. Definition of the SR (A region) and the CRs (B , C and D regions) used in the background estimation.

Requirement / Region	A	B	C	D
Lead $eLJ p_T^{\text{imb}}$	< 0.82	< 0.82	> 0.82	> 0.82
Far $eLJ R_\phi$	< 0.96	> 0.96	< 0.96	> 0.96

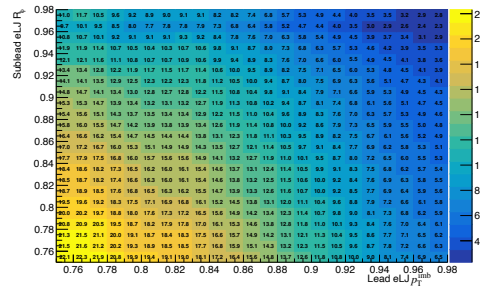
Yields for the various regions are reported in Tab. 6.21 and Tab. 6.22 for the full Run-2 dataset and for different m_{γ_d} hypotheses respectively in the FRVZ and the HAHM benchmark models.

Region	FRVZ Signal samples							Run-2 data
	γ_d mass [GeV]	0.017	0.03	0.06	0.1	0.24	0.4	
A (exp.)								276 ± 32
A (SR)		130.18 ± 3.97	94.99 ± 3.41	71.11 ± 3.0	54.95 ± 2.56	14.05 ± 1.29	2.53 ± 0.56	
B		13.3 ± 1.27	10.38 ± 1.15	7.2 ± 0.93	5.42 ± 0.88	2.32 ± 0.53	0.5 ± 0.25	111
C		21.74 ± 1.64	17.67 ± 1.52	13.49 ± 1.28	12.41 ± 1.21	1.77 ± 0.45	1.38 ± 0.4	839
D		2.19 ± 0.5	1.77 ± 0.54	1.53 ± 0.51	1.42 ± 0.39	0 ± 0	0 ± 0	338

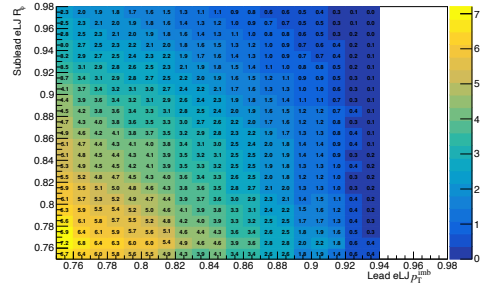
Table 6.21. ABCD yields in the FRVZ signal and data driven estimate for background in the eLJ – eLJ channel. Signal yields are normalised to $BR(H \rightarrow 2\gamma_d + X) = 0.5\%$. Uncertainties on the signal are statistical only, while the uncertainty on the number of expected events in data in region A is obtained from the propagation of the statistical uncertainty on regions B , C and D .

Region	HAHM Signal samples			Run-2 data
	γ_d mass [GeV]	0.017	0.1	0.4
A (exp.)				276 \pm 32
A (SR)		1076.52 \pm 11.72	259.66 \pm 5.71	34.36 \pm 2.0
B		66.43 \pm 2.93	23.17 \pm 1.71	4.77 \pm 0.73
C		104.96 \pm 3.59	52.07 \pm 2.67	9.01 \pm 1.09
D		6.88 \pm 0.89	4.53 \pm 0.73	1.82 \pm 0.49

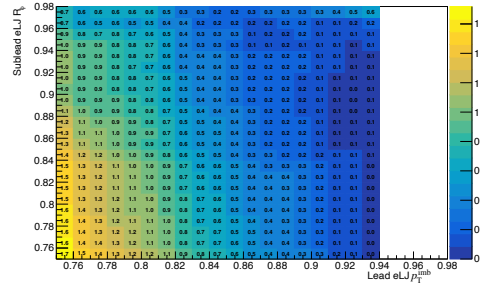
Table 6.22. ABCD yields in the HAHM signal and data driven estimate for background in the eLJ - eLJ channel. Signal yields are normalised to $BR(H \rightarrow 2\gamma_d) = 0.5\%$. Uncertainties on the signal are statistical only, while the uncertainty on the number of expected events in data in region A is obtained from the propagation of the statistical uncertainty on regions B , C and D .



(a) Percentage leakage in CR B



(b) Percentage leakage in CR C



(c) Percentage leakage in CR D

Figure 6.24. Ratio (in percentage) of the number of signal events predicted in the FRVZ benchmark model for a $m_{\gamma_d} = 17\text{MeV}$ γ_d over the number of events in data in CR B (a), CR C (b) and CR D (c), for different values of the leading $eLJ p_T^{\text{imb}}$ and of the farthest $eLJ R_\phi$. The signal yield is normalised to $BR(H \rightarrow 2\gamma_d + X) = 0.5\%$.

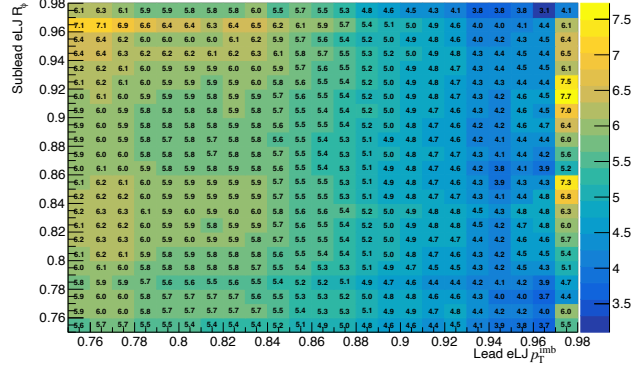


Figure 6.25. Ratio (in percentage) of the number of signal events predicted in the FRVZ benchmark model for a $m_{\gamma_d} = 17 \text{ MeV}$ γ_d in SR A over the number of expected data events for different values of the leading $eLJ p_T^{\text{imb}}$ and of the farthest $eLJ R_\phi$. The signal yield is normalised to $BR(H \rightarrow 2\gamma_d + X) = 0.5\%$.

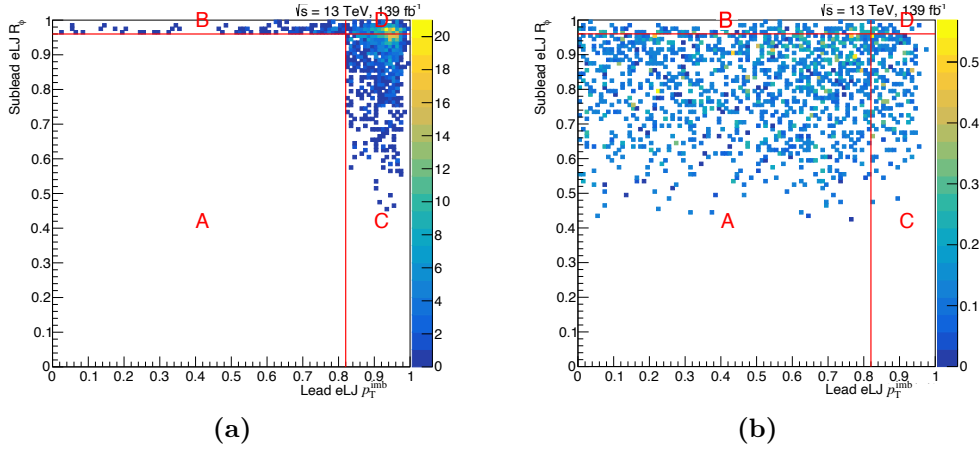


Figure 6.26. ABCD plane, defined in terms of the leading $eLJ p_T^{\text{imb}}$ and farthest $eLJ R_\phi$ variables, for the full Run-2 dataset (a) and the FRVZ benchmark signal sample with $m_{\gamma_d} = 0.1 \text{ GeV}$ (b), where events are normalised to the full Run-2 luminosity.

Validations

The background estimation method is validated on the full Run-2 dataset by using the ABCD method in regions orthogonal to the SR. In such a way, it is possible to check that the number of events extrapolated in the A region via the ABCD method coincides with observed number of events in the same region. This check is performed varying the boundaries of such regions, by sliding either on the leading $e\text{LJ } p_{\text{T}}^{\text{imb}}$ or on the sub-leading $e\text{LJ } R_{\phi}$. Two regions which are orthogonal to the SR are defined via a combination of the B , C and D CRs of the ABCD plane. Such regions are further divided into a new $A'B'C'D'$ plane, where the ABCD ansatz is tested. The B and D regions are merged together, forming a CR (called BD) with $R_{\phi} > 0.96$ for the sub-leading $e\text{LJ}$. Here the test is performed by sliding on the leading $e\text{LJ } p_{\text{T}}^{\text{imb}}$, as can be observed in Fig. 6.27 (a). The C and D regions

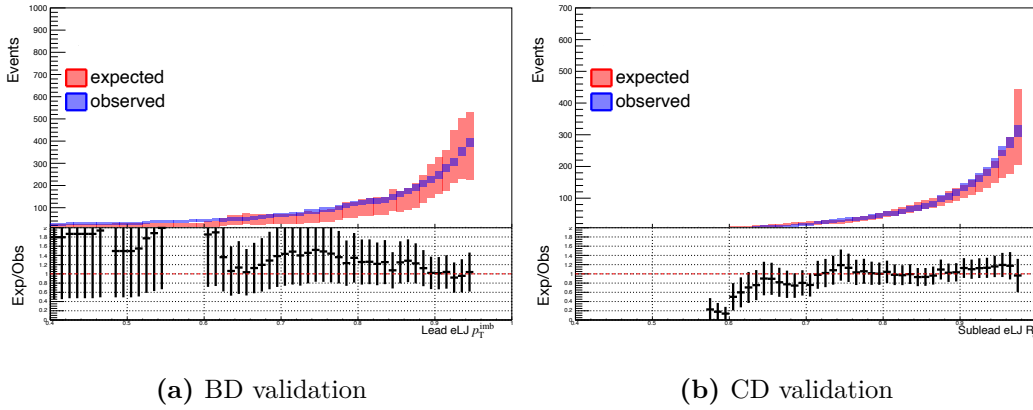


Figure 6.27. Observed (blue) vs. expected (red) number of events in data in the $e\text{LJ}-e\text{LJ}$ channel BD (a) and CD (b) subplanes as a function of the cut on leading $e\text{LJ } p_{\text{T}}^{\text{imb}}$ and on the sub-leading $e\text{LJ } R_{\phi}$ respectively.

are merged together as well, forming a CR (called CD) with $p_{\text{T}}^{\text{imb}} > 0.82$ for the leading $e\text{LJ}$. Here the test is performed by sliding on the sub-leading $e\text{LJ } R_{\phi}$, as can be observed in Fig. 6.27 (b). The expected number of events is in agreement with observed one within 1σ (derived from a combination of the statistical uncertainty of the single B, C and D regions) for all values of $p_{\text{T}}^{\text{imb}}$ and R_{ϕ} .

To further validate the background estimation method, three additional VRs orthogonal to the ABCD plane in Fig. 6.26 (and therefore to the SR) are exploited to confirm the validity of the ABCD plane in the full $p_{\text{T}}^{\text{imb}}$ and R_{ϕ} phase space, including region A . Such VRs are obtained by inverting some of the requirements outlined in Tab. 6.3 and Tab. 6.4:

- VR1 is obtained by requiring that at least one of the $e\text{LJ}$ has $q_{e\text{LJ}} \neq 0$;
- VR2 is obtained by requiring $m_{e\text{LJ}-e\text{LJ}} \in [81, 101]\text{GeV}$;
- VR3 is obtained by requiring $|\eta_{e\text{LJ}}| > 1.52$.

Fig. 6.28, Fig. 6.29 and Fig. 6.30 show respectively the agreement between the number of events observed and extracted with the ABCD method in the A region in the three VRs sliding on the leading $eLJ p_T^{\text{imb}}$ (a) or on the sub-leading $eLJ R_\phi$ (b). As for the previous validation, the expected number of events is in agreement with

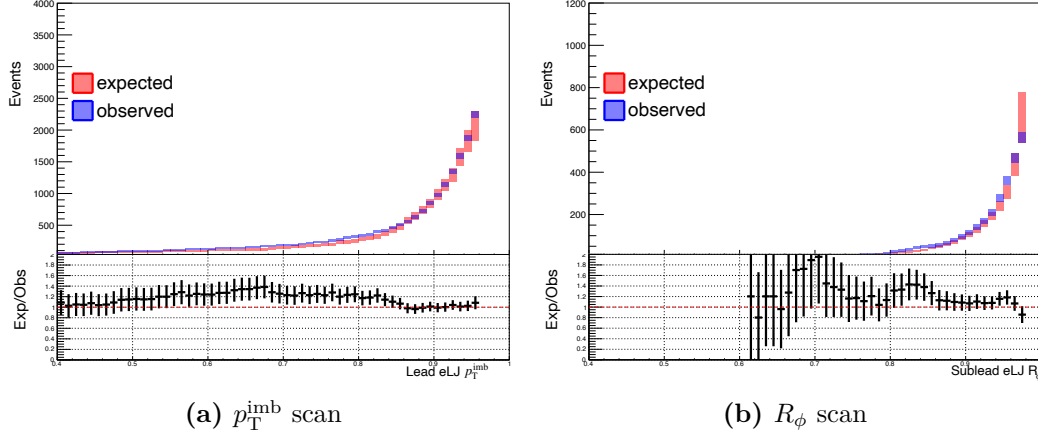


Figure 6.28. Observed (blue) vs. expected (red) number of events in the VR1 data in the eLJ – eLJ channel as a function of the cut on the leading $eLJ p_T^{\text{imb}}$ (a) and on the sub-leading $eLJ R_\phi$ (b).

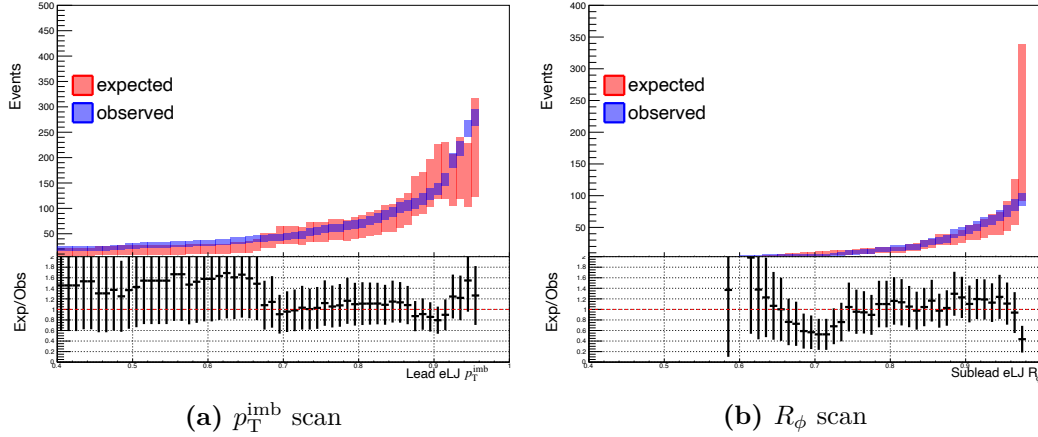


Figure 6.29. Observed (blue) vs. expected (red) number of events in the VR2 data in the eLJ – eLJ channel as a function of the cut on the leading $eLJ p_T^{\text{imb}}$ (a) and on the sub-leading $eLJ R_\phi$ (b).

observed one within 1σ (derived from a combination of the statistical uncertainty of the single B, C and D regions) for all values of p_T^{imb} and R_ϕ .

The impact of the signal contamination in the B, C and D regions is evaluated by testing the agreement between the observed and expected number of events in the BD and CD sub-planes previously defined, after subtracting the simulated signal contributions. Fig. 6.31 shows the robustness of ABCD method under the assumption of a 17 MeV γ_d in the FRVZ benchmark model, and with $BR(H \rightarrow 2\gamma_d + X) = 1\%$ signal contamination. Even when considering a (rather high) signal

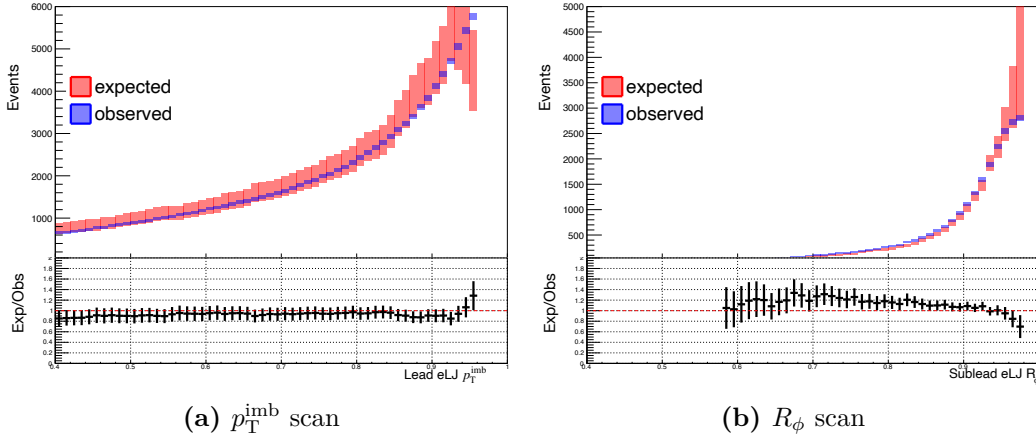


Figure 6.30. Observed (blue) vs. expected (red) number of events in the VR3 data in the $e\text{LJ}-e\text{LJ}$ channel as a function of the cut on the leading $e\text{LJ } p_T^{\text{imb}}$ (a) and on the sub-leading $e\text{LJ } R_\phi$ (b).

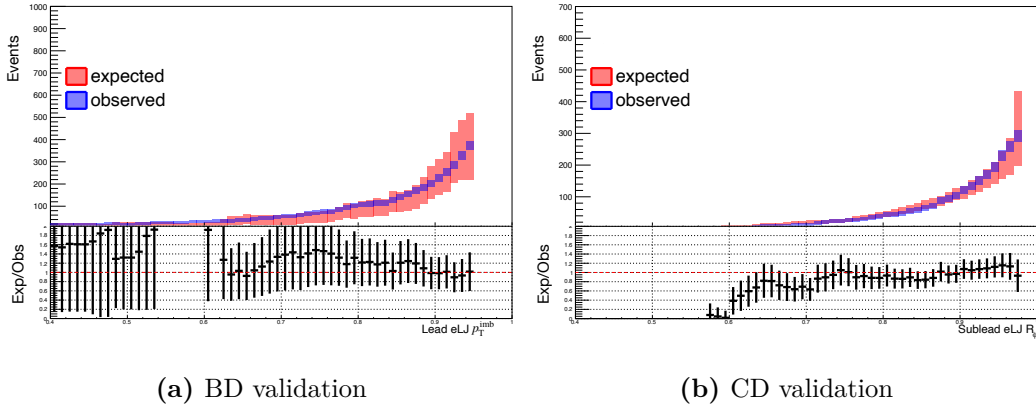


Figure 6.31. Observed (blue) vs. expected (red) number of events in data in the $e\text{LJ}-e\text{LJ}$ channel BD (a) and CD (b) subplanes as a function of the cut on the leading $e\text{LJ } p_T^{\text{imb}}$ and on the sub-leading $e\text{LJ } R_\phi$ respectively, taking into account a $BR(H \rightarrow 2\gamma_d + X) = 1\%$ of signal contamination, assuming a 17 MeV γ_d in the FRVZ benchmark model.

contamination in all the CRs, the expected number of events is in agreement with observed one within 1σ (derived from a combination of the statistical uncertainty of the single B, C and D regions) for all values of p_T^{imb} and R_ϕ . The impact of the signal contamination is evaluated on the expected limits as well, as described in Sec. 6.4.2.

6.3 Systematic Uncertainties

This search relies on fully-data driven background estimation, therefore experimental and theoretical uncertainties affect only the signal. Furthermore, being

a rare phenomena search, its results are expected to be statistically limited. This notwithstanding, potential sources of experimental and theoretical uncertainties are considered for the SR signal yields (and shape as well for the $\mu\text{LJ}-\mu\text{LJ}$ and the $\mu\text{LJ}-e\text{LJ}$ channels). The sources of experimental systematics affecting the three search channels are described in Sec. 6.3.1.

How these uncertainties are included in the fit for the $e\text{LJ}-e\text{LJ}$ channel is described in Sec. 6.4.1 and in Sec. 6.3.2 for both the $\mu\text{LJ}-\mu\text{LJ}$ and the $\mu\text{LJ}-e\text{LJ}$ channels fit. For both the $\mu\text{LJ}-\mu\text{LJ}$ and the $\mu\text{LJ}-e\text{LJ}$ channels, in which the background estimation is performed via a background template extracted from a CR (see Sec. 6.2.1), systematic uncertainties related to the background model and the signal model are considered as well. The uncertainty associated to the signal modelling is describe with the *injection test*, as explained in Sec. 6.3.2, while the bias from the choice of the background model is evaluated with the *spurious signal* method, as discussed in Sec. 6.3.3, while t.

6.3.1 Experimental systematics

The sources of experimental systematics affecting the different search channels are listed below. Such uncertainties can be divided into:

- uncertainties that impact per event weights, that are the per-object uncertainties, such as the ones associated to lepton reconstruction, identification and isolation, and the per-event uncertainties, that are the trigger and the PU reweighting uncertainties;
- uncertainties that impact the net number of events entering the SR, that are the momentum/energy scale and resolution uncertainties;
- uncertainties that impact the overall normalisation of the final event yields in SR, like the luminosity uncertainty.

The luminosity uncertainty impacts in the same way all the channels, the per-event weight impact only the relevant channels (as an example, muon identification uncertainties impact only the $\mu\text{LJ}-\mu\text{LJ}$ and the $\mu\text{LJ}-e\text{LJ}$ channels), while the muon/electron-photon momentum/energy scale and resolution could impact in principle all the search channels.

Luminosity The systematic uncertainty on the integrated luminosity measurement is 0.8%. It is derived following a methodology similar to that detailed in [97], based on a calibration of the luminosity scale using a x-y beam-separation scan with the Luminosity Cherenkov Integrating Detector (LUCID) detector [154].

Pile-Up reweighting Simulated events are re-weighted in such a way that the distribution of the average number of interactions per bunch crossing (PU) matches the one observed in data. A variation in the PU reweighting of the simulation is performed to cover the difference between the predicted and measured inelastic pp

cross-section in the fiducial volume of the detector. This is achieved by shifting the data PU distribution by $\pm 3\%$ before reweighting the MC sample. This uncertainty is propagated through the event selection, and results at most in a $\pm 10\%$ effect on the events yield for the $m_{\gamma_d} = 2 \text{ GeV}$ γ_d hypothesis in the $\mu\text{LJ}-e\text{LJ}$ channel, for the FRVZ model. This uncertainty is conservative as it is affected by the loss of statistics associated in the relative MC sample in the channel SR.

Standard object uncertainties Per-lepton Scale Factors are used to correct the distributions of their reconstruction efficiencies, in terms of isolation and identification, of muons and electrons (see Chap. 4), in such a way that the simulated distributions match the ones observed in data. The uncertainties on these SFs are treated as systematic uncertainties on the final signal selection efficiency. For the $e\text{LJ}-e\text{LJ}$ channel, the largest impact observed is associated to the electron identification uncertainty, resulting at most in a $\pm 2.31\%$ uncertainty on the events yield in the FRVZ model, for a γ_d with $m_{\gamma_d} = 0.06 \text{ GeV}$. For the $\mu\text{LJ}-\mu\text{LJ}$ channel, the largest impact observed is associated to the muon isolation uncertainty (that will be discussed thoroughly in the following), resulting at most in a $\pm 1.2\%$ uncertainty on the events yield in the FRVZ model, for a γ_d with $m_{\gamma_d} = 0.4 \text{ GeV}$. For the $\mu\text{LJ}-e\text{LJ}$ channel, the largest impact observed is associated to the electron identification uncertainty, resulting at most in a $\pm 3.98\%$ uncertainty on the events yield in the FRVZ model, for a γ_d with $m_{\gamma_d} = 6 \text{ GeV}$.

Trigger uncertainties Per-event Scale Factors are used to correct the distributions of the trigger efficiencies (see Sec. 3.2.6), in such a way that the simulated distributions match the ones observed in data. The uncertainties on these SFs are treated as systematic uncertainties on the final signal selection efficiency. For the $e\text{LJ}-e\text{LJ}$ channel, the impact of this uncertainty is negligible for the HAHM model and is a flat $\pm 0.2\%$ on the events yield for all the m_{γ_d} hypotheses for FRVZ model. For the $\mu\text{LJ}-\mu\text{LJ}$ channel, the largest impact result in a $\pm 1.8\%$ uncertainty on the events yield in the FRVZ model, for a γ_d with $m_{\gamma_d} = 0.4 \text{ GeV}$. For the $\mu\text{LJ}-e\text{LJ}$ channel, the largest impact result in a $\pm 1.84\%$ uncertainty on the events yield in the FRVZ model, for a γ_d with $m_{\gamma_d} = 6 \text{ GeV}$.

$e - \gamma$ energy scale and resolution The $e\gamma$ energy scale and resolution uncertainties are considered as well. It is expected that such uncertainties should impact mostly channels where $e\text{LJs}$ are reconstructed. For the $e\text{LJ}-e\text{LJ}$ channel, the largest impact observed is associated to the electron energy scale, resulting at most in a $\pm 1.11\%$ uncertainty on the events yield in the FRVZ model, with a γ_d with $m_{\gamma_d} = 0.06 \text{ GeV}$. For the $\mu\text{LJ}-e\text{LJ}$ channel, the largest impact observed is associated to the electron energy scale, resulting at most in a $\pm 4.75\%$ uncertainty on the events yield in the FRVZ model, with a γ_d with $m_{\gamma_d} = 2 \text{ GeV}$. Such uncertainties have been evaluated in the $\mu\text{LJ}-\mu\text{LJ}$ channel as well and they were found to be negligible.

Muon energy scale and resolution The muon momentum scale and resolution uncertainties are considered as well. It is expected that such uncertainties should impact mostly channels where μ LJs are reconstructed. For the μ LJ- μ LJ channel, the largest impact observed is associated to the muon momentum resolution, resulting at most in a $\pm 0.92\%$ uncertainty on the events yield in the FRVZ model, with a γ_d with $m_{\gamma_d} = 0.24$ GeV. For the μ LJ- e LJ channel, the largest impact observed is associated to the muon momentum resolution, resulting at most in a $\pm 0.76\%$ uncertainty on the events yield in the FRVZ model, with a γ_d with $m_{\gamma_d} = 6$ GeV. Such uncertainties have been evaluated in the e LJ- e LJ channel as well and they were found to be negligible.

Muon corrected isolation A corrected isolation is applied for muons reconstructed in μ LJs (see Sec. 5.3.1), in order to recover the sensitivity to the very boosted topology studied in this search. Since the improvements in the signal efficiency via the usage of this corrected variable are extremely sizeable, additional validation studies are performed to assess whether the uncertainties derived for the standard isolation can be used for this corrected isolation too.

The goal of such cross-checks is evaluating whether the subtraction of tracks or clusters associated with high-level objects modifies the performance of the isolation WP or the estimation of the truth level isolation. To do so, the FRVZ simulated signal sample with $m_{\gamma_d} = 6$ GeV is used, since for such a m_{γ_d} the distribution of the angular separation between the two muons reconstructed within a μ LJ peaks around the isolation cone size used in this search ($\Delta R = 0.3$) (see Sec. 5.2). Both muons found in the μ LJ cone are required to pass the *Loose* identification criteria (as in Sec. 5.2), while no isolation requirement is obviously applied.

The first check performed is aimed at ensuring that the subtraction of the track associated with an additional muon found in the μ LJ cone would yield a `ptvarcone30` distribution compatible with the one obtained for muons in μ LJs that are open enough to not fall within the same isolation cone. To do so, μ LJs candidates are separated into two categories depending on the opening angle $\Delta R_{\mu\mu}$ between muons: the boosted category, where $\Delta R_{\mu\mu} < 0.29$, so that each muon fall in the isolation cone of the other, and the resolved category, where $\Delta R_{\mu\mu} > 0.31$, so that each muon fall outside the isolation cone of the other. Fig. 6.32 (a) shows the reconstructed corrected track isolation distributions for these two categories, that are compatible with a $\chi^2 = 49.5$ ($p(\chi^2) = 45\%$).

Therefore, no change in performance is expected in the transition region for muons separated by an angular distance close to the isolation cone.

After the subtraction, additional tracks or clusters not belonging to the additional muons might be also mistakenly removed, biasing the estimation of the truth isolation energy (even though this is not likely, since muons leave a rather clean signature in the detector). To demonstrate that this is not the case, the corrected truth charged isolation energy is compared to the corrected reconstructed one as a function of the angular separation $\Delta R_{\mu\mu}$ between the two muon candidates within the μ LJ. The corrected truth charged isolation energy is defined as the scalar sum of the transverse momentum of all stable particles found within a cone of $\Delta R = 0.3$

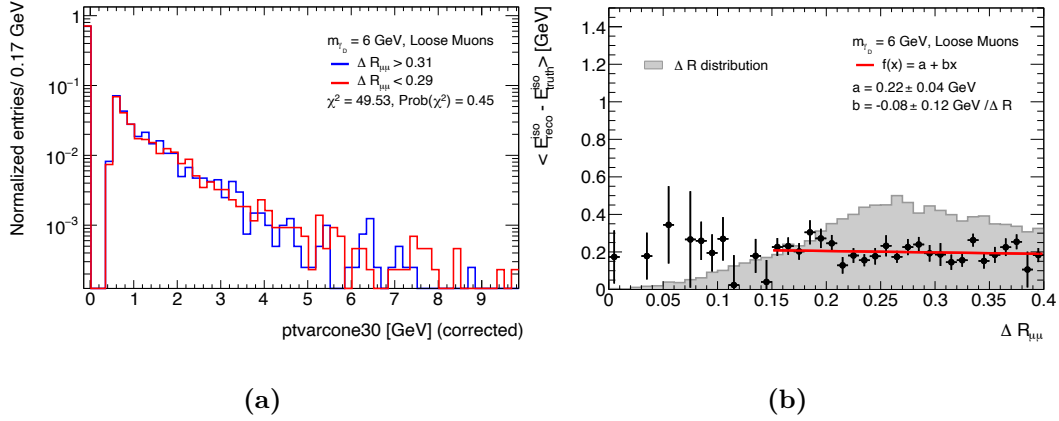


Figure 6.32. (a) Corrected track isolation distribution `ptvarcone30` for μ LJs muons found within (red) and outside (blue) the same isolation cone for a γ_d with $m_{\gamma_d} = 6$ GeV produced via the FRVZ benchmark model; (b) difference between the truth and reconstructed corrected track isolation for muons inside μ LJs as a function of their truth opening angle $\Delta R_{\mu\mu}$ for a γ_d with $m_{\gamma_d} = 6$ GeV produced via the FRVZ benchmark model. In grey the $\Delta R_{\mu\mu}$ distribution for the studied MC sample is shown as well.

around each muon candidate, where, if a second muon is found within the cone, its true transverse momentum is subtracted (as in the reconstructed charged isolation energy). Fig. 6.32 (b) shows that the average difference between the reconstructed and the truth level track isolation variables is constant around the transition region ($\Delta R_{\mu\mu} \sim 0.3$). Given the results obtained, no additional systematic uncertainty is considered for the correction of the isolation variables due to the nearby muon.

Impact on the signal yields

The impact of these experimental systematic uncertainties on the signal yields is determined from a reprocessed simulation, in which variations by $\pm 1\sigma$ (called *up* and *down* variations, referring respectively to a $+1\sigma$ and -1σ variations) of each uncertainty are evaluated. The absolute impact on the yields associated to $+1\sigma$ variations differ in principle from the one associated to -1σ variations. Therefore, per each systematic uncertainty the largest deviation from the nominal yield is taken as a symmetric uncertainty on the signal yields.

A summary of the experimental systematic uncertainties taken into account in this analysis are given for the muonic channel in Tab. 6.23 and Tab. 6.24, respectively for the FRVZ and HAHM benchmark models, for the electronic channel in Tab. 6.25 Tab. 6.26, respectively for the FRVZ and HAHM benchmark models and for the mixed channel in Tab. 6.27 Tab. 6.27, respectively for the FRVZ and HAHM benchmark models. The systematics not found in the tables are negligible ($< 0.1\%$ impact on the signal yields).

As can be seen by these tables, the overall impact of the systematic uncertainties (which are assumed to be uncorrelated) is rather small, being at most the 10% for the μ LJ- e LJ channel.

m_{γ_d} [GeV]	Muon triggers (%)	Muon isolation (%)	Momentum resolution (%)	Momentum scale (%)	Lumi (%)	PRW (%)	Total (%)
0.24	1.34	1.03	0.92	0.57	0.83	1.37	2.56
0.40	1.77	1.16	0.91	0.71	0.83	1.46	2.92
0.90	1.47	1.09	0.51	0.20	0.83	1.38	2.49
2	1.45	1.05	0.76	0.43	0.83	1.94	2.89
6	0.67	0.64	0.68	0.64	0.83	1.78	2.35
10	0.13	0.27	0.10	0.11	0.83	2.95	3.07
15	0.10	0.18	-	-	0.83	3.76	3.85

Table 6.23. Summary table of the impact of the experimental systematic uncertainties for the FRVZ signal samples in the $\mu\text{LJ}-\mu\text{LJ}$ channel. Uncertainties below the per-mill level are not shown. PRW stands for the uncertainty associated to the PU reweighting.

m_{γ_d} [GeV]	Muon triggers (%)	Muon isolation (%)	Momentum resolution (%)	Momentum scale (%)	Lumi (%)	PRW (%)	Total (%)
0.40	0.62	0.51	0.59	0.35	0.83	0.91	1.60
2	0.58	0.51	0.39	0.17	0.83	0.94	1.51
10	0.17	0.25	0.28	0.23	0.83	0.60	1.11
15	0.1	0.14	-	-	0.83	0.41	0.91
25	0.1	0.14	-	-	0.83	1.55	1.75

Table 6.24. Summary table of the impact of the experimental systematic uncertainties for the HAHM signal samples in the $\mu\text{LJ}-\mu\text{LJ}$ channel. Uncertainties below the per-mill level are not shown. PRW stands for the uncertainty associated to the PU reweighting.

m_{γ_d} [GeV]	Electron triggers (%)	Electron isolation (%)	Electron ID (%)	Electron reconstruction (%)	Energy resolution (%)	Energy scale (%)	Lumi (%)	PRW (%)	Total (%)
0.017	0.2	0.3	2.15	1.26	0.65	0.4	0.83	0.8	2.7
0.03	0.2	0.3	2.26	1.29	0.66	0.3	0.83	2.2	3.5
0.06	0.2	0.3	2.31	1.29	1.11	0.8	0.83	3.9	4.9
0.10	0.2	0.3	2.21	1.27	0.69	0.7	0.83	3.6	4.5
0.24	0.2	0.3	2.19	1.33	0.7	0.1	0.83	8.6	9.0

Table 6.25. Summary table of the impact of the experimental systematic uncertainties for the FRVZ signal samples in the $e\text{LJ}-e\text{LJ}$ channel. Uncertainties below the per-mill level are not shown. PRW stands for the uncertainty associated to the PU reweighting.

m_{γ_d} [GeV]	Electron triggers (%)	Electron isolation (%)	Electron ID (%)	Electron reconstruction (%)	Energy resolution (%)	Energy scale (%)	Lumi (%)	PRW (%)	Total (%)
0.017	-	0.1	0.69	1.11	0.20	0.16	0.83	1.0	1.7
0.1	-	0.1	0.83	1.08	0.27	0.3	0.83	1.0	1.7
0.4	-	0.1	0.70	1.06	0.50	0.7	0.83	1.0	1.8
2	-	-	0.46	1.15	-	-	0.83	7.4	7.5

Table 6.26. Summary table of the impact of the experimental systematic uncertainties for the HAHM signal samples in the $e\text{LJ}-e\text{LJ}$ channel. Uncertainties below the per-mill level are not shown. PRW stands for the uncertainty associated to the PU reweighting.

m_{γ_d} (GeV)	Triggers (%)	Muon isolation (%)	Electron reconstruction (%)	Electron ID (%)	Electron isolation (%)	PRW reconstruction (%)	Energy resolution (%)	Energy scale (%)	Momentum resolution (%)	Momentum scale (%)	Total (%)
0.24	0.77	1.10	0.38	0.53	0.10	2.17	0.23	0.29	0.12	0.25	2.68
0.40	0.49	1.16	0.36	0.48	0.10	1.33	0.15	-	0.19	0.35	1.98
0.90	0.63	1.14	0.25	0.26	-	6.56	0.56	0.58	0.52	-	6.77
2	0.65	1.00	0.69	1.33	0.91	7.59	4.75	4.71	-	-	10.34
6	1.84	0.55	1.37	3.98	2.66	2.66	-	0.32	0.76	0.66	6.06

Table 6.27. Summary table of the impact of the experimental systematic uncertainties for the FRVZ signal samples in the μ LJ- e LJ channel. Uncertainties below the per-mill level are not shown. PRW stands for the uncertainty associated to the PU reweighting.

m_{γ_d} (GeV)	Triggers (%)	Muon reconstruction (%)	Muon isolation (%)	Electron reconstruction (%)	Electron ID (%)	Electron isolation (%)	PRW (%)	Energy scale (%)	Momentum scale (%)	Total (%)
0.40	0.28	0.10	0.53	0.36	0.25	-	-	0.10	0.17	0.78
2	0.15	0.12	0.56	0.37	0.26	-	3.9	0.48	-	4.00
10	0.35	0.16	0.28	1.14	0.42	0.10	0.43	0.11	-	1.38

Table 6.28. Summary table of the impact of the experimental systematic uncertainties for the HAHM signal samples in the μ LJ- e LJ channel. Uncertainties below the per-mill level are not shown. PRW stands for the uncertainty associated to the PU reweighting.

Impact on the signal shape

The muon momentum scale and resolution uncertainties, beside affecting the signal yields as shown in the previous section, could have a non negligible impact on the signal shape. Muon momentum scale variations translate into shifts in the peak position of the invariant mass distribution, while muon momentum resolution variations shrink/widen this distribution. The effect of both uncertainties in the signal shape is determined from a reprocessed simulation, in which variations by $\pm 1\sigma$ of the momentum scale and resolution are used instead of nominal ones.

The impact of such variations are shown as an example in Fig. 6.33 for a γ_d with $m_{\gamma_d} = 2$ GeV, where the γ_d is produced via the HAHM benchmark model.

The reconstructed invariant mass distributions are parametrised using the same signal model as the one explained in Sec. 6.2.1, fixing all the parameters of the model except for the peak position μ_{CB} (the width σ_{CB}) when evaluating the uncertainty related to the muon momentum scale (resolution). The measured peak position (width) for the reprocessed samples, $\mu_{CB}^{\text{up/down}}$ ($\sigma_{CB}^{\text{up/down}}$), is compared to the values obtained in Sec. 6.2.1. The systematic effect is then estimated by quantifying the difference on the peak (width) for both variations with respect to the nominal value. The effect of changing the muon momentum scale (resolution) by $\pm 1\sigma$ for each simulated signal is found to be negligible and therefore this systematic is not included.

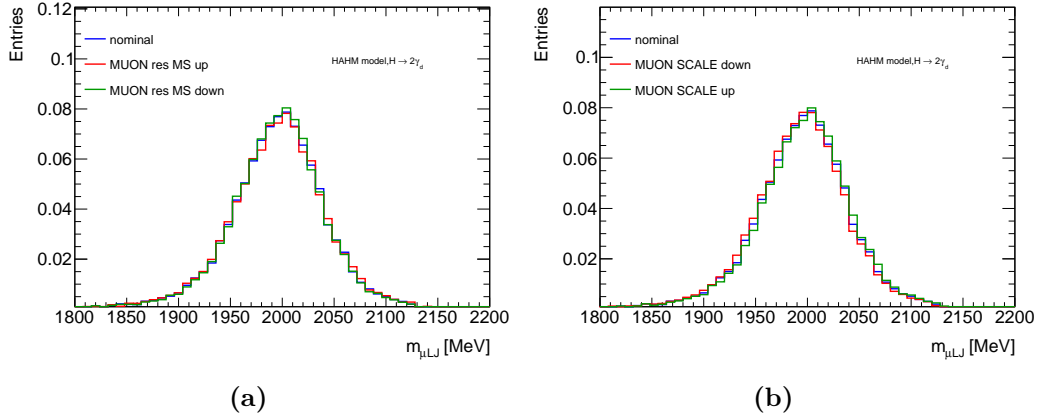


Figure 6.33. (a) Muon momentum resolution up (red) and down (green) variations and (b) muon momentum scale up (green) and down (red) variations impact on the μLJ invariant mass spectrum for a γ_d with $m_{\gamma_d} = 2\text{ GeV}$ produced via the HAHM model.

6.3.2 Signal model uncertainties

For the $\mu\text{LJ}-\mu\text{LJ}$ and $\mu\text{LJ}-e\text{LJ}$ channels, where a bump-hunt strategy is used (see Sec. 6.2.1) for the background estimation, uncertainty on the signal modelling is considered as well. The uncertainties shown in Sec. 6.3.1 impact the normalisation of the DSCB PDF used for the modelling of the signal. These uncertainties are included in the fit via nuisance parameters constrained by Gaussian or log-normal penalty terms, as explained in Sec. 6.5.1. As said in the previous section, uncertainties related to the muon momentum scale and resolution on the μLJ invariant mass shape are found to be negligible and are therefore not included. In order to account for the imperfect description of the invariant mass distribution of the generated signal MC events by the chosen parameterisation, a so-called *injection test*, briefly outlined in the following, is performed.

Injection test

The potential bias introduced by the signal modelling is evaluated with an *injection test*, using generated pseudo-data from the background model described in Eq. 6.1. Signal events from the different MC samples associated to the various signal hypotheses are injected, with a normalisation N_{Inj} , on top of the generated pseudo-data.

The normalisation of injected signal events N_{Inj} used is obtained from the expected sensitivity to an excess of events over the background found below the signal peak, denominated effective background $N_{B,\text{eff}}$:

$$N_{\text{Inj}} = 2 * \sqrt{N_{B,\text{eff}}}; \quad N_{B,\text{eff}} = \int_{\mu_{\text{DSCB}} - 2\sigma_{\text{DSCB}}}^{\mu_{\text{DSCB}} + 2\sigma_{\text{DSCB}}} B(m_{\mu\mu}) dm_{\mu\mu}. \quad (6.8)$$

where $B(m_{\mu\mu})$ is the background PDF in Eq. 6.1 and μ_{DSCB} and σ_{DSCB} are respectively the peak and the width of the Gaussian core of the DSCB PDF used

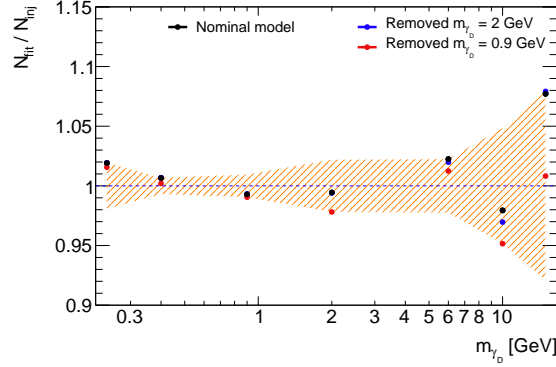


Figure 6.34. Ratio between the fitted number of signal events N_{fit} and the injected N_{inj} ones for the FRVZ model in the $\mu\text{LJ}-\mu\text{LJ}$ channel. The markers denote the different parameterisations used to perform the injection tests: in black, the nominal parameterisation exploiting all the available mass points, in red (blue) the parameterisation of the model obtained without the 0.9 GeV (2 GeV) mass point.

for describing the signal μLJ invariant mass shape. A fit using the model $N_{\text{fit}}f_S + N_{B,\text{eff}}B(m_{\mu\mu})$ is performed, with f_S being the signal DSCB PDF of Eq. 6.2 and N_B being the number of fitted background events. The obtained value for N_{fit} is compared to the injected N_{inj} . Such a test is performed for the different signal models (for different m_{γ_d} hypotheses and for both the HAHM and FRVZ benchmark model) for both the $\mu\text{LJ}-\mu\text{LJ}$ and the $e\text{LJ}-\mu\text{LJ}$ channels. The results of this test are shown in Fig. 6.34 for the FRVZ model in the $\mu\text{LJ}-\mu\text{LJ}$ channel.

To validate the parameterisation of the DSCB parameters as a function of m_{γ_d} , the injection test is performed also by removing an intermediate mass point (0.9 GeV and 2 GeV) from the interpolation fit of the DSCB parameters as a function of m_{γ_d} . The largest difference per mass point between the injected and fitted signal for each of the configurations is assigned as a systematic uncertainty.

Such uncertainty on the signal modeling ranges from 1% up to 5% for m_{γ_d} below 10 GeV in the FRVZ benchmark model and for the $\mu\text{LJ}-\mu\text{LJ}$ channel⁴.

The same test is repeated for the $e\text{LJ}-\mu\text{LJ}$ channel using the $\mu\text{LJ}-\mu\text{LJ}$ channel signal shape modelling, since, as discussed in Sec. 6.2.1, it accurately describes the μLJ invariant mass spectrum in this channel as well.

As for the $\mu\text{LJ}-\mu\text{LJ}$ channel, the injection test has been performed both including the full signal modelling and excluding two intermediate mass points, namely the $m_{\gamma_d} = 0.9\text{ GeV}$ and $m_{\gamma_d} = 2\text{ GeV}$ ones. In addition, the test including all the points has been performed by injecting not only $N_{\text{inj}} = 2 * \sqrt{N_{B,\text{eff}}}$, but also $N_{\text{inj}} = 4 * \sqrt{N_{B,\text{eff}}}$ and $N_{\text{inj}} = 10 * \sqrt{N_{B,\text{eff}}}$, compatible respectively with a 4σ and a 10σ fluctuation. These tests are shown respectively in Fig. 6.35 (a) and Fig. 6.35 (b).

⁴As already said in Sec. 6.2.1, the point at $m_{\text{gamma}_d} = 15\text{ GeV}$ suffers from lack of statistics and is thus excluded from the signal shape modelling. The discrepancy between the number of injected and fitted signal events for such a signal hypothesis is precisely due to the fact that this point is excluded from the modelling.

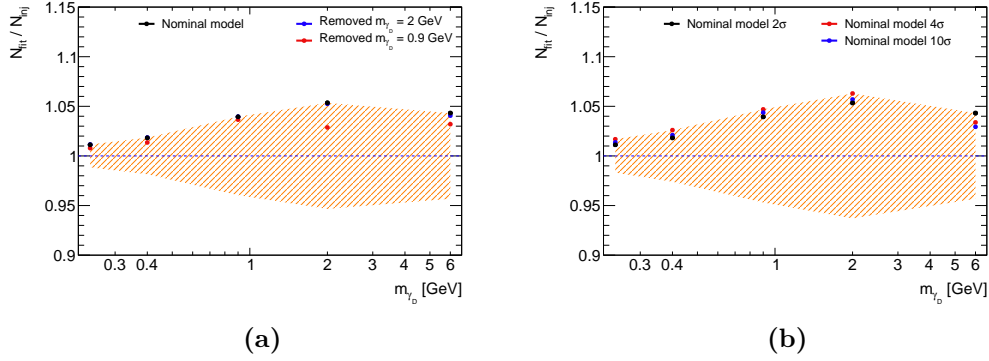


Figure 6.35. Ratio between the fitted number of signal events N_{fit} and the injected N_{inj} ones for the FRVZ model in the $\mu\text{LJ}-e\text{LJ}$ channel. In (a) the markers denote the different parameterisations used to perform the injection tests: in black, the nominal parameterisation exploiting all the available mass points, in (a) in red (blue) the parameterisation of the model obtained without the 0.9 GeV (2 GeV) mass point. In (b) the markers denote the different number of injected events: in black a 2σ fluctuation of the background, while in red (blue) a 4σ (10σ) fluctuation of the background.

Fig. 6.35 (a) further shows how the $\mu\text{LJ}-\mu\text{LJ}$ modelling is accurate to describe the μLJ invariant mass spectrum in the $\mu\text{LJ}-e\text{LJ}$ channel as well, while Fig. 6.35 (b) shows how the discrepancy between the number of injected and fitted signal events is stable against different number of injected events, showing at most a 5% discrepancy.

The injection test is performed for the HAHM model for both the channels, and the resulting uncertainties are included in the relevant fits. Being this systematic an uncertainty on the overall signal normalisation it is included in the fit as such via a nuisance parameter constrained a log-normal penalty term.

6.3.3 Background modelling systematics

The *true* shape of the non-resonant background distribution in data is unknown and the strategy chosen in this analysis is to describe it with an analytical function with a finite number of parameters. However, a particular functional form may not provide a sufficiently good description of the background shape, leading to a fit bias denominated *spurious signal*. A poor description of the background template could indeed either induce or absorb potential signal events. To perform the so called *spurious signal test*, the signal plus background model is fitted to a background-only template, on the CR distribution, which is known to be signal-free. The test is repeated for different γ_d mass hypotheses and using the signal shape and acceptance modellings respectively in Eq. 6.2 and Eqs. 6.6, 6.4. Since the CR sample contains by definition only background events, the fitted signal is actually just a symptom of the discrepancy between the analytic function used to model the background shape

and the real background shape itself⁵ (therefore the use of the term *spurious* signal). A cartoon illustration of the spurious signal test for a given tested m_{γ_d} hypothesis is presented in Fig. 6.36.

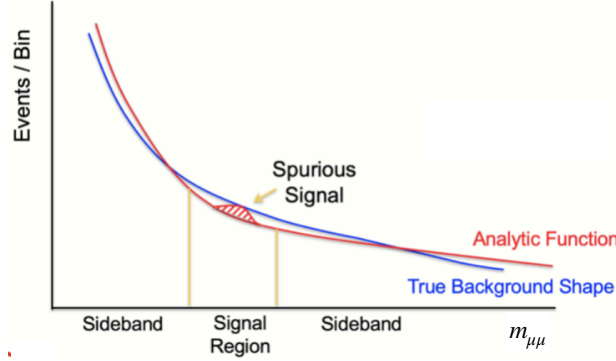


Figure 6.36. Cartoon illustration of the spurious signal test. The *true* shape of the continuum background is shown in blue. The fitted signal plus background PDF is shown in red. Due to the mis-modelling of the analytic background of the real shape, a non-zero signal is fit as well, in order to improve the overall fit quality. In this manner, the background mis-modelling is parameterised in terms of a signal yield [155].

Background template smoothing

The *spurious signal test* requires either very-large statistic templates or smoothed versions of them, since otherwise the fitted signal yield would be heavily affected by statistical fluctuations, providing a poor estimate of the spurious signal itself. Since generating very-large statistic templates require expensive computational resources, and specifically doing so in such an unconventional phase space would be highly inefficient, a smoothing technique is used in this search.

Such procedures rely on the assumption that the content of a given bin can be estimated using the surrounding bins as constraints. One of the possible smoothing techniques is the so called Gaussian Processing Regression (GPR) [156], where the bin contents ν_i (i being the bin index) that define the templates are constrained by the Gaussian PDF G :

$$G(\nu_i; r_i, C) = \frac{1}{\sqrt{(2\pi)^N |C|}} \exp \left(-\frac{1}{2} \sum_{i,j=1}^N (r_i - \nu_i) C_{ij}^{-1} (r_j - \nu_j) \right),$$

with N being the total number of bins, r_i the reference unconstrained content of the bin, C the covariance matrix between the bins of the templates and $|C|$

⁵However, being derived from a signal plus background fit, the *spurious signal* is not exactly the difference between the true background shape and the functional form used to describe it, since it also depends on the shape of the signal being looked for, though it is largely correlated to the choice of the background modelling.

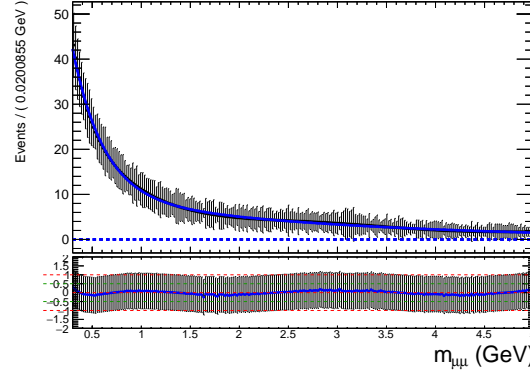


Figure 6.37. Smoothed background template for the $\mu\text{LJ}-\mu\text{LJ}$ channel CR.

being the determinant of such a matrix. The covariance matrix can be written as $C_{i,j} = K(m_i, m_j)$ with m_i and m_j being the central values of the bins and K being the so-called *kernel* function, a smooth function of the observable considered (in this case the μLJ invariant mass) that encodes the correlation between two different bins.

Such a kernel function can be either derived from auxiliary measurements or from MC simulations that constraint the background shape. Instead, when looking for narrow resonances (like in this search) over a falling background, an ad-hoc kernel can be built to impose correlation between bins at a scale small enough to accommodate the variations of the background but large enough to avoid absorbing a possible signal in the background model.

An example of such a kernel is provided by the so-called Radial Basis Function (RBF) or *squared exponential kernel*, defined as:

$$K(m, m') = \exp\left(-\frac{(m - m')^2}{2l^2}\right),$$

where $(m - m')^2$ is the Euclidean distance and l is the correlation length scale: if any two points m, m' are farther than l they are uncorrelated, whilst if they are closer than l they are correlated, with the correlation encoded in K . The length scale should then be larger than the resonances resolution but small enough to capture background variations between bins.

The obtained template has small statistical fluctuations, similarly to an Asimov dataset. However, the template should be normalized to the same total yield as the real dataset, in order for the bin per bin uncertainties to be representative of those in data.

This smoothing procedure is applied on both the $\mu\text{LJ}-\mu\text{LJ}$ and the $e\text{LJ}-\mu\text{LJ}$ channels CRs defined in Sec. 6.2.1, since those templates have such a limited statistics that the spurious signal test would be completely dominated by the statistical fluctuations of the templates themselves. In Fig. 6.37 the smoothed distribution obtained from the $\mu\text{LJ}-\mu\text{LJ}$ CR background template of Fig. 6.9 is shown as an example.

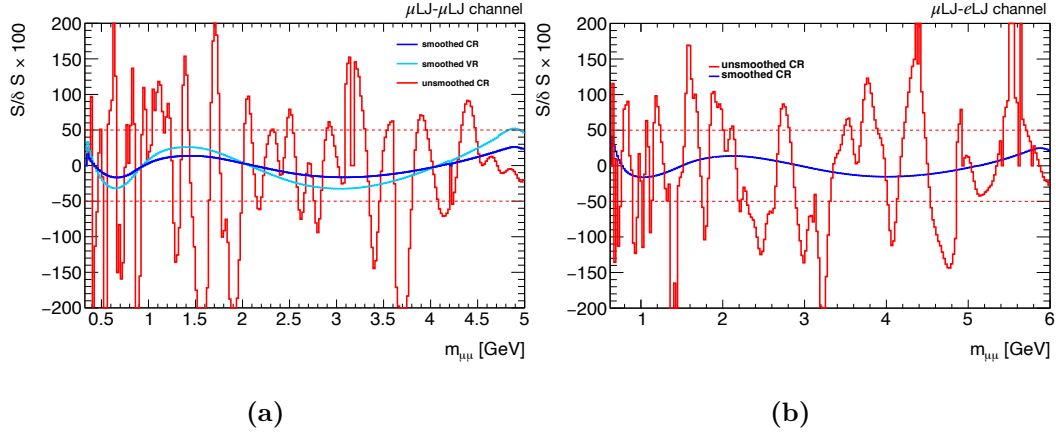


Figure 6.38. Number of fitted spurious signal events for different m_{γ_d} hypotheses over the uncertainty on the number of background events found below the signal resonance for the smoothed (un-smoothed) background template in blue (red) in the $\mu\text{LJ}-\mu\text{LJ}$ CR (a) and in the $\mu\text{LJ}-e\text{LJ}$ CR (b). In the $\mu\text{LJ}-\mu\text{LJ}$ channel the same test is performed for the VR as well, and is reported in azure.

Spurious signal test

The smoothed background templates (signal free by construction) are fitted using $N_{SS}f_S + N_{B,\text{eff}}B(m_{\mu\mu})$, with N_{SS} being the number of spurious signal events, $N_{B,\text{eff}}$ being the number of events found below the signal resonance, as defined in Eq. 6.8, and f_S and $B(m_{\mu\mu})$ being respectively the signal PDF of Eq. 6.2 and the background PDF of Eq. 6.1. The number of fitted spurious signal events is compared to the uncertainty on $N_{B,\text{eff}}$: if N_{SS} is larger than $0.5 \times \sqrt{N_{B,\text{eff}}}$, the background modelling is considered to be not reliable, as the number spurious signal events would dominate over the statistical uncertainty of the background found in the resonance region [157].

The $N_{SS}/\sqrt{N_{B,\text{eff}}}$ for the $\mu\text{LJ}-\mu\text{LJ}$ in Fig. 6.38 (a) ($\mu\text{LJ}-e\text{LJ}$ in Fig. 6.38 (b)) CR background template before the smoothing is compared to the one associated to the smoothed $\mu\text{LJ}-\mu\text{LJ}$ CR template.

The spurious signal derived from the un-smoothed CR is heavily affected by the statistical fluctuations of the background template, therefore yielding a spurious signal uncertainty that greatly exceeds $0.5 \times \sqrt{N_{B,\text{eff}}}$. The smoothed template, instead, yields a number of spurious signal events which is contained within the prescriptions.

The absolute value of N_{SS} for the $\mu\text{LJ}-\mu\text{LJ}$ CR background template before the smoothing is compared to the one associated to the smoothed $\mu\text{LJ}-\mu\text{LJ}$ CR and to the smoothed $\mu\text{LJ}-\mu\text{LJ}$ VR in Fig. 6.39 (a), while Fig. 6.39 (b) shows N_{SS} for the $\mu\text{LJ}-e\text{LJ}$ CR background template before (red) and after (blue) the smoothing. The maximum number of fitted spurious signal events is 3, obtained through the spurious signal test performed on the VR smoothed template for the $\mu\text{LJ}-\mu\text{LJ}$ channel and on the CR smoothed template for the $\mu\text{LJ}-e\text{LJ}$ channel. Therefore, 3 spurious signal events are taken as flat uncertainty on the background modelling over the full mass

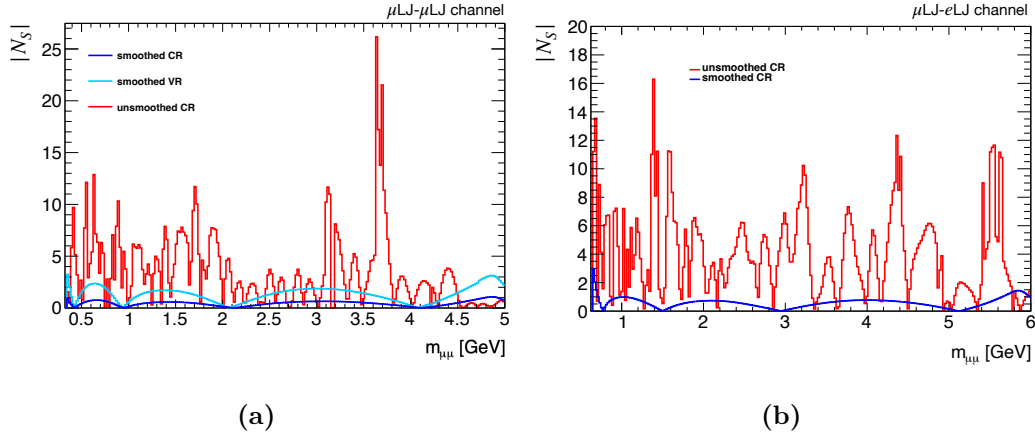


Figure 6.39. Number of fitted spurious signal events for different m_{γ_d} hypotheses for the smoothed (un-smoothed) background template in blue (red) in the $\mu\text{LJ}-\mu\text{LJ}$ CR (a) and in the $\mu\text{LJ}-e\text{LJ}$ CR (b). In the $\mu\text{LJ}-\mu\text{LJ}$ channel the same test is performed for the VR as well, and is reported in azure.

range investigated for both the channels.

However, since the normalisation of the background in the SR is unknown, the spurious signal test is performed assuming different normalisation of the background, as shown in Fig. 6.40.

In the $\mu\text{LJ}-\mu\text{LJ}$ CR 600 events are found, and it can be seen how the spurious signal uncertainty is contained below the prescription even when the background normalisation is 8 times larger than the one observed in the CR. This notwithstanding, the number of background events in the SR is expected to be much less than the one in the CR, since the $2\mu\text{LJ}$ s reconstruction requirement is expected to greatly suppress the number of background events.

The same test with analogous conclusions has been performed for the modelling of the $e\text{LJ}-\mu\text{LJ}$ channel background as well, and the resulting uncertainty is included for this channel too.

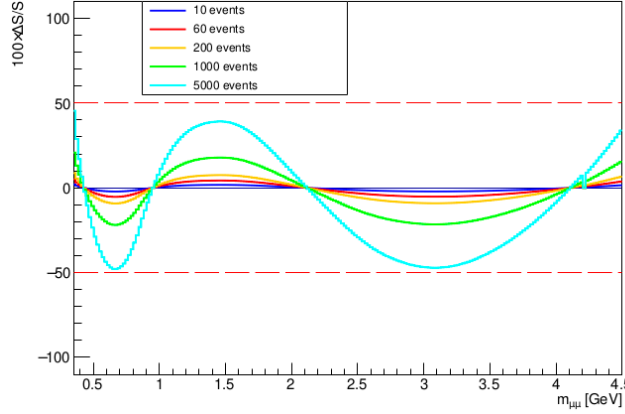


Figure 6.40. Number of fitted spurious signal events for different m_{γ_d} hypotheses for the smoothed $\mu\text{LJ}-\mu\text{LJ}$ CR background template, assumig different normalisation of the template itself.

6.4 Results for the electronic channel

In this section, the fitting technique for the $e\text{LJ}-e\text{LJ}$ channel is outlined in Sec. 6.4.1, while in Sec. 6.4.2 the results of this search are given in terms of expected sensitivity of the channel for both the investigated models.

6.4.1 Fitting technique

A likelihood based ABCD method [152] has been developed for the simultaneous data-driven background estimation and signal hypothesis test. The background estimation in signal region A is obtained by performing a fit to the background and signal yields in the four regions. The fitted likelihood describes the signal and background expectation in each region, defined by products of Poisson functions, and takes the following form:

$$\mathcal{L}(n_A, n_B, n_C, n_D | s, b, \tau_B, \tau_C) = \prod_{i=A,B,C,D} \frac{e^{-N_i} N_i^{n_i}}{n_i!},$$

where n_A, n_B, n_C, n_D are the number of events observed in each region in data, τ_B and τ_C are the nuisance parameters that describe the ABCD ansatz and N_i are linear combinations of the signal and background expectations in each region, defined as follows:

$$\begin{aligned} N_A &= s + b \\ N_B &= s \varepsilon_B + b \tau_B \\ N_C &= s \varepsilon_C + b \tau_C \\ N_D &= s \varepsilon_D + b \tau_C / \tau_B, \end{aligned}$$

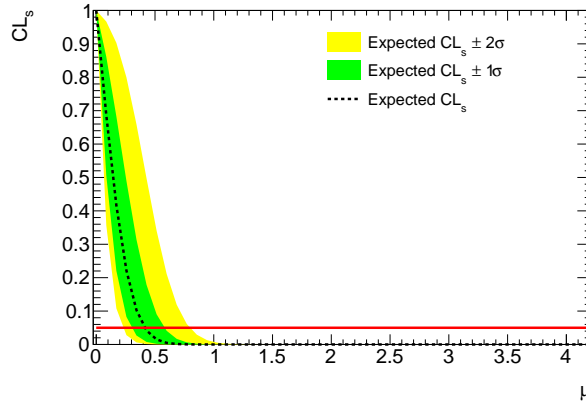
where s and b are respectively the signal and the background yield in region A and the signal contamination in the region i is described by ε_i ⁶.

All the parameter values are allowed to float in the fit to the four data regions. The upper limit on the signal strength is obtained with the CL_s method [158], performing a global simultaneous fit, with the asymptotic calculator based on the profile likelihood test statistics [159], in order to normalise the observed data in all the regions to the signal expectation. The presence of an excess generated by the signal is then evaluated by comparing the estimated number of events in the SR to the observed data.

All the systematic uncertainties described in Sec. 6.3 are included in the fit as nuisance parameters, parametrised with Gaussian PDFs that multiply the fit likelihood. The Gaussian PDFs mean values are constrained by the parameter nominal value and the variance is defined by the 68% of the systematic uncertainty associated to the parameter.

6.4.2 Expected sensitivity

Upper limits on the signal strength, and conversely on $BR(H \rightarrow 2\gamma_d + X)$ and on $BR(H \rightarrow 2\gamma_d)$ respectively for the FRVZ and HAHM model are obtained performing a fit as described in Sec. 6.4.1. Fig. 6.41 shows the expected upper limit at the 95% CL on the signal strength for the $e\text{LJ}-e\text{LJ}$ channel, for the FRVZ benchmark model assuming a Dark Photon mass of 0.1 GeV.



(a)

Figure 6.41. Expected upper limit at 95% CL on the signal strength μ for the $e\text{LJ}-e\text{LJ}$ channel, when assuming a 0.1 GeV Dark Photon in the FRVZ benchmark model. Here $BR(H \rightarrow 2\gamma_d + X) = 1\%$ and a 10% systematic uncertainty is used.

Expected upper limits on $BR(H \rightarrow 2\gamma_d + X)$ as a function of the γ_d mass for

⁶The signal contamination in the CR i , with $i = B, C, D$, is defined as $\frac{s_i}{s_A}$, with s_A being the signal yield in SR A and s_i being the signal yield in the i -th CR. Such contaminations can be derived per each m_{γ_d} hypothesis from Tab. 6.21 and Tab. 6.22 for respectively the FRVZ and the HAHM models. For all the CRs and signal hypotheses in both the models ε_i is below the 10%.

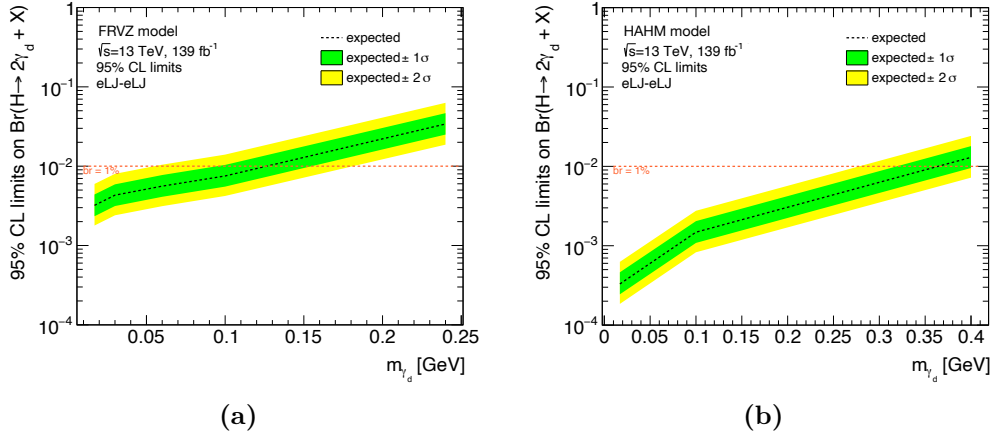


Figure 6.42. Expected upper limits at the 95% CL on (a) $BR(H \rightarrow 2\gamma_d + X)$ for the FRVZ benchmark model and on (b) $BR(H \rightarrow 2\gamma_d)$ for the HAHM benchmark model in the full γ_d mass range in the eLJ - eLJ channel.

the FRVZ and the HAHM benchmark models are shown respectively in Fig. 6.42 (a) and Fig. 6.42 (b).

6.5 Results for the muonic and mixed channel

In this section, the fitting technique for both the eLJ - μLJ and μLJ - μLJ channels is outlined in Sec. 6.5.1. The results of this search are given in Sec. 6.5.2 in terms of expected sensitivity for the mixed channel and in Sec. 6.5.3 in terms of observed limits for the muonic channel.

6.5.1 Fitting technique

Signal and background yields for the μLJ - μLJ and eLJ - μLJ channels are estimated from an un-binned maximum-likelihood fit of the signal-plus-background model to the data. The full likelihood can be written as:

$$F(m_{\mu\mu}; \sigma_{fid}, m_{\gamma_d}, N_b, \mathbf{a}, \mathbf{a}_{\gamma_d}, \boldsymbol{\theta}) = N_{sig}^{channel}(\sigma_{fid}, m_{\gamma_d}, \boldsymbol{\theta}) f_s(m_{\mu\mu}; m_{\gamma_d}, \mathbf{a}_{\gamma_d}) + N_b B(m_{\mu\mu}, \mathbf{a}),$$

where f_s and $B(m_{\mu\mu})$ are the PDF describing respectively the signal (Eq. 6.2), through the set of parameters \mathbf{a}_{γ_d} , and the background (Eq. 6.1), through the set of parameters \mathbf{a} ; $N_{sig}^{channel}$ and N_b are respectively the number of signal or background events in a specific channel (either the μLJ - μLJ or the eLJ - μLJ one) SR; σ_{fid} is the fiducial cross section of the investigated process and $\boldsymbol{\theta}$ denotes the set of systematic uncertainties affecting N_{γ_d} , as listed below:

- θ_{exp} : the total experimental uncertainty (Sec. 6.3.1);
- θ_{lumi} : the uncertainty on the integrated luminosity of the data sample (Sec. 6.3.1);
- θ_{sig} : the signal modelling systematic derived from the injection test (Sec. 6.3.2);

- θ_{SS} : the spurious signal systematic (Sec. 6.3.3).

The background yield N_b is a free parameter in the fit, while the signal yield N_{sig}^{channel} is parametrised as:

$$N_{sig}^{\text{channel}}(\sigma_{fid}, \boldsymbol{\theta}_{N_{\gamma_d}}, \theta_{SS}) = \sigma_{fid} L_{int}(\mathcal{A} \times \epsilon(m_{\gamma_d}))|_{\text{channel}} \prod_k^{\dim \boldsymbol{\theta}_{N_{\gamma_d}}} K_k(\theta_k) + \sigma_{ss} \theta_{ss} + \sigma_{sig} \theta_{sig},$$

where L_{int} is the integrated luminosity of the sample; $(\mathcal{A} \times \epsilon(m_{\gamma_d}))|_{\text{channel}}$ is the acceptance times efficiency of the specified channel (see Eq. 6.4 and Eq. 6.6); K_k is a function characterizing the effect of the k -th normalisation systematic, θ_{ss} and σ_{ss} are respectively the background modelling uncertainty and its associated nuisance parameter and θ_{sig} and σ_{sig} are respectively the signal modelling uncertainty and its associated nuisance parameter. The fiducial cross section can be parametrised as

$$\sigma_{fid} = \sigma_{\text{ggF}} \times \text{BR}(H \rightarrow 2\gamma_d(+X))$$

with (without) the $+X$ in the BR expression for the FRVZ (HAHM) benchmark model and with σ_{ggF} being the ggF cross section. The $\text{BR}(\gamma_d \rightarrow l\bar{l})$ dependency is instead encoded in the acceptance times efficiency, as in Eq. 6.4 and Eq. 6.6. The index k runs over the set of systematic uncertainties affecting N_{sig} , so the $K_i(\theta_i)$ factors implement each of the systematic uncertainties on the number of signal events as listed above. The expression $K_k(\theta_k)$ is:

$$K_k(\theta_k) = [r_k m_{\gamma_d}]^{\theta_k} \quad \text{with} \quad r_k(m_{\gamma_d}) = \begin{cases} \frac{N_{sig,+k}(m_{\gamma_d})}{N_{sig}(m_{\gamma_d})} & \text{if } \theta_k > 0 \\ \frac{N_{sig}(m_{\gamma_d})}{N_{sig,-k}(m_{\gamma_d})} & \text{if } \theta_k < 0 \end{cases}$$

where $\pm k$ represents the positive/negative systematic variation on $N_{sig}(m_{\gamma_d})$ for a given systematic i . This expression ensures that the modifications to the signal event yields for $\theta_k = \pm 1$ are equal to the $\pm 1\sigma$ variations used to define the uncertainties.

6.5.2 Expected sensitivity for the mixed channel

Upper limits on the signal strength, and conversely on $\text{BR}(H \rightarrow 2\gamma_d + X)$ and on $\text{BR}(H \rightarrow 2\gamma_d)$ respectively for the FRVZ and HAHM model, are obtained with the CL_s method performing the global simultaneous fit as described in Sec. 6.5.1, with the asymptotic calculator based on the profile likelihood test statistics.

A plot for the 95% CL limit on the $\text{BR}(H \rightarrow 2\gamma_d(+X))$ for different γ_d mass hypotheses for the $\mu\text{LJ}-e\text{LJ}$ channel is shown for the FRVZ model in Fig. 6.43 and for the HAHM model in Fig. 6.44.

These exclusion plots are obtained assuming the normalisation of the background template found in the $\mu\text{LJ}-e\text{LJ}$ CR, that is one thousand events. Fig. 6.43 (a) and Fig. 6.44 (a) show the excluded $\text{BR}(H \rightarrow 2\gamma_d + X)$ when taking into account

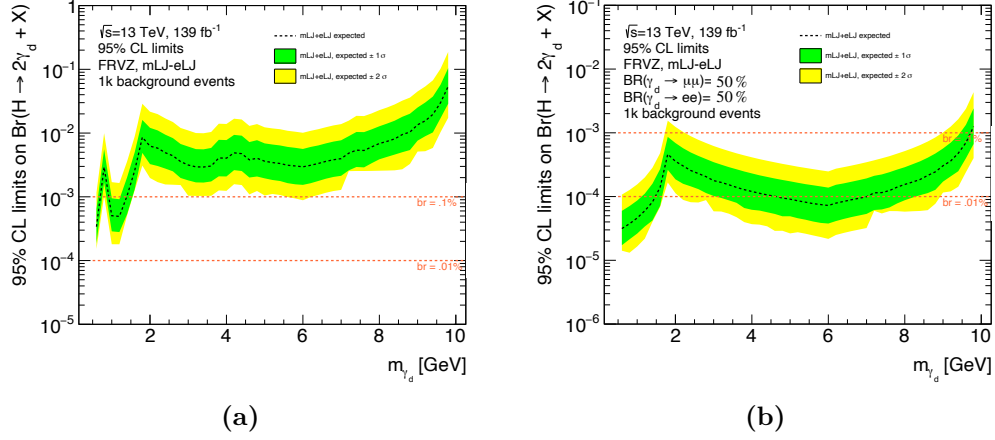


Figure 6.43. 95% CL exclusion limit on the $BR(H \rightarrow 2\gamma_d + X)$ in the $eLJ\text{--}\mu LJ$ channel: (a) taking into account $BR(\gamma_d \rightarrow \mu\mu)$ and $BR(\gamma_d \rightarrow ee)$ and (b) assuming both $BR(\gamma_d \rightarrow \mu\mu) = 100\%$ and $BR(\gamma_d \rightarrow ee) = 100\%$ per each m_{γ_d} hypothesis in the FRVZ benchmark model. The expected limit (dotted line) is shown along with its $\pm 1\sigma$ (green) and $\pm 2\sigma$ (yellow) bands uncertainties. The background template is normalised to the event yield observed in the $eLJ\text{--}\mu LJ$ CR in data, which is one thousand events.

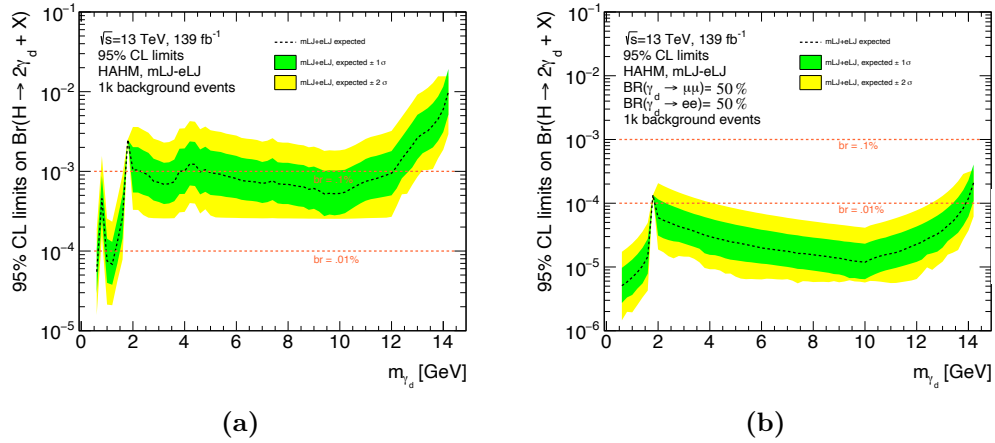


Figure 6.44. 95% CL exclusion limit on the $BR(H \rightarrow 2\gamma_d)$ in the $eLJ\text{--}\mu LJ$ channel: (a) taking into account $BR(\gamma_d \rightarrow \mu\mu)$ and $BR(\gamma_d \rightarrow ee)$ and (b) assuming both $BR(\gamma_d \rightarrow \mu\mu) = 100\%$ and $BR(\gamma_d \rightarrow ee) = 100\%$ per each m_{γ_d} hypothesis in the HAHM benchmark model. The expected limit (dotted line) is shown along with its $\pm 1\sigma$ (green) and $\pm 2\sigma$ (yellow) bands uncertainties. The background template is normalised to the event yield observed in the $eLJ\text{--}\mu LJ$ CR in data, which is one thousand events.

$2BR(\gamma \rightarrow \mu\mu) \times BR(\gamma \rightarrow ee)$ in the normalisation of the signal yields (see Eq. 6.6), while in Fig. 6.43 (b) and Fig. 6.44 (b) $BR(\gamma \rightarrow \mu\mu) = 50\%$ and $BR(\gamma \rightarrow ee) = 50\%$ is assumed. In such a way, it's clear how the expected exclusion limit is driven by the interplay between the background shape and the acceptance times efficiency shown in Fig. 6.20 (b).

6.5.3 Observed limits for the muonic channel

The number of events found in the μLJ - μLJ channel SR is 112, a much smaller yield, roughly 1/6, of what is observed in the respective CR (as expected). The μLJ invariant mass distribution for data in SR is shown in Fig. 6.45 (a) along with the fitted background PDF (see Eq. 6.1), while Fig. 6.45 (b) and Fig. 6.45 (c) show the μLJ invariant mass distribution for respectively the leading and the sub-leading μLJ found in the event.

The p_T of the μLJ impacts the μLJ invariant mass distribution: the more boosted the μLJ the more the combinatorial background is suppressed and the more instead the resonances production is enhanced. The combinatorial background is more prominent in the CR as well, since the leading muon was often found in the open μ pair rather than in the μLJ . Some discrepancies were indeed expected and the functional form used to model the background template is flexible enough to capture the differences in these shapes. Tab. 6.29 shows the fitted background PDF parameters (see Eq. 6.1) for the inclusive SR, for the one with the leading μLJ only (b) and the one with the sub-leading μLJ (c).

The mean and the width of the J/ψ are taken from the CR fit, while the fractions of events due to production of other resonances, around whose the exclusion fit is not performed, were found to be negligible and they are therefore not reported.

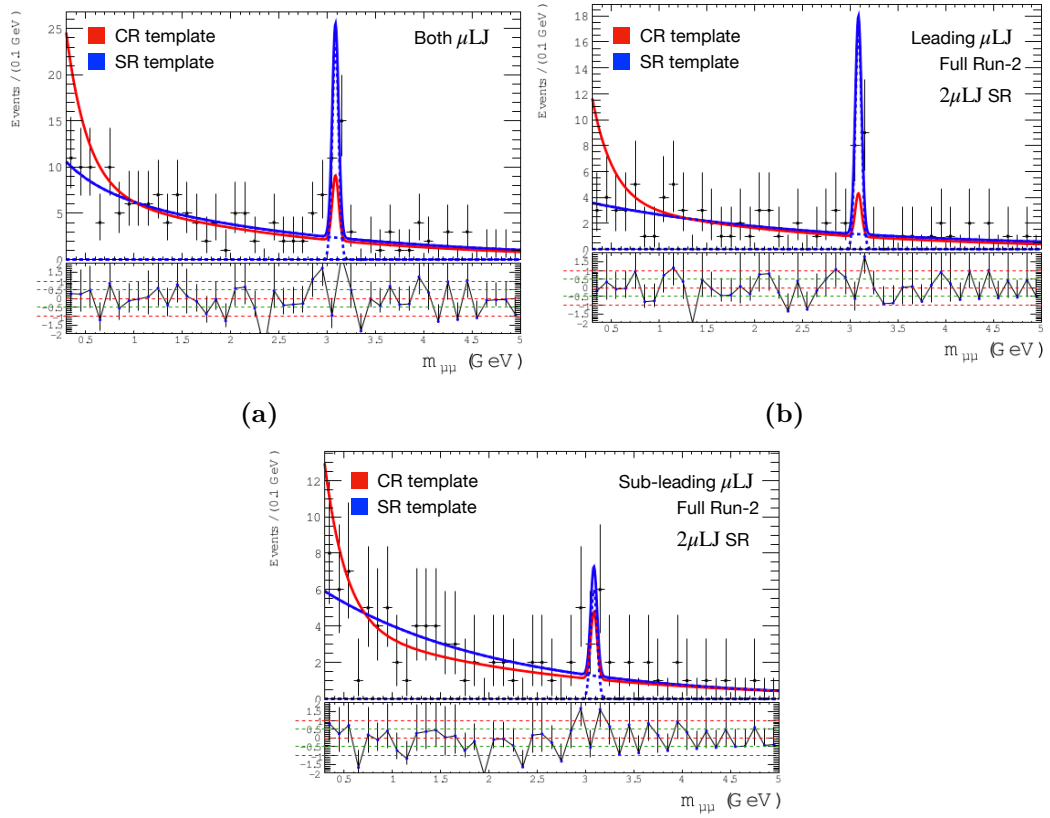


Figure 6.45. Invariant mass distribution for (a) both μLJ s (b) leading μLJ and (c) sub-leading μLJ found in events in the $\mu\text{LJ}-\mu\text{LJ}$ SR in the full Run-2 dataset in the $\mu\text{LJ}-\mu\text{LJ}$ SR. The fitted background only PDF (blue solid line) is overlaid to data points (black dots). The background PDF with the parameters extracted from the $\mu\text{LJ}-\mu\text{LJ}$ CR reported in Tab. 6.11 is shown as well (red solid line).

Parameter	Fitted value	Parameter	Fitted value
f_{exp}	0.6 ± 0.3	f_{exp}	0.61 ± 0.20
$f_{J/\psi}$	0.1 ± 0.03	$f_{J/\psi}$	0.15 ± 0.05
τ	$(1.2 \pm 0.9) \text{ GeV}$	τ	$(3.2 \pm 0.7) \text{ GeV}$
τ_2	$(3.0 \pm 0.3) \text{ GeV}$	τ_2	$(1.3 \pm 1.8) \text{ GeV}$
(a)		(b)	

Parameter	Fitted value
f_{exp}	0.6 ± 0.2
$f_{J/\psi}$	0.04 ± 0.03
τ	$(2.08 \pm 0.24) \text{ GeV}$
τ_2	$(0.4 \pm 0.3) \text{ GeV}$
(c)	

Table 6.29. Fitted parameters of the $B(m_{\mu\mu})$ PDF (see Eq. 6.1) with their relative uncertainty extracted from a fit on the $2\mu\text{LJs}$ (a), leading (b) and sub-leading μLJ (c) invariant mass distribution observed in data in the $\mu\text{LJ}-\mu\text{LJ}$ SR.

No local excess compatible with two DPs decaying into muon pairs has been found, and this results into exclusion limits on $BR(H \rightarrow 2\gamma_d(+X))$. By using the fitting technique outlined in Sec. 6.5.1, upper limits on the $BR(H \rightarrow 2\gamma_d(+X))$ are therefore obtained with the CL_s method performing the global simultaneous fit as described in Sec. 6.5.1, with the asymptotic calculator based on the profile likelihood test statistics.

Plots for the 95% CL limit on the $BR(H \rightarrow 2\gamma_d(+X))$ for different γ_d mass hypotheses for the $\mu\text{LJ}-\mu\text{LJ}$ channel for the FRVZ model and the HAHM one are shown respectively in Fig. 6.46 and in Fig. 6.47.

The expected limit is obtained from a fit over an Asimov template extracted from the observed distribution of data in SR. Fig. 6.46 (a) and Fig. 6.47 (a) show respectively the excluded $BR(H \rightarrow 2\gamma_d(+X))$ when taking into account $BR(\gamma \rightarrow \mu\mu)^2$ in the normalisation of the signal yields, while in Fig. 6.46 (b) and in Fig. 6.47 (b) $BR(\gamma \rightarrow \mu\mu) = 100\%$ is assumed. In such a way, it's easy to see how the exclusion limit is driven, where the background flattens out, only by the acceptance times efficiency of this channel (see Fig. 6.20 (a)).

In the FRVZ model, $BR(H \rightarrow 2\gamma_d + X) < 2\%$ are excluded for $m_{\gamma_d} < 15 \text{ GeV}$. In the same mass range, a constraint of $BR(H \rightarrow 2\gamma_d) < 0.5\%$ is obtained for the HAHM model, which is able to extend the constraint up to $m_{\gamma_d} = 22 \text{ GeV}$, with $BR(H \rightarrow 2\gamma_d) < 10\%$. The limits obtained in the HAHM model are thus more stringent than the ones obtained in the FRVZ model, as a consequence of the more boosted (and collimated) topology foreseen in the former model.

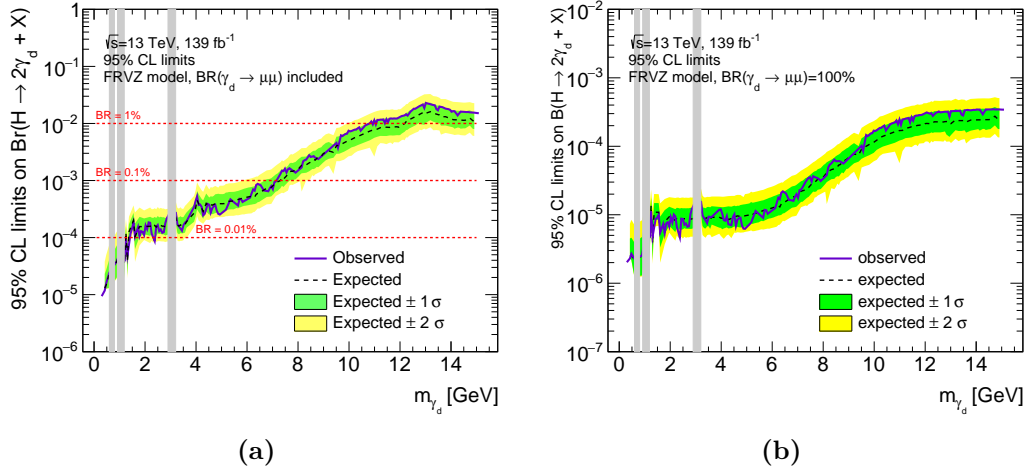


Figure 6.46. 95% CL exclusion limit on $BR(H \rightarrow 2\gamma_d + X)$ in the $\mu LJ-\mu LJ$ channel: (a) taking into account the $BR(\gamma_d \rightarrow \mu\mu)$ and (b) assuming $BR(\gamma_d \rightarrow \mu\mu) = 100\%$ per each m_{γ_d} hypothesis in the FRVZ benchmark model. The observed limit (solid line) is compared to the expected one (dashed line) along with its $\pm 1\sigma$ (green) and $\pm 2\sigma$ (yellow) bands uncertainties. Grey areas are vetoed as they correspond to μLJ invariant masses compatible to the mass of SM resonances decaying into muons.

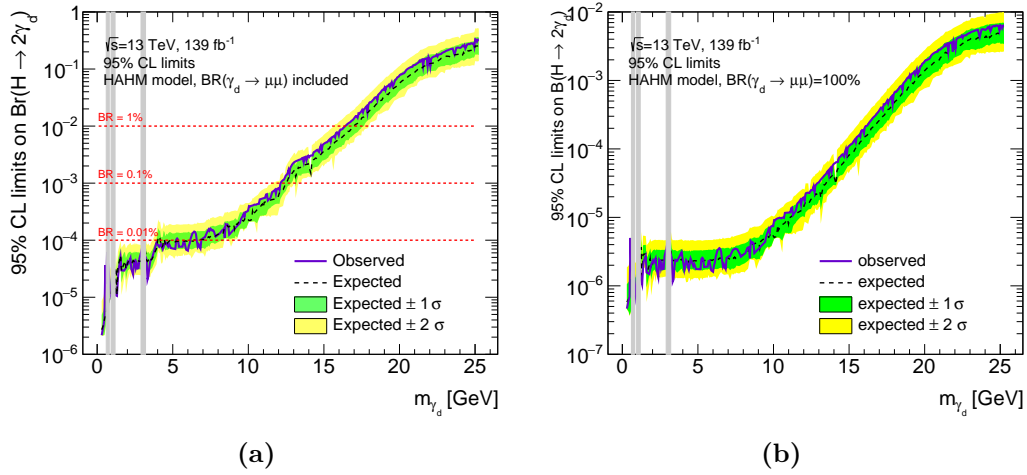


Figure 6.47. 95% CL exclusion limit on $BR(H \rightarrow 2\gamma_d)$ in the $\mu LJ-\mu LJ$ channel: (a) taking into account the $BR(\gamma_d \rightarrow \mu\mu)$ and (b) assuming $BR(\gamma_d \rightarrow \mu\mu) = 100\%$ per each m_{γ_d} hypothesis in the HAHM benchmark model. The observed limit (solid line) is compared to the expected one (dashed line) along with its $\pm 1\sigma$ (green) and $\pm 2\sigma$ (yellow) bands uncertainties. Grey areas are vetoed as they correspond to μLJ invariant masses compatible to the mass of SM resonances decaying into muons.

6.6 Comparison with the Run-1 search

The search for prompt Lepton-Jets carried out during Run-1 [81] by the ATLAS collaboration investigated a DP mass range of $[0.24, 2]\text{GeV}$ exploiting the FRVZ benchmark signature. This search exploits for the first time the HAHM benchmark signature as well, a standard benchmark used in DPs searches carried out by both the ATLAS and the CMS collaborations.

From the expected sensitivity obtained in the $e\text{LJ}-e\text{LJ}$ channel, it's clear how here the mass range $m_{\gamma_d} < 0.24\text{GeV}$ is for the first time probed for promptly decaying DPs. From such studies, this mass range is expected to be ruled out assuming $BR(H \rightarrow 2\gamma_d + X)$ well below the $BR(H \rightarrow inv)$ constraint.

This search extends the sensitivity to promptly decaying DPs for the mass range $m_{\gamma_d} > 2\text{GeV}$ as well. The $\mu\text{LJ}-\mu\text{LJ}$ channel alone indeed excludes the existence of DPs with masses up to 15GeV with $BR(H \rightarrow 2\gamma_d + X)$ at most of the order of the 2%, and the mixed channel is expected to further tighten these constraints.

In the mass range already probed by the Run-1 search, here competitive constraints are set. As an example, the Run-1 exclusion limit on $BR(H \rightarrow 2\gamma_d + X)$ as a function of the mean proper lifetime of the DP itself is shown in Fig. 6.48 for a DP produced in the FRVZ benchmark model and with $m_{\gamma_d} = 0.4\text{GeV}$.

In the prompt regime, a $\sigma_{\text{ggF}}(8\text{TeV}) \times BR(H \rightarrow 2\gamma_d + X) = 4 \cdot 10^{-2}\text{pb}$ is excluded, corresponding to roughly $BR(H \rightarrow 2\gamma_d + X) = 10^{-3}$ (taking into account the ggF cross section, that at $\sqrt{s} = 8\text{TeV}$ is 21.4pb [20]). Such a constraint is obtained by combining all the three search channels (defined like the ones of this search) of the Run-1 analysis. Using the $\mu\text{LJ}-\mu\text{LJ}$ channel alone, a $BR(H \rightarrow 2\gamma_d + X) < 10^{-4}$ is instead excluded in this search in the same mass range.

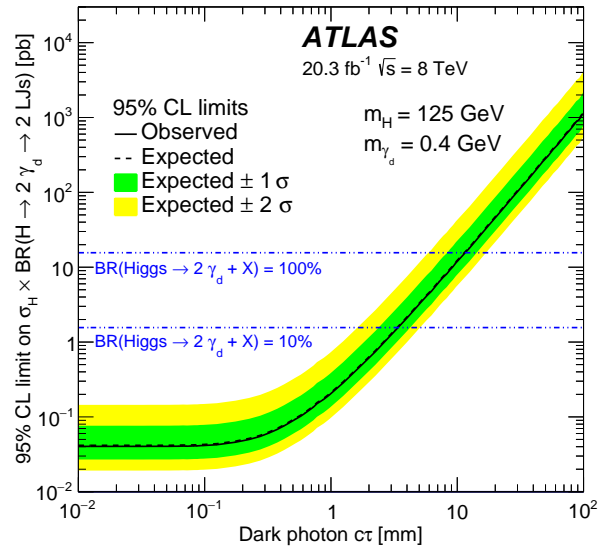


Figure 6.48. 95% CL exclusion limit on $BR(H \rightarrow 2\gamma_d + X)$ as a function of the γ_d mean proper lifetime for the three search channels of the Run-1 prompt search [81] combined. The DP has a mass of 400 MeV and is produced via the FRVZ benchmark model. Plot from Ref. [81].

Chapter 7

LLPs search using the monojet signature

In this chapter, a search for BSM LLPs using the so-called *monojet* signature [2] (already introduced in Sec. 2.3.2) is described. LLPs are foreseen in the SM, as explained in Sec. 7.1, since they arise whenever their decay is suppressed. For this reason, LLPs could exist in BSM scenarios as well, and they have been looked for by the LHC collaborations in the recent years (see [160, 161] for a review of BSM LLPs searches at the LHC).

If LLPs are so long-lived that they decay outside the detectors they are produced in, they would yield as signature of their passage missing energy E_T^{miss} (see Sec. 4.3), that could be potentially high if they are produced in association with ISR jets, yielding the aforementioned *monojet* signature. This search investigates the possibility that either the Dark Photon or an additional BSM scalar (see Sec. 2.4.3) could be detector stable.

In Sec. 7.2 the dataset and the MC samples exploited in this search are listed. A brief overview of the *monojet* search is given in 7.3 along with its analysis regions (Sec. 7.3.1), the fitting technique (Sec. 7.3.2) and the most relevant sources of systematic uncertainties (Sec. 7.3.3). In Sec. 7.4, *reweightings* of the MC samples performed in this analysis are described, with Sec. 7.4.1 discussing the so-called *Higgs p_T reweighting* and Sec. 7.4.2 the so-called Life-Time Reweighting (LTR). Finally, in Sec. 7.5, the results of this search, obtained with the Request Efficiency Computation for Alternative Signal Theories (RECAST) framework [162], are given. This framework allows to use the background predictions of the original search [2] to test new physics models, and to include detector-related systematic uncertainties for the signal samples. The results presented in this chapter have been published by the ATLAS collaboration as a public note in June 2021 [3].

7.1 The life-time frontier

The mean proper lifetime τ_X of a particle X is related to its decay width Γ_X via

$$\Gamma_X = \frac{1}{\tau_X} = \frac{1}{2m_X} \int d\Pi_f |M(m_X \rightarrow p_f)|^2, \quad (7.1)$$

with m_X being the X particle mass, M the matrix element for its decay into the decay products p_f and $d\Pi_f$ the phase space associated to the decay. Therefore, a particle could gain a sizeable proper lifetime if the matrix element and/or the phase space associated to its decay are small.

The matrix element can be small when the process happens as consequence of a small symmetry breaking or of effective higher order dimension operators (this being the mechanism which gives rise to long lifetimes to weakly decaying particles in the SM), whilst the phase space can suppress the process if almost mass-degenerate spectra or if a highly virtual intermediate state is present. SM particles can therefore become long-lived in a variety of ways, with their lifetimes spanning an extremely wide range of magnitudes, as can be seen from Fig. 7.1, from the Z boson with $\tau_Z \sim 2 \times 10^{-25}$ s to the proton with $\tau_p > 10^{34}$ yr and the electron, which is instead stable. It is therefore reasonable to assume that BSM particles could be long-lived,

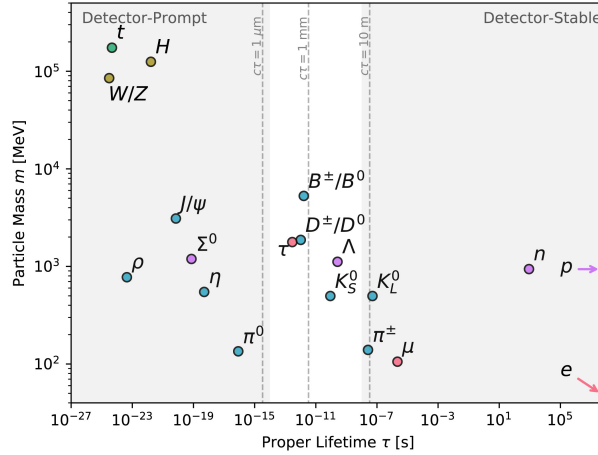


Figure 7.1. SM particles in terms of their mass (x-axis) and their mean proper lifetime (y-axis). Plot from Ref. [160].

if they were to exist. In the past, however, searches for BSM particles have largely assumed that they would be prompt, impacting detector design, trigger algorithms and reconstruction and identification techniques. BSM LLPs searches are therefore extremely challenging, pushing the detectors to the limit of their capabilities. In the following, a search that looks for LLPs that are so long-lived that they decay outside the reach of the ATLAS detector is presented.

7.2 Data and simulated event samples

The search here presented is based on the full Run-2 dataset. Monte Carlo simulations of the benchmark models investigated (Sec. 2.4.3) are exploited in order to optimize selection criteria to maximize the sensitivity to signal-like events.

7.2.1 Full Run-2 dataset

Data were collected during 2015-2018 in pp collisions at a center-of-mass energy of $\sqrt{s} = 13$ TeV (see Tab. 3.1), with a total integrated luminosity of $L = 139 \text{ fb}^{-1}$ (see Sec. 3.1.3).

7.2.2 Monte Carlo simulated samples

The SM background samples were processed with the full simulation outlined Sec. 3.2.7. Simulated events are then reconstructed and analyzed with the same analysis chain as for the data, using the same trigger and event selection criteria. The PU effects were taken into account as explained in Sec. 3.2.7.

Signal models simulations

The search presented exploits the FRVZ benchmark model and the $H \rightarrow ss$ one, both outlined in Sec. 2.4.3. An additional scenario in which the γ_d are produced in the FRVZ model by an heavier BSM Higgs-like scalar H' , with $m_{H'} = 800$ GeV, is considered as well. Since this search looks for LLPs, the γ_d and the s scalar are generated with sizable mean proper lifetimes. Details about the parameters used in the generation of the MC samples for the FRVZ and the $H \rightarrow ss$ model are given in Tab. 7.1 and Tab. 7.2 respectively. The simulations chain used

Model 1		Model 2	
m_H	125 GeV	$m_{H'}$	800 GeV
$c\tau_d$	5, 50, 500 mm	$c\tau_d$	10, 100 mm
Common parameters			
m_{γ_d}		400 MeV	
m_{f_d}		5 GeV	
m_{HLSP}		2 GeV	

Table 7.1. Values of the parameters for the two simulated benchmark FRVZ models. Table from Ref. [3].

for the FRVZ benchmark samples is like the one outlined in Sec. 5.1. For the $H \rightarrow ss$ benchmark model, instead, MC samples are generated at the Leading Order (LO) using MG5_AMC@NLO v2.6.2 generator [111] linked together with the PYTHIA8 generator [112] using the A14 tune of parameters [163], with the NNPDF2.3LO PDF set [146]. For the FRVZ foreseeing the SM Higgs boson and

m_H [GeV]	m_s [GeV]	$c\tau_s$ [mm]
125	5	223, 411
125	35	1310, 2630
125	55	1050, 5320

Table 7.2. Values of the parameters used in the MC signal generation for the $H \rightarrow ss$ model. Table from Ref. [3]

the $H \rightarrow ss$ MC samples, the Higgs boson is produced via the ggF production mechanism, with the associated cross section at $\sqrt{s} = 13 \text{ TeV}$ quoted in Tab. 1.1.

Background processes simulations

As will be discussed in Sec. 7.3.1, $W^-(\rightarrow l^-\bar{\nu}) + \text{jets}$, $W^+(\rightarrow l^+\nu) + \text{jets}$, $Z(\rightarrow l^-l^+) + \text{jets}$ and $Z(\rightarrow \nu\bar{\nu}) + \text{jets}$ processes constitute the 80% of the total background, with the latter being an irreducible background. For these reasons, details about simulations of such SM processes are given in this section. The reader is referred to [2] for further details about such simulations as well as for the ones of the other backgrounds taken into account, namely $t\bar{t}$, single-top and di-boson processes, which are here not discussed.

Simulations of $V + \text{jets}$ processes are performed separately for strong V boson production and for the EW one, via VBF (subdominant with respect to the strong mode). The latter were generated using HERWIG++, with the NNPDF30 PDF set (with the default tune for the parton showering, hadronisation and underlying event) and NLO QCD accuracy [164]. The former were instead generated using the SHERPA 2.2.1 event generator. Matrix elements were calculated including up to two extra parton emissions at NLO and up to four extra parton emissions at LO. The NNPDF3.0NNLO PDF set was used, along with a parton showering tuning provided by the SHERPA developers themselves.

To provide a better description of $V + \text{jets}$ processes (not initiated by VBF) a reweighting is performed to account for higher order QCD (NNLO [165, 166, 167]) and EW (NLO [168, 169, 170, 171]) corrections. Such reweighting procedure is based on parton level predictions of $V + \text{jets}$ processes from Ref. [172] and is performed via a per-event weight as a function of the vector boson p_T . Uncertainties in these corrections are briefly described in Sec. 7.3.

7.3 Monojet search in a nutshell

The *monojet* search selects events where a high- p_T jet recoils against a large E_T^{miss} . A brief overview of the event selection, both in the SR and in the different CRs used for the background estimation, is given in Sec. 7.3.1. The likelihood model is outlined as well in Sec. 7.3.2 and the sources of the leading uncertainties are listed in Sec. 7.3.3. For more details about the treated topics as well as about simulations of the background processes and the object reconstruction criteria the reader is

referred to the paper [2].

7.3.1 Analysis regions

The *monojet* search exploits E_T^{miss} as main discriminant, via a shape fit, since the background E_T^{miss} shape is expected to be steeply falling while the one associated to BSM scenarios, such as LLPs escaping detection, foresees a more prominent tail in its high end.

In order to identify events with the *monojet* signature, high E_T^{miss} calorimeter-based triggers are used. Such triggers do not include any information on the MS hits, and thus muons energy is included in the E_T^{miss} reconstructed at the online level.

The (offline) reconstructed E_T^{miss} should be larger than 200 GeV and at least one PV must be found. The leading jet must have a high p_T of at least 150 GeV and should satisfy the **Loose** WP requirements. Events where a highly energetic jet recoils against a high E_T^{miss} can be reconstructed in *NCB*. An event display of a BIB event with a monojet signature is shown in Fig. 7.2.

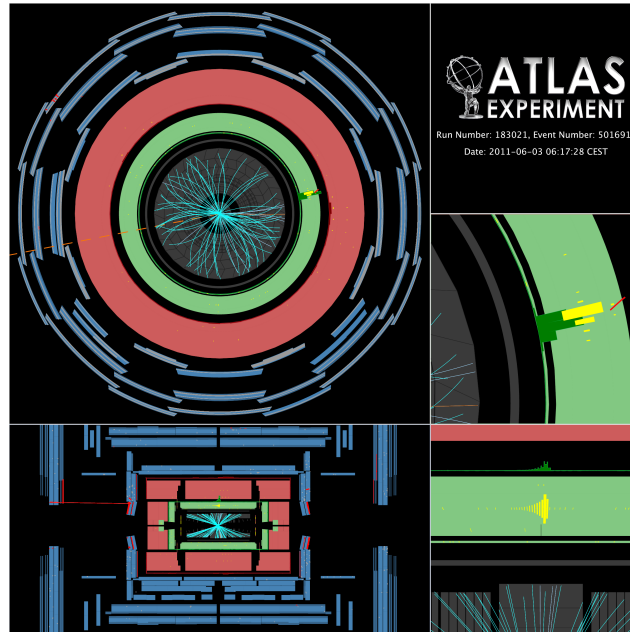


Figure 7.2. Event display of an event with a *monojet* signature collected during Run-1. In the bottom left plot, showing the ATLAS detector in the $z - y$ plane, a BIB muon track (red line) is reconstructed parallel to the beam axis in the MS, with CSC hits (highlighted in red over the blue rectangles) reconstructed on both sides of the detector. Through its passage, the BIB muon leaves hits in the ECAL (highlighted in yellow over the green background), with no ID track (top left plot) associated to it. Since the BIB muon is not arising from the primary collision, E_T^{miss} (red dashed line) is reconstructed back to back to the BIB muon energy clusters. Plot from Ref. [173].

In such events, the jet is usually not pointing to the IP, and thus it has a reduced associated activity in the ID. In order to suppress this source of background,

the leading jet is required to have a non-negligible associated activity in the ID. The latter is achieved by imposing that $f_{\text{ch}}/f_{\text{max}} > 0.1$ (and $|\eta_{\text{jet}}| < 2.4$, the ID coverage), thus satisfying the **Tight** WP (see Sec. 4.2).

All the other jets considered must have $|\eta| < 2.8$ (the HCAL coverage), $p_{\text{T}} > 30$ GeV and they must satisfy the **Loose** WP as well. The jets with $p_{\text{T}} < 120$ GeV must have a JVT score (see Sec. 4.2) larger than 0.59, to reject PU jets.

In events due to the multi-jet background, mis-reconstructions of jets energy could lead to a high $E_{\text{T}}^{\text{miss}}$. To ensure genuine $E_{\text{T}}^{\text{miss}}$ reconstruction, a maximum number of 4 jets is thus allowed, with a minimum angular separation between each of them and the $E_{\text{T}}^{\text{miss}}$ ($\Delta\phi_{\text{jet}-E_{\text{T}}^{\text{miss}}} > 0.4$ for $E_{\text{T}}^{\text{miss}} > 250$ GeV and $\Delta\phi_{\text{jet}-E_{\text{T}}^{\text{miss}}} > 0.6$ for $E_{\text{T}}^{\text{miss}} \leq 250$ GeV). Finally, the presence of leptons and photons is vetoed. The residual multi-jets and BIB background events are negligible compared to other sources of backgrounds and are mostly contributing to the low $E_{\text{T}}^{\text{miss}}$ region. Their contribution is estimated via pure data-driven techniques, as described in the dedicated paper [2].

Different SM processes can however yield events with a *monojet* signature. Among them, the $Z(\rightarrow \nu\bar{\nu}) + \text{jets}$ background is irreducible and contributes to the 60% of the total background. Other sources of background processes are due to events where final state leptons are either not reconstructed and produced in association with jets or mis-identified as jets themselves. Finally, jets and $E_{\text{T}}^{\text{miss}}$ could be reconstructed in processes where τ leptons decay hadronically. These listed events could arise in $W^-(\rightarrow l^-\bar{\nu}) + \text{jets}$, $W^+(\rightarrow l^+\nu) + \text{jets}$ or $Z(\rightarrow l^-l^+) + \text{jets}$ processes, contributing to the 20% of the total background. At a smaller extent, they could be produced as well in di-vector boson, $t\bar{t}$ or single t production.

The estimation of these different background contributions is performed using 5 different dedicated CRs, each of which is enriched by a specific background component. Two orthogonal CRs, enriched in $W + \text{jets}$ events, are defined by requiring exactly one reconstructed electron¹ or muon. It is additionally required that the transverse mass of the lepton- $E_{\text{T}}^{\text{miss}}$ system should be within the W mass peak, and that events should not contain b -tagged jets, the latter requirement suppressing top-quark related processes. Although such processes are a sub-leading component of the total background ($\sim 4\%$), an additional CR enriched in single- t and $t\bar{t}$ events is defined, inverting the mentioned b -jet veto and merging the two lepton flavours. Finally, two additional two-leptons CRs, enriched in $Z + \text{jets}$ events, are defined by requiring exactly two electrons or muons with an invariant mass within ± 25 GeV around the Z mass peak.

In order to emulate the kinematic distribution of the $E_{\text{T}}^{\text{miss}}$ in the SR, all the selected leptons in the CRs are considered as invisible particles², and their p_{T} is therefore summed to the reconstructed $E_{\text{T}}^{\text{miss}}$, yielding the so-called $p_{\text{T}}^{\text{recoil}}$, which is thus the magnitude of the total p_{T} recoiling against hadronic activity in the event. By construction, $p_{\text{T}}^{\text{recoil}}$ corresponds to the $E_{\text{T}}^{\text{miss}}$ in the SR. The background contribution in each of this CR is extracted using a shape fit on the $p_{\text{T}}^{\text{recoil}}$ spectrum,

¹For CRs where electron reconstruction is foreseen, electron triggers are considered as well

²since no MS hits is used in the $E_{\text{T}}^{\text{miss}}$ triggers, muons are treated as invisible in the online reconstruction as well

described in the following.

7.3.2 Fitting technique

A binned-likelihood fit of the p_T^{recoil} distributions is performed on data, across the different CRs and the SR. The number of events in each bin in each region is treated as a random variable with a Poisson PDF, with the associated expectation value extracted from the MC sample simulating the SM process of which the given CR is enriched. Three free floating factors accounting for the normalisation of the SM processes are included in the fit, respectively for $V + \text{jets}$, single-top and $t\bar{t}$ events.

The systematic uncertainties outlined in Sec. 7.3.3 are taken into account as nuisance parameters, constrained with Gaussian PDFs centered around the nominal value, with a variance corresponding to the systematic uncertainty. These parameters are fully correlated among the different background processes, bins and regions.

The fit strategy foresees an initial CR-only fit, where the normalisation of the SM processes is extracted. Fig. 7.3 shows no significant excess in the SR, after the first stage of the fit including only the CRs.

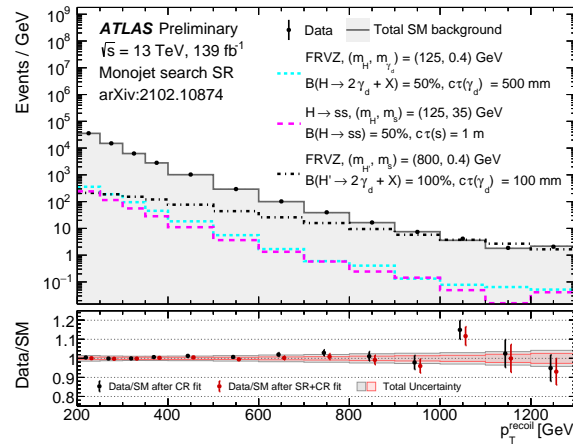


Figure 7.3. p_T^{recoil} distribution observed in SR for data (black dots) and for the SM MC background samples (grey histogram). The p_T^{recoil} distributions for the three benchmark models investigated are shown as well (dotted lines), for the parameters specified in the legend. p_T^{recoil} bins are exclusive and are 50 GeV wide for $p_T^{\text{recoil}} < 400$ GeV and 100 GeV wide for $p_T^{\text{recoil}} \geq 400$ GeV. The last bin instead includes all the events with $p_T^{\text{recoil}} \geq 1200$ GeV. The bottom pad shows the level of agreement between the data and the SM predictions, after a fit to the CRs only (black dots) and after a fit to both the CRs and the SR in the background only hypothesis (red dots). Plot from Ref. [3].

A second step performs the fit including the SR. Fig. 7.3 shows as well the result of this second fit in the background only hypothesis, showing that the SM predictions are only slightly affected by the contribution of the SR in the fit.

To test the signal plus background hypothesis, the inclusion of an additional free-floating parameter, scaling inclusively the signal strength of the investigated

model, is foreseen. Since no excess of *monojet* events is found in [2], an upper limit on the signal strengths of the investigated models is obtained. The signal strength coincides with $BR(H \rightarrow ss)$ for $H \rightarrow ss$ model and with $BR(H \rightarrow 2\gamma_d + X)$ and $\sigma(pp \rightarrow H' \rightarrow 2\gamma_d + X)$ for the FRVZ model foreseeing respectively the SM Higgs boson and the BSM heavier Higgs like scalar. Such upper limits are obtained using the CLs method [174] and are discussed in Sec. 7.5.

7.3.3 Systematic uncertainties

The overall normalization and shape of the p_T^{recoil} distributions used in the fit is impacted by systematic uncertainties, both for the backgrounds and for the signal processes investigated. Those uncertainties affect only simulated events, thus the multi-jet and the NCB processes, whose contributions is estimated through data-driven techniques, are not affected. A brief outline of such uncertainties is provided in the following sections, while the reader is referred to Refs.[2, 3] for further details.

Background uncertainties

Both experimental and theoretical modelling uncertainties affect the backgrounds p_T^{recoil} distributions. Their impact is estimated after performing a background-only fit to data from the five CRs, by evaluating such impact in the total background yield in each bin of the p_T^{recoil} distribution in the SR.

Experimental uncertainties include lepton reconstruction, identification and isolation efficiencies, as well as scale and resolution uncertainties associated to the muons momentum, to the jets, the electrons and the photon energy and to the E_T^{miss} . For all simulated SM background processes theoretical uncertainties due to the QCD factorisation and normalisation scale and to the choice of the parton showering scheme are taken into account.

The leading source of theoretical uncertainty is due to the predictions of $V + \text{jets}$ processes, with the strong production of the vector boson. Such processes are affected as well by uncertainties due to the reweighting to QCD and EW higher order corrections briefly outlined in Sec. 7.2.2. Three uncertainties are considered for both the EW and the QCD corrections, and one source of mixed QCD-EW corrections is considered as well, for a total of seven sources of uncertainty, evaluated as prescribed by Ref. [172].

The total uncertainty on the background yield in the SR varies between 1.5% and 4.2% respectively for $p_T^{\text{recoil}} < 250 \text{ GeV}$ and $p_T^{\text{recoil}} \geq 1.2 \text{ TeV}$.

Signal uncertainties

The main sources of systematic uncertainties associated to the signal yields, for the three model considered, are summarised below. In evaluating them, it is assumed that the standard description of physics objects holds for these models as well, since LLPs decay products are visible SM particles. While muon and electron associated uncertainties are found to be negligible, jet and E_T^{miss} energy scale and resolution

were found to impact the expected signal yields. A detailed view of the impact of the most relevant systematic uncertainties on the expected pre-fit signal yields for one benchmark point of each model considered is given in Tab. 7.3. An additional

Source of uncertainty and impact on the prefit signal yields (%)	
FRVZ model, $m_H = 125$ GeV, $m_{\gamma_d} = 400$ MeV, $c\tau_d = 500$ mm	
Jet energy scale and resolution	3 – 3.5
E_T^{miss} scale and resolution	1.4 – 2.5
FRVZ model, $m_{H'} = 800$ GeV, $m_{\gamma_d} = 400$ MeV, $c\tau_d = 500$ mm	
Jet energy scale and resolution	1.2 – 6.3
E_T^{miss} scale and resolution	0.3 – 0.5
Hss model, $m_H = 125$ GeV, $m_s = 5$ GeV, $c\tau_s = 411$ mm	
Jet energy scale and resolution	3 – 7
E_T^{miss} scale and resolution	0.2 – 3.5

Table 7.3. Impact of different components of the systematic uncertainties on the prefit yields for three benchmark signal points.

1.7% uncertainty is assigned on the expected yields of each signal model, to take into account the uncertainty on the measurement of the ATLAS integrated luminosity during Run-2 operations (see Sec. 3.1.3). Modelling uncertainties related to scale and PDF variations on the signal samples are neglected.

7.4 MC signal samples reweightings

The signal MC samples are generated at LO in QCD. For this reason, the Higgs p_T distribution is reweighted so to match the NLO one, as explained in Sec. 7.4.1. Furthermore, in order to extrapolate the excluded limits on the signal strengths of the investigated processes to other LLP mean proper lifetimes with respect to the ones at which the MC samples were generated, the Life-Time Reweighting procedure, outlined in Sec. 7.4.2, is performed as well.

7.4.1 Higgs p_T reweighting

The signal MC samples, as said, are based on the LO QCD calculations of the ggF Higgs boson production mechanism, leading to differences greater than 50% in the jet p_T distributions with respect to the ones obtained via NNLO QCD calculations. Since the E_T^{miss} arising in the signal is due to LLPs recoiling on such jets, the E_T^{miss} shape is greatly affected by the calculation order at which the ggF production process is simulated. For this reason, signal samples are corrected in order to match the NLO QCD accuracy available for the $gg \rightarrow H \rightarrow \text{inv}$ process investigated in the dedicated *monojet* search [2]. Particle level distributions obtained in the LO QCD samples are therefore matched to the ones predicted at NLO via a per event reweighting based on the truth Higgs boson p_T^H . After this correction, samples are normalised to the N3LO QCD and NLO EW cross-section.

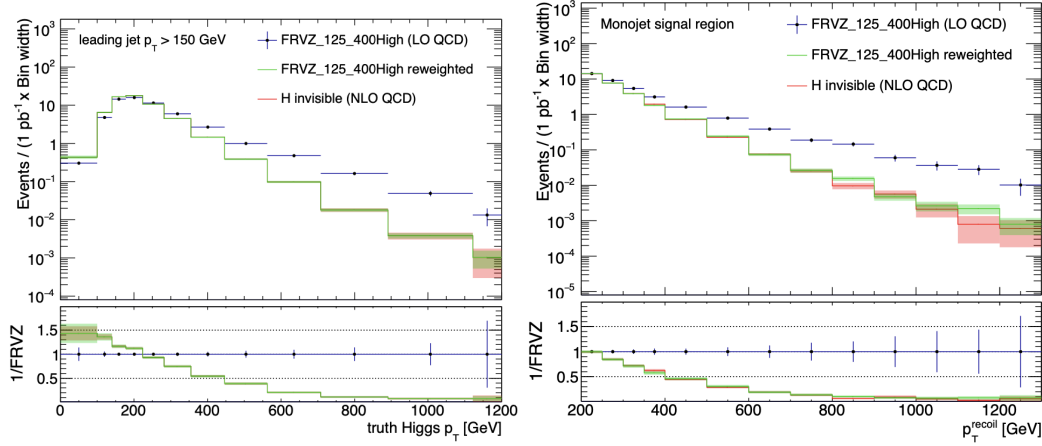


Figure 7.4. Higgs p_T^H (a) and p_T^{recoil} (b) distributions for the $gg \rightarrow H \rightarrow \text{inv}$ process (red) and for the nominal (blue) and reweighted (green) signal sample generated via the FRVZ benchmark model with the SM Higgs boson and with $c\tau = 500$ mm. The bottom pad shows the ratio between these three processes and the nominal sample generated according to the FRVZ benchmark model.

Fig. 7.4 (a) shows the p_T^H distribution (requiring the leading jet p_T to be larger than 150 GeV) for the $gg \rightarrow H \rightarrow \text{inv}$ process alongside with the nominal and the reweighted p_T^H distribution for the FRVZ benchmark model with the SM Higgs boson and with a DP with a mean proper lifetime $c\tau = 500$ mm. Fig. 7.4 (b) shows instead the p_T^{recoil} distributions in the *monojet* SR for the same processes.

After the p_T^H reweighting the p_T^{recoil} distributions for the FRVZ benchmark model and the $gg \rightarrow H \rightarrow \text{inv}$ one are compatible. The residual minimal differences are due to the fact that not all the DPs produced decay outside ATLAS, thus impacting the p_T^{recoil} shape.

7.4.2 Life-time reweighting

A Life-Time Reweighting procedure is used in LLPs searches in order to probe such models for different mean proper lifetimes τ with respect to generated ones. To do so, given a sample where the LLP proper lifetime t_i follows a distribution $f(t_i|\tau_{\text{sim}})$ with mean τ_{sim} , the events are reweighted in such a way to produce a LLP t_i distribution with a mean proper lifetime τ_{new} . Given the $f(t_i|\tau_{\text{sim}})$ PDF describing the t_i distribution

$$f(t_i|\tau_{\text{sim}}) = \frac{1}{\tau_{\text{sim}}} \exp\left(-\frac{t_i}{\tau_{\text{sim}}}\right),$$

each event is reweighted via

$$w(t_i|\tau_{\text{sim}} \rightarrow \tau_{\text{new}}) = \frac{\tau_{\text{sim}}}{\tau_{\text{new}}} \exp\left(-t_i \left(\frac{1}{\tau_{\text{new}}} - \frac{1}{\tau_{\text{sim}}}\right)\right),$$

which is basically the ratio between the $f(t_i|\tau_{\text{sim}})$ and the $f(t_i|\tau_{\text{new}})$ PDFs. Since, however, in all the investigated models two LLPs are produced per event, the PDF

of the sum of the decay times $t_1 + t_2$ of the two LLPs $f(t_1 + t_2|\tau_{sim})$ is considered:

$$f(t_1 + t_2|\tau_{sim}) = \frac{1}{\tau_{sim}^2} \exp\left(-\frac{t_1 + t_2}{\tau_{sim}}\right). \quad (7.2)$$

To reweight the full event, the weight $w(t_1 + t_2|\tau_{sim} \rightarrow \tau_{new})$ applied is

$$w(t_1 + t_2|\tau_{sim} \rightarrow \tau_{new}) = \frac{\tau_{sim}^2}{\tau_{new}^2} \exp\left(-(t_1 + t_2) \left(\frac{1}{\tau_{new}} - \frac{1}{\tau_{sim}}\right)\right).$$

However, if this procedure is applied to reweight a sample from τ_{sim} to $\tau_{new} \gg \tau_{sim}$ or $\tau_{new} \ll \tau_{sim}$, to reproduce the desired $t_1 + t_2$ distribution with mean proper lifetime τ_{new} many events are reweighted with a very small LTR weight, while a few are reweighted with a very large LTR weight. The resulting reweighted sample is therefore affected by a large statistical uncertainty. To overcome such a limitation, if multiple samples are generated with different mean proper lifetimes, the so-called *multi-sample LTR* can be exploited. The idea behind it is to use for the LTR multiple templates with different mean proper lifetimes, and to reweight an event from a given template only if such event lies in a proper lifetime range which is sufficiently populated in that template. Given two MC samples with τ_1 and τ_2 , where $\tau_1 < \tau_2$, their two PDFs (as expressed in Eq. 7.2) intersect in the critical time τ_c

$$\tau_c = 2 \ln \frac{\tau_1}{\tau_2} / \left(\frac{1}{\tau_2} - \frac{1}{\tau_1} \right).$$

Such critical time determines after which proper lifetime the template with τ_1 as a negligible statistics with respect to the one with τ_2 , and therefore events should be drawn for the template with τ_2 . Thus in order to obtain a new sample with τ_{new} , events from the sample with τ_1 are kept if $t_1 + t_2 < \tau_c$ and events from the sample with τ_2 are kept if $t_1 + t_2 > \tau_c$. With N generated samples, $N - 1$ critical times can be found. The multi-sample LTR procedure can be further understood by looking at Fig. 7.5, showing the distributions of the sum $t_1 + t_2$ of the proper lifetime of the lifetime of the two LLPs for the three generated mean proper lifetimes $c\tau_1 = 5$ mm, $c\tau_2 = 50$ mm and $c\tau_3 = 500$ mm and for a new hypothetical sample with $c\tau_{new} = 225$ mm. Being $c\tau_{12}$ the critical time among the PDF with $c\tau_1$ and the one with $c\tau_2$, and $c\tau_{23}$ the critical time among the PDF with $c\tau_2$ and the one with $c\tau_3$, events are drawn from the sample with $c\tau_1$ only if $ct_1 + ct_2 < c\tau_{12}$, from the sample with $c\tau_2$ only if $c\tau_{12} < ct_1 + ct_2 < c\tau_{23}$ and from the sample with $c\tau_3$ only if $ct_1 + ct_2 > c\tau_{23}$. In such a way, the sample with $c\tau_{new} = 225$ mm is obtained with the smallest possible uncertainty given the available MC samples. In the case of the FRVZ model with the SM Higgs boson the three available MC samples at $c\tau = 5$ mm, 50 mm, 500 mm are used in the LTR, while for all the other models the two available MC samples are used (see Tab. 7.1, 7.2). The LTR is cross-validated by producing new samples that have the same mean proper lifetime of generated ones and comparing the reweighted E_T^{miss} spectrum to the generated one. A perfect closure is observed in these checks for all the simulated MC samples. An example of such a closure check for the FRVZ benchmark model foreseeing the SM Higgs boson can be seen in Fig. 7.6.

Given this LTR procedure and the fact that (for the models foreseeing the SM Higgs boson) the Higgs p_T was reweighted as explained in the previous section so to

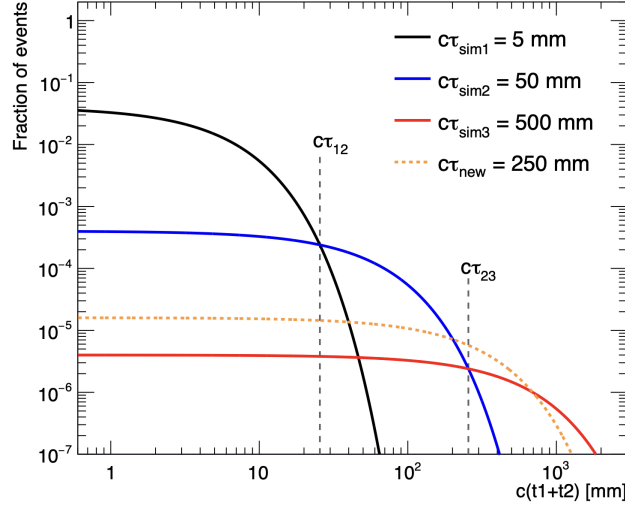


Figure 7.5. Distributions of the sum of the decay time of two dark photons ($t_1 + t_2$) for the three generated FRVZ benchmark samples (solid lines). These are compared to the distribution of an hypothetical new sample of $c\tau_{new} = 225$ mm (dotted line). The vertical lines represent the critical times, as defined in the text.

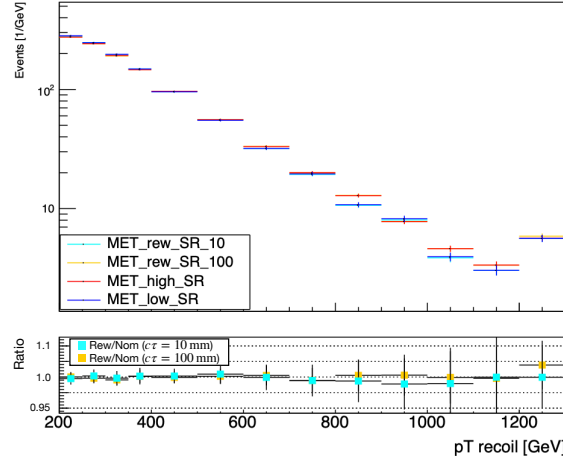


Figure 7.6. p_T^{recoil} distributions in the *monojet* SR for the FRVZ benchmark model with the SM Higgs boson for the sample with a generated $c\tau_{sim,1} = 10$ mm (blue) and with a generated $c\tau_{sim,2} = 100$ mm (red). The nominal distribution are compared to the ones obtained via the LTR procedure at $c\tau_{new,1} = 10$ mm (cyan) and $c\tau_{new,2} = 100$ mm (orange). The bottom pad shows the agreement between the nominal and the reweighted p_T^{recoil} distributions for $c\tau_1 = 10$ mm (cyan) and $c\tau_2 = 100$ mm (orange).

match the NNLO one on which the *monojet* search is relying, one would expect that the upper limit on the $BR(H \rightarrow 2LLPs)$ for the LLPs models foreseeing the SM Higgs boson would converge to the *monojet* constraint on the $B(gg \rightarrow H \rightarrow inv)$. But this is not the case and it is due to the LTR procedure. Even though the multi-sample LTR allows for a reduction of the MC statistical uncertainty of the newly emulated samples, its impact at very large $c\tau_{new}$ (far from the generated ones) is still non negligible. For weighted events, the relative MC statistical uncertainty σ_{rel}

is indeed given by:

$$\sigma_{rel} = \frac{\sqrt{\sum_i^{N_{gen}} w_i^2}}{\sum_i^{N_{gen}} w_i} = \frac{1}{\sqrt{N_{gen}}} \sqrt{1 + \frac{\sigma_{w_i}^2}{\langle w^2 \rangle}} \quad (7.3)$$

where N_{gen} is the number of generated raw events, w_i is the weight of each event, $\sigma_{w_i}^2$ is the variance of the event weights, and $\langle w \rangle$ their mean value. Fig. 7.7 shows the impact of the LTR procedure on the MC statistical uncertainty $\frac{\sigma_{w_i}^2}{\langle w^2 \rangle}$ of the emulated benchmark samples for the FRVZ benchmark model with the SM Higgs boson. From the picture, it can be seen how the MC statistical uncertainty

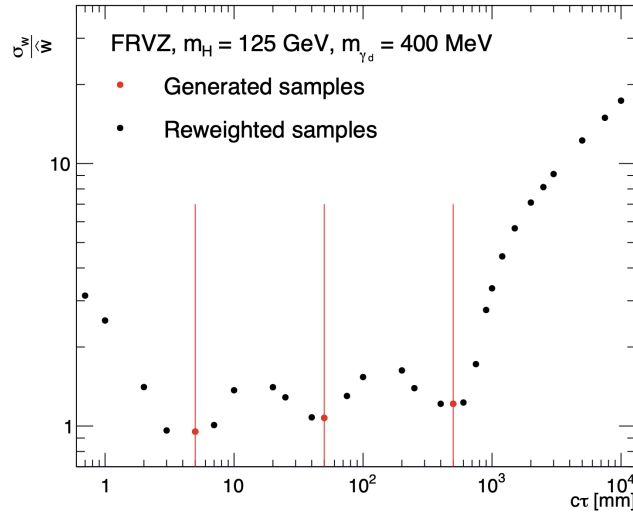


Figure 7.7. Ratio between the standard deviation of the event weights $\sigma_{w_i}^2$ and their mean (in the plot indicated with $\langle w \rangle$), as a function of the mean lifetime $c\tau$ of the benchmark signal samples emulated using the LTR procedure for the FRVZ benchmark model with the SM Higgs boson. The red lines indicate the values of the mean proper lifetimes $c\tau$ of the generated signal samples.

increases moving far from the $c\tau$ of the generated samples. This causes a worsening of the exclusion power of the search for extremely long lived LLPs. However, the Higgs p_T reweighting allows to extrapolate the limits obtained as a function of $c\tau$ of the LLPs up to very large lifetime values, since that for those extremely large LLPs $c\tau$ the E_T^{miss} distribution matches the $gg \rightarrow inv$ one. For the model with the BSM Higgs like scalar, such a matching is obviously not a viable option, and therefore the exclusion limits in this a model will show a worsening at extremely large $c\tau$ (see Sec. 7.5.1).

7.5 Reinterpretation results

In this section, the results obtained with the RECAST framework on the considered signal models are reported and compared to the ones of dedicated ATLAS analyses. Sec. 7.5.1 presents the constraints found for the FRVZ models foreseeing both the

SM Higgs boson and the heavier BSM Higgs-like scalar, while Sec. 7.5.2 presents the constraints found for the $H \rightarrow ss$ model.

7.5.1 Constraints for the FRVZ benchmark model

The analysis efficiency varies for the different DP decay modes, as the different decay products may fail to satisfy the reconstruction requirements of Ref. [2] and therefore they may not be reconstructed in the final state, yielding E_T^{miss} . For this reason, three separate channels are considered, based on the truth decay products of the DPs produced in the events:

- **Muonic channel:** both γ_d decay into a pair of muons;
- **Hadronic channel:** both γ_d decay into a pair of electrons or light hadrons;
- **Mixed channel:** one γ_d decays into a pair of muons and the other one into a pair of either electrons or light hadrons.

The definition of these channels is closely related to the one adopted in Ref. [79], based on reconstructed final state objects.

Constraints for the FRVZ benchmark model with the SM Higgs boson

Upper limits at 95% of CL on the BR of the Higgs boson decaying into a pair of γ_d are reported in Fig. 7.8 as a function of the Dark Photon mean proper lifetime. At large lifetimes, $c\tau_d \gtrsim 10^2$ mm, the observed limit, setting competitive constraints with respect to the ones of the dedicated search of Ref. [79], flatten out and are independent of the γ_d decay channel, since most of the γ_d decay outside the fiducial volume of the ATLAS experiment. The upper limit obtained at very large γ_d lifetimes is consistent with the one on the $\mathcal{B}(gg \rightarrow H \rightarrow \text{inv})$ by Ref. [2] and corresponds to $\mathcal{B}(H \rightarrow 2\gamma_d + X) < 50\%$ @95% CL. The excluded $\mathcal{B}(H \rightarrow 2\gamma_d + X)$ is higher than $\mathcal{B}(H \rightarrow \text{inv})$ obtained by the *monojet* search [2], $\mathcal{B}(H \rightarrow \text{inv}) < 34\%$ @95% CL, since in this reinterpretation only the $gg \rightarrow H$ production mechanism is considered, which accounts only for about 73% of the total cross-section. Furthermore, a larger tail at high p_T^{recoil} is observed in the *monojet* SR for the inclusive $H \rightarrow \text{inv}$ process than for the $gg \rightarrow H \rightarrow \text{inv}$ one, as can be seen in Fig. 7.9, this affecting as well the constraint on $\mathcal{B}(H \rightarrow \text{inv})$.

At extremely low mean proper lifetimes, $c\tau_d < 0.9$ mm, this search extends the previous bounds of Ref. [79], as it recovers sensitivity, regardless of the mean proper lifetimes of the DP, when the γ_d decay products do not satisfy the reconstruction requirements of Ref. [2] but they are not sufficiently displaced to be reconstructed as in the search of Ref. [79].

In the muonic channel, the sensitivity recovered in the *muonic channel* is due to the lower efficiency of the prompt lepton veto, since muons fail to be reconstructed. Muons are indeed required to be associated with the PV and to have a minimum number of ID hits (see Sec. 4.5), and even, for small proper lifetimes, the γ_d can

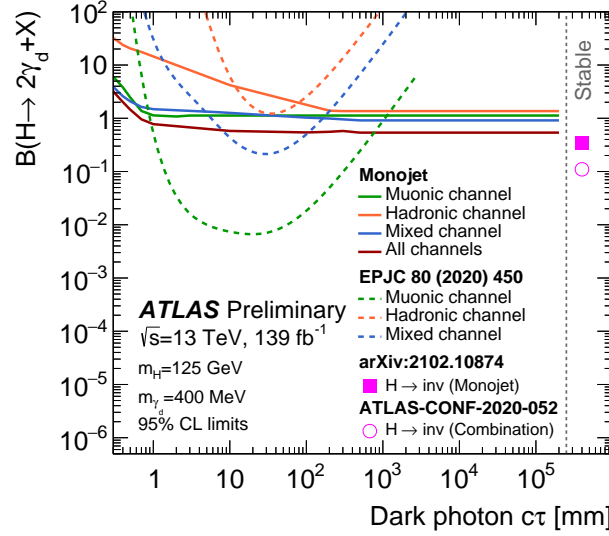


Figure 7.8. Exclusion contours obtained for a γ_d with $m_{\gamma_d} = 400$ MeV in the *muonic* (green), *hadronic* (orange) and *mixed* (blue) channels, produced in the FRVZ model in the decay of the SM Higgs boson. The results of the dedicated displaced search [78] (dashed lines) are compared to the ones obtained in this work (solid lines). The red line shows the exclusion limit obtained in this reinterpretation when combining the three aforementioned channels. The $\mathcal{B}(H \rightarrow \text{inv})$ limit from the *monojet* [2] analysis (pink square) and the combination of ATLAS Run-1 and Run-2 results [175] (pink dot) are shown as well. Plot from Ref. [3].

be so boosted that the muons they produced may not satisfy such requirements. However, the sensitivity decreases rapidly in more prompt-like regimes, with the muons being identified by the standard reconstruction algorithms.

The hadronic channel loses sensitivity in the region $c\tau_d < 10^2$ mm as a consequence of the photon veto, which can suppress events due to displaced electrons (reconstructed as photons since they leave no ID track, see Sec. 4.4).

The results of both this work and the dedicated ATLAS searches are shown in Fig. 7.10 as well, as a function of the kinetic mixing parameter ε and of the γ_d mass. In this case, the limits are shown at 90% of CL, to be compared with the results of other non-ATLAS searches [177]. The exclusion contour corresponding to $\mathcal{B}(H \rightarrow 2\gamma_d + X) = 50\%$ is used as a benchmark in this plot. In the range of γ_d mass $[0.2, 0.6]$ GeV, the *monojet* reinterpretation excludes $\varepsilon \leq 3 \cdot 10^{-6}$, while for γ_d with $m_{\gamma_d} > 0.6$ GeV $\varepsilon \leq 2 \cdot 10^{-6}$ is excluded. The shape of the contour is directly related to the BR of the γ_d decays: for γ_d masses below 0.5 GeV the sensitivity slightly increases because of the increase of the γ_d BR into muons, to which the analysis is the most sensitive, as can be seen in Fig. 7.8. Fig. 7.10 clearly highlights the complementarity of the searches carried out by the ATLAS experiment as well: the dedicated Run-1 prompt search [81] excludes values of $\varepsilon \geq 10^{-5} \sim 2 \cdot 10^{-6}$ with $\mathcal{B}(H \rightarrow 2\gamma_d + X) > 10\%$, while the dedicated displaced DPs [78] search fills the gap between the prompt and the *monojet* contours, with a $\mathcal{B}(H \rightarrow 2\gamma_d + X)$ down to the order of 1%.

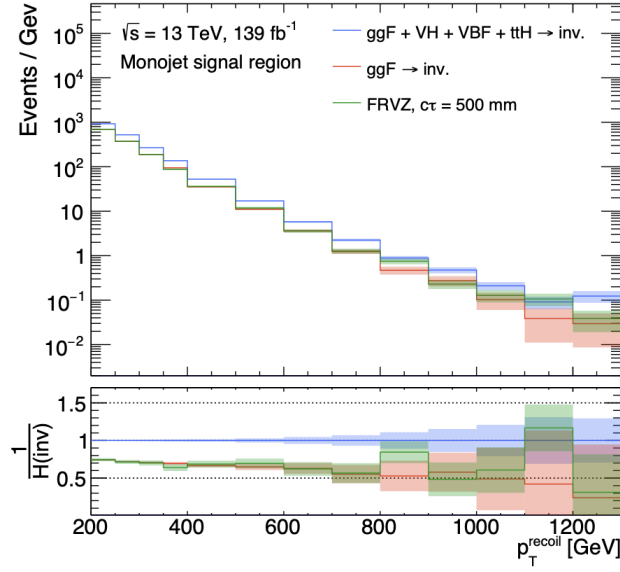


Figure 7.9. p_T^{recoil} spectrum in the *monojet* SR for the signal sample generated via the FRVZ benchmark model with the γ_d with mean proper lifetime $c\tau = 500$ mm (green), for the $H \rightarrow \text{inv}$ process considering only the ggF production (red) or including all the Higgs boson production mechanisms (blue). The bottom pad shows the ration between the aforementioned processes and the inclusive $H \rightarrow \text{inv}$ one.

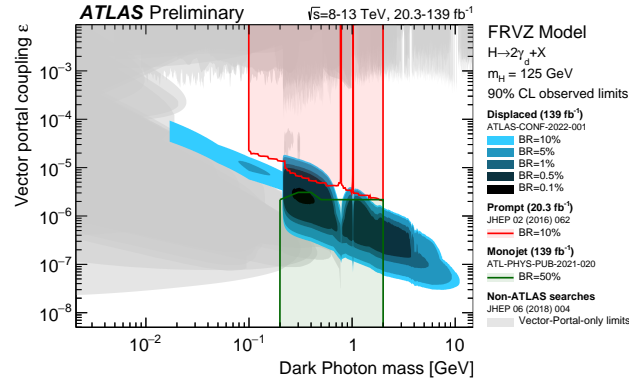


Figure 7.10. Exclusion contours obtained in this *monojet* reinterpretation (green) shown in the DP mass - kinetic mixing parameter (ϵ) plane compared to previous results of the dedicated prompt [81] (red) and displaced [78] (blue) ATLAS searches. The DPs are assumed to be produced in the FRVZ model from the decay of the SM Higgs boson. Plot from Ref. [176].

Constraints for the FRVZ benchmark model with the BSM heavier Higgs-like scalar

In the case in which the γ_d are produced by the decay of the heavy scalar H' , complementary results to the ones reported in Ref. [79] are obtained as well, as shown in Fig. 7.11. The γ_d produced by the heavier Higgs like scalar are more

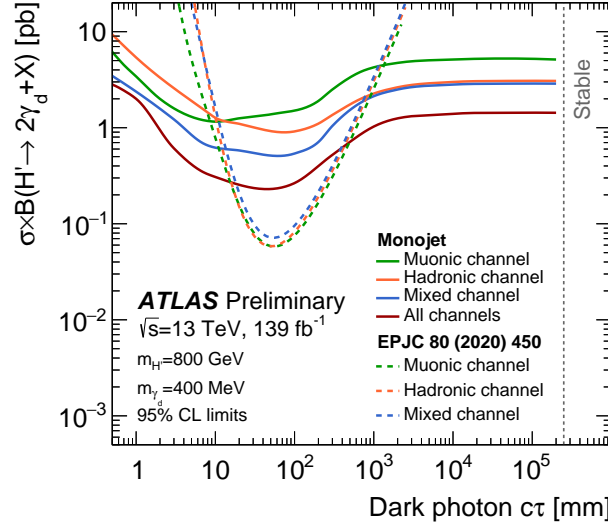


Figure 7.11. Exclusion contours obtained for a γ_d with $m_{\gamma_d} = 400$ MeV in the *muonic* (green), *hadronic* (orange) and *mixed* (blue) channels, produced in the FRVZ model in the decay of the heavy scalar mediator with $m_{H'} = 800$ GeV. The results of the dedicated displaced search [78] (dashed lines) are compared to the ones obtained in this work (solid lines). The red line shows the exclusion limit obtained in this reinterpretation when combining the three aforementioned channels. The results are compared to the exclusion limits of the dedicated ATLAS search (dashed lines with same colour scheme) [78]. Plot from Ref. [3].

boosted than the ones produced by the decay of the SM Higgs boson, this resulting in higher sensitivities for this model. A similar sensitivity is achieved for the three different decay modes at large γ_d mean proper lifetimes, as was observed in Fig. 7.8. The combined upper limit on the cross-section times BR of the heavy scalar particle reaches asymptotically $\sigma \times \mathcal{B}(H \rightarrow 2\gamma_d + X) = 1.5$ pb, extending the existing limits [79].

The loss in sensitivity for $\tau_d > 100$ mm is a consequence of the increased MC statistical uncertainty due to the LTR procedure, as explained in Sec. 7.4.2. As for the case of the model with SM Higgs boson, for lower γ_d mean proper lifetimes the lepton veto selection cut is more efficient, thus reducing the sensitivity of this *monojet* reinterpretation. However, as for the previous scenario, constraints competitive to the ones of the dedicated displaced search can be set at $c\tau_d \lesssim 10$ mm, for events where the lepton veto is inefficient and the γ_d are not enough displaced for their decay products to be identified in the dedicated search.

7.5.2 Constraints for the $H \rightarrow ss$ benchmark model

Fig. 7.12 shows the 95% CL limit on the BR of the SM Higgs boson decaying into a pair of BSM scalar particles s as a function of their mean proper lifetime. The results obtained in this work are compared to then ones of the dedicated searches [178, 179, 180]. A complementarity among such constraints is found for all the investigated

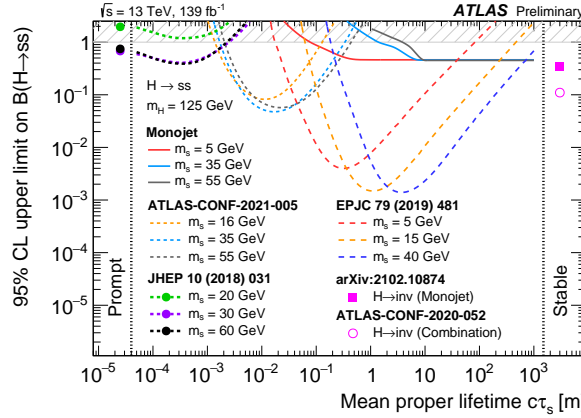


Figure 7.12. Exclusion contours on $\mathcal{B}(H \rightarrow ss)$ at 95% CL obtained in this search as a function of the s particle proper decay length, compared to the ones of dedicated searches [178, 179, 180], for the $H \rightarrow ss$ benchmark model. The s bosons are allowed to decay inclusively to all kinematically-allowed final states, with mass-dependent s boson BRs. For $m_s > 25$ GeV, the BRs to $b\bar{b}$, $c\bar{c}$, and $\tau^+\tau^-$ are approximately constant and given by 85%, 5%, and 8%, respectively. The prompt [178] and ID Displaced Vertices based results [180] assume negligible signal efficiency for decays channel different from the $s \rightarrow b\bar{b}$ one. The $\mathcal{B}(H \rightarrow \text{inv})$ limit from the monojet [2] analysis and the combination of ATLAS Run-1 and Run-2 results [175] are shown as well. The dashed area indicates the region with $\mathcal{B}(H \rightarrow ss) > 1$. Plot from Ref. [3].

s mass hypotheses, for which different lifetimes regimes are probed by different detection techniques. In this context, as in the previous scenarios, this *monojet* reinterpretation extends the upper limits to larger s particle mean proper lifetimes τ_s . Since different scalar mass hypotheses imply different boosts of their decay products, different exclusion contours are found for the different m_s .

For extremely large τ_s , the *monojet* constraint tends to of $\mathcal{B}(H \rightarrow ss) = 50\%$ @95% CL, which is the upper value on $\mathcal{B}(gg \rightarrow H \rightarrow \text{inv})$ obtained using the *monojet* signature. For comparison purposes, the constraints on the invisible BR of the Higgs boson set by the combination of the ATLAS Run-1 and Run-2 results [175], $\mathcal{B}(H \rightarrow \text{inv}) < 0.11$, and by the *monojet* analysis [2], $\mathcal{B}(H \rightarrow \text{inv}) < 0.34$, are shown in the plot as well.

Chapter 8

The ATLAS Phase-II upgrade of the L0 barrel muon trigger

During the LS3, that will take place from 2026 to 2028, a series of LHC upgrades relying on cutting-edge technologies will increase its instantaneous luminosity of a factor five, with this operation phase being called High-Luminosity (HL) LHC. A scheme of the LHC operations phases is given in Fig. 8.1. In order to cope with such



Figure 8.1. LHC planning as a function of the years.

an increase of luminosity, implying a PU more than 5 times larger than the Run-2 one, an extensive upgrade plan, referred to as *Phase-II*, is foreseen by all the LHC experiments. In this phase, the total integrated luminosity that will be delivered by the HL-LHC will be $L = 3000 \text{ fb}^{-1}$, roughly 20 times more than the Run-2 one.

While for a more extensive overview of the HL-LHC upgrades the reader is referred to Ref. [181], Sec. 8.1 gives a broad introduction of the ATLAS Phase-II upgrades. The Istituto Nazionale di Fisica Nucleare (INFN) Rome I group, to which I belong, is involved in ATLAS upgrade projects, specifically the one regarding the ATLAS MS Barrel Trigger. I have been involved in the development of the firmware of the Phase-II Sector Logic (SL) board, collecting hits from the RPC on-detector boards and performing the trigger algorithm. A description of the upgrade of the L0 muon barrel trigger is provided in Sec. 8.2. Specific focus is given on the Trigger and Data Acquisition (TDAQ) interface of the SL board in Secs. 8.2.1, 8.2.2. Finally,

Sec. 8.2.3 describes the studies I carried out in this context.

8.1 Overview of the ATLAS Phase-II upgrade

As a consequence of the increased instantaneous luminosity foreseen during the HL-LHC phase, an increase of the data stream and therefore of the radiation dose experienced by the LHC experiments is foreseen. In order to cope with such a challenging environment, along with the already mentioned PU increase, the different LHC experiments will undergo a series of upgrades, and ATLAS is no exception. All its different subsystems will indeed demand advanced upgrades, with the most important ones being briefly summarised in the following.

8.1.1 The Inner TracKer

Being the detector closest to the IP, the ID is the ATLAS sub-detector which will be mostly affected by the extreme running conditions of the HL-LHC, and therefore is going to be completely replaced by the Inner TracKer (ITk). The ITk is a detector completely based on semi-conductor technology and it will extend the ID η coverage from $|\eta| < 2.5$ to $|\eta| < 4$. It is comprised of two different sub-detectors:

- the Pixel Detector [182], in the innermost region ($r < 350$ mm), that will be comprised of 5 layers of pixels that, in the forward region, will be tilted so not to be orthogonal to the beam axis, reducing the material traversed by particles;
- the Strip Detector [183], in the outermost region, that will be comprised of 4 cylindrical layers in the barrel and six wheels in the endcap.

8.1.2 The High Granularity Timing Detector

As a consequence of the worsening of the longitudinal impact parameter resolution, the track reconstruction and Track-To-Vertex Association will become a major challenge for the ITk in the forward region. Therefore, the ITk will be complemented in such a region by the High Granularity Timing Detector (HGTD) [184], that will grant tracks timing information with a time resolution of the order of 30 ps, allowing the rejection of out-of-time PU (see Sec. 3.1.3) tracks in the dense environment foreseen. The detector will be placed in $z = \pm 3.5$ m, between the ITk and the FCal, and it will be comprised of disks based on silicon technology.

8.1.3 The calorimeter system

While the calorimeter system is expected to remain reliable during the operation of the HL-LHC, its FE electronics need to be completely replaced as outlined in Ref. [185], as a consequence of the more stringent requirements on the data rate and latency due to the increased luminosity. This will allow, at the lowest trigger

level, to exploit the full calorimeters granularity, increasing the performance and the capabilities of the current L1Calo trigger algorithms.

8.1.4 The muon system

The ATLAS muon system has already undergone a substantial upgrade during the LS2, with the installment of the so-called New Small Wheels (NSWs) [186], replacing the Run-2 small wheels (see Sec. 3.2.5). The two NSWs are based on small Thin Gap Chambers (sTGCs) and MicroMegas (MM) and they allow both for a reduction of the trigger rate due to noisy events and a better muon reconstruction efficiency in the endcap region. A series of additional upgrades are foreseen for the HL-LHC phase as well [187]. MDT chambers in the BI layer will be substituted with more compact ones, so to host a new RPCs *triplet*, consisting of three layers of RPCs. The MDTs will be used by the trigger system along with the RPCs and TGCs, and the FE electronics of these three sub-detectors are going to be completely replaced. More details about the L0 Muon Barrel trigger upgrade is given in Sec. 8.2.

8.1.5 The TDAQ

As already said, the increase in instantaneous luminosity foreseen in the HL-LHC phase implies a revised Trigger and Data Acquisition (TDAQ) system able to cope with the increased data rate and PU. The design of the Phase-II trigger, outlined in detail in Ref. [188], is still based on a two-levels trigger system: the L0 hardware trigger, providing a rate of 1 MHz with 10 μ s of latency, and a software based trigger referred to as Event-Filter (EF). The larger latency will allow more complex trigger algorithms, as well as to maintain the current trigger thresholds. The hardware-based L0 trigger comprises a calorimeter-based trigger (L0Calo), a muon trigger (L0Muon), and the Global Trigger. The latter, replacing the functionalities of the L1Topo (see Sec. 3.2.6), exploits granular information from the entire calorimeter system and runs sophisticated offline-like algorithms, implementing clustering of calorimeter cells, so to improve the e , τ and γ reconstruction and isolation evaluation as well as the identification of exotics objects. The final L0 trigger decision is made by the so-called Central Trigger Processor (CTP). In the next section, additional details about the upgrade of the L0 barrel muon trigger are given.

8.2 The ATLAS L0 muon barrel trigger upgrade

As of Run-3, the ATLAS barrel muon system relied on three stations of doublets of RPCs, two in the BM and one in the BO (see Sec. 3.2.5). During the LS3, as already mentioned, a fourth RPC triplet station will be installed in the BI, allowing for more redundancy of the trigger system as well as for an increase in its performances in terms of trigger acceptance, with an expected trigger efficiency of 92%. A schematic picture of the muon system after the Phase-II upgrade is given in Fig. 8.2

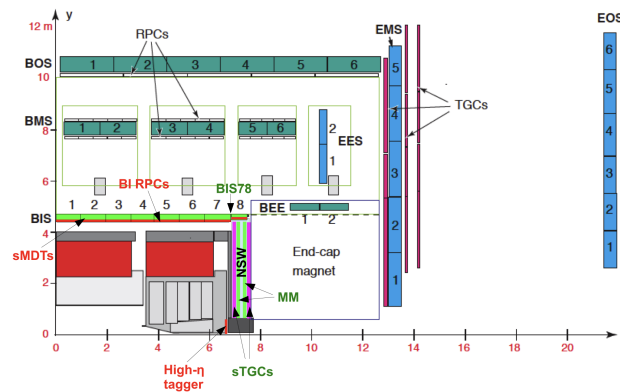


Figure 8.2. Muon system for the HL-LHC phase in the (z, y) plane.

8.2.1 Overview of the TDAQ interface

The Run-2 FE boards of the BO and BM RPCs, collecting the data from the RPCs and performing the Amplifier Shaper Discriminator (ASD)¹, will be used for the HL-LHC too, while a new FE board, including the Time to Digital Converter (TDC) as well, will be installed for the RPCs BI. The TDC will perform a timing measurement with a resolution of 0.4 ns through the Time-Over-Threshold (TOT) method, where the timing information is extracted from the time-interval between the trailing edge and the falling edge of the collected charge signal, when the latter is above a certain threshold.

All the other RPCs electronics will be instead completely replaced. 1542 Data Collector Transmitters (DCTs) will replace the now used Pad and Splitter boxes and they will collect data from up to 288 RPCs FE channels and perform the signal digitisation. 32 off-detector Sector Logic (SL) boards, one per ATLAS sector (see Sec. 3.2.1) will be located in the counting room (Underground Service ATLAS 15 (USA15)) outside the experimental cavern (Underground eXperimental 15 (UX15)). Each SL board will receive data from up to 50 DCTs through bi-directional optical fibers via the low power GigaBit Transceiver (lpGBT), a radiation tolerant ASIC working as a serialiser/deserialiser, and then perform the trigger algorithm.

Both the DCT and the SL board will rely on Field Programmable Gate Array (FPGA) technologies, rather than CPUs, on which the Run-3 ATLAS muon trigger system is based. FPGAs are hardware accelerators that outperform CPUs in terms of flexibility and parallelizability. They are Integrated Circuits (ICs)² which contain programmable logic blocks, interconnects and configuration memories. Logic blocks are the basic FPGA building blocks allowing for logic functions, from simple OR or

¹The signal collected by RPCs is amplified, so that even weak signals are made detectable, shaped, to optimize discrimination with respect to noise signals, and then discriminated, determining whether the signal exceeds a predefined threshold.

²An IC, also known as a microchip or chip, is a miniaturized electronic circuit consisting of semiconductor devices and passive components placed on a single piece of semiconductor material. ICs vary in complexity and functionality, ranging from simple logic gates to System on Chip devices containing entire electronic systems on a single chip.

AND gates to flip-flops and multiplexers; interconnects route the signals through the various logic blocks; configuration memories store the information about the implementation and the connections between such logic blocks. FPGAs are thus extremely flexible and reconfigurable, since different digital circuits can be implemented in a single chip after the hardware has been built, and they allow for parallel processing, making them exploitable in high throughput conditions. For these reasons, FPGAs are extremely suitable for triggering purposes.

The SL board will rely as well on a so-called System on Chip (SoC), which is an IC that integrates most or all components of a computer or electronic system onto a single chip. The SoC exploited in the SL board comprises a multi-core CPU, meaning that multiple CPU processors are found within the same chip, and is thus referred to as Multi-Processor System on Chip (MPSoC). Furthermore, it comprises Input/Output interfaces such as Ethernet controllers, peripheral devices and an FPGA hardware accelerator.

The FPGA exploited by the DCT board is from the Xilinx Artix-7 family (XC7A200), while the SL board consists of:

- a Xilinx Virtex Ultrascale+ XCVU13P FPGA implementing the SL firmware;
- a Xilinx Zynq Ultrascale+ MPSoC (Mercury XU5 ME-XU5-5EV-2I-D12E) allowing for monitoring and configuration functionalities via communication with the Detector Control Systems (DCS) and the L0 barrel TDAQ server.

The SL is compliant with the Advanced Telecommunications Computing Architecture (ATCA) standard, which provides a modular and scalable platform for integrating computing, networking, and storage resources into a single chassis-based system. The SL can be thus controlled and monitored remotely through the ATCA protocol via the Intelligent Platform Management Controller (IPMC), which is a dedicated micro-controller, implemented on the SL board itself and independent of its the main computing elements. The IPMC collects information from the SL board, such as temperatures, voltage levels, fan speed and power supply status. Such information are sent from the IPMC, upon request, via a standardised communication protocol called Intelligent Platform Management Interface (IPMI), which allows for remote management and monitoring of hardware components, even when the system is powered off or unresponsive.

Data flow

The SL board performs the trigger algorithm using information from both the RPCs and the Tile calorimeter. The trigger candidates so generated are sent within 390 ns to the Monitored Drift Tube Trigger Processor (MDTTP) that performs a more precise p_T measurement using MDT information through which the trigger candidates will be either confirmed or rejected. The trigger decision is then sent to the MUon Central Trigger Processor Interface (MUCTPI). In the meanwhile, the SL stores the data received from the DCTs, waiting for the so-called *L0-accept* signal, which is asserted by the Central Trigger Processor (CTP) if the event has fired at least

one of the L0 triggers. When such a signal is received, the data stored in the SL are sent through Front-End Link Interface eXchange (FELIX) to readout systems. The barrel RPC TDAQ system is schematically shown in Fig. 8.3. Since my main

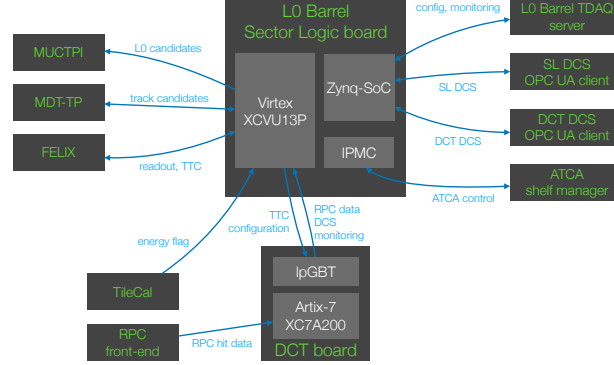


Figure 8.3. Muon system for the HL-LHC phase in the (z, y) plane.

task was providing an interface between the MPSoC and the FPGA of the SL, in the following more details about this interface and its implementation are given.

8.2.2 SL FPGA-SoC interface

The MPSoC, hosted on the SL board, allows remote control and data transfer to the L0 barrel TDAQ server and to the DCS server. The MPSoC includes the following functionalities:

- implementing the Ethernet protocol with the L0 barrel TDAQ server;
- receiving the SL and DCT firmwares from the L0 barrel TDAQ server and programming them respectively on the SL FPGA and on the DCT FPGA through respectively the SL configuration block and the lpGBT interface block;
- routing the SL (DCT) configuration data (stored in FPGA internal registers) between the SL(DCT) monitoring block and the L0 barrel TDAQ server, with a bidirectional protocol;
- receiving and decoding the configuration and monitoring commands from the L0 barrel TDAQ server;
- sending the SL and DCT monitoring data from the SL monitoring block to the L0 barrel TDAQ server;
- implementing the SL and DCT DCS Open Platform Communications Unified Architecture (OPC UA)³ server functionality, by interfacing with the external

³The OPC UA system is a crucial component for managing and monitoring the detector hardware and associated systems. It provides commands such as ones for activating or deactivating specific detector subsystems, adjusting operational parameters, initiating calibration procedures, and performing diagnostic tests.

DCS OPC UA clients and receiving the SL and DCT DCS data (voltages and temperature values, RPC hit rates) from the monitoring block.

The MPSoC mezzanine is interfaced with the SL FPGA through an Advanced eXtensible Interface-4 (AXI-4) Chip-2-Chip serial bus.

The AXI protocol

The AXI protocol is a standard developed by Advanced RISC Machines (ARM)⁴ used for interfacing the different MPSoC Intellectual Property (IPs)⁵. There exist three different types of AXI protocols:

- the AXI-stream protocol: the simplest one, is designed for streaming data transfers, where data is continuously transferred without addressing or acknowledgment signals;
- the AXI-lite protocol: is a transaction based protocol, also called memory-mapped, where both addressing and acknowledgment signals are exploited. Burst transactions, where multiple data transfers occur consecutively without the need for separate address and data phases for each transfer, are allowed as well;
- the AXI-full protocol: the more flexible, like the AXI-lite is a transaction based protocol, that, in addition to burst transactions, grants various other transactions, such as multiple-outstanding ones, where multiple memory accesses are performed at the same time, and concurrent read and write operations, where both read and write transactions occur at the same time.

Given the fact that multiple read and writes operations are foreseen between the SL MPSoC and the FPGA, the AXI-full is chosen as communication protocol.

The so-called *manager* module is the one initiating the transaction, by either writing or reading the subordinate. While the write transaction relies on three channels, the write address channel, the write data channel and the write response channel, the read transaction relies on two channels, the read address channel and the read data channel. The read response has therefore no dedicated channel and is given in the read data channel. Fig. 8.4 shows schematically a read (a) and a write (b) transaction for the AXI-full protocol.

Each of the five independent channels consists of a set of information signals and uses a synchronous two-way **VALID** and **READY** handshake mechanism. The information source uses the **VALID** signal to show when valid data or control information is available on the channel, while the destination uses the **READY** signal to show when it can accept the data. The transaction happens when both the **VALID** is asserted from the source and the **READY** is asserted from the destination, ensuring that the

⁴RISC stands for *Reduced Instruction Set Computer*, referring to micro-processors with linear and simple architecture.

⁵IPs are pre-designed, reusable blocks of logic or functionality that can be integrated into an IC. Examples of IPs are memory controllers or CPU cores.

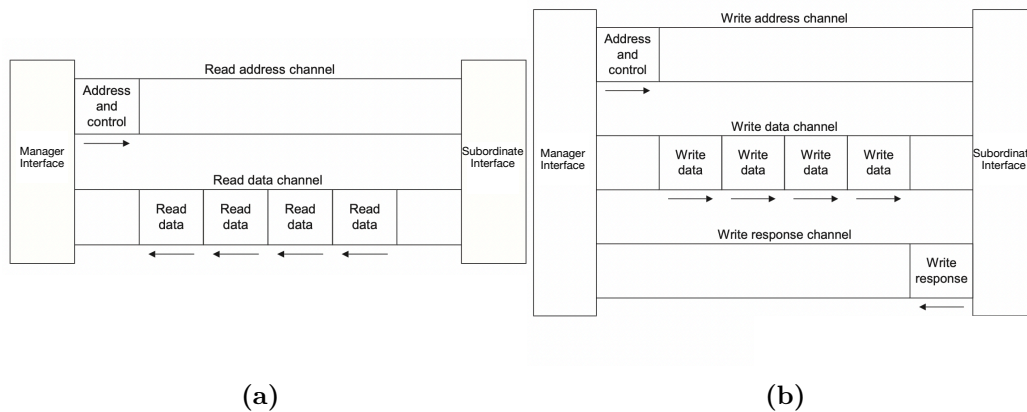


Figure 8.4. Data flows between a manager module and a subordinate module for the read (a) and the write (b) transactions in the AXI-full protocol.

transaction happens only when valid data are on the source and the destination is ready to receive them.

A manager and a subordinate instance can be both a source or a destination, depending on the channel considered (as schematically pictured in Fig. 8.4). In the address channels for both the read and the write transactions, the manager module is the source while the subordinate one is the destination. For the read data channel the manager instance acts instead as a destination and the subordinate one as the source, while the opposite holds for the write data channel. In the write response channel, the subordinate is the source and the manager is the destination.

The AXI Chip-2-Chip

The MPSoC and the FPGA on the SL board are connected through the AXI C2C⁶ core, that acts as bridge that connects the two devices over a full AXI interface, bridging transactions in compliance with AXI protocol specifications.

Fig. 8.5 shows a block-diagram of a generic AXI C2C core.

Two instances of the AXI C2C core, one subordinate and one manager, are required for performing the bridging function. The AXI C2C manager instance, that provides an AXI subordinate interface that can be connected to an AXI manager, will be interfaced with the Zynq UltraScale+, while the AXI C2C subordinate instance, that provides an AXI manager interface that can be connected to an AXI subordinate, will be interfaced with the Virtex UltraScale+. Each AXI C2C core has to be interfaced with an **Aurora64b66b**⁷ module, implementing a link-layer protocol

⁶The AXI C2C is an interface protocol designed for high-bandwidth and low-latency communications between multiple chips, as in this case, or between the same SoC. It provides a standardized interface for chip-to-chip communication, particularly in complex systems where multiple processing elements, accelerators, or peripherals need to communicate efficiently.

⁷The **Aurora64b66b** protocol is a high-speed serial communication protocol used for transmitting and receiving data over point-to-point links between FPGA devices. It employs a technique called **64b66b** encoding, exploited to achieve reliable and efficient data transmission.

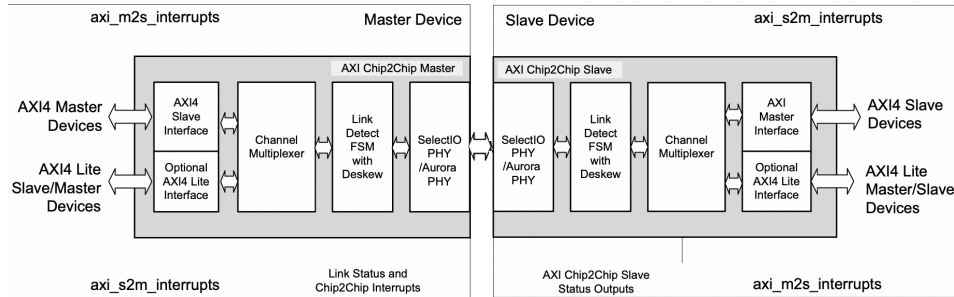


Figure 8.5. AXI C2C instances for a generic project.

for high-speed serial communication. Alternatively, the two AXI C2C instances can be connected using the Select IO interface, implementing a high speed parallel communication. Since a lower latency is associated to the Select IO interface, while a larger throughput is associated to the Aurora one, the choice of the communication interface depends on the use case. Given the fact that the communication between the MPSoC and the FPGA is used for monitoring and configuration purposes, a larger throughput is preferred over a lower latency, and thus the Aurora protocol is exploited in this scenario.

The data flow from the Zynq UltraScale+ to the Virtex UltraScale+ through the two C2C modules is described in the following:

- the Zynq UltraScale+ initiates the data transmission by sending data packets to the AXI C2C subordinate instance;
- the channel multiplexer within the AXI C2C subordinate instance selects the appropriate communication channel for routing the incoming data packets;
- data packets are passed through the detect link Finite State Machine (FSM) with deskew module, ensuring proper alignment and synchronization of the incoming data signals;

Each 64b word sent to the Aurora module is mapped into a pre-defined 66b word, the latter being used for transmission. The two additional bits, referred to as *disparity bits*, represent the difference between the number of 0 and the 1 bits over the 64b mapped word. From these two control bits errors in the data transmission can be detected.

- the data packets are then sent to the AXI C2C manager module, through the Aurora64b66b protocol;
- data flows with the same (reversed) logic within the AXI C2C manager module, reaching finally the Virtex UltraScale+.

8.2.3 MPSoC interface test using the ZCU104 evaluation board

Since when this work was carried out the SL board was not available, the communication protocol between the MPSoC and the FPGA was firstly probed in an evaluation board⁸, the so-called ZCU104, a Zynq featuring both a Processing System (PS) and a Programmable Logic (PL). While the PL is roughly an FPGA containing Block Random Access Memorys (BRAMs), Look Up Tables (LUTs), Registers and AXI interfaces, the PS contains a "full computer" with multiple CPU cores, a very large number of different peripherals, Distributed Random Access Memory (DRAM) controller and Interconnects, acting as a MPSoC.

Since the ZCU104 evaluation board does not comprise transceivers⁹ that can be used in the serial communication protocol implemented by Aurora, the two C2C instances are connected using two First In First Outs (FIFOs), as explained in the following.

Furthermore, to test the Aurora protocol, a single Aurora module is tested in so-called *loopback* configuration, where transmitted signals are sent back (*looped back*) to the receiver within the same device, allowing for the monitoring and verification of signal integrity.

Both these tests were performed using the Vivado toolkit, a design environment developed by Xilinx for designing and implementing digital systems using their SoC and FPGA devices. Such design is realised using a Hardware Description Language (HDL), namely Very High-Speed Integrated Circuit (VHSIC) Hardware Description Language (VHDL), used for designing and modeling ICs and complex digital systems, and block diagrams, providing graphical design entries.

Aurora protocol test

As already said, the Aurora protocol is tested with the Aurora core in loopback configuration. The block diagram of such test is given in Fig. 8.6.

To have the Aurora core in loopback configuration, the information sent out from the Aurora core, from the `USER_DATA_S_AXI_TX` port, is sent back to the core itself, to the `USER_DATA_M_AXI_RX` port. The FIFO used between the `USER_DATA_S_AXI_TX` port to the `USER_DATA_M_AXI_RX` is exploited to mimic the normal latency that would be present between transceivers.

⁸An evaluation board, also known as a development board, is a circuit board equipped with various components, interfaces, and functionalities designed to help in evaluating, prototyping, and experimenting a particular electronic component, system, or technology.

⁹Transceivers, short for transmitter-receiver, are electronic devices or circuits capable of transmitting and receiving signals. They are exploited in high-speed serial communication protocols, like Aurora.

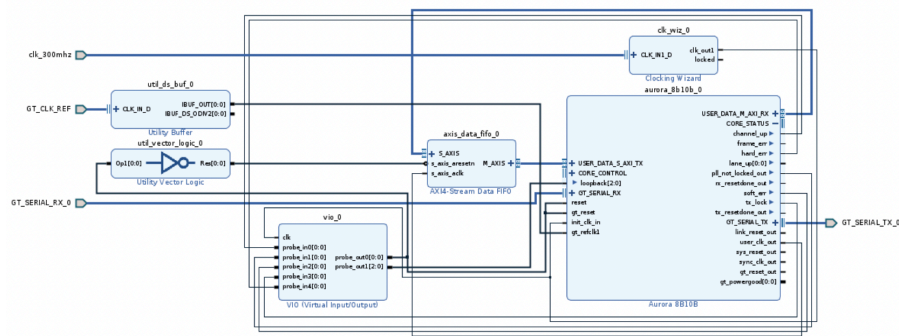


Figure 8.6. Schematic picture of the Aurora configuration in loopback mode used for testing the protocol.

Furthermore, for the Aurora core to be in loopback, a '1' or '2' signal has to be sent to the loopback channel in the Aurora core itself. This is achieved through a Virtual Input\Output (VIO) IP core, which allows to route user defined signals to different peripherals and check control signals during a full simulation. Fig. 8.7 shows the signals routed from the VIO from the two `probe_outi` ports (with `i=0,1`), and the signals checked by the VIO from the five `probe_ini` ports (`i=0-4`).

hw_vio_1				
Name	Value	Activity	Direction	VIO
> design_1_1/Vio_0_probe_out1[2:0]	[H] 1		Output	hw_vio_1
design_1_1/Vio_0_probe_out0	0		Output	hw_vio_1
design_1_1/aurora_8b10b_0_soft_err	[B] 0		Input	hw_vio_1
design_1_1/aurora_8b10b_0_pll_not_locked_out	[B] 0		Input	hw_vio_1
design_1_1/aurora_8b10b_0_hard_err	[B] 0		Input	hw_vio_1
design_1_1/aurora_8b10b_0_channel_up	[B] 1		Input	hw_vio_1
design_1_1/aurora_8b10b_0_tx_lock	[B] 1		Input	hw_vio_1

Figure 8.7. VIO signals during Aurora loopback test: all the errors signals are not asserted while the channel up, indicating that the Aurora module is correctly locked, is asserted.

The `probe_out0` port is connected to a reset (thus is 0 when the communication test is performed), while the `probe_out1` is connected to the loopback port on the Aurora core and is set to 1, allowing for the Aurora loopback configuration.

The correct initialisation of the Aurora module is checked by verifying the control

signals sent out from the core itself, which are connected to the VIO `probe_ini` ports. The three error signals (called `soft_err`, `not_locked_out` and `hard_err`, indicating respectively a recoverable error, a non recoverable error and an error in the synchronisation of the transmitted and received signals) are all null, indicating that no error is recovered. The `channel_up` signal asserted indicates instead that a link between the transmitter port and the receiver one in the Aurora core is established, while the `tx_lock` signal asserted indicates that the received and the transmitted signals are synchronised, this allowing for a reliable and error-free data transmission.

C2C test

The C2C bridging functionalities are instead tested connecting the PS of the ZCU104 to a BRAM on the PL via the two C2C cores needed to implement the protocol; the PS is as well connected directly to the same BRAM, providing additional crosschecks (see Fig. 8.8).

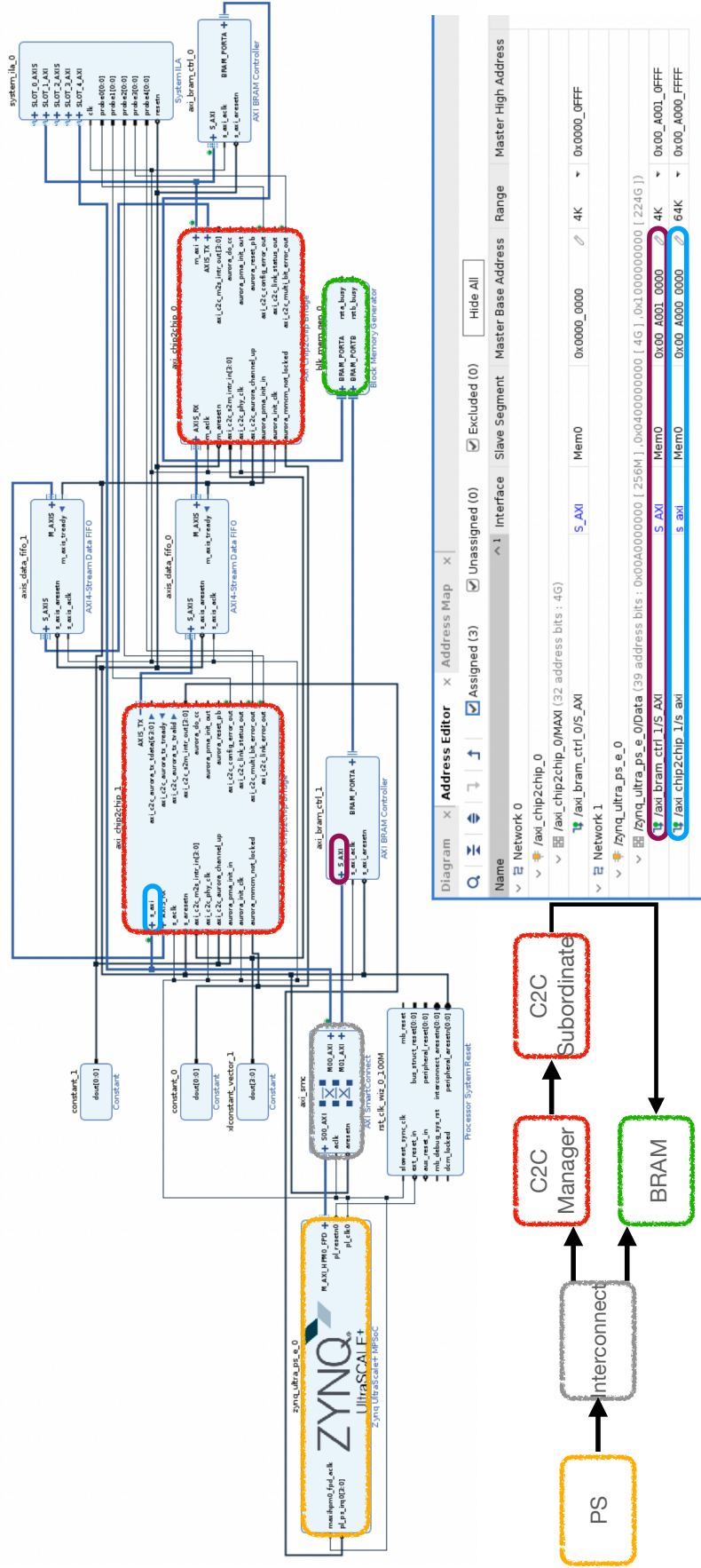


Figure 8.8. Schematic picture and block diagram of the project used to test the C2C protocol. The PS of the ZCU104 (orange) is connected through the interconnect (grey) both to the series of C2C cores (red), that in turn are interfaced to the BRAM (green), and to the BRAM directly. The PS has access to the address space of the BRAM_CTRL1 (prune) that connects the PS to the BRAM, and to the one of the C2C manager core (azure).

The PS, the manager of the read and write transactions, is connected through the `M_AXI_HPMO_FPD` port to an interconnect¹⁰, labelled `axi_smc` in Fig. 8.8, sited on the PL. The interconnect sends signals received from the PS either through the `M00_AXI` port to the manager instance of the AXI C2C, labelled `axi_chip2chip_1`, or through the `M01_AXI` port to a BRAM Controller labelled as `axi_bram_ctrl_1`. The PS has therefore access to the address space of the `axi_bram_ctrl_1` and to the one of the `axi_chip2chip_1`, respectively with addresses `0xA0010000` and `0xA0000000`, as can be seen from the table in Fig. 8.8.

The `axi_bram_ctrl_1` is then connected to the `BRAM_PORTB` of the BRAM. If transceivers were to be present, the `AXIS_TX` on the `axi_chip2chip_1` should have been connected to an `AXIS_RX` port on one Aurora module. The `AXIS_TX` port of such module should have been connected to the `AXIS_RX` port of another Aurora module, and its `AXIS_TX` port should have been connected in turn to the `AXIS_RX` `axi_chip2chip_0` module.

However, since as already said transceivers cannot be exploited in this evaluation board, the `AXIS_TX` port of the `axi_chip2chip_1` core is connected via the `axis_data_fifo_0` to the `AXIS_RX` port of the `axi_chip2chip_0` core. Conversely, the `AXIS_TX` port of the `axi_chip2chip_0` module is connected via the `axis_data_fifo_1` to the `AXIS_RX` port of the `axi_chip2chip_1` module. As for the Aurora protocol test, such FIFOs are used to add a fake latency. Both the AXI C2C cores are set in the Aurora configuration mode, with the relevant signals manually asserted so to emulate such protocol.

The `m_AXI` port of the `axi_chip2chip_0` module is finally connected to the `axi_bram_ctrl_0`, which is in turn connected to the `BRAM_PORTA` of the BRAM.

Write and read transactions are thus performed on the BRAM both via the C2C (by accessing to the address `0xA0000000`) and directly (by accessing to the address `0xA0010000`).

PetaLinux¹¹ is implemented on the PS of the ZCU104. Through it, it is possible to read from and write to physical memory addresses directly from the command line, through the command `devmem`, whose syntax is outlined in the following:

- `devmem <memory_address_towrite> <n_bits> <number>`: writes on the memory address `<memory_address_towrite>` with width `<n_bits>` the content `<number>`;
- `devmem <memory_address_toread>`: reads the memory address `<memory_address_toread>`.

Read and write transactions are performed as in Fig. 8.9.

Firstly `0xAABBCCDD` is written on the BRAM via the C2C (address `0xA0000000`), and then the same number is read back through the C2C and directly from the BRAM (address `0xA0010000`). Hence `0xA0000000` is written on the BRAM directly,

¹⁰An interconnect is a device which provides a connection between multiple manager and subordinate instances

¹¹PetaLinux is a development environment and embedded Linux distribution specifically tailored for use with Xilinx FPGAs and SoCs

```

root@linux_3:~# devmem 0xA0000000 32 0xAABBCCDD
root@linux_3:~# devmem 0xA0000000
0xAABBCCDD
root@linux_3:~# devmem 0xA0010000
0xAABBCCDD
root@linux_3:~# devmem 0xA0010000 32 0xAAAAAAAA
root@linux_3:~# devmem 0xA0010000
0xAAAAAAAA
root@linux_3:~# devmem 0xA0000000
0xAAAAAAAA

```

Figure 8.9. Read and write transactions performed using the `devmem` command available on PetaLinux which is installed on the SoC on the PS. Such transactions are performed either directly on a BRAM connected to the PS (address `0xA0010000`) or through the AXI C2C (address `0xA0000000`), to test its bridging functionality. Details about the `devmem` syntax can be found in the text.

and then same number is read back both through the C2C and directly. Such transactions show that the AXI C2C cores have been correctly implemented.

The communication protocol has been further validated via a so-called Integrated Logic Analyzer (ILA), a logic core able to control the internal signals of a design. Differently from the VIO, ILAs allow for the study of the full signals evolution over time, after a certain condition, referred to as trigger, is verified. As can be seen from the top right of Fig. 8.8, an ILA is connected through the port `slot_1` to the `M00_AXI` port of the interconnect, which is the one that connects the PS to the `axi_chip2chip_1`. The ILA is connected as well through the port `slot_4` to the `m_axi` port of the `axi_chip2chip_0`, that connects the `axi_chip2chip_0` to the `axi_bram_ctrl_0`.

In this way, it is possible to trigger on the write transaction handshake occurring between the the PS and `axi_chip2chip_1` through the `slot_4` and then check if the information is correctly propagated to the BRAM through the `slot_1`. Conversely, it is possible to trigger on the read transaction handshake occurring between the BRAM and the `axi_chip2chip_0` through the `slot_1` and then check if the information is correctly propagated to the PS through the `slot_4`.

Fig. 8.10 shows a write transaction as seen by the ILA.

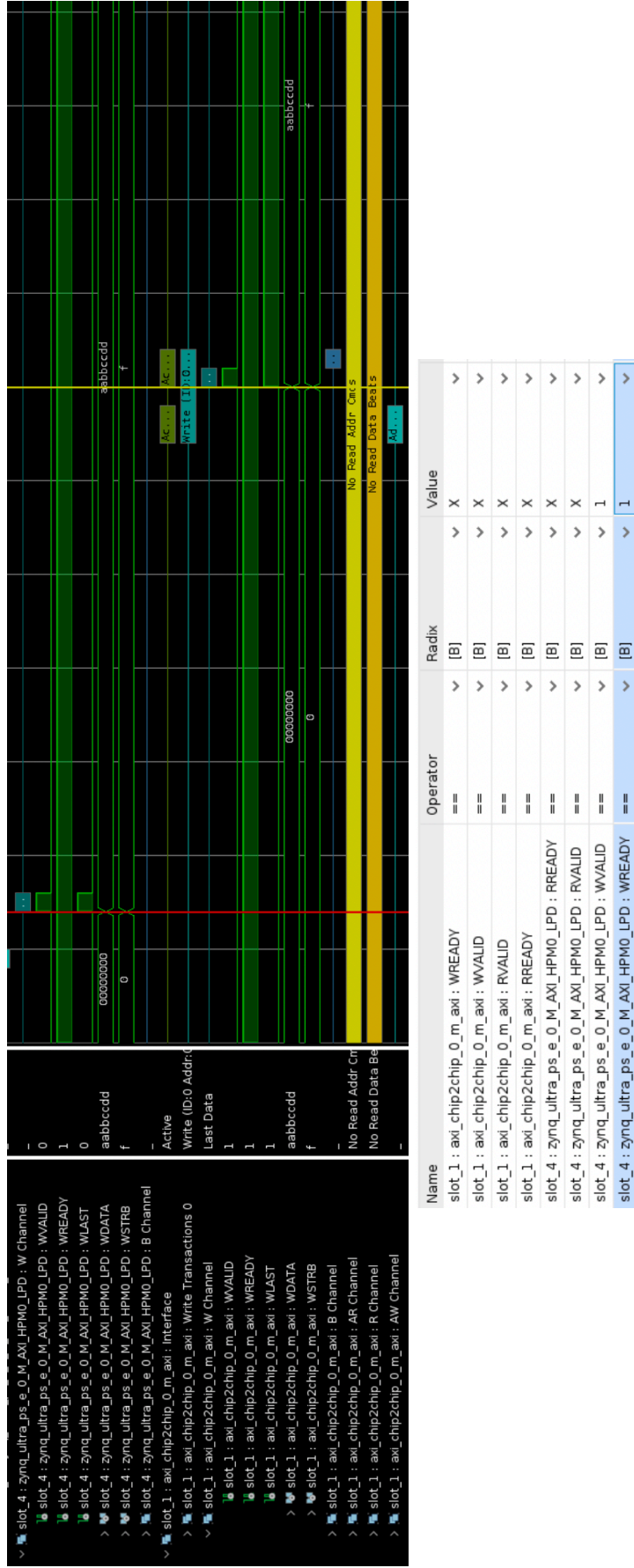


Figure 8.10. Signals for the write transaction issued by the PS onto the BRAM via the C2C. By triggering on the write handshake between the PS and the Interconnect (the red line shows the trigger signal, verified as indicated in the table below when both the `w_valid` from the PS and the `w_ready` from the interconnect are asserted) it's possible to follow the flow of the transaction, ending after a few clock cycles with the writing onto the BRAM.

By asserting through the ILA both the `WVALID` of the PS and `WREADY` of the `axi_chip2chip_1` (in Fig. 8.10 the last two lines in the table and the red line in the graph), the write transaction issued by the PS takes place. `aabbccdd` is written on the `WDATA` channel of the PS, and after a few clock cycles the same information is propagated onto the `WDATA` channel of the `axi_chip2chip_0`, as can be seen from the picture. Thus the write transaction succeeded.

Fig. 8.11 shows instead a read transaction as seen by the ILA.

By asserting through the ILA both the `RVALID` of the BRAM and `RREADY` of the `axi_chip2chip_0` (in Fig. 8.11 the third and fourth lines in the table and the red line in the graph), the read transaction, issued by the PS, takes place. Therefore, `aabbccdd` is written on the `RDATA` channel of the `axi_chip2chip_0`, and after a few clock cycles the same information is propagated onto the `RDATA` channel of the PS, as can be seen from the picture. Thus the read transaction succeeded.

MPSoC interface test using the SL

The previous test has been repeated once the SL became available in 2023. Fig. 8.12 and Fig. 8.13 are the block diagrams of the instantiation AXI C2C core respectively on the Virtex UltraScale+ and on the Zynq UltraScale+ on the SL.

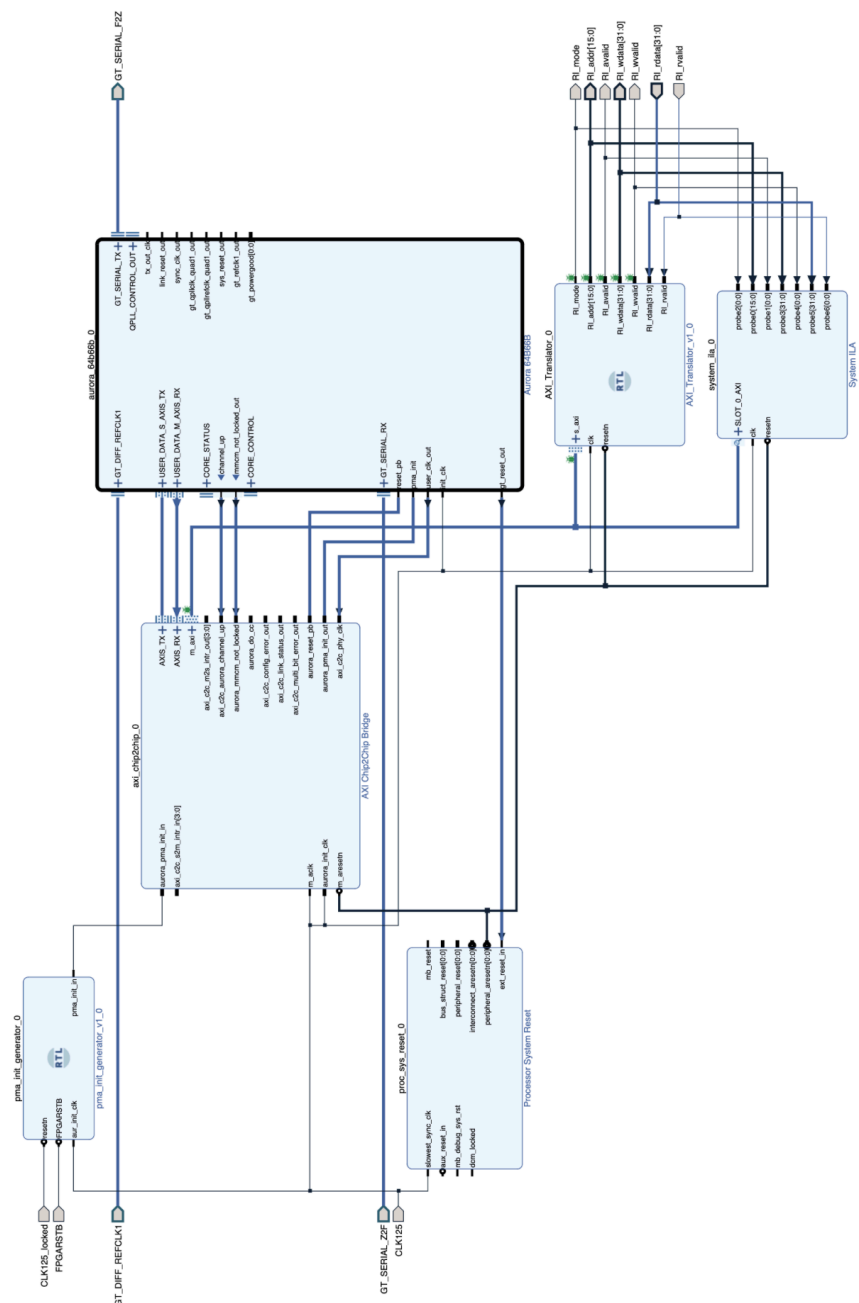


Figure 8.13. The AXI C2C manager instance interfaced with Aurora64b66b is connected to the SoC Mercury XU5 Zynq UltraScale+ MPSoC SOM/ZU2CG mezzanine board.

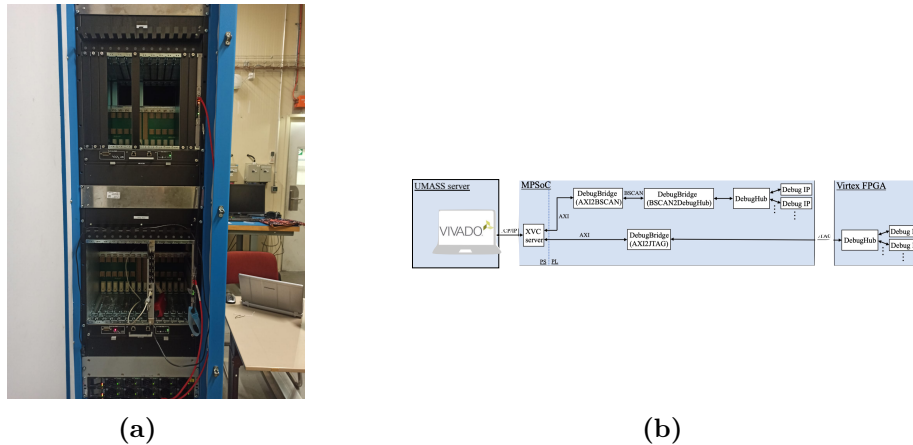


Figure 8.14. Test setup for MPSoC-FPGA communications tests. The physical (a) and schematic (b) setup.

Fig. 8.14 shows instead the SL testing setup ((a) a photo of it and (b) the schematics). The SL is inserted in the lower ATCA chassis (almost in the middle of it).

Multiple ATCA blades, such as the SL board, can be inserted within the same ATCA chassis. Each ATCA blade is controlled via the so-called *shelf-manager* (in the photo the one with the red connector), which allows for remote access, control and monitoring of the whole ATCA chassis. The shelf manager monitoring of the SL board is ensured by the IPMC.

The MPSoC can be accessed remotely through a server (called UMSS in Fig. 8.14 (b)) via the Xilinx Virtual Cable (XVC)¹². As for the test on the ZCU104, Petalinux has been installed on the MPSoC, and therefore read and write transactions are performed via the command `devmem`. Read and write transactions are performed as in Fig. 8.15, showing that the AXI C2C cores have been correctly implemented in this scenario as well.

¹²The XVC is a feature provided by Xilinx for debugging FPGA designs remotely. It emulates the behaviour of a Joint Test Action Group (JTAG) cable over a network connection, allowing for the same functionalities provide by the physical cable, such as accessing/programming/debugging the FPGA, via a remote access.

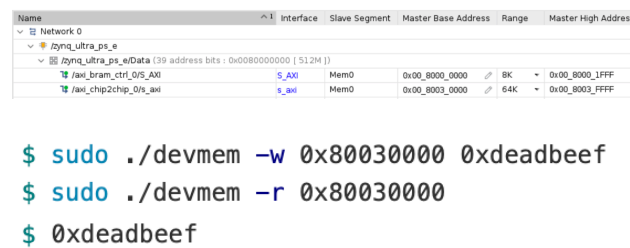


Figure 8.15. Read and write transactions. Firstly `0xdeadbeef` is written on the BRAM via the C2C (address `0x80030000`), and then the same number is read back through the C2C.

Chapter 9

Conclusion

In this thesis work, Dark Sectors were investigated by studying pp collisions produced by the LHC at $\sqrt{s} = 13$ TeV and recorded by the ATLAS experiment between 2015 and 2018, during Run-2.

Dark Sectors are appealing extensions of the SM which could provide, among the particles they foresee, DM candidates. They can be described by simplified models that are characterised by few parameters, allowing for an easy comparison among different searches and with theoretical predictions. Such models result in a rich phenomenology with a wide variety of signatures, which depend on the model and on the region of parameter space being probed.

The simplified DS model here investigated foresees a $U(1)_d$ symmetry, whose vector boson is the Dark Photon γ_d that can decay back to visible SM particles if it mixes, via a coupling ε , with the SM photon. DS particles can be produced by BSM decays of the SM Higgs boson, whose invisible decays are still largely unconstrained.

Searches probing the free parameters space of such simplified DS model have been carried out by both the ATLAS and the CMS collaborations.

Searches looking for DPs decaying within the active volume of the detector were carried out by the CMS collaboration, looking for pairs of muons produced in DP decays. The ATLAS collaboration has instead looked in the Run-2 dataset for displaced DP decays (outside the ATLAS innermost detector) into electrons and light hadrons as well. The collaboration has also searched for prompt DP decays (inside the ATLAS innermost detector) into electrons and muons, this search being based on the dataset collected during Run-1.

This work investigates the latter scenario exploiting the dataset collected during Run-2. With respect to the Run-1 search, this search benefits from improved reconstruction requirements, a new trigger strategy and a new background estimation technique, that in two out of three search channels is more model independent than the one exploited in the Run-1 search. Observed exclusions in the fully-muonic channel extend the sensitivity of the previous search to larger DP masses and smaller couplings of the SM Higgs boson to the dark Higgs boson. From expected sensitivities studies of the fully-electronic channel, the search is expected to extend the sensitivity to a smaller DP masses and smaller couplings of the SM Higgs boson to

the dark one. A combination of these two channels along with the mixed one (foreseeing both muons and electrons) is expected to tighten significantly the constraints on couplings between the dark and the visible sector in the wider DP mass range. I presented the preliminary results of this work at the 2022 SIF national congress, with the parallel talk I gave that resulted in a proceeding [1].

DPS searches have always assumed that the DPs decay back into the detectors they are produced in, while in this thesis, for the first time, the possibility that the DPs are detector stable is studied as well. In this scenario, the DPs escaping the detector result in missing energy being reconstructed. A golden channel for probing this scenario is through the *monojet* signature, where a high missing energy recoils against a highly energetic jet. Therefore, this work looked for excesses of events with a *monojet* signature which could be interpreted in terms of the DP model under investigation. Since the observed event yield is compatible with the SM expectation, exclusion limits are found in the free parameters of the investigated models. This search probed complementary parameter space with respect to dedicated searches, excluding DP mean proper lifetimes larger than 1 m. The search probing another DS model, which foresees an additional scalar particle, excludes hidden scalar mean proper lifetimes larger than 10 m. I presented the results of this work, which were published in Ref. [3], at the LHCP conference and at the SIF national congress in 2021, with the parallel talk I gave that resulted in a proceeding [6].

Since searches for unconventional final states are mostly limited by the trigger systems, performing an online event selection which often discards non-standard events, the last part of this thesis work was focused on the upgrade of the muon trigger system in the barrel for the next LHC Run. The muon trigger system has always played a major role in the online data taking, thanks to the clean signature muons provide. Furthermore, since the muon detector is the outermost detector in ATLAS, and since it is able to provide a standalone muon reconstruction, the muon trigger is also the trigger system best suited to the detection of LLPs. Before the next LHC Run, in the so called High-Luminosity (HL) phase, the luminosity is expected to be five times higher than the nominal value, with an average of 200 pp collisions per event recorded. The identification of unconventional signatures will be even more challenging in this phase, as a consequence of the busier environment that is foreseen. Thus, extremely flexible and parallelisable hardware designs are needed, and this will be granted in the barrel muon trigger system through the usage of FPGAs. An FPGA-based board, placed upon the muon trigger chambers, will collect the recorded hits and will send them to an off-detector FPGA-based board, which will perform the muon trigger logic and store the muon candidates while waiting for a trigger signal asserted by the Central Trigger Processor. The off-detector board needs to be monitored, initialised and configured during the data-taking, with such functionalities being implemented by a multi-processor CPU sited on the board itself. I developed a communication protocol between such an on-chip multi-processor CPU and the FPGA performing the trigger logic. This protocol has been tested on an emulator of the full board and then on the actual board itself. These tests were successful, allowing for the required functionalities to be implemented.

List of Acronyms

ACS Advanced Camera for Surveys

ALICE A Large Ion Collider Experiment

AMS-02 Alpha Magnetic Spectrometer 02

ARM Advanced RISC Machines

ASD Amplifier Shaper Discriminator

ASIC Application Specific Integrated Circuit

ATCA Advanced Telecommunications Computing Architecture

ATLAS A Toroidal LHC ApparatuS

AXI Advanced eXtensible Interface

BAO Baryonic Acoustic Oscillations

BBN Big Bang Nucleosynthesis

BDT Boosted Decision Tree

BI Barrel Inner

BIB Beam Induced Background

BM Barrel Middle

BO Barrel Outer

BR Branching Ratio

BRAM Block Random Access Memory

BSM Beyond the Standard Model

C2C Chip-2-Chip

CB ComBined

CDMSlite Cryogenic Dark Matter Search low ionization threshold experiment

CERN	Conseil Européen pour la Recherche Nucléaire
CL	Confidence Level
CMB	Cosmic Microwave Background
CMS	Compact Muon Solenoid
COBE	COsmic Background Explorer
CP	Charge-Parity
CPU	Central Processing Unit
CR	Control Region
CRESST	Cryogenic Rare Event Search with Superconducting Thermometers
CSC	Cathode Strip Chamber
CST	Calorimeter Soft Term
CT	CaloTagged
CTP	Central Trigger Processor
DCS	Detector Control Systems
DCT	Data Collector Transmitter
DE	Dark Energy
DM	Dark Matter
DNN	Deep Neural Network
DP	Dark Photon
DRAM	Distributed Random Access Memory
DS	Dark Sector
DSCB	Double-Sided Crystal Ball
ECAL	Electromagnetic CALorimeter
EF	Event-Filter
EI	Endcap Inner
EM	Electro-Magnetic
EMEC	ElectronMagnetic EndCap
EO	Endcap Outer

EROS Experience pour la Recherche d'Objets Sombres

EW Electro-Weak

FCal Forward Calorimeter

FE Front End

FELIX Front-End Link Interface eXchange

Fermi-LAT Fermi Large Area Telescope

FIFO First In First Out

FIMP Feebly Interactive Massive Particle

FPGA Field Programmable Gate Array

FRVZ Falkowsky-Ruderman-Volansky- Zupan

FSM Finite State Machine

FSR Final State Radiation

GEANT GEometry ANd Tracking

ggF gluon-gluon Fusion

GPR Gaussian Processing Regression

GSF Gaussian Sum Filter

HAHM Hidden Abelian Higgs Model

HCAL Hadronic CALorimeter

HDL Hardware Description Language

HEC Hadronic EndCap

HERWIG Hadron Emission Reactions With Interfering Gluons

HGTD High Granularity Timing Detector

HL High-Luminosity

HLSP Hidden Lightest Stable Particle

HLT High Level Trigger

IBL Insertable B-Layer

IC Integrated Circuit

ID Inner Detector

ILA Integrated Logic Analyzer

INFN Istituto Nazionale di Fisica Nucleare

IO Inside-Out

IP Interaction Point

IPMC Intelligent Platform Management Controller

IPMI Intelligent Platform Management Interface

ISR Initial State Radiation

ITk Inner TracKer

JEP Jet/Energy-sum Processor

JER Jet Energy Resolution

JES Jet Energy Scale

JTAG Joint Test Action Group

JVF Jet Vertex Fraction

JVT Jet Vertex Tagger

KF Kalman Filter

L0 Level-0

L1 Level-1

LAr Liquid Argon

LEP Large Electron Positron collider

LHC Large Hadron Collider

LHCb Large Hadron Collider beauty

LHCf Large Hadron Collider forward

LHCP LHC Physics

LINAC LINear ACcelerator

LJ Lepton-Jet

LLP Long Lived Particle

LO Leading Order

lpGBT low power GigaBit Transceiver

LS	Long Shutdown
LTR	Life-Time Reweighting
LUCID	LUminosity Cherenkov Integrating Detector
LUT	Look Up Table
MACHO	Massive Astrophysical Compact Halo Objects
MC	Monte Carlo
MDT	Monitored Drift Tube
MDTTP	Monitored Drift Tube Trigger Processor
ME	MS Extrapolated
MET	Missing Energy Transverse
MG	MadGraph
MIP	Minimum Ionizing Particle
MM	MicroMegas
MOND	MOdified Newtonian Dynamics
MPI	Multiple Partons Interaction
MPSoC	Multi-Processor System on Chip
MS	Muon Spectrometer
MUCTPI	MUon Central Trigger Processor Interface
MVA	Multi-Variate Analysis
NCB	Non Collisional Background
NLO	Next-to-Leading-Order
NNLO	Next-to-Next-Leading-Order
NNPDF	Next-to-Next-leading-order Parton Density Function
NSW	New Small Wheel
OGLE	Optical Gravitational Lensing Experiment
OPC UA	Open Platform Communications Unified Architecture
OR	Overlap Removal

PAMELA	Payload for Antimatter Matter Exploration and Light-nuclei Astrophysics
PandaX	Particle and Astrophysical Xenon Experiments
PD	Pixel Detector
PDF	Parton Distribution Function
PFlow	Particle-Flow
PL	Programmable Logic
pLJ	prompt Lepton-Jet
POWHEG	Positive Weight Hardest Emission Generator
PS	Proton Synchrotron
PSB	Proton Synchrotron Booster
PU	Pile-Up
PV	Primary Vertex
QCD	Quantum Chromo Dynamics
RBF	Radial Basis Function
RECAST	Request Efficiency Computation for Alternative Signal Theories
RF	Radio-Frequency
RNN	Recursive Neural Network
ROD	Read-Out Driver
ROI	Region Of Interest
ROS	Read-Out System
RPC	Resistive Plate Chamber
SA	StandAlone
SC	SynchroCyclotron
SCT	Semi-Conductor Tracker
SD	Spin-Dependent
SF	Scale Factor
SHERPA	Simulation of High-Energy Reactions of PArticles

SI	Spin-Independent
SiF	Silicon Forward
SL	Sector Logic
SLACS	Sloan Lens ACS
SM	Standard Model
SN	SuperNovae
SoC	System on Chip
SPS	Super Proton Synchrotron
SR	Signal Region
SSB	Spontaneous Symmetry Breaking
SSDS	Sloan Digital Sky Survey
ST	Segmented Tagged
sTGC	small Thin Gap Chamber
Super-Kamiokande	Super-Kamioka neutrino detection experiment
SUSY	SUper SYmmetry
SW	Small Wheels
TDAQ	Trigger and Data AcQuisition
TDC	Time to Digital Converter
TGC	Thin Gap Chamber
TLA	Trigger-Level Analysis
TOT	Time-Over-Threshold
TOTEM	TOTal Elastic and diffractive cross section Measurement
TP	Trigger Processor
TR	Transition Radiation
TRT	Transition Radiation Tracker
TST	Track Soft Term
TTVA	Track-To-Vertex Association
USA15	Underground Service ATLAS 15

UX15 Underground eXperimental 15

VBF Vector Boson Fusion

VEV Vacuum Expectation Value

VH Higgs-strahlung of a Vector boson

VHDL Very High-Speed Integrated Circuit (VHSIC) Hardware Description Language

VHSIC Very High-Speed Integrated Circuit

VIO Virtual Input\Output

VR Validation Region

WH Higgs-strahlung of a W boson

WIMP Weakly Interactive Massive Particle

WP Working Point

XVC Xilinx Virtual Cable

ZH Higgs-strahlung of a Z boson

Bibliography

- [1] E Pompa Pacchi. “Dark Sector searches in final states with prompt neutral particles with the ATLAS detector”. In: *Nuovo Cimento C* 46.4 (2023), p. 100. DOI: [10.1393/ncc/i2023-23100-4](https://doi.org/10.1393/ncc/i2023-23100-4). URL: <https://cds.cern.ch/record/2887357>.
- [2] Georges Aad et al. “Search for new phenomena in events with an energetic jet and missing transverse momentum in pp collisions at $\sqrt{s}=13$ TeV with the ATLAS detector”. In: *Phys. Rev. D* 103.11 (2021), p. 112006. DOI: [10.1103/PhysRevD.103.112006](https://doi.org/10.1103/PhysRevD.103.112006). arXiv: [2102.10874](https://arxiv.org/abs/2102.10874) [hep-ex].
- [3] ATLAS Collaboration. *Constraining the Dark Sector with the monojet signature in the ATLAS experiment*. Tech. rep. Geneva: CERN, 2021. URL: <https://cds.cern.ch/record/2772627>.
- [4] Elena Pompa Pacchi. “Constraining the Dark Sector with the Mono-jet signature”. In: (2021). URL: <https://cds.cern.ch/record/2773225>.
- [5] Elena Pompa Pacchi. “Constraining the Dark Sector with the Mono-jet signature with the ATLAS detector at the LHC”. In: *PoS LHCP2021* (2021), p. 254. DOI: [10.22323/1.397.0254](https://doi.org/10.22323/1.397.0254).
- [6] Elena Pompa Pacchi. “Dark sector searches with the mono-jet signature at the ATLAS detector at the LHC”. In: *Nuovo Cimento C* 45.5 (2022), p. 126. DOI: [10.1393/ncc/i2022-22126-4](https://doi.org/10.1393/ncc/i2022-22126-4). URL: <https://cds.cern.ch/record/2837856>.
- [7] ATLAS Collaboration. “Observation of a new particle in the search for the Standard Model Higgs boson with the ATLAS detector at the LHC”. In: *Phys. Lett. B* 716:1-29 (2012).
- [8] CMS Collaboration. “Observation of a new boson at a mass of 125 GeV with the CMS experiment at the LHC”. In: *Phys. Lett. B* 716:30–61 (2012).
- [9] Cush. *Standard Model of Elementary Particles*. URL: https://en.wikipedia.org/wiki/File:Standard_Model_of_Elementary_Particles.svg.
- [10] E. Fermi. “Attempt at a Theory of β -rays”. In: *Il Nuovo Cimento* 11 (1934).
- [11] T.D Lee et al. “Question of parity conservation in weak Interactions”. In: *Phys. Rev.* 104, 254 (1956).
- [12] C.S Wu et al. “Experimental test of parity conservation in β -decay”. In: *Phys.Rev.* 105 (1957).

- [13] F.J. Hasert et al. “Observation of neutrino-like interactions without muon or electron in the Gargamelle neutrino experiment”. In: *Phys. Rev.* 46B, 138 (1973).
- [14] A. Salam. “Weak and electromagnetic interactions”. In: *Nuovo Cimento* 11:568–577 (1959).
- [15] S. Weinberg. “A Model of Leptons”. In: *Phys. Rev. Lett.* 19:1264–1266 (1967).
- [16] P. W. Higgs. “Broken Symmetries and the Masses of Gauge Bosons”. In: *Phys. Rev. Lett.* 13:508–509 (1964).
- [17] F. Englert et al. “Broken Symmetries and the Mass of Gauge Vector Mesons”. In: *Phys. Rev. Lett.* 13:321–323 (1964).
- [18] John Ellis, Mary K. Gaillard, and Dimitri V. Nanopoulos. “A Historical Profile of the Higgs Boson”. In: *The standard theory of particle physics: Essays to celebrate CERN’s 60th anniversary*. Ed. by Luciano Maiani and Luigi Rolandi. 2016, pp. 255–274. DOI: [10.1142/9789814733519_0014](https://doi.org/10.1142/9789814733519_0014). arXiv: [1504.07217](https://arxiv.org/abs/1504.07217) [hep-ph].
- [19] J. Goldstone. In: *Nuovo Cimento* 19,154 (1961).
- [20] M. Carena et al. “Status of the Higgs Boson Physics”. In: *PDG* (2023). URL: <https://pdg.lbl.gov/2023/reviews/rpp2022-rev-higgs-boson.pdf>.
- [21] ATLAS Collaboration. “Combination of searches for invisible decays of the Higgs boson using 139 fb^{−1} of proton-proton collision data at s=13 TeV collected with the ATLAS experiment”. In: *Phys. Lett. B* 842 (2023), p. 137963. DOI: [10.1016/j.physletb.2023.137963](https://doi.org/10.1016/j.physletb.2023.137963). arXiv: [2301.10731](https://arxiv.org/abs/2301.10731) [hep-ex].
- [22] CMS Collaboration. “A search for decays of the Higgs boson to invisible particles in events with a top-antitop quark pair or a vector boson in proton-proton collisions at $\sqrt{s} = 13$ TeV”. In: *Eur. Phys. J. C* 83.10 (2023), p. 933. DOI: [10.1140/epjc/s10052-023-11952-7](https://doi.org/10.1140/epjc/s10052-023-11952-7). arXiv: [2303.01214](https://arxiv.org/abs/2303.01214) [hep-ex].
- [23] F. W. Bessel. “On the variations of the proper motions of Procyon and Sirius”. In: 6 (Dec. 1844), pp. 136–141. DOI: [10.1093/mnras/6.11.136](https://doi.org/10.1093/mnras/6.11.136).
- [24] H. Poincare. “The Milky Way and the Theory of Gases”. In: *Popular Astronomy* 14 (Oct. 1906), pp. 475–488.
- [25] Edwin Hubble and Milton L. Humason. “The Velocity-Distance Relation among Extra-Galactic Nebulae”. In: 74 (July 1931), p. 43. DOI: [10.1086/143323](https://doi.org/10.1086/143323).
- [26] F. Zwicky. “Republication of: The redshift of extragalactic nebulae”. In: *General Relativity and Gravitation* 41.1 (Jan. 2009), pp. 207–224. DOI: [10.1007/s10714-008-0707-4](https://doi.org/10.1007/s10714-008-0707-4).
- [27] A.G. Doroshkevich, Vladimir N. Lukash, and E.V. Mikheeva. “A solution to the problems of cusps and rotation curves in dark matter halos in the cosmological standard model”. In: *Uspekhi Fizicheskikh Nauk* 182.1 (2012), p. 3. ISSN: 1996-6652. DOI: [10.3367/ufnr.0182.201201a.0003](https://doi.org/10.3367/ufnr.0182.201201a.0003). URL: <http://dx.doi.org/10.3367/UFNr.0182.201201a.0003>.

- [28] M. Schwarzschild. “Mass distribution and mass-luminosity ratio in galaxies”. In: 59 (Sept. 1954), p. 273. DOI: [10.1086/107013](https://doi.org/10.1086/107013).
- [29] H. C. van de Hulst. “1945, The Origin of Radio Waves from Space”. In: *Classics in Radio Astronomy*. Vol. 10. 1982, p. 302. DOI: [10.1007/978-94-009-7752-5_34](https://doi.org/10.1007/978-94-009-7752-5_34).
- [30] I. Newton and W. Abendroth. *Optik: 1704*. Ostwalds Klassiker der exakten Wissenschaften v. 2-3. Engelmann, 1898. URL: <https://books.google.it/books?id=JgfaNAECAAJ>.
- [31] A. Einstein. “Lens-like action of a star by the deviation of light in the gravitational field”. In: *Science* 84(2188):506-507 (1936).
- [32] Adam S. Bolton et al. “The Sloan Lens ACS Survey. V. The Full ACS Strong-Lens Sample”. In: *Astrophys. J.* 682 (2008), pp. 964–984. DOI: [10.1086/589327](https://doi.org/10.1086/589327). arXiv: [0805.1931](https://arxiv.org/abs/0805.1931) [astro-ph].
- [33] Adam S. Bolton et al. “The Sloan Lens ACS Survey. V. The Full ACS Strong-Lens Sample*”. In: *The Astrophysical Journal* 682.2 (Aug. 2008), p. 964. DOI: [10.1086/589327](https://doi.org/10.1086/589327). URL: <https://dx.doi.org/10.1086/589327>.
- [34] D. Paraficz et al. *The Bullet cluster at its best: weighing stars, gas and dark matter*. 2012. arXiv: [1209.0384](https://arxiv.org/abs/1209.0384) [astro-ph.CO].
- [35] Douglas Clowe et al. “A direct empirical proof of the existence of dark matter”. In: *Astrophys. J. Lett.* 648 (2006), pp. L109–L113. DOI: [10.1086/508162](https://doi.org/10.1086/508162). arXiv: [astro-ph/0608407](https://arxiv.org/abs/astro-ph/0608407).
- [36] Robert V. Wagoner, William A. Fowler, and F. Hoyle. “On the Synthesis of Elements at Very High Temperatures”. In: 148 (Apr. 1967), p. 3. DOI: [10.1086/149126](https://doi.org/10.1086/149126).
- [37] E. Margaret Burbidge et al. “Synthesis of the Elements in Stars”. In: *Rev. Mod. Phys.* 29 (4 Oct. 1957), pp. 547–650. DOI: [10.1103/RevModPhys.29.547](https://doi.org/10.1103/RevModPhys.29.547). URL: <https://link.aps.org/doi/10.1103/RevModPhys.29.547>.
- [38] H. P. Robertson. “On the Foundations of Relativistic Cosmology”. In: *Proceedings of the National Academy of Science* 15.11 (Nov. 1929), pp. 822–829. DOI: [10.1073/pnas.15.11.822](https://doi.org/10.1073/pnas.15.11.822).
- [39] A. Friedmann. “On the Curvature of Space”. In: *General Relativity and Gravitation* 31 (Dec. 1999), p. 1991. DOI: [10.1023/A:1026751225741](https://doi.org/10.1023/A:1026751225741).
- [40] COBE Collaboration. “A preliminary measurement of the cosmic microwave background spectrum by the Cosmic Background Explorer (COBE) satellite”. In: *Ap J.* 354 (1990).
- [41] Planck Collaboration et al. *Planck 2018 results. I. Overview and the cosmological legacy of Planck*. 2018. arXiv: [1807.06205](https://arxiv.org/abs/1807.06205) [astro-ph.CO].
- [42] N. Suzuki et al. “The Hubble Space Telescope Cluster Supernova Survey. V. Improving the Dark-energy Constraints above $z > 1$ and Building an Early-type-hosted Supernova Sample”. In: 746.1, 85 (Feb. 2012), p. 85. DOI: [10.1088/0004-637X/746/1/85](https://doi.org/10.1088/0004-637X/746/1/85). arXiv: [1105.3470](https://arxiv.org/abs/1105.3470) [astro-ph.CO].

- [43] UCLA. *BBN UCLA*. <https://www.astro.ucla.edu/~wright/BBNS.html> [UCLA_{BBN}]. 2012.
- [44] M. Milgrom. “A modification of the Newtonian dynamics as a possible alternative to the hidden mass hypothesis.” In: 270 (July 1983), pp. 365–370. DOI: [10.1086/161130](https://doi.org/10.1086/161130).
- [45] C. Alcock et al. “EROS and MACHO combined limits on planetary mass dark matter in the galactic halo”. In: *Astrophys. J. Lett.* 499 (1998), p. L9. DOI: [10.1086/311355](https://doi.org/10.1086/311355). arXiv: [astro-ph/9803082](https://arxiv.org/abs/astro-ph/9803082).
- [46] Ł. Wyrzykowski et al. “Black Hole, Neutron Star and White Dwarf Candidates from Microlensing with OGLE-III”. In: *Mon. Not. Roy. Astron. Soc.* 458.3 (2016), pp. 3012–3026. DOI: [10.1093/mnras/stw426](https://doi.org/10.1093/mnras/stw426). arXiv: [1509.04899](https://arxiv.org/abs/1509.04899) [astro-ph.SR].
- [47] Lawrence J. Hall et al. “Freeze-In Production of FIMP Dark Matter”. In: *JHEP* 03 (2010), p. 080. DOI: [10.1007/JHEP03\(2010\)080](https://doi.org/10.1007/JHEP03(2010)080). arXiv: [0911.1120](https://arxiv.org/abs/0911.1120) [hep-ph].
- [48] Xiao-Rui Wang and Ke-Pan Xie. “Freeze-in of WIMP dark matter”. In: *Phys. Rev. D* 108 (5 Sept. 2023), p. 055035. DOI: [10.1103/PhysRevD.108.055035](https://doi.org/10.1103/PhysRevD.108.055035). URL: <https://link.aps.org/doi/10.1103/PhysRevD.108.055035>.
- [49] Russell Kirk. “Dark Matter Genesis”. PhD thesis. Royal Holloway, U. of London, Royal Holloway, U. of London, 2017.
- [50] L. Roszkowski et al. *WIMP dark matter candidates and searches - current status and future prospects*. 2017. arXiv: [1707.06277](https://arxiv.org/abs/1707.06277) [hep-ph].
- [51] P. Agnes et al. “Search for low-mass dark matter WIMPs with 12 ton-day exposure of DarkSide-50”. In: *Phys. Rev. D* 107.6 (2023), p. 063001. DOI: [10.1103/PhysRevD.107.063001](https://doi.org/10.1103/PhysRevD.107.063001). arXiv: [2207.11966](https://arxiv.org/abs/2207.11966) [hep-ex].
- [52] PandaX-II Collaboration. “Dark Matter Results From 54-Ton-Day Exposure of PandaX-II Experiment”. In: *Phys. Rev.* 119(18):181302 (2017).
- [53] XENON1T Collaboration. “Light Dark Matter Search with Ionization Signals in XENON1T”. In: *Phys. Rev. Lett.* 123 (2019).
- [54] P. Agnes et al. “Low-Mass Dark Matter Search with the DarkSide-50 Experiment”. In: *Physical Review Letters* 121.8 (Aug. 2018). ISSN: 1079-7114. DOI: [10.1103/physrevlett.121.081307](https://doi.org/10.1103/physrevlett.121.081307). URL: <http://dx.doi.org/10.1103/PhysRevLett.121.081307>.
- [55] R. Agnese et al. “Search for low-mass dark matter with CDMSlite using a profile likelihood fit”. In: *Physical Review D* 99.6 (Mar. 2019). ISSN: 2470-0029. DOI: [10.1103/physrevd.99.062001](https://doi.org/10.1103/physrevd.99.062001). URL: <http://dx.doi.org/10.1103/PhysRevD.99.062001>.
- [56] A. H. Abdelhameed et al. “First results from the CRESST-III low-mass dark matter program”. In: *Physical Review D* 100.10 (Nov. 2019). ISSN: 2470-0029. DOI: [10.1103/physrevd.100.102002](https://doi.org/10.1103/physrevd.100.102002). URL: <http://dx.doi.org/10.1103/PhysRevD.100.102002>.

- [57] David N. Spergel. “Motion of the Earth and the detection of weakly interacting massive particles”. In: *Phys. Rev. D* 37 (6 Mar. 1988), pp. 1353–1355. DOI: [10.1103/PhysRevD.37.1353](https://doi.org/10.1103/PhysRevD.37.1353). URL: <https://link.aps.org/doi/10.1103/PhysRevD.37.1353>.
- [58] F. Mayet et al. “A review of the discovery reach of directional Dark Matter detection”. In: *Physics Reports* 627 (2016). A review of the discovery reach of directional Dark Matter detection, pp. 1–49. ISSN: 0370-1573. DOI: <https://doi.org/10.1016/j.physrep.2016.02.007>. URL: <https://www.sciencedirect.com/science/article/pii/S0370157316001022>.
- [59] M. G. Aartsen et al. “Search for Dark Matter Annihilations in the Sun with the 79-String IceCube Detector”. In: *Physical Review Letters* 110.13 (Mar. 2013). ISSN: 1079-7114. DOI: [10.1103/physrevlett.110.131302](https://doi.org/10.1103/physrevlett.110.131302). URL: <http://dx.doi.org/10.1103/PhysRevLett.110.131302>.
- [60] T. Tanaka et al. “AN INDIRECT SEARCH FOR WEAKLY INTERACTING MASSIVE PARTICLES IN THE SUN USING 3109.6 DAYS OF UPWARD-GOING MUONS IN SUPER-KAMIOKANDE”. In: *The Astrophysical Journal* 742.2 (Nov. 2011), p. 78. ISSN: 1538-4357. DOI: [10.1088/0004-637x/742/2/78](https://doi.org/10.1088/0004-637x/742/2/78). URL: <http://dx.doi.org/10.1088/0004-637x/742/2/78>.
- [61] M. Ackermann et al. “Searching for Dark Matter Annihilation from Milky Way Dwarf Spheroidal Galaxies with Six Years of Fermi Large Area Telescope Data”. In: *Physical Review Letters* 115.23 (Nov. 2015). ISSN: 1079-7114. DOI: [10.1103/physrevlett.115.231301](https://doi.org/10.1103/physrevlett.115.231301). URL: <http://dx.doi.org/10.1103/PhysRevLett.115.231301>.
- [62] M. Aguilar et al. “First Result from the Alpha Magnetic Spectrometer on the International Space Station: Precision Measurement of the Positron Fraction in Primary Cosmic Rays of 0.5–350 GeV”. In: *Phys. Rev. Lett.* 110 (14 Apr. 2013), p. 141102. DOI: [10.1103/PhysRevLett.110.141102](https://doi.org/10.1103/PhysRevLett.110.141102). URL: <https://link.aps.org/doi/10.1103/PhysRevLett.110.141102>.
- [63] O. Adriani et al. “An anomalous positron abundance in cosmic rays with energies 1.5–100 GeV”. In: *Nature* 458.7238 (Apr. 2009), pp. 607–609. ISSN: 1476-4687. DOI: [10.1038/nature07942](https://doi.org/10.1038/nature07942). URL: <http://dx.doi.org/10.1038/nature07942>.
- [64] M. Aguilar et al. “First Result from the Alpha Magnetic Spectrometer on the International Space Station: Precision Measurement of the Positron Fraction in Primary Cosmic Rays of 0.5–350 GeV”. In: 110.14, 141102 (Apr. 2013), p. 141102. DOI: [10.1103/PhysRevLett.110.141102](https://doi.org/10.1103/PhysRevLett.110.141102).
- [65] Armen Tumasyan et al. “Search for new particles in events with energetic jets and large missing transverse momentum in proton-proton collisions at $\sqrt{s} = 13$ TeV”. In: *JHEP* 11 (2021), p. 153. DOI: [10.1007/JHEP11\(2021\)153](https://doi.org/10.1007/JHEP11(2021)153). arXiv: [2107.13021](https://arxiv.org/abs/2107.13021) [hep-ex].
- [66] Marco Fabbrichesi, Emidio Gabrielli, and Gaia Lanfranchi. “The Dark Photon”. In: (May 2020). DOI: [10.1007/978-3-030-62519-1](https://doi.org/10.1007/978-3-030-62519-1). arXiv: [2005.01515](https://arxiv.org/abs/2005.01515) [hep-ph].

- [67] B. Batell et al. “Probing a secluded $U(1)$ at B factories”. In: *Phys. Rev.* 79:115008 (2009).
- [68] P. Meade et al. “Dark matter sees the light”. In: *JHEP* 12:052 (2009).
- [69] Iacopo Longarini. “A search for long-lived particles with the ATLAS Experiment”. PhD thesis. Rome U., 2022.
- [70] CMS Collaboration. “Search for direct production of GeV-scale resonances decaying to a pair of muons in proton-proton collisions at $\sqrt{s} = 13$ TeV”. In: *JHEP* 12 (2023), p. 070. DOI: [10.1007/JHEP12\(2023\)070](https://doi.org/10.1007/JHEP12(2023)070). arXiv: [2309.16003](https://arxiv.org/abs/2309.16003) [hep-ex].
- [71] ATLAS Collaboration. “Observation of electroweak production of two jets in association with an isolated photon and missing transverse momentum, and search for a Higgs boson decaying into invisible particles at 13 TeV with the ATLAS detector”. In: *Eur. Phys. J. C* 82.2 (2022), p. 105. DOI: [10.1140/epjc/s10052-021-09878-z](https://doi.org/10.1140/epjc/s10052-021-09878-z). arXiv: [2109.00925](https://arxiv.org/abs/2109.00925) [hep-ex].
- [72] ATLAS Collaboration. “Search for dark photons from Higgs boson decays via ZH production with a photon plus missing transverse momentum signature from pp collisions at $\sqrt{s} = 13$ TeV with the ATLAS detector”. In: *JHEP* 07 (2023), p. 133. DOI: [10.1007/JHEP07\(2023\)133](https://doi.org/10.1007/JHEP07(2023)133). arXiv: [2212.09649](https://arxiv.org/abs/2212.09649) [hep-ex].
- [73] CMS Collaboration. “Search for dark photons in Higgs boson production via vector boson fusion in proton-proton collisions at $\sqrt{s} = 13$ TeV”. In: *JHEP* 03 (2021), p. 011. DOI: [10.1007/JHEP03\(2021\)011](https://doi.org/10.1007/JHEP03(2021)011). arXiv: [2009.14009](https://arxiv.org/abs/2009.14009) [hep-ex].
- [74] CMS Collaboration. “Search for dark photons in decays of Higgs bosons produced in association with Z bosons in proton-proton collisions at $\sqrt{s} = 13$ TeV”. In: *JHEP* 10 (2019), p. 139. DOI: [10.1007/JHEP10\(2019\)139](https://doi.org/10.1007/JHEP10(2019)139). arXiv: [1908.02699](https://arxiv.org/abs/1908.02699) [hep-ex].
- [75] “Search for long-lived particles decaying in the CMS muon detectors in proton-proton collisions at $\sqrt{s} = 13$ TeV”. In: (Feb. 2024). arXiv: [2402.01898](https://arxiv.org/abs/2402.01898) [hep-ex].
- [76] CMS Collaboration. “Search for long-lived particles decaying into muon pairs in proton-proton collisions at $\sqrt{s} = 13$ TeV collected with a dedicated high-rate data stream”. In: *JHEP* 04 (2022), p. 062. DOI: [10.1007/JHEP04\(2022\)062](https://doi.org/10.1007/JHEP04(2022)062). arXiv: [2112.13769](https://arxiv.org/abs/2112.13769) [hep-ex].
- [77] CMS Collaboration. “Search for long-lived particles decaying to a pair of muons in proton-proton collisions at $\sqrt{s} = 13$ TeV”. In: *JHEP* 05 (2023), p. 228. DOI: [10.1007/JHEP05\(2023\)228](https://doi.org/10.1007/JHEP05(2023)228). arXiv: [2205.08582](https://arxiv.org/abs/2205.08582) [hep-ex].
- [78] ATLAS Collaboration. “Search for light long-lived neutral particles that decay to collimated pairs of leptons or light hadrons in pp collisions at $\sqrt{s} = 13$ TeV with the ATLAS detector”. In: *JHEP* 06 (2023), p. 153. DOI: [10.1007/JHEP06\(2023\)153](https://doi.org/10.1007/JHEP06(2023)153). arXiv: [2206.12181](https://arxiv.org/abs/2206.12181) [hep-ex].

- [79] *Search for light long-lived neutral particles from Higgs boson decays via vector-boson-fusion production from pp collisions at $\sqrt{s} = 13$ TeV with the ATLAS detector*. Tech. rep. Geneva: CERN, 2023. URL: <https://cds.cern.ch/record/2870215>.
- [80] CMS Collaboration. “A search for pair production of new light bosons decaying into muons in proton-proton collisions at 13 TeV”. In: *Phys. Lett. B* 796 (2019), pp. 131–154. DOI: [10.1016/j.physletb.2019.07.013](https://doi.org/10.1016/j.physletb.2019.07.013). arXiv: [1812.00380](https://arxiv.org/abs/1812.00380) [hep-ex].
- [81] Georges Aad et al. “A search for prompt lepton-jets in pp collisions at $\sqrt{s} = 8$ TeV with the ATLAS detector”. In: *JHEP* 02 (2016), p. 062. DOI: [10.1007/JHEP02\(2016\)062](https://doi.org/10.1007/JHEP02(2016)062). arXiv: [1511.05542](https://arxiv.org/abs/1511.05542) [hep-ex].
- [82] ATLAS Collaboration. “A search for prompt lepton-jets in pp collisions at $\sqrt{s} = 8$ TeV with the ATLAS detector”. In: *JHEP* 02 (2016), p. 062. DOI: [10.1007/JHEP02\(2016\)062](https://doi.org/10.1007/JHEP02(2016)062). arXiv: [1511.05542](https://arxiv.org/abs/1511.05542) [hep-ex].
- [83] ATLAS Collaboration. “A search for prompt lepton-jets in pp collisions at $\sqrt{s} = 8$ TeV with the ATLAS detector”. In: *JHEP* 02:062 (2016).
- [84] A. Falkowski et al. “Hidden Higgs decaying to lepton jets”. In: *JHEP* 05 (2010), p. 077. DOI: [10.1007/JHEP05\(2010\)077](https://doi.org/10.1007/JHEP05(2010)077). arXiv: [1002.2952](https://arxiv.org/abs/1002.2952) [hep-ph].
- [85] A. Falkowski et al. “Discovering Higgs Boson Decays to Lepton Jets at Hadron Colliders”. In: *Phys. Rev. Lett.* 105 (2010), p. 241801. DOI: [10.1103/PhysRevLett.105.241801](https://doi.org/10.1103/PhysRevLett.105.241801). arXiv: [1007.3496](https://arxiv.org/abs/1007.3496) [hep-ph].
- [86] D. Curtin et al. “Illuminating dark photons with high-energy colliders”. In: *JHEP* 02 (2015), p. 157. DOI: [10.1007/JHEP02\(2015\)157](https://doi.org/10.1007/JHEP02(2015)157). arXiv: [1412.0018](https://arxiv.org/abs/1412.0018) [hep-ph].
- [87] David Curtin et al. “Exotic decays of the 125 GeV Higgs boson”. In: *Phys. Rev. D* 90.7 (2014), p. 075004. DOI: [10.1103/PhysRevD.90.075004](https://doi.org/10.1103/PhysRevD.90.075004). arXiv: [1312.4992](https://arxiv.org/abs/1312.4992) [hep-ph].
- [88] L. Evans et al. “LHC Machine”. In: *JINTS* 3:S08001 (2008).
- [89] M. Benedikt et al. “LHC Design Report. 3. The LHC injector chain”. In: (2004).
- [90] ATLAS Collaboration. “The ATLAS Experiment at the CERN Large Hadron Collider”. In: *JINTS* 3:S08003 (2008).
- [91] CMS Collaboration. “The CMS Experiment at the CERN LHC”. In: *JINTS* 3:S08004 (2008).
- [92] ALICE Collaboration. “The ALICE experiment at the CERN LHC”. In: *JINTS* 3:S08002 (2008).
- [93] ATLAS Collaboration. “Luminosity determination in pp collisions at $\sqrt{s} = 13$ TeV using the ATLAS detector at the LHC”. In: *ATLAS-CONF-2019* 021 (2019).
- [94] Ruth Pöttgen. *Proton-Proton Collisions*. Cham: Springer International Publishing, 2016, pp. 45–60. ISBN: 978-3-319-41045-6. DOI: [10.1007/978-3-319-41045-6_4](https://doi.org/10.1007/978-3-319-41045-6_4). URL: https://doi.org/10.1007/978-3-319-41045-6_4.

- [95] The ATLAS collaboration. “Operation of the ATLAS trigger system in Run 2”. In: *Journal of Instrumentation* 15.10 (Oct. 2020), P10004. DOI: [10.1088/1748-0221/15/10/P10004](https://doi.org/10.1088/1748-0221/15/10/P10004). URL: <https://dx.doi.org/10.1088/1748-0221/15/10/P10004>.
- [96] Georges Aad et al. “ATLAS data quality operations and performance for 2015–2018 data-taking”. In: *JINST* 15.04 (2020), P04003. DOI: [10.1088/1748-0221/15/04/P04003](https://doi.org/10.1088/1748-0221/15/04/P04003). arXiv: [1911.04632](https://arxiv.org/abs/1911.04632) [[physics.ins-det](https://arxiv.org/archive/hep)].
- [97] ATLAS Collaboration. “Luminosity determination in pp collisions at $\sqrt{s} = 13$ TeV using the ATLAS detector at the LHC”. In: (2022). arXiv: [2212.09379](https://arxiv.org/abs/2212.09379) [[hep-ex](https://arxiv.org/archive/hep)].
- [98] Joao Pequenaio. “Computer generated image of the whole ATLAS detector”. 2008. URL: <https://cds.cern.ch/record/1095924>.
- [99] Joao Pequenaio and Paul Schaffner. “How ATLAS detects particles: diagram of particle paths in the detector”. 2013. URL: <https://cds.cern.ch/record/1505342>.
- [100] *ATLAS technical coordination: Technical Design Report*. Technical design report. ATLAS. Geneva: CERN, 1999. URL: <https://cds.cern.ch/record/385482>.
- [101] ATLAS Collaboration. “ATLAS magnet system: Technical design report”. In: (1997).
- [102] ATLAS Collaboration. “Track Reconstruction Performance of the ATLAS Inner Detector at $\sqrt{s} = 13$ TeV”. In: *ATL-PHYS-PUB-2015* 018 (2015).
- [103] ATLAS Collaboration. “Experiment Briefing: Keeping the ATLAS Inner Detector in perfect alignment”. General Photo. 2020. URL: <https://cds.cern.ch/record/2723878>.
- [104] Lucia Masetti. “ATLAS Inner Detector: Commissioning with Cosmics Data”. In: *Proceedings of European Physical Society Europhysics Conference on High Energy Physics — PoS(EPS-HEP 2009)*. Vol. 084. 2010, p. 127. DOI: [10.22323/1.084.0127](https://doi.org/10.22323/1.084.0127).
- [105] ATLAS Collaboration. “Construction, assembly and tests of the ATLAS electromagnetic barrel calorimeter”. In: *Nucl. Instrum. Meth.* A558:388–418 (2006).
- [106] ATLAS Collaboration. *ATLAS tile calorimeter: Technical design report*. 1996.
- [107] ATLAS Collaboration. “Construction, assembly and testing of the ATLAS hadronic end-cap calorimeter”. In: *JINST* 2:P05005 (2007).
- [108] ATLAS Collaboration. *ATLAS muon spectrometer: Technical design report*. 1997.
- [109] ATLAS Collaboration. “2015 start-up trigger menu and initial performance assessment of the ATLAS trigger using Run-2 data”. In: *ATL-DAQ-PUB-2016* 001 (2016).
- [110] ATLAS Collaboration. “Performance of the ATLAS Trigger System in 2015”. In: *Eur. Phys. J.* C77(5):317 (2017).

- [111] J. Alwall et al. “The automated computation of tree-level and next-to-leading order differential cross sections, and their matching to parton shower simulations”. In: *JHEP* 07 (2014), p. 079. DOI: [10.1007/JHEP07\(2014\)079](https://doi.org/10.1007/JHEP07(2014)079). arXiv: [1405.0301](https://arxiv.org/abs/1405.0301) [hep-ph].
- [112] T. Sjöstrand, S. Mrenna, and P. Skands. “A brief introduction to PYTHIA 8.1”. In: *Comput. Phys. Commun.* 178 (2008), pp. 852–867. DOI: [10.1016/j.cpc.2008.01.036](https://doi.org/10.1016/j.cpc.2008.01.036). arXiv: [0710.3820](https://arxiv.org/abs/0710.3820) [hep-ph].
- [113] ATLAS Collaboration. *The Pythia 8 A3 tune description of ATLAS minimum bias and inelastic measurements incorporating the Donnachie–Landshoff diffractive model*. ATL-PHYS-PUB-2016-017. 2016. URL: <https://cds.cern.ch/record/2206965>.
- [114] NNPDF Collaboration, Richard D. Ball, et al. “Parton distributions with LHC data”. In: *Nucl. Phys. B* 867 (2013), p. 244. DOI: [10.1016/j.nuclphysb.2012.10.003](https://doi.org/10.1016/j.nuclphysb.2012.10.003). arXiv: [1207.1303](https://arxiv.org/abs/1207.1303) [hep-ph].
- [115] Torbjorn Sjöstrand, Stephen Mrenna, and Peter Z. Skands. “PYTHIA 6.4 physics and manual”. In: *JHEP* 05 (2006), p. 026. DOI: [10.1088/1126-6708/2006/05/026](https://doi.org/10.1088/1126-6708/2006/05/026). arXiv: [hep-ph/0603175](https://arxiv.org/abs/hep-ph/0603175).
- [116] S. Frixione et al. “A positive-weight next-to-leading-order Monte Carlo for heavy flavour hadroproduction”. In: *JHEP* 09 (2007), p. 126. DOI: [10.1088/1126-6708/2007/09/126](https://doi.org/10.1088/1126-6708/2007/09/126). arXiv: [0707.3088](https://arxiv.org/abs/0707.3088) [hep-ph].
- [117] T. Gleisberg et al. “Event generation with SHERPA 1.1”. In: *JHEP* 02 (2009), p. 007. DOI: [10.1088/1126-6708/2009/02/007](https://doi.org/10.1088/1126-6708/2009/02/007). arXiv: [0811.4622](https://arxiv.org/abs/0811.4622) [hep-ph].
- [118] M. Bahr et al. “Herwig++ Physics and Manual”. In: *Eur. Phys. J. C* 58 (2008), pp. 639–707. DOI: [10.1140/epjc/s10052-008-0798-9](https://doi.org/10.1140/epjc/s10052-008-0798-9). arXiv: [0803.0883](https://arxiv.org/abs/0803.0883) [hep-ph].
- [119] V. N. Ivanchenko. “Geant4 toolkit for simulation of HEP experiments”. In: *Nucl. Instrum. Meth. A* 502 (2003), pp. 666–668. DOI: [10.1016/S0168-9002\(03\)00538-2](https://doi.org/10.1016/S0168-9002(03)00538-2).
- [120] ATLAS Collaboration. “The ATLAS Simulation Infrastructure”. In: *Eur. Phys. J. C* 70 (2010), p. 823. DOI: [10.1140/epjc/s10052-010-1429-9](https://doi.org/10.1140/epjc/s10052-010-1429-9). arXiv: [1005.4568](https://arxiv.org/abs/1005.4568) [physics.ins-det].
- [121] R. Frühwirth. “Application of Kalman filtering to track and vertex fitting”. In: *Nuclear Instruments and Methods in Physics Research Section A: Accelerators, Spectrometers, Detectors and Associated Equipment* 262.2 (1987), pp. 444–450. ISSN: 0168-9002. DOI: [https://doi.org/10.1016/0168-9002\(87\)90887-4](https://doi.org/10.1016/0168-9002(87)90887-4). URL: <https://www.sciencedirect.com/science/article/pii/0168900287908874>.
- [122] ATLAS Collaboration. “Performance of the ATLAS track reconstruction algorithms in dense environments in LHC Run 2”. In: *Eur. Phys. J. C* 77 (2017), p. 673. DOI: [10.1140/epjc/s10052-017-5225-7](https://doi.org/10.1140/epjc/s10052-017-5225-7). arXiv: [1704.07983](https://arxiv.org/abs/1704.07983) [hep-ex].

- [123] ATLAS Collaboration. “Reconstruction of primary vertices at the ATLAS experiment in Run 1 proton–proton collisions at the LHC”. In: *Eur. Phys. J. C* 77 (2017), p. 332. DOI: [10.1140/epjc/s10052-017-4887-5](https://doi.org/10.1140/epjc/s10052-017-4887-5). arXiv: [1611.10235](https://arxiv.org/abs/1611.10235) [hep-ex].
- [124] ATLAS Collaboration. “Topological cell clustering in the ATLAS calorimeters and its performance in LHC Run 1”. In: *Eur. Phys. J. C* 77 (2017), p. 490. DOI: [10.1140/epjc/s10052-017-5004-5](https://doi.org/10.1140/epjc/s10052-017-5004-5). arXiv: [1603.02934](https://arxiv.org/abs/1603.02934) [hep-ex].
- [125] Stephen D. Ellis and Davison E. Soper. “Successive combination jet algorithm for hadron collisions”. In: *Phys. Rev. D* 48 (1993), pp. 3160–3166. DOI: [10.1103/PhysRevD.48.3160](https://doi.org/10.1103/PhysRevD.48.3160). arXiv: [hep-ph/9305266](https://arxiv.org/abs/hep-ph/9305266).
- [126] Yu.L. Dokshitzer et al. “Better jet clustering algorithms”. In: *Journal of High Energy Physics* 1997.08 (Sept. 1997), p. 001. DOI: [10.1088/1126-6708/1997/08/001](https://doi.org/10.1088/1126-6708/1997/08/001). URL: <https://dx.doi.org/10.1088/1126-6708/1997/08/001>.
- [127] Matteo Cacciari, Gavin P. Salam, and Gregory Soyez. “The anti- k_t jet clustering algorithm”. In: *JHEP* 04 (2008), p. 063. DOI: [10.1088/1126-6708/2008/04/063](https://doi.org/10.1088/1126-6708/2008/04/063). arXiv: [0802.1189](https://arxiv.org/abs/0802.1189) [hep-ph].
- [128] ATLAS Collaboration. “Jet reconstruction and performance using particle flow with the ATLAS Detector”. In: *Eur. Phys. J. C* 77 (2017), p. 466. DOI: [10.1140/epjc/s10052-017-5031-2](https://doi.org/10.1140/epjc/s10052-017-5031-2). arXiv: [1703.10485](https://arxiv.org/abs/1703.10485) [hep-ex].
- [129] ATLAS Collaboration. “Optimisation of large-radius jet reconstruction for the ATLAS detector in 13 TeV proton–proton collisions”. In: *Eur. Phys. J. C* 81 (2020), p. 334. DOI: [10.1140/epjc/s10052-021-09054-3](https://doi.org/10.1140/epjc/s10052-021-09054-3). arXiv: [2009.04986](https://arxiv.org/abs/2009.04986) [hep-ex].
- [130] David Krohn, Jesse Thaler, and Lian-Tao Wang. “Jets with Variable R”. In: *JHEP* 06 (2009), p. 059. DOI: [10.1088/1126-6708/2009/06/059](https://doi.org/10.1088/1126-6708/2009/06/059). arXiv: [0903.0392](https://arxiv.org/abs/0903.0392) [hep-ph].
- [131] ATLAS Collaboration. “Jet energy scale and resolution measured in proton–proton collisions at $\sqrt{s} = 13$ TeV with the ATLAS detector”. In: *Eur. Phys. J. C* 81 (2020), p. 689. DOI: [10.1140/epjc/s10052-021-09402-3](https://doi.org/10.1140/epjc/s10052-021-09402-3). arXiv: [2007.02645](https://arxiv.org/abs/2007.02645) [hep-ex].
- [132] ATLAS Collaboration. “Jet energy scale measurements and their systematic uncertainties in proton–proton collisions at $\sqrt{s} = 13$ TeV with the ATLAS detector”. In: *Phys. Rev. D* 96 (2017), p. 072002. DOI: [10.1103/PhysRevD.96.072002](https://doi.org/10.1103/PhysRevD.96.072002). arXiv: [1703.09665](https://arxiv.org/abs/1703.09665) [hep-ex].
- [133] ATLAS Collaboration. *Tagging and suppression of pileup jets with the ATLAS detector*. ATLAS-CONF-2014-018. 2014. URL: <https://cds.cern.ch/record/1700870>.
- [134] ATLAS Collaboration. *Optimisation and performance studies of the ATLAS b-tagging algorithms for the 2017-18 LHC run*. ATL-PHYS-PUB-2017-013. 2017. URL: <https://cds.cern.ch/record/2273281>.

- [135] ATLAS Collaboration. *Secondary vertex finding for jet flavour identification with the ATLAS detector*. ATL-PHYS-PUB-2017-011. 2017. URL: <https://cds.cern.ch/record/2270366>.
- [136] ATLAS Collaboration. *Topological b -hadron decay reconstruction and identification of b -jets with the JetFitter package in the ATLAS experiment at the LHC*. ATL-PHYS-PUB-2018-025. 2018. URL: <https://cds.cern.ch/record/2645405>.
- [137] ATLAS Collaboration. *Identification of Jets Containing b -Hadrons with Recurrent Neural Networks at the ATLAS Experiment*. ATL-PHYS-PUB-2017-003. 2017. URL: <https://cds.cern.ch/record/2255226>.
- [138] ATLAS Collaboration. “ATLAS b -jet identification performance and efficiency measurement with $t\bar{t}$ events in pp collisions at $\sqrt{s} = 13$ TeV”. In: *Eur. Phys. J. C* 79 (2019), p. 970. DOI: [10.1140/epjc/s10052-019-7450-8](https://doi.org/10.1140/epjc/s10052-019-7450-8). arXiv: [1907.05120](https://arxiv.org/abs/1907.05120) [hep-ex].
- [139] “ $E_{\text{T}}^{\text{miss}}$ performance in the ATLAS detector using 2015-2016 LHC pp collisions”. In: (June 2018).
- [140] Georges Aad et al. “Electron and photon performance measurements with the ATLAS detector using the 2015–2017 LHC proton-proton collision data”. In: *JINST* 14.12 (2019), P12006. DOI: [10.1088/1748-0221/14/12/P12006](https://doi.org/10.1088/1748-0221/14/12/P12006). arXiv: [1908.00005](https://arxiv.org/abs/1908.00005) [hep-ex].
- [141] ATLAS Collaboration. *Improved electron reconstruction in ATLAS using the Gaussian Sum Filter-based model for bremsstrahlung*. ATLAS-CONF-2012-047. 2012. URL: <https://cds.cern.ch/record/1449796>.
- [142] ATLAS Collaboration. “Electron reconstruction and identification in the ATLAS experiment using the 2015 and 2016 LHC proton-proton collision data at $\sqrt{s} = 13$ TeV”. In: *Eur. Phys. J. C* 79(8):639 (2019).
- [143] ATLAS Collaboration. “Muon reconstruction and identification efficiency in ATLAS using the full Run 2 pp collision data set at $\sqrt{s} = 13$ TeV”. In: *Eur. Phys. J. C* 81 (2021), p. 578. DOI: [10.1140/epjc/s10052-021-09233-2](https://doi.org/10.1140/epjc/s10052-021-09233-2). arXiv: [2012.00578](https://arxiv.org/abs/2012.00578) [hep-ex].
- [144] ATLAS Collaboration. “Identification and energy calibration of hadronically decaying tau leptons with the ATLAS experiment in pp collisions at $\sqrt{s} = 8$ TeV”. In: *Eur. Phys. J. C* 75 (2015), p. 303. DOI: [10.1140/epjc/s10052-015-3500-z](https://doi.org/10.1140/epjc/s10052-015-3500-z). arXiv: [1412.7086](https://arxiv.org/abs/1412.7086) [hep-ex].
- [145] ATLAS Collaboration. *Reconstruction, Energy Calibration, and Identification of Hadronically Decaying Tau Leptons in the ATLAS Experiment for Run-2 of the LHC*. ATL-PHYS-PUB-2015-045. 2015. URL: <https://cds.cern.ch/record/2064383>.
- [146] The NNPDF Collaboration, Richard D. Ball, et al. “Parton distributions for the LHC run II”. In: *JHEP* 04 (2015), p. 040. DOI: [10.1007/JHEP04\(2015\)040](https://doi.org/10.1007/JHEP04(2015)040). arXiv: [1410.8849](https://arxiv.org/abs/1410.8849) [hep-ph].

- [147] P. Z. Skands. “Tuning Monte Carlo generators: The Perugia tunes”. In: *Phys. Rev. D* 82 (2010), p. 074018. DOI: [10.1103/PhysRevD.82.074018](https://doi.org/10.1103/PhysRevD.82.074018). arXiv: [1005.3457](https://arxiv.org/abs/1005.3457) [hep-ph].
- [148] H. L. Lai et al. “New parton distributions for collider physics”. In: *Phys. Rev. D* 82 (2010), p. 074024. DOI: [10.1103/PhysRevD.82.074024](https://doi.org/10.1103/PhysRevD.82.074024). arXiv: [1007.2241](https://arxiv.org/abs/1007.2241) [hep-ph].
- [149] J. Pumplin et al. “New Generation of Parton Distributions with Uncertainties from Global QCD Analysis”. In: *JHEP* 07 (2002), p. 012. DOI: [10.1088/1126-6708/2002/07/012](https://doi.org/10.1088/1126-6708/2002/07/012). arXiv: [hep-ph/0201195](https://arxiv.org/abs/hep-ph/0201195).
- [150] Georges Aad et al. “Performance of the ATLAS muon triggers in Run 2”. In: *JINST* 15.09 (2020), P09015. DOI: [10.1088/1748-0221/15/09/p09015](https://doi.org/10.1088/1748-0221/15/09/p09015). arXiv: [2004.13447](https://arxiv.org/abs/2004.13447) [physics.ins-det].
- [151] Georges Aad et al. “Search for chargino–neutralino pair production in final states with three leptons and missing transverse momentum in $\sqrt{s} = 13$ TeV pp collisions with the ATLAS detector”. In: *Eur. Phys. J. C* 81.12 (2021), p. 1118. DOI: [10.1140/epjc/s10052-021-09749-7](https://doi.org/10.1140/epjc/s10052-021-09749-7). arXiv: [2106.01676](https://arxiv.org/abs/2106.01676) [hep-ex].
- [152] ATLAS Statistics Forum. “ABCD Method in Searches”. In: (). URL: <https://twiki.cern.ch/twiki/bin/view/AtlasProtected/ATLASStatisticsFAQ/ABCD.pdf>.
- [153] R. L. Workman et al. “Review of Particle Physics”. In: *PTEP* 2022 (2022), p. 083C01. DOI: [10.1093/ptep/ptac097](https://doi.org/10.1093/ptep/ptac097).
- [154] G. Avoni et al. “The new LUCID-2 detector for luminosity measurement and monitoring in ATLAS”. In: *JINST* 13.07 (2018), P07017. DOI: [10.1088/1748-0221/13/07/P07017](https://doi.org/10.1088/1748-0221/13/07/P07017).
- [155] Rachel Jordan Hyneman. “Measuring Higgs Boson Couplings, including to the Top Quark, in the Diphoton Decay Channel with Run 2 Data Collected by the ATLAS Detector”. Presented 04 Feb 2020. Michigan U., 2020. URL: <https://cds.cern.ch/record/2712576>.
- [156] Mark N. Gibbs. “Bayesian Gaussian Processes for Regression and Classification”. Presented 04 Feb 2020. Cambridge U., 2020. URL: <https://cds.cern.ch/record/2712576>.
- [157] “Recommendations for the Modeling of Smooth Backgrounds”. In: (2020).
- [158] A. L. Read. “Presentation of search results: the CL_s technique”. In: *J. Phys. G* 28 (2002), pp. 2693–2704. DOI: [10.1088/0954-3899/28/10/313](https://doi.org/10.1088/0954-3899/28/10/313).
- [159] Glen Cowan et al. “Asymptotic formulae for likelihood-based tests of new physics”. In: *Eur. Phys. J. C* 71 (2011), p. 1554. DOI: [10.1140/epjc/s10052-011-1554-0](https://doi.org/10.1140/epjc/s10052-011-1554-0). arXiv: [1007.1727](https://arxiv.org/abs/1007.1727) [physics.data-an]. Erratum: in: *Eur. Phys. J. C* 73 (2013), p. 2501. DOI: [10.1140/epjc/s10052-013-2501-z](https://doi.org/10.1140/epjc/s10052-013-2501-z).

- [160] Lawrence Lee et al. “Collider searches for long-lived particles beyond the Standard Model”. In: *Progress in Particle and Nuclear Physics* 106 (2019), pp. 210–255. ISSN: 0146-6410. DOI: <https://doi.org/10.1016/j.pnpnp.2019.02.006>. URL: <https://www.sciencedirect.com/science/article/pii/S0146641019300109>.
- [161] Alimena J. et al. “Searching for long-lived particles beyond the Standard Model at the Large Hadron Collider”. In: *Journal of Physics G: Nuclear and Particle Physics* 47.9 (Sept. 2020), p. 090501. DOI: [10.1088/1361-6471/ab4574](https://doi.org/10.1088/1361-6471/ab4574). URL: <https://dx.doi.org/10.1088/1361-6471/ab4574>.
- [162] Kyle Cranmer and Itay Yavin. “RECAST: Extending the Impact of Existing Analyses”. In: *JHEP* 04 (2011), p. 038. DOI: [10.1007/JHEP04\(2011\)038](https://doi.org/10.1007/JHEP04(2011)038). arXiv: [1010.2506](https://arxiv.org/abs/1010.2506) [hep-ex].
- [163] ATLAS Collaboration. *ATLAS Pythia 8 tunes to 7 TeV data*. ATL-PHYS-PUB-2014-021. 2014. URL: <https://cds.cern.ch/record/1966419>.
- [164] J. Baglio et al. “Release Note - VBFNLO 2.7.0”. In: (Apr. 2014). arXiv: [1404.3940](https://arxiv.org/abs/1404.3940) [hep-ph].
- [165] Radja Boughezal, Xiaohui Liu, and Frank Petriello. “W-boson plus jet differential distributions at NNLO in QCD”. In: *Phys. Rev. D* 94.11 (2016), p. 113009. DOI: [10.1103/PhysRevD.94.113009](https://doi.org/10.1103/PhysRevD.94.113009). arXiv: [1602.06965](https://arxiv.org/abs/1602.06965) [hep-ph].
- [166] Radja Boughezal, Xiaohui Liu, and Frank Petriello. “Phenomenology of the Z-boson plus jet process at NNLO”. In: *Phys. Rev. D* 94.7 (2016), p. 074015. DOI: [10.1103/PhysRevD.94.074015](https://doi.org/10.1103/PhysRevD.94.074015). arXiv: [1602.08140](https://arxiv.org/abs/1602.08140) [hep-ph].
- [167] Aude Gehrmann-De Ridder et al. “The NNLO QCD corrections to Z boson production at large transverse momentum”. In: *JHEP* 07 (2016), p. 133. DOI: [10.1007/JHEP07\(2016\)133](https://doi.org/10.1007/JHEP07(2016)133). arXiv: [1605.04295](https://arxiv.org/abs/1605.04295) [hep-ph].
- [168] Ansgar Denner et al. “Electroweak corrections to monojet production at the LHC”. In: *Eur. Phys. J. C* 73.2 (2013), p. 2297. DOI: [10.1140/epjc/s10052-013-2297-x](https://doi.org/10.1140/epjc/s10052-013-2297-x). arXiv: [1211.5078](https://arxiv.org/abs/1211.5078) [hep-ph].
- [169] Stefan Kallweit et al. “NLO QCD+EW predictions for V + jets including off-shell vector-boson decays and multijet merging”. In: *JHEP* 04 (2016), p. 021. DOI: [10.1007/JHEP04\(2016\)021](https://doi.org/10.1007/JHEP04(2016)021). arXiv: [1511.08692](https://arxiv.org/abs/1511.08692) [hep-ph].
- [170] Ansgar Denner et al. “Electroweak corrections to W + jet hadroproduction including leptonic W-boson decays”. In: *JHEP* 08 (2009), p. 075. DOI: [10.1088/1126-6708/2009/08/075](https://doi.org/10.1088/1126-6708/2009/08/075). arXiv: [0906.1656](https://arxiv.org/abs/0906.1656) [hep-ph].
- [171] Ansgar Denner et al. “Electroweak corrections to dilepton + jet production at hadron colliders”. In: *JHEP* 06 (2011), p. 069. DOI: [10.1007/JHEP06\(2011\)069](https://doi.org/10.1007/JHEP06(2011)069). arXiv: [1103.0914](https://arxiv.org/abs/1103.0914) [hep-ph].
- [172] J. M. Lindert et al. “Precise predictions for V+ jets dark matter backgrounds”. In: *Eur. Phys. J. C* 77.12 (2017), p. 829. DOI: [10.1140/epjc/s10052-017-5389-1](https://doi.org/10.1140/epjc/s10052-017-5389-1). arXiv: [1705.04664](https://arxiv.org/abs/1705.04664) [hep-ph].

- [173] ATLAS Collaboration. “Characterisation and mitigation of beam-induced backgrounds observed in the ATLAS detector during the 2011 proton–proton run”. In: *JINST* 8 (2013), P07004. DOI: [10.1088/1748-0221/8/07/P07004](https://doi.org/10.1088/1748-0221/8/07/P07004). arXiv: [1303.0223](https://arxiv.org/abs/1303.0223) [hep-ex].
- [174] Alexander L. Read. “Presentation of search results: the CL_S technique”. In: *J. Phys. G* 28 (2002), p. 2693. DOI: [10.1088/0954-3899/28/10/313](https://doi.org/10.1088/0954-3899/28/10/313).
- [175] ATLAS Collaboration. *Combination of searches for invisible Higgs boson decays with the ATLAS experiment*. ATLAS-CONF-2020-052. 2020. URL: <https://cds.cern.ch/record/2743055>.
- [176] *Long-lived particle summary plots for Hidden Sector and Dark Photon models*. Tech. rep. All figures including auxiliary figures are available at <https://atlas.web.cern.ch/Atlas> PHYS-PUB-2022-007. Geneva: CERN, 2022. URL: <https://cds.cern.ch/record/2803320>.
- [177] P. Ilten et al. “Serendipity in dark photon searches”. In: *JHEP* 06 (2018), p. 004. DOI: [10.1007/JHEP06\(2018\)004](https://doi.org/10.1007/JHEP06(2018)004). arXiv: [1801.04847](https://arxiv.org/abs/1801.04847) [hep-ph].
- [178] M. Aaboud et al. “Search for the Higgs boson produced in association with a vector boson and decaying into two spin-zero particles in the $H \rightarrow aa \rightarrow 4b$ channel in pp collisions at $\sqrt{s} = 13$ TeV with the ATLAS detector”. In: *JHEP* 10 (2018), p. 031. DOI: [10.1007/JHEP10\(2018\)031](https://doi.org/10.1007/JHEP10(2018)031). arXiv: [1806.07355](https://arxiv.org/abs/1806.07355) [hep-ex].
- [179] ATLAS Collaboration. “Search for long-lived neutral particles in pp collisions at $\sqrt{s} = 13$ TeV that decay into displaced hadronic jets in the ATLAS calorimeter”. In: (2019). arXiv: [1902.03094](https://arxiv.org/abs/1902.03094) [hep-ex].
- [180] ATLAS Collaboration. *Search for exotic decays of the Higgs boson to long-lived particles in pp collisions at $\sqrt{s} = 13$ TeV using displaced vertices in the ATLAS inner detector*. ATLAS-CONF-2021-005. 2021. URL: <https://cds.cern.ch/record/2759209>.
- [181] I. Zurbano Fernandez et al. “High-Luminosity Large Hadron Collider (HL-LHC): Technical design report”. In: 10/2020 (Dec. 2020). Ed. by I. Béjar Alonso et al. DOI: [10.23731/CYRM-2020-0010](https://doi.org/10.23731/CYRM-2020-0010).
- [182] *Technical Design Report for the ATLAS Inner Tracker Pixel Detector*. Tech. rep. Geneva: CERN, 2017. DOI: [10.17181/CERN.FOZZ.ZP3Q](https://doi.org/10.17181/CERN.FOZZ.ZP3Q). URL: <https://cds.cern.ch/record/2285585>.
- [183] *Technical Design Report for the ATLAS Inner Tracker Strip Detector*. Tech. rep. Geneva: CERN, 2017. URL: <https://cds.cern.ch/record/2257755>.
- [184] *Technical Design Report: A High-Granularity Timing Detector for the ATLAS Phase-II Upgrade*. Tech. rep. Geneva: CERN, 2020. URL: <https://cds.cern.ch/record/2719855>.
- [185] *ATLAS Liquid Argon Calorimeter Phase-II Upgrade: Technical Design Report*. Tech. rep. Geneva: CERN, 2017. DOI: [10.17181/CERN.6QIO.YGHO](https://doi.org/10.17181/CERN.6QIO.YGHO). URL: <https://cds.cern.ch/record/2285582>.

- [186] T Kawamoto et al. *New Small Wheel Technical Design Report*. Tech. rep. ATLAS New Small Wheel Technical Design Report. 2013. URL: <https://cds.cern.ch/record/1552862>.
- [187] *Technical Design Report for the Phase-II Upgrade of the ATLAS Muon Spectrometer*. Tech. rep. Geneva: CERN, 2017. URL: <https://cds.cern.ch/record/2285580>.
- [188] *Technical Design Report for the Phase-II Upgrade of the ATLAS TDAQ System*. Tech. rep. Geneva: CERN, 2017. DOI: [10.17181/CERN.2LBB.4IAL](https://cds.cern.ch/record/2285584). URL: <https://cds.cern.ch/record/2285584>.